MEMBRANES FOR HEAT INTEGRATED CARBON DIOXIDE CAPTURE VIA COLD CONDITIONS OPERATION

A Dissertation
Presented to
The Academic Faculty

By

Lu (Lucy) Liu

In Partial Fulfillment
Of the Requirements for the Degree
Doctor of Philosophy in the
School of Chemical & Biomolecular Engineering

Georgia Institute of Technology
May 2015

MEMBRANES FOR HEAT INTEGRATED CARBON DIOXIDE CAPTURE VIA COLD CONDITIONS OPERATION

Approved by:

Dr. William J. Koros, Advisor
School of Chemical & Biomolecular Engineering
Georgia Institute of Technology

Dr. Haskell Beckham
School of Materials Science & Engineering
Georgia Institute of Technology

Dr. Dennis W. Hess
School of Chemical & Biomolecular Engineering
Georgia Institute of Technology

Dr. Edgar S. Sanders
Global Lab Director-Process Engineering
American Air Liquide

Dr. J. Carson Meredith
School of Chemical & Biomolecular Engineering
Georgia Institute of Technology

Date Approved: Dec. 17, 2014

Dedicated to
My dear parents

ACKNOWLEDGEMENTS

The experience in graduate school is a precious and unique stop in my life journey. I am truly grateful to everyone who has accompanied and supported me through the peaks and valleys in obtaining a Ph.D. degree.

First of all, I want to express my sincere gratitude to my advisor, Dr. William J. Koros. He gave me the opportunity to start my Ph.D. journey in such an excellent Chemical Engineering program and to study under his guidance. Our first met in Dalian was a turning point in my life, and I will never forget that chilly winter. To me, he is not only a mentor, but a parent and friend. His constant encouragement has been the most important driving force for my growth. When I was doubtful about myself, it was him who made me regain confidence. Apart from professional advices, he has been amazingly generous with attention on life wisdom based on his experience. His enthusiasm for research, dedication to work, modesty, humor and nice way to deal with people have been and will continue to influence me profoundly. I will carry with me the invaluable lessons learned from him in my new life journey.

I would also like to thank members of my dissertation committee - Dr. Ed Sanders, Dr. Dennis Hess, Dr. Carson Meredith and Dr. Haskell Beckham. I appreciate all your constructive feedback and valuable inputs that led to an improved piece of work.

To my colleges in the Koros Research Group, past and present; it has been a great pleasure to work with all of you. Special thanks to Dr. J.R. Johnson and Dr. Oguz Karvan for building the sub-ambient lab for my project. My work would not have been possible without them. Also, I would like to recognize Dr. Liren Xu for generously offering me

his fibers and for all the technical discussions. I would like to recognize Dr. Canghai Ma for teaching me fiber spinning and other technical skills. I am also very thankful for Dr. Brian Kraftschik, Dr. Justin Vaughn, Dr. Nitesh Bhuwania and my sub-ambient lab fellow John Hessler for their technical assistance. Especially John, who helped me troubleshoot the GC and let me use his cold sorption systems. I am blessed to have Ying Labreche and Shilu Fu as my bosom friends, who share everything with me. The interactions with them made my stay in the office more joyful. Besides, I want to thank them for their innumerable help in both work and life. I would also like to thank Shweta Karwa and Steven Burgess for their support during job hunting and information sharing. There are many more to thank for their friendship and discussions: Dr. Wulin Qiu, Dr. Kuang Zhang, Dr. Chen Zhang, Dr. Xue Ning, Dr. Carine Achoundong, Dr. Fuyue Li, Dr. Shouliang Yi, Dr. Vinod Babu, Gram Wenz and Yu-Han Chu. Last but not the least, I would like to express my gratitude to Michelle Martin for her essential assistance with the smooth operation of our large research group.

Meanwhile, I am very fortunate to have many other great friends at Georgia Tech, who have peppered my stay in graduate school with cherished memories. I would like to thank them for the good times, which made my graduate life more colorful and cheerful. I could never do justice if I were to name every one of them. However, I would like to mention two dear friends, Yu Ning and Jialiang Wang, who are not here at Georgia Tech, but supported me spiritually throughout the stressful periods.

Most importantly, to my family, they supported me with constant care and love. I would like to thank my father, Xingwen Liu, for being so open-minded and always respecting my decisions. To my mother, Guimin Xu, who is my strongest supporter no

matter where I am. To my brother, Shuo Liu, for taking care of our parents while I am thousands miles away. I am also beyond grateful to meet my fiancé, Qingyang Wang, at Georgia Tech. He always has faith in me and helps me improve in every aspect, both professionally and personally. He made me happier, prettier and more confident. I know I always have him to count on when I am helpless.

Finally, I would like to thank American Air Liquide for the generous funding for this project.

TABLE OF CONTENTS

LIST OF TABLES

Page

LIST OF FIGURES

Page

SUMMARY

Flue gas carbon dioxide emissions from coal-based power plants are suggested as a factor causing climate change. The U.S. Department of Energy (DOE) is actively pursuing the goal of achieving at least 90 % CO_2 removal from flue gas, with less than 35 % increase in the cost of delivered electricity. Three technological pathways have been suggested for flue gas CO_2 capture, among which the post-combustion capture scheme has the greatest near-term potential. Membranes are attractive for this application; however, the low CO_2 concentration and the low feed pressure of flue gas result in a high energy penalty due to low membrane driving force and large capture system requirements. To achieve cost effective CO_2 capture, a hybrid membrane and cryogenic distillation process was developed at American Air Liquide, which significantly reduced the overall energy penalty. The low cost commercially available Air Liquide membranes showed an unprecedented combination of permeability and selectivity at cold conditions for the important CO_2/N_2 penetrant pair; however, the underlying reason was not clear. The overarching goal of this research was to clarify fundamentals of the cold membrane CO_2/N_2 separation process, in order to engineer membrane performance and identify second generation improved membrane materials for this application. The primary target to address in this work is to understand the phenomena of cold temperature CO_2 and N_2 permeation in glassy polyimide membranes.

The Matrimid® 5218 was chosen as a starting membrane material, and the asymmetric hollow fiber configuration was investigated intensively with focus on the morphology of the membrane's selective skin layer. Hollow fiber membranes with

"homogeneous dense" and "fused nodular" selective layers were successfully formed. Different skin formation mechanisms were pursued. In the formation of the nodular skins, phase separation in the skin layer was induced, and the SEM images of resultant membranes confirmed the formation of nodules in the selective layer.

The PDMS post-treated nodular fibers showed better cold performance than the dense fibers under bore side feed. A hypothesis with regards to the different morphologies of the selective layers was proposed. The nodular skin was envisioned to be comprised of several layers of "nodules", and its higher selectivity was hypothesized to result from enhanced sorption selectivity as well as enhanced diffusion selectivity due to the dilation and orientation of the inter-nodular domains. Enhanced sorption selectivity was believed to arise from increased sorption capacity due to the introduction of more Langmuir sites coupled with the stronger competitive power of CO_2 molecules for the sorption sites. Enhanced diffusion selectivity was believed to arise from a local orientation of polymer chain segments due to the uniaxial draw of the selective layer, resulting in increased size discrimination capability. This hypothesis was supported by indirect evidences.

Based on the understanding of cold CO_2 and N_2 transport in Matrimid® hollow fiber membranes, a second generation of cold membranes with superior performance was developed. The high free volume, rigid 6FDA/BPDA-DAM asymmetric hollow fiber membranes with both dense and nodular selective layers were successfully formed, which showed similar selectivity but much higher permeance than the high performing nodular Matrimid® hollow fiber membranes.

CHAPTER 1

INTRODUCTION

1.1 Carbon dioxide emissions

There is growing consensus that human-related carbon dioxide (CO_2) emissions are contributing to a warming world [1, 2]. Climate scientists observed that the carbon dioxide concentrations in the atmosphere have been increasing exponentially over the past century, from a pre-industrial value of about 280 ppm to 394 ppm in 2012 [3, 4]. The atmospheric carbon dioxide concentration in 2012 was about 40 % higher than in the mid-1800s, with an average growth of 2 ppm/year in the last ten years. Figure 1.1 shows the monthly mean atmospheric carbon dioxide concentration measured at Mauna Loa Observatory, Hawaii, since 1958. On May 9, 2013, atmospheric carbon dioxide concentration reached 400 ppm for the first time in history. According to the prediction of climate models, this value will increase to 540-970 ppm by 2100 if no carbon dioxide emission mitigation measure is carried out [1].

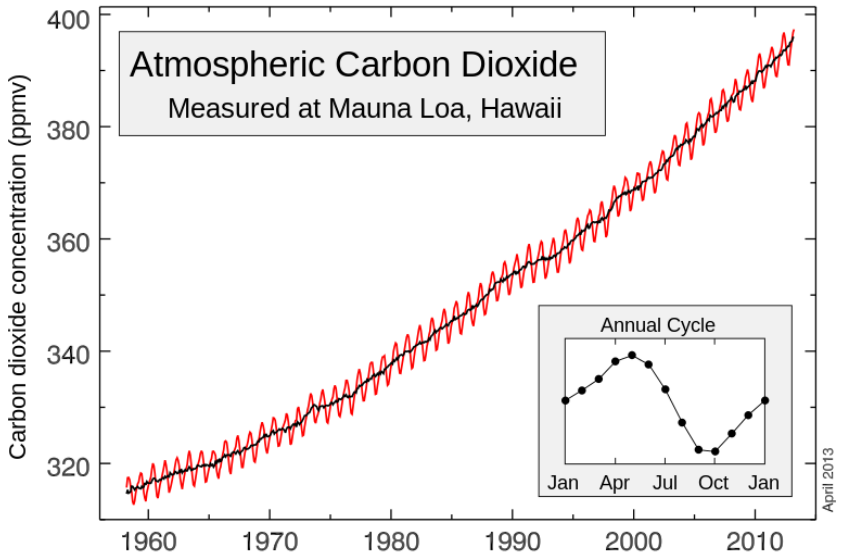

Figure 1.1: Monthly mean atmospheric carbon dioxide concentration measured at Mauna Loa Observatory, Hawaii.

1.1.1 Sources of carbon dioxide emissions

Among the many human activities that produce carbon dioxide, the combustion of fossil fuels (coal, oil and natural gas) is the largest source of CO_2 emissions. Fossil fuels generate the majority of the world energy. Due to worldwide economic growth and development, the demand for energy is increasing. Global total primary energy supply (TPES) more than doubled between 1971 and 2011 (Figure 1.2). In 2011, fossil fuels generated 82 % of the global total primary energy supply. The International Energy Agency (IEA) statistics show that annual CO_2 emissions from fossil fuel combustion increased dramatically from near zero before the Industrial Revolution to over 13 $GtCO_2$ in 2011 [4].

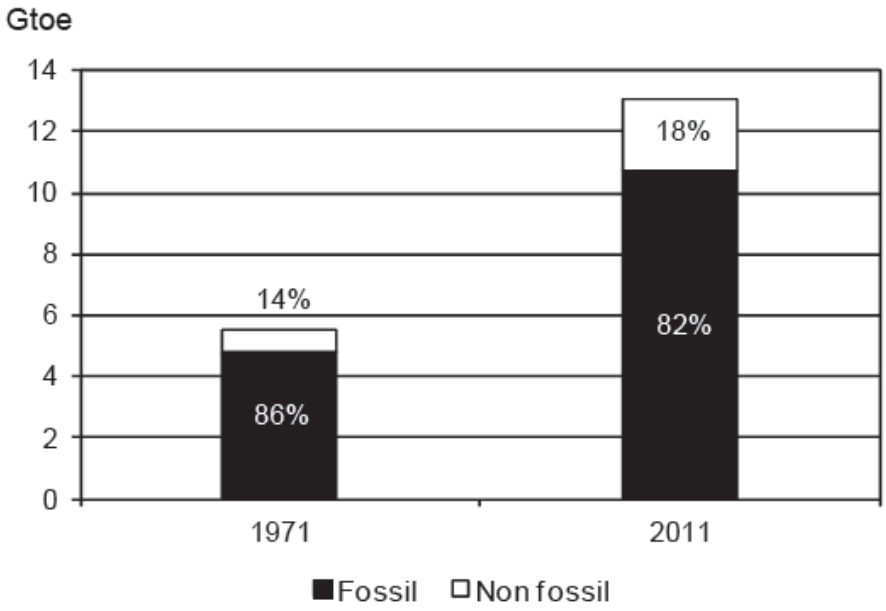

Figure 1.2: Global total primary energy supply (TPES) in 1971 and 2011, including international bunkers [4].

1.1.2 Carbon dioxide emissions from coal combustion

Coal, a main component of fossil fuels, provides the lowest cost method of producing electric power compared to oil and gas, and is relatively abundant in large energy-consuming nations. The combustion of coal generates the largest share of electricity in the United States (Figure 1.3). Worldwide, the burning of coal contributes to more than one-third of the anthropogenic CO_2 emissions. Figure 1.4 shows the history of coal shares in global CO_2 emissions. In the last ten years, the CO_2 emissions from coal combustion increased rapidly and surpassed oil to become the largest emission source. Due to the heavy carbon content per unit of energy released by coal combustion, it is nearly twice as emission intensive as natural gas [4]. However, in the near future, coal is expected to continue to play a critical role in powering the world's electricity generation.

A recent MIT study concluded that coal use will continue to increase under any foreseeable scenario [5]. The average age of the coal-based power plants in the United States is around 35 years [5]. With current life-extension capabilities, many of these units could, on-average, operate another 30+ years. Therefore, it is very important to control CO_2 emissions from coal-based power plants.

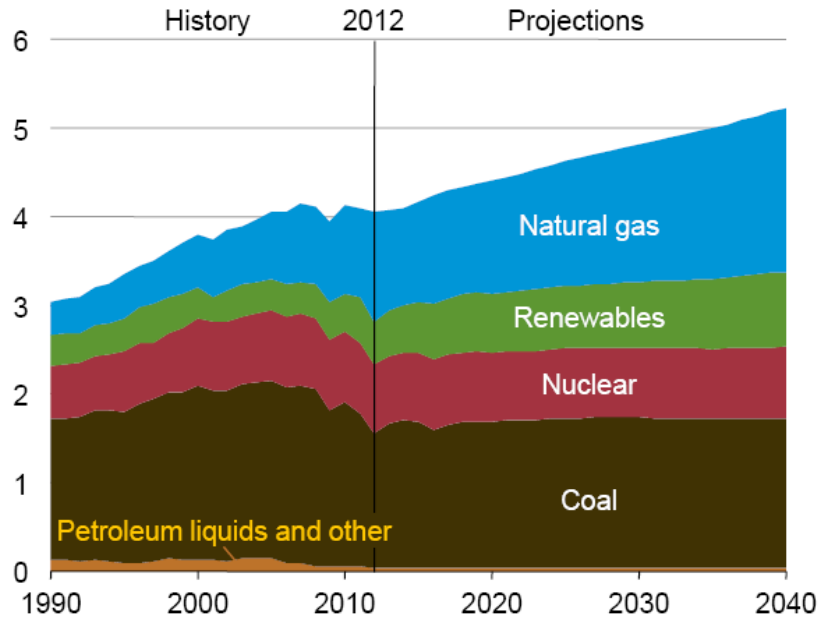

Figure 1.3: Electricity generatrion by fuel in U.S., 1990-2040 (trillion kilowatthours) [6].

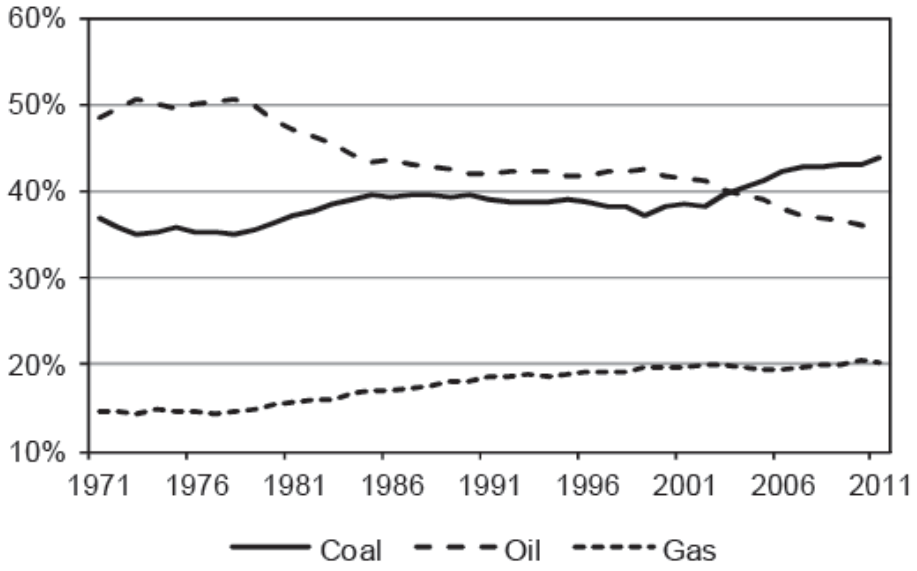

Figure 1.4: Fossil fuel shares in global CO_2 emissions [4].

1.2 **Carbon dioxide capture from coal-based power plants**

1.2.1 General approaches to carbon dioxide capture

One promising approach to reduce CO_2 emissions is carbon capture and sequestration (CCS). In this strategy, carbon dioxide will be captured from large point sources (e.g. power plants) and sequestered underground for long periods of time [7]. The U.S. Department of Energy (DOE) is considering three ways to capture CO_2 generated in coal-based power production: post-combustion CO_2 capture; pre-combustion CO_2 capture, and oxy-combustion, which separates oxygen from air prior to combustion and produces a nearly sequestration-ready CO_2 exhaust. These three approaches are shown schematically in Figure 1.5.

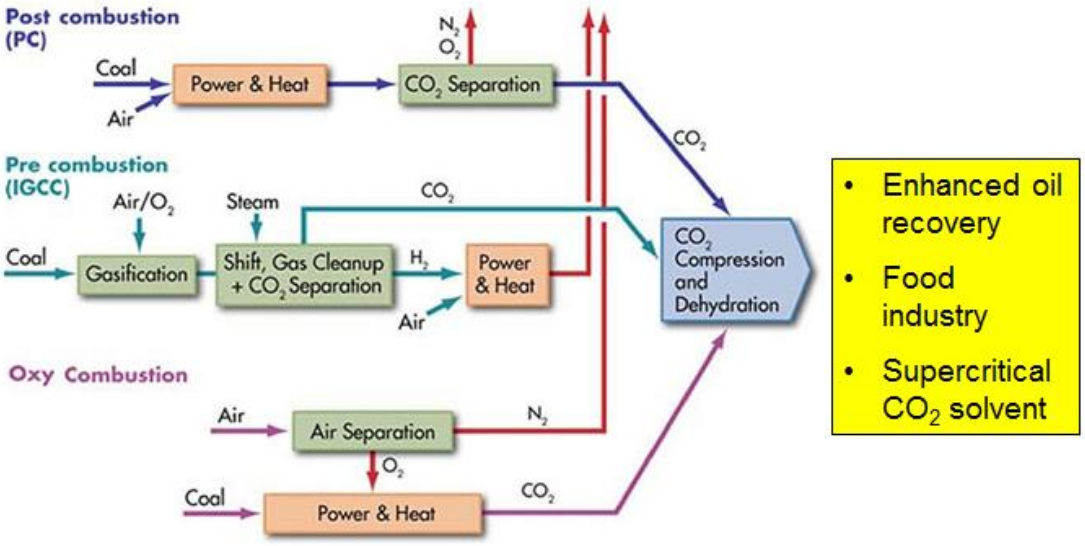

Figure 1.5: Approaches to carbon dioxide capture from coal-base power production [8].

Post-combustion CO_2 capture

Post-combustion CO_2 capture refers to the removal of CO_2 from flue gas prior to being discharged to the atmosphere. In a typical coal-based power plant, coal is burned with air in a boiler to produce steam which drives a turbine/generator to produce electricity. The CO_2 capture process will be located downstream of the conventional pollutant controls.

The challenges for this approach are: a high volume of flue gas must be treated because the CO_2 concentration is low (13-15 vol%); the flue gas is at low pressure (15-20 psia); the presence of trace impurities that can degrade the CO_2 capture equipment (particulate matter, sulfur oxides, nitrogen oxides, etc.); and compressing captured CO_2 from near atmospheric pressure to pipeline pressure (about 2,200 psia) requires a large auxiliary power load. Typical flue gas stream properties are tabulated in Table 1.1.

Despite the above challenges, post-combustion CO_2 capture offers the greatest near-term potential for reducing CO_2 emissions because it can be retrofit to existing state-of-the-art power plants with reasonable changes in the plants. It can also be tuned for various levels of CO_2 capture to accelerate market acceptance.

Table 1.1: Typical flue gas composition, temperature and pressure

Pressure: ~ 1 atm
Temperature: 100-250 °C

Components	Concentration
CO_2	13 - 15 vol%
N_2	Balance
H_2O	~ 5 - 12 vol%
O_2	~ 5 vol%
Particulate matter	-
SO_x	-
NO_x	-

Pre-combustion CO_2 capture

In pre-combustion CO_2 capture, CO_2 at much higher pressure will be separated from gasified coal syngas (largely H_2 and CO) prior to entering a combustion turbine. Pre-combustion capture is mainly applicable to gasification plants, where fuel is converted into gaseous components by applying heat under pressure.

Due to the fact that CO_2 is present at much higher concentrations in syngas (after water gas shift reaction) than in flue gas, and that the syngas is at higher pressure, pre-combustion CO_2 capture should be easier and less expensive than post-combustion capture. In addition, the volume of syngas that requires processing is much lower than the volume of flue gas from a comparable coal-based power plant, thus reducing capital cost.

Oxy-combustion CO_2 capture

For oxy-combustion CO_2 capture, coal is burned with high purity O_2 separated from air. The primary products of combustion are water and CO_2 (~ 60 vol%), with the CO_2 separated by condensing water through cooling and compression. The high purity oxygen is mixed with recycled flue gas prior to combustion to maintain conditions similar to an air fired situation. This is necessary because currently available equipment materials cannot withstand the high temperatures resulting from coal combustion in pure oxygen.

The cost of CO_2 capture in an oxy-combustion power plant should be lower than for a conventional coal-based power plant, due to decreased flue gas volume and increased CO_2 concentration. However, the cost of air separation and flue gas recirculation significantly reduces its economic benefits.

A summary of the inherent advantages and disadvantages of each approach to flue gas CO_2 capture is shown in Table 1.2. Although gasification and oxy-fuel processes show future promise for clean, efficient energy production, all current coal-based power plants generate electricity by direct combustion of coal with air in a boiler. There are more than 600 of such pulverized coal-based power plants in the United States, and more

than 5000 worldwide. New power plants will continue to be of this type for at least the next few decades [5]. Consequently, to address current CO_2 emission concerns, capture technology must be applicable to the standard air combustion system.

Table 1.2: Advantages and disadvantages of different flue gas CO_2 capture approaches [9]

	Advantages	Disadvantages
Post-combustion	• Applicable to the majority of existing coal-based power plants • Retrofit technology option	Flue gas is… • Dilute in CO_2 • At ambient pressure … resulting in … • Low CO_2 partial pressure • Significantly higher performance or circulation volume required for high capture levels • CO_2 produced at low pressure compared to sequestration requirements
Pre-combustion	Synthesis gas is… • Concentrated in CO_2 • High pressure … resulting in … • High CO_2 partial pressure -Increased driving force for separation -More technologies available for separation • Potential for reduction in compression costs/loads	• Applicable mainly to new plants, as few gasification plants are currently in operation • Barriers to commercial application of gasification are common to pre-combustion capture • Availability • Cost of equipment • Extensive supporting systems requirements
Oxy-combustion	• Very high CO_2 concentration in flue gas • Retrofit and repowering technology option	• Large cryogenic O_2 production requirement may be cost prohibitive • Cooled CO_2 recycle required to maintain temperatures within limits of combustor materials • Decreased process efficiency • Added auxiliary load

1.2.2 Post-combustion carbon dioxide capture technologies

There are four main technologies that can be applied to post-combustion CO_2 capture from coal-based power plants: absorption, adsorption, membranes and low temperature separation.

Absorption

Absorption is a process that relies on a solvent's affinity with a solute to preferably dissolve one species over another. In the application of this technology to post-combustion CO_2 capture, a desirable solvent should preferably dissolve CO_2, but not N_2 or any other component in a flue gas stream. The CO_2-rich solution is typically pumped to a regeneration column, where CO_2 is stripped from the solution by increasing temperature or reducing pressure. The solvent is recycled for a new batch of flue gas.

Amine absorption is a mature technology, which has been successfully used to treat industrial gas streams for decades. However, a number of studies have shown that amine absorption, when applied to flue gas CO_2 capture, will be costly and energy intensive [9, 10]. It is predicted that the use of an amine system to capture 90 % of the CO_2 in flue gas will require more than 50 % increase in the cost of electricity (COE). This value is well above the DOE target of less than 35 % increase in the cost of electricity for 90 % CO_2 capture [9]. Merkel [11] notes there are unlikely to be significant future improvements in this process.

Adsorption

Adsorption refers to the phenomenon that a fluid (gas, vapor, or liquid) is adsorbed at the surface (or in the pores) of a solid. Different fluid molecules have different affinity to the surface of a solid, allowing for the separation of a specific species from a mixture. Based on the interaction between fluid molecules and the solid surface, adsorption can be classified into chemical adsorption and physical adsorption. Since adsorption involves a solid sorbent, the operation of an adsorption process can be more difficult compared to an absorption process. This distinction could be critical when the process scale is extremely large, such as a power plant. The sorbent regeneration is typically accomplished via increasing temperature or decreasing pressure. Sorbent properties (e.g. mechanical, thermal and chemical stability, porosity, particle size, adsorption capacity, heat of adsorption, etc.) will affect an adsorption process significantly.

Membranes

Membrane-based post-combustion CO_2 capture uses permeable or semipermeable materials that allow for the selective separation of CO_2 from other components in the flue gas. Hendricks et al. [12, 13] reported as early as 1989 that commercial gas separation membranes available at that time could not compete with absorption techniques for flue gas treatment. Subsequent researchers have largely focused on improving membrane CO_2/N_2 selectivity to increase the purity of captured CO_2, often via facilitated transport mechanisms [14-17]. Recently, feasibility studies by Favre and co-workers have rekindled interest in using membranes for CO_2 capture from flue gas [18-21].

Membranes potentially could be a more cost-effective technology option for post-combustion CO_2 capture, compared to absorption or adsorption which requires a large amount of regeneration energy. Membranes are energy-efficient with low operating costs, and have a small footprint that is easily expandable.

The major disadvantage in using conventional polymeric membranes for post-combustion CO_2 capture is the potentially large membrane surface area required, due to the large flue gas volume that needs to be processed coupled with the low concentration and low partial pressure of CO_2 in the flue gas. Another potential disadvantage is, although 90 % CO_2 separation is technically achievable in a single-step process, a high level of CO_2 purity will require a multi-step process. Therefore, high performance membranes need to be developed to overcome those disadvantages.

Low temperature separation

Low-temperature separation is possible since the flue gas constituents have different freezing temperatures. Although this technology is physically possible, its cost-effectiveness is limited due to the large amount of energy need to accomplish the flue gas cooling.

1.3 Introduction to Air Liquide post-combustion carbon dioxide capture

1.3.1 Hybrid membrane and cryogenic distillation process

To address the challenges related to post-combustion CO_2 capture, American Air Liquide developed a hybrid process based on the operation of a hollow fiber membrane at cold conditions in combination with cryogenic distillation [22, 23]. The cold membrane

process design concept is shown in Figure 1.6. This process couples a high performance cold membrane with the cryogenic processing technology, which is achieved by energy integration between the membrane and the CO_2 cryo-phase separator. Process feasibility is enabled by the exceptional selectivity-permeance characteristics of the Air Liquide (AL) cold membranes. Both high membrane selectivity and high permeance are critical for cost-efficient CO_2 capture [24-27]. High selectivity reduces the overall energy cost while high permeance reduces the capital cost. Simulations show the high membrane selectivity achieved by low temperature operation greatly increases efficiency of subsequent CO_2 liquefaction, thereby reducing the specific energy required for CO_2 capture. Preliminary analyses suggests this hybrid process can efficiently capture at least 90 % CO_2 in the flue gas from an air fired power plant with reasonable increase in the cost of electricity.

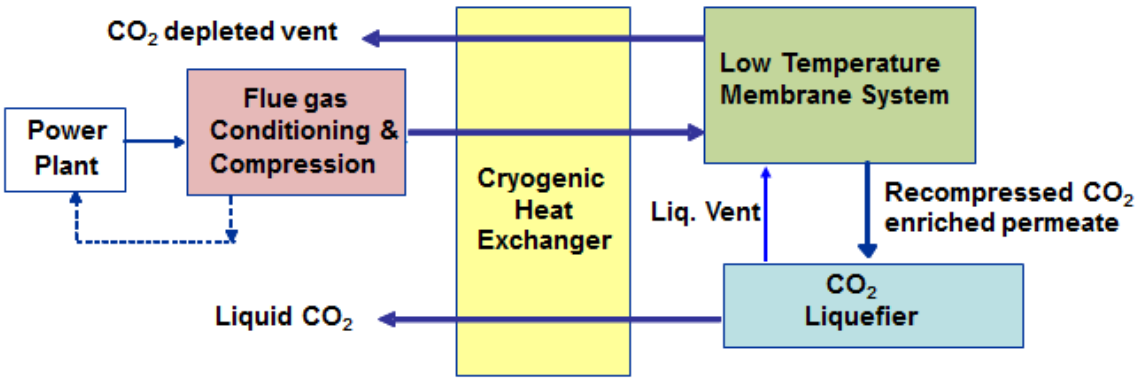

Figure 1.6: Block diagram of Air Liquide cold membrane process [22].

The detailed process design is presented in Figure 1.7 [22]. The highly selective cold membrane provides efficient pre-concentration of CO_2 prior to its partial condensation in a liquefaction unit. The flue gas is firstly purified, compressed to 230 psi and dried before being sent to a cold membrane system. The heat of compression is captured by a boiler. After membrane separation, the CO_2 enriched permeate is recompressed, cooled in a heat exchanger and undergoes phase separation in the cryo-phase separator. Liquid CO_2 is pumped from the separator through the heat exchanger to extract more energy, and a sequestration-ready product at 20 °C is obtained. The overhead from the cryogenic separator is warmed through the heat exchanger and undergoes energy recovery in a turbo-expander. This stream is mixed with the incoming dried flue gas, raising the mixed feed CO_2 concentration to 18 %. The higher CO_2 concentration in the feed improves membrane separation. The residue stream from the cold membrane is sent through one pass of the heat exchanger, further cooling and energy recovery is done via a series of turbo-expanders with the resulting cold residue stream at -57 °C sent through the heat exchanger. The cryogenic heat exchanger system provides energy integration between the membrane and the CO_2 liquefaction unit. Finally, the excess energy remaining in the pressurized warmed residue is partially recovered in a warm turbo-expander before venting.

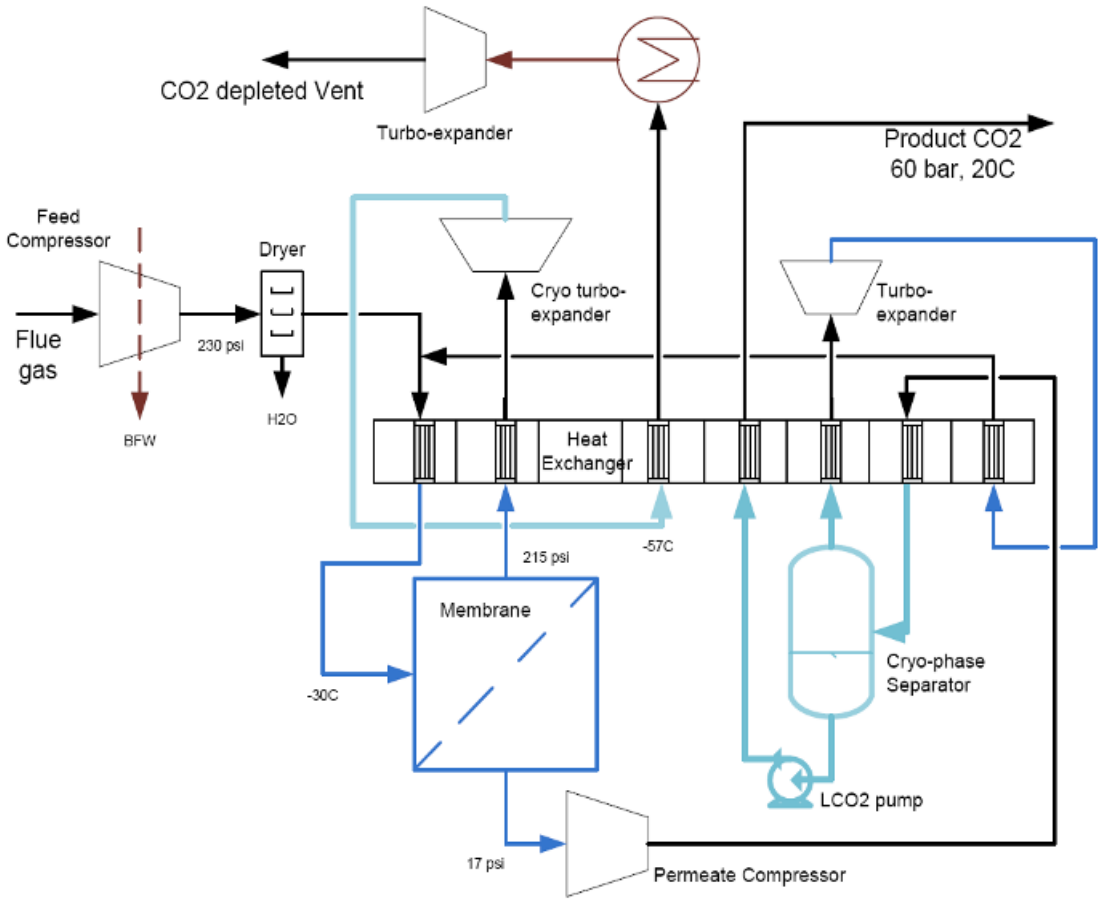

Figure 1.7: Air Liquide hybrid membrane and cryogenic distillation process for post-combustion CO_2 capture [22].

1.3.2 Air Liquide membrane performance at cold conditions

The existing low cost commercially available asymmetric hollow fiber membranes produced at Air Liquide showed an unprecedented combination of permeance and selectivity at cold conditions for the important CO_2/N_2 penetrant pair. It was discovered that when operating temperatures were lower than -10 °C, the membrane displayed unique high permeance and high selectivity (Figure 1.8). Specifically, the CO_2 permeance was above 100 GPU and the CO_2/N_2 selectivity was 50-150 within the

temperature range of -50 °C to -10 °C (The room temperature CO_2/N_2 selectivity for most polymeric membranes is around 20-30 [28]).

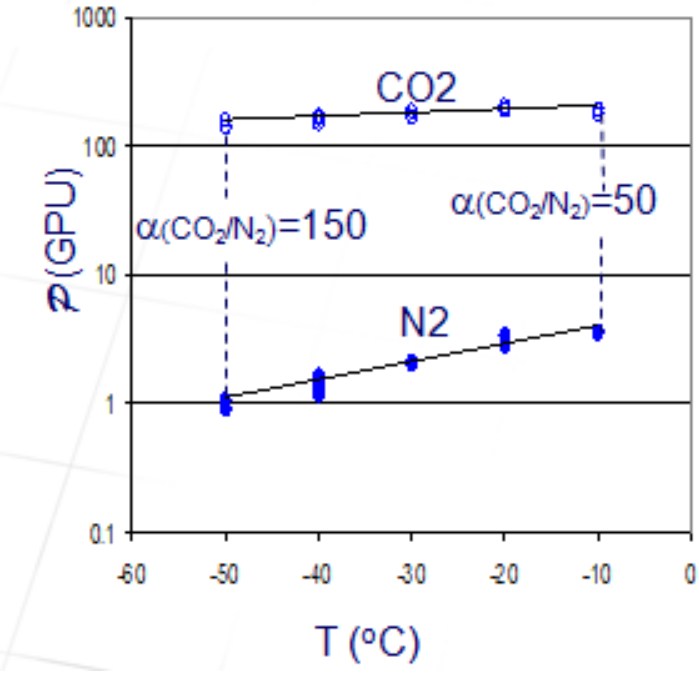

Figure 1.8: Permeation results of Air Liquide high performing hollow fiber membranes at cold conditions. Results were obtained at the Air Liquide Delaware Research and Technology Center [29]. $1\ GPU = 1\times10^{-6} cm^3(STP)/cm^2 \cdot s \cdot cmHg$

For most polymeric membranes, permeability generally decreases and selectivity increases with a decrease in operating temperature. However, the Air Liquide membranes showed increased selectivity but minimal loss in permeance with the drop of temperature. Figure 1.9 shows the back-calculated equivalent permeability and selectivity for the CO_2/N_2 penetrant pair on a Robeson Plot [30, 31] (the effective separation layer thickness of the hollow fiber membrane was estimated from room temperature data of hollow fiber

membrane and dense film). The yellow point represents Air Liquide membrane performance at room temperature; the blue point represents predicted membrane performance at -30 °C based on the data at 20-50 °C; and the green point represents actual membrane performance at -30 °C. It is obvious that the measured membrane permeance and selectivity are much higher than predicted, but the underlying reason was not clear. Increased understanding can result in further optimization of the operating parameters and possibly membrane fabrication parameters as well as identification of membrane materials with superior performance.

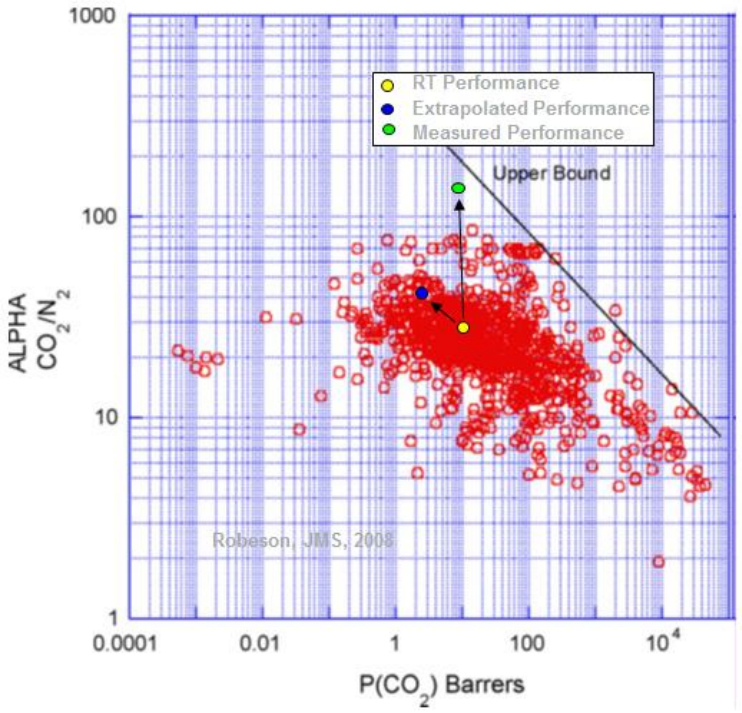

Figure 1.9: Plot of back-calculated equivalent permeability and selectivity for CO_2/N_2 at ambient temperature (yellow point) and at -30 °C (green point) on a Robeson plot [29]. Membrane sample: Air Liquide high performance hollow fiber membrane.

1.4 Research objectives

This research aims to clarify fundamentals of the cold membrane CO_2/N_2 separation process, in order to engineer membrane performance and identify second generation improved membrane materials for this application. The primary target to address in this work is to understand the phenomena of cold temperature CO_2 and N_2 permeation in glassy polyimide membranes. The asymmetric hollow fiber configuration was investigated intensively with focus on the membrane's selective skin layer. Two types of skin layers, (i) fused nodular and (ii) homogeneous dense, were probed. Two types of feeds, (iii) bore side feed and (iv) shell side feed, were explored (Figure 1.10). Items i-iv helped to understand how the nature of the membrane and its detailed exposure to a transmembrane perturbing condition might alter its segmental and super-segmental structure.

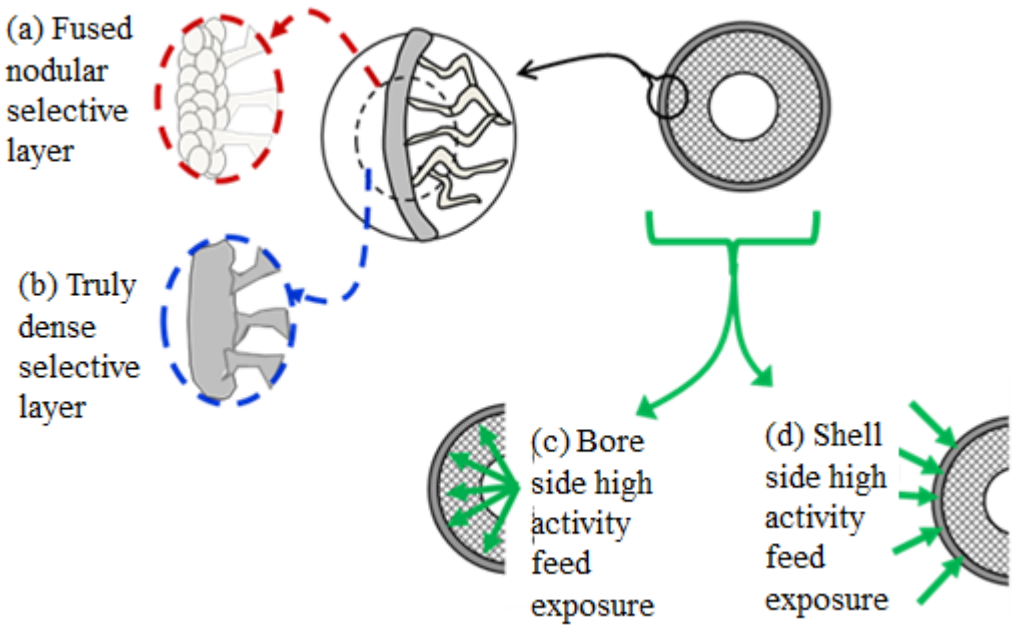

Figure 1.10: Different selective skin morphologies [(i) nodular & (ii) homogeneous] and two types of exposure [(iii) bore side feed and (iv) shell side feed] to high activity feeds to "vector" the glassy state properties of the selective layers.

Specifically, the objectives of this research are:

Objective 1: Verify Air Liquid's discovery that some Matrimid® hollow fiber membranes can achieve both high selectivity and high permeance at cold conditions

While an attractive economic case is shown with existing commercial Air Liquide membranes, there is still huge potential for further improvement in membrane performance in this new area. The first objective aims to fabricate hollow fiber membranes with similar or even better performance than Air Liquide membranes at cold conditions, using the same membrane material, Matrimid®. The increased understanding of membrane formation process that led to well-performing membranes at cold conditions shed light on further optimization of the membrane fabrication parameters. It

was believed that the micro-structural morphologies in the effective separation layer greatly affected membrane performance at cold conditions. Therefore, two types of selective layers, "fused nodular" and "homogeneous dense", were studied in this work. The "homogeneous dense" selective layer is an ideal defect free separation layer, and its formation protocol had been well established by previous researchers [32, 33]; however, the formation of the "fused nodular" morphology had not been developed and the investigation of its formation protocol was the focus of the first objective.

Objective 2: The interpretation of performance difference between hollow fiber membranes with nodular and dense selective layers

The second objective relates to the different membranes formed in the first objective. The performance of membranes with "fused nodular" and "homogeneous dense" selective layers at sub-ambient temperatures were investigated and compared. It was discovered that the two selective layer morphologies led to significantly different separation performances under the sub-ambient testing conditions of interest. Great efforts were spent on the exploration of the underlying reason for such difference as well as the investigation of the reason for the exceptionally high cold membrane selectivity combined with high permeance. The study of the physical chemistry of cold temperature CO_2 permeation in rigid glassy polymers coupled with the research on membrane selective layer structure on gas transport properties resulted in better understanding of the unusual membranes.

Objective 3: Identify membrane materials and structures with superior performance for cold conditions

Based on the understanding of CO_2 and N_2 transport in Matrimid® hollow fiber membranes at cold conditions, the third objective aims to identify a second generation, improved membrane materials and structures with superior performance. The higher free volume, more rigid 6FDA based polyimides were explored. Those materials were made into hollow fiber configurations with "fused nodular" and "homogeneous dense" selective layers, and their performance at low temperatures were studied and compared with Matrimid® fibers.

1.5 Dissertation organization

This dissertation is divided into seven chapters including the current chapter. After the introduction presented in Chapter 1, the dissertation expands in Chapter 2 into gas transport mechanisms through polymeric materials, Arrhenius relationships and other essential theories and backgrounds relevant to this research. Chapter 3 summarizes all the materials used in the experiments as well as describes characterization techniques and hollow fiber spinning process. Chapter 4 explores the spinning protocols of Matrimid® hollow fiber membranes with "fused nodular" selective layers. Chapter 5 studies the performance difference between nodular and dense hollow fiber membranes. In this chapter, a hypothetical model to explain the special performance of nodular-skinned bore-fed fibers at cold conditions is proposed and indirect evidences are presented to support the hypothesis. Chapter 6 presents the discovery of new membrane materials and

structures that lead to superior cold performance. Finally, Chapter 7 summarizes the findings of this research and proposes recommendations for future work.

1.6 References

[1] J. T. Houghton, Y. Ding, D. J. Griggs, M. Noguer, P. J. van der Linden, X. Dai, et al., Climate change 2001: the scientific basis vol. 881: Cambridge University Press Cambridge, 2001.

[2] D. Aaron and C. Tsouris, Separation of CO_2 from flue gas: a review, Separation Science and Technology, vol. 40, pp. 321-348, 2005.

[3] Climate change 2007: The physical science basis, Intergovernmental Panel On Climate, 2007.

[4] CO_2 Emissions From Fuel Combustion Highlights 2013 Edition, International Energy Agency, 2013.

[5] The Future of Coal - Options for a Carbon-Constrained World, MIT Interdisciplianry Study, 2007.

[6] Annual Energy Outlook 2014, Energy Information Administration, 2014.

[7] S. M. Klara, R. D. Srivastava, and H. G. McIlvried, Integrated collaborative technology development program for CO_2 sequestration in geologic formations-United States Department of Energy R&D, Energy Conversion and Management, vol. 44, pp. 2699-2712, 2003.

[8] Brief description of major technologies for CO_2 capture. Retrieved from http://decarboni.se/publications/technology-options-co2-capture/brief-description-major-technologies-co2-capture.

[9] J. D. Figueroa, T. Fout, S. Plasynski, H. McIlvried, and R. D. Srivastava, Advances in CO_2 capture technology--The US Department of Energy's carbon sequestration program, International Journal of Greenhouse Gas Control, vol. 2, pp. 9-20, 2008.

[10] Cost and Performance Baseline for Fossil Energy Plants, vol. 1. Bituminous Coal and Natural Gas to Electricity, 2007.

[11] T. C. Merkel, H. Lin, X. Wei, and R. Baker, Power plant post-combustion carbon dioxide capture: An opportunity for membranes, Journal of Membrane Science, vol. 359, pp. 126-139, 2010.

[12] C. Hendriks, K. Blok, and W. Turkenburg, The recovery of carbon dioxide from power plants, in Climate and Energy: The Feasibility of Controlling CO_2 Emissions, ed: Springer, 1989, pp. 125-142.

[13] J. Van Der Sluijs, C. Hendriks, and K. Blok, Feasibility of polymer membranes for carbon dioxide recovery from flue gases, Energy Conversion and Management, vol. 33, pp. 429-436, 1992.

[14] T. Kai, T. Kouketsu, S. Duan, S. Kazama, and K. Yamada, Development of commercial-sized dendrimer composite membrane modules for CO_2 removal from flue gas, Separation and Purification Technology, vol. 63, pp. 524-530, 2008.

[15] L. Bao and M. C. Trachtenberg, Facilitated transport of CO_2 across a liquid membrane: Comparing enzyme, amine, and alkaline, Journal of Membrane Science, vol. 280, pp. 330-334, 2006.

[16] T. J. Kim, B. Li, and M. B. Hägg, Novel fixed-site-carrier polyvinylamine membrane for carbon dioxide capture, Journal of Polymer Science Part B: Polymer Physics, vol. 42, pp. 4326-4336, 2004.

[17] J. Huang, J. Zou, and W. W. Ho, Carbon dioxide capture using a CO_2-selective facilitated transport membrane, Industrial & Engineering Chemistry Research, vol. 47, pp. 1261-1267, 2008.

[18] E. Favre, Carbon dioxide recovery from post-combustion processes: Can gas permeation membranes compete with absorption?, Journal of Membrane Science, vol. 294, pp. 50-59, May 2007.

[19] R. Bounaceur, N. Lape, D. Roizard, C. Vallieres, and E. Favre, Membrane processes for post-combustion carbon dioxide capture: a parametric study, Energy, vol. 31, pp. 2556-2570, 2006.

[20] M. T. Ho, G. Leamon, G. W. Allinson, and D. E. Wiley, Economics of CO_2 and mixed gas geosequestration of flue gas using gas separation membranes, Industrial & engineering chemistry research, vol. 45, pp. 2546-2552, 2006.

[21] M. T. Ho, G. W. Allinson, and D. E. Wiley, Reducing the cost of CO_2 capture from flue gases using membrane technology, Industrial & Engineering Chemistry Research, vol. 47, pp. 1562-1568, 2008.

[22] D. Hasse, S. Kulkarni, E. Sanders, E. Corson, and J.-P. Tranier, CO_2 capture by sub-ambient membrane operation, Energy Procedia, vol. 37, pp. 993-1003, 2013.

[23] D. J. Hasse, S. S. Kulkarni, E. S. Sanders Jr, J.-p. Tranier, and P. Terrien, Method of obtaining carbon dioxide from a carbon dioxide-containing gas mixture, ed: EP Patent 2,512,634, 2012.

[24] J. Kotowicz, T. Chmielniak, and K. Janusz-Szymańska, The influence of membrane CO_2 separation on the efficiency of a coal-fired power plant, Energy, vol. 35, pp. 841-850, 2010.

[25] P. Luis, T. Van Gerven, and B. Van der Bruggen, Recent developments in membrane-based technologies for CO_2 capture, Progress in Energy and Combustion Science, vol. 38, pp. 419-448, 2012.

[26] K. Ramasubramanian, H. Verweij, and W. Winston Ho, Membrane processes for carbon capture from coal-fired power plant flue gas: A modeling and cost study, Journal of Membrane Science, vol. 421, pp. 299-310, 2012.

[27] L. Zhao, E. Riensche, L. Blum, and D. Stolten, Multi-stage gas separation membrane processes used in post-combustion capture: Energetic and economic analyses, Journal of Membrane Science, vol. 359, pp. 160-172, 2010.

[28] C. E. Powell and G. G. Qiao, Polymeric CO_2/N_2 gas separation membranes for the capture of carbon dioxide from power plant flue gases, Journal of Membrane Science, vol. 279, pp. 1-49, 2006.

[29] D. J. Hasse, S. S. Kulkarni, and E. S. Sanders Jr, CO_2 Capture by sub-ambient membrane operation, 22nd NAMS Annual Meeting, New Orleans, LA., ed, 2012.

[30] L. M. Robeson, Correlation of separation factor versus permeability for polymeric membranes, Journal of Membrane Science, vol. 62, pp. 165-185, Oct 1991.

[31] L. M. Robeson, The upper bound revisited, Journal of Membrane Science, vol. 320, pp. 390-400, Jul 2008.

[32] D. T. Clausi and W. J. Koros, Formation of defect-free polyimide hollow fiber membranes for gas separations, Journal of Membrane Science, vol. 167, pp. 79-89, 2000.

[33] S. B. Carruthers, Ph.D. thesis, Integral-skin formation in hollow fiber membranes for gas separations, The University of Texas at Austin, 2001.

CHAPTER 2

BACKGROUND AND THEORY

This chapter introduces essential background, theory and terminology related to the current work. A brief introduction about polymeric membranes for gas separations is presented in Section 2.1. Sections 2.2 and 2.3 include fundamental gas transport theory in membranes. Sections 2.4 and 2.5 describe the influence of temperature on gas permeation in membranes. A brief background on the effects of polymer-penetrant interactions and polymer chains orientation on gas transport properties is included in Sections 2.6 and 2.7. Finally, asymmetric hollow fiber membrane spinning fundamentals are discussed in Section 2.8.

2.1 Polymeric membranes for gas separations

Polymeric membranes have been widely used for gas separations due to their robustness, excellent processability and low manufacturing cost compared to inorganic membranes. Among the polymeric membrane materials, amorphous polymers are the most commonly chosen for gas separation due to their high selectivity for many gas pairs. Amorphous polymers can exist in either “rubbery” or “glassy” state, depending on the proximity of their glass transition temperatures (Tg) to the operating temperature of interest [1]. The glass transition temperature (Tg) is defined as the temperature where the molecular chains of a polymer obtain sufficient energy to surmount the energy barriers for bond rotation. The “rubbery” and “glassy” states reflect the level of molecular motions and the packing structure of the polymer matrix. A plot of an amorphous

polymer's specific volume as a function of temperature is shown in Figure 2.1. Above Tg, the polymer exists in its rubbery state; and below Tg, the polymer exists in its glassy state.

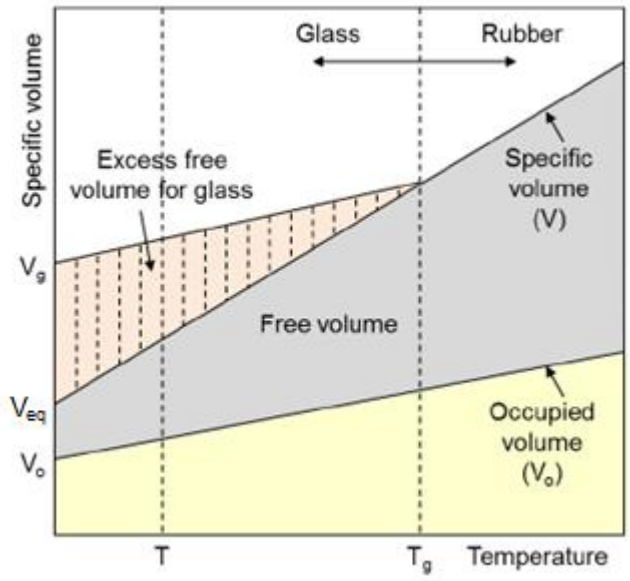

Figure 2.1: Specific volume of an amorphous polymer as a function of temperature [2].

The rubbery state is an equilibrium state where the polymer chains are densely packed with a high degree of rotational and vibrational mobility. Due to the long range cooperative motions of the polymer chain segments, a rubbery polymer behaves like a highly viscous liquid. The thermally activated molecular motions create transient fluctuations in inter-chain spacing, resulting in the formation of transient gaps volume where penetrant molecules can absorb into and diffuse through the polymer matrix.

Rubbery polymers usually have higher penetrant flux than the corresponding glassy polymers, but lower size discriminating capabilities.

On the contrary, the glassy state is a non-equilibrium state where the polymer chains lose mobility and can only execute limited segmental motions. In this "frozen state", polymer chains lack sufficient rotational and vibrational mobility to assume their thermodynamically favored configurations and are "trapped" in the non-equilibrium conformations, leading to long-lived molecular-scale packing defects, known as excess free volume or microvoids. As is shown in Figure 2.1, the specific volume of a glassy polymer (V_g) is greater than the hypothetical equilibrium specific volume (V_{eq}). The hypothetical equilibrium specific volume (V_{eq}) represents the volume a material would have if it behaved as a rubbery polymer at the same temperature. The difference between V_g and V_{eq} (V_g - V_{eq}) is the excess free volume. Note that, the hypothetical equilibrium specific volume (V_{eq}) doesn't equal to the specific volume occupied by the polymer chains (V_o).

The materials used in this work are all glassy polymers. Localized, non-cooperative thermally activated oscillations along the polymer backbone lead to a distribution of inter-segmental spacing and free volume that enable glassy polymers to precisely distinguish gas molecules based on their size and shape [1]. The amount of excess free volume in a glassy polymer depends on the rate of quenching below Tg [3-5]; the slower the cooling rate, the more time is allowed for the polymer chains to relax to the equilibrium conformation, and the smaller the excess free volume the polymer will have. In the case of infinitely slow cooling, the excess free volume would ideally be eliminated, and the specific volume of the glassy polymer would be equal to the

equilibrium hypothetical rubbery volume [1]. The high glass transition temperatures of the amorphous polymers used in this work allow long-lived "conditioning" effects to be introduced and vitrified semi-permanently into the glassy matrix.

2.2 Fundamentals of gas transport in membranes

2.2.1 Membrane gas transport mechanisms

A membrane is defined as a selective barrier between two phases [6]. For a gas separation membrane, a gas mixture is applied to the upstream of the membrane; the majority of the faster penetrants pass through the membrane to form a permeate stream, and the majority of the slower penetrants are rejected by the membrane to form a retentate stream. There are several mechanisms to describe the transport of gas molecules through a membrane. Depending on the morphology of the membrane and the mean free path of the penetrant molecules, the following mechanisms may apply: (i) viscous flow, (ii) Knudsen diffusion, (iii) surface diffusion, (iv) capillary condensation, (v) molecular sieving and (vi) sorption-diffusion. A schematic showing the various transport mechanisms through membranes is shown in Figure 2.2.

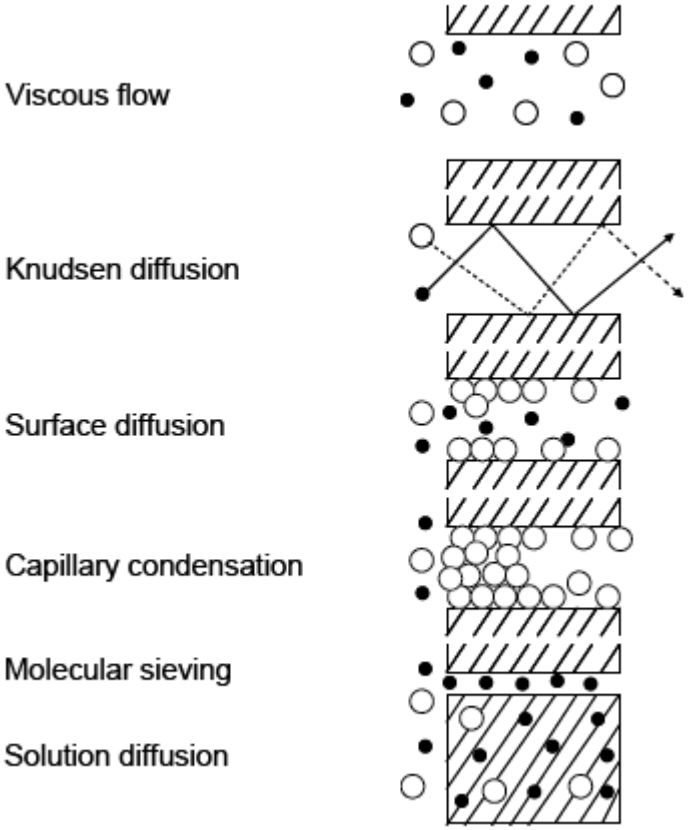

Figure 2.2: Gas transport mechanisms through membranes [7].

At a given temperature and pressure, viscous flow occurs when the pore radius is much larger than the mean free path of the penetrant molecules. In this case, there is no discrimination between the penetrants [8]. As the pore size reduces to the point where it is less than the mean free path of the penetrant molecules, gas transport through the membrane follows the Knudsen diffusion mechanism [9]. In this case, discrimination between the penetrants may exist depending on their molecular weights and temperature. The diffusion coefficient of component A for Knudsen diffusion is equal to [10]:

$$D_{A,K} = 97.0 \cdot r \cdot \left(\frac{T}{M_A} \right)^{0.5} \tag{2.1}$$

where, r is the pore radius in meters, T is the absolute temperature in Kelvin, and M_A is the molecular weight of component A.

The separation efficiency of component A over B for Knudsen diffusion is equal to:

$$\alpha_{A/B} = \sqrt{\frac{M_A}{M_B}} \tag{2.2}$$

From Equation 2.2 we can see that, the separation efficiency of a Knudsen type transport is limited by the penetrants' molecular weight. For gases with similar molecular weights, the separation efficiency is very low. As the pore sizes are further reduced below the mean free path of the penetrants, mechanisms like surface diffusion, capillary condensation, and molecular sieving may exist. For surface diffusion, certain gas molecules are preferentially adsorbed onto membrane pore surfaces while excluding other components, followed by diffusion of the adsorbed molecules across the membrane from one absorbed site to the next [11]. The separation efficiency is driven by the nature of the pore surface and size. For capillary condensation, certain penetrants in the vapor phase are adsorbed into the porous membrane to a point at which the pores are filled with condensed liquid from the vapor, excluding other penetrants. Molecular sieving mechanism separates penetrant molecules based on their size and the pore structure of the

membranes. Diffusion through the critical pores requires molecules to overcome repulsion from the pore wall constrictions, and even small changes in the constrictions can result in significant difference in the activation energy for diffusion [12, 13]. In this work, the materials under investigation are *nonporous* glassy polymers that follow a sorption-diffusion mechanism.

2.2.2 Permeation

Gas transport in nonporous glassy polymer membranes follows the sorption-diffusion mechanism [14]. Penetrant molecules first sorb into the polymer at the upstream, then diffuse across the polymer driven by a chemical potential gradient, and finally desorb from the polymer at the downstream. Figure 2.3 shows a schematic illustrating the transport of CO_2 and N_2 through a polymeric membrane.

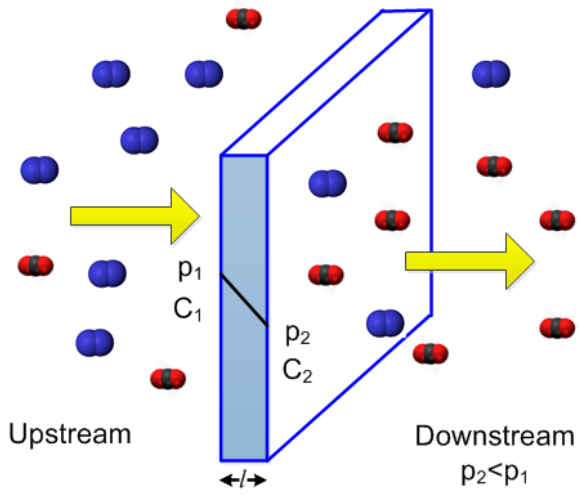

Figure 2.3: Schematic representation of CO_2 and N_2 transport through a polymeric membrane via the sorption diffusion mechanism.

Two key parameters are commonly used to characterize the productivity and efficiency of a membrane: permeability and selectivity. The permeability of component A (P_A) is defined as the steady state gas flux (N_A) normalized by the transmembrane fugacity difference (Δf_A) and the effective thickness of the membrane's separation layer (l):

$$P_A = \frac{N_A \cdot l}{\Delta f_A} \tag{2.3}$$

Under ideal conditions, the fugacity difference can be replaced by the partial pressure difference. The unit of the permeability is "Barrer", which is defined as:

$$1\ Barrer = 1\times 10^{-10}\ \frac{cm^3(STP)\cdot cm}{cm^2 \cdot s \cdot cmHg} \tag{2.4}$$

In asymmetric hollow fiber membranes, the actual thickness of the effective separation layer is not easily known, so productivity is described by membrane permeance, which is a fugacity normalized flux:

$$\left(\frac{P}{l}\right)_A = \frac{n_A}{\Delta f_A} \tag{2.5}$$

"Gas Permeation Unit" (GPU) is usually used as the unit for permeance, which is defined as:

$$1\ GPU = 1\times10^{-6}\ \frac{cm^3(STP)}{cm^2\cdot s\cdot cmHg} \tag{2.6}$$

The membrane's ability to provide a selective barrier for penetrant A relative to penetrant B is measured by its selectivity. The intrinsic selectivity ($\alpha_{A/B}$) is defined as the ratio of the penetrants' pure gas permeabilities for the case of an infinite total upstream to downstream pressure ratio [15-17]:

$$\alpha_{A/B} = \frac{P_A}{P_B} \tag{2.7}$$

Based on the sorption-diffusion model, the permeability of component A (P_A) can further be expressed as the product of a mean diffusion coefficient (D_A, a kinetic factor) and a mean sorption coefficient (S_A, a thermodynamic factor), which is expressed as:

$$P_A = D_A \cdot S_A \tag{2.8}$$

This relationship can be derived by representing the flux (N_A) using Fick's first law of diffusion [10]. In the absence of any bulk flow effect, the expression of flux (N_A) is shown in Equation 2.9.

$$N_A = -D_A \frac{dC_A}{dx} \tag{2.9}$$

where, C_A represents the concentration of component A in the membrane.

Substituting Equation 2.9 into Equation 2.3, an expression for permeability is derived (Equation 2.10).

$$P_A = \frac{N_A \cdot l}{\Delta f_A} = -D_A \cdot \frac{dC_A}{dx} \cdot \frac{l}{\Delta f_A} \tag{2.10}$$

Applying the following boundary conditions:

At $x = 0$, $C_A = C_{A,up}$ (upstream of the membrane)

At $x = l$, $C_A = C_{A,down}$ (downstream of the membrane)

Thus,

$$\int_0^l \frac{P_A}{l} dx = -\int_{C_{A,u}}^{C_{A,d}} D_A(C_A) \frac{dC_A}{\Delta f_A} \tag{2.11}$$

$$P_A = -\int_{C_{A,u}}^{C_{A,d}} \frac{D_A(C_A) dC_A}{(C_{A,u} - C_{A,d})} \cdot \frac{(C_{A,u} - C_{A,d})}{\Delta f_A} \tag{2.12}$$

The right hand side of equation 2.12 is simplified by introducing the mean diffusion coefficient (D_A) and the mean sorption coefficient (S_A), which are defined as follows [18, 19]:

$$D_A = \frac{\int_{C_{A,u}}^{C_{A,d}} D_A(C_A) dC_A}{\int_{C_{A,u}}^{C_{A,d}} dC_A} = -\int_{C_{A,u}}^{C_{A,d}} \frac{D_A(C_A) dC_A}{(C_{A,u} - C_{A,d})} \tag{2.13}$$

$$S_A = \frac{\int_{C_{A,u}}^{C_{A,d}} dC_A}{\int_{f_{A,u}}^{f_{A,d}} df_A} = \frac{(C_{A,u} - C_{A,d})}{\Delta f_A} \tag{2.14}$$

Substituting equation 2.13 and 2.14 into equation 2.12, the permeability of component A can be expressed as:

$$P_A = D_A \cdot S_A \tag{2.15}$$

In this manner, selectivity can be expressed as the product of diffusion selectivity (D_A / D_B) and sorption selectivity (S_A / S_B):

$$\alpha_{A/B} = \frac{P_A}{P_B} = \left[\frac{D_A}{D_B}\right] \cdot \left[\frac{S_A}{S_B}\right] \tag{2.16}$$

2.2.3 Diffusion

The diffusion coefficient of a penetrant in a polymeric membrane depends on the penetrant properties and the free volume and morphology of the polymer matrix. The diffusion coefficient is affected by penetrant size, polymer chain packing and mobility, and the cohesive energy [20]. Gas molecules diffuse through the membrane down a concentration gradient by way of random jumps from one site to the next. Diffusive jumps of penetrant within the polymer matrix occur when thermally activated motions of

chain segments generate transient gaps that are larger than the size of the penetrant, as is depicted in Figure 2.4. The diffusion coefficient of a penetrant molecule can be described as a function of the frequency of the diffusive jumps (f) and the average jump length (λ) [13]:

$$D = \frac{f \cdot \lambda^2}{6} \tag{2.17}$$

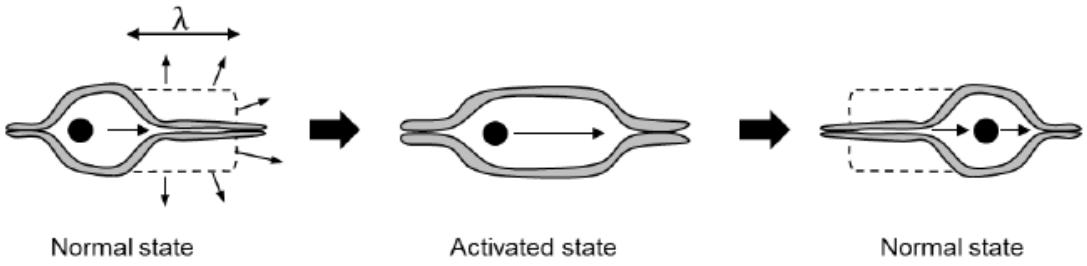

Figure 2.4: Schematic of gas diffusion through a nonporous polymeric membrane via transient gap formation. λ is the average length of random diffusion jumps [2].

2.2.4 Sorption

2.2.4.1 Dual-mode sorption

Gas sorption in glassy polymers depends on the penetrant activity and affinity for the polymer, and can be described by the dual-mode sorption model [16, 21]. The dual-mode model assumes there are two types of idealized sorption regions: the "Langmuir sorption sites" (non-equilibrium sites, provided by the excess free volume [22]) and the "Henry's sorption sites" (equilibrium sites). Penetrants sorbed in the Langmuir sites are held in microvoids or "holes" which can be modeled using Langmuir type sorption

(Equation 2.18). The solubility increases with pressure and asymptotes as the microvoids are saturated.

$$C_H = \frac{C_H^{'} bp}{1+bp} \tag{2.18}$$

In Equation 2.18, C_H is the local concentration of penetrant molecules in the microviods, $cm^3(STP)/(cm^3 polymer)$; $C_H^{'}$ is the Langmuir capacity constant, which characterizes the total sorption capacity of the unrelaxed volume region, $cm^3(STP)/(cm^3 polymer)$; and b is the Langmuir affinity constant, which characterizes the tendency of a penetrant to be sorbed into the microvoids and is usually correlated with the condensability of the gas, psi^{-1}. Penetrants sorbed in the Henry's sites are visualized as being 'dissolved' in the densely packed region and this type of sorption obeys the Henry's law at low and intermediate pressures (Equation 2.19).

$$C_D = k_D p \tag{2.19}$$

C_D is the local concentration of penetrant molecules in the dissolved region, $cm^3(STP)/(cm^3 polymer)$, k_D is the Henry's law constant, which can be interpreted as the ordinary solubility coefficient in the densely packed region of the polymer matrix [23], $cm^3(STP)/(cm^3 polymer \cdot psi)$. The total penetrant concentration in the glassy polymer is the superposition of both the "Langmuir population" and the "Henry's

population" (Equation 2.20). Figure 2.5 shows the typical sorption isotherms of a dual-mode type sorption.

$$C = C_D + C_H = k_D p + \frac{C_H' bp}{1+bp} \tag{2.20}$$

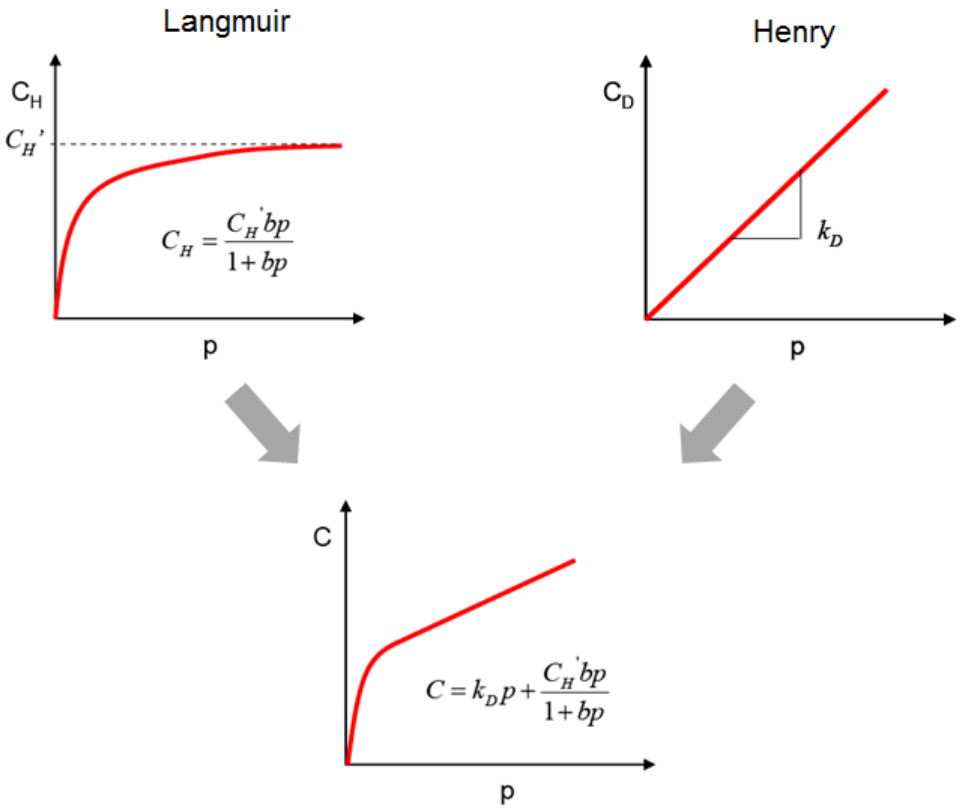

Figure 2.5: Dual-mode sorption isotherms [24].

The sorption coefficient is defined as the secant slope of the sorption isotherm:

$$S = \frac{C}{p} = k_D + \frac{C_H' b}{1 + bp} \tag{2.21}$$

Sorption coefficients of gases in a membrane are strongly influenced by the condensability of the gas molecules and their physiochemical interactions with the membrane material. Critical temperature is a good indicator of the gas condensability. Generally, gases with higher critical temperatures tend to be more condensable in the membrane.

2.2.4.2 Competitive sorption

The preceding section discusses the sorption of single penetrant into a glassy polymer. In fact, the dual-mode theory can be extended to model multicomponent sorption. The primary effect exists in multiple components sorption is the competition between the penetrants for the fixed number of Langmuir sorption sites. Such an effect may cause significant depression in the sorption of the more soluble components, resulting in decreased permeability and selectivity [25].

Take a binary system for example. It is assumed that saturation of the Langmuir capacity of a glassy polymer with a pure penetrant (A or B) involves complete filling of the unrelaxed volume in the polymer at the penetrant's characteristic molar density, $\rho_{A,0}^*$ or $\rho_{B,0}^*$ [26]. The fraction of unrelaxed volume claimed by component A (θ_A) is predicted to be:

$$\theta_A = \frac{b_A \cdot p_A}{1 + b_A \cdot p_A + b_B \cdot p_B} \tag{2.22}$$

Similarly, the fraction of unrelaxed volume claimed by component B (θ_B) is given by:

$$\theta_B = \frac{b_B \cdot p_B}{1 + b_A \cdot p_A + b_B \cdot p_B} \tag{2.23}$$

The parameters b_A and b_B are the Langmuir affinity constants of pure components A and B, respectively.

The volume fraction θ_A can be expressed as the ratio of the unrelaxed volume occupied by component A to the total unrelaxed volume:

$$\theta_A = \frac{C_{H,A} / \rho_A^*}{C_{H,A}^{'} / \rho_{A,0}^*} \tag{2.24}$$

where $C_{H,A}$ is the concentration of component A in the Langmuir mode, and $C_{H,A}^{'}$ is the Langmuir capacity for pure component A. Also, ρ_A^* is the effective molar density of component A in the Langmuir mode in the *presence* of a second component, and $\rho_{A,0}^*$ is the effective molar density of component A in the *absence* of a second component [26]. Assuming $\rho_A^* = \rho_{A,0}^*$, the equilibrium sorbed concentration of component A is given by:

$$C_A = k_{D,A} \cdot p_A + \frac{C'_{H,A} \cdot b_A \cdot p_A}{1 + b_A \cdot p_A + b_B \cdot p_B} \tag{2.25}$$

Similarly, assuming $\rho_B^* = \rho_{B,0}^*$, the equilibrium sorbed concentration of component B is given by:

$$C_B = k_{D,B} \cdot p_B + \frac{C'_{H,B} \cdot b_B \cdot p_b}{1 + b_A \cdot p_A + b_B \cdot p_B} \tag{2.26}$$

The denominator of the Langmuir tem contains the affinity constants and partial pressures of all components. Therefore, the total concentration of one component is reduced as the partial pressure of the other components increases.

2.3 Models of gas transport in glassy polymers

2.3.1 Partial immobilization model

The dual-mode model can be extended to analyze the influence of competitive sorption on the penetrant's permeability [25]. The steady state flux of component A can be expressed in terms of its flux in the Henry's law and Langmuir regions:

$$N_A = -D_{D,A} \cdot \frac{dC_{D,A}}{dx} - D_{H,A} \cdot \frac{dC_{H,A}}{dx} \tag{2.27}$$

$D_{H,A}$ represents the diffusion coefficient for penetrant diffusing from the Langmuir region to the dissolved (Henry's law) region, and $D_{D,A}$ represents the diffusion

coefficient from one dissolved site to the next [16]. The partial immobilization model assumes the gas molecules sorbed in the dissolved region are free to diffuse, while those sorbed in the Langmuir sites are partially immobilized [27].

Let $F_A \equiv \frac{D_{H,A}}{D_{D,A}}$ (0 < F < 1), and Equation 2.27 can be expressed as:

$$N_A = -D_{D,A} \cdot \frac{d(C_{D,A} + F_A \cdot C_{H,A})}{dx} \tag{2.28}$$

Assume local equilibrium between the Langmuir and Henry's law regions, and define $K_A \equiv \frac{C'_{H,A}}{b_A \cdot K_{D,A}}$ as the equilibrium constant between these two regions. Ultimately, the permeance of component A is expressed as a function of its fugacities at the upstream and downstream of the membrane (Equation 2.29). A complete derivation can be found in Koros's work [25].

$$\frac{P_A}{l} = \frac{D_{D,A} \cdot k_{D,A}}{l} \cdot \left(1 + \frac{F_A \cdot K_A \cdot \frac{f_{A,up}}{f_{A,up} - f_{A,down}}}{1 + b_A \cdot f_{A,up} + b_B \cdot f_{B,up}} - \frac{F_A \cdot K_A \cdot \frac{f_{A,down}}{f_{A,up} - f_{A,down}}}{1 + b_A \cdot f_{A,down} + b_B \cdot f_{B,down}} \right) \tag{2.29}$$

Under negligible downstream pressures, Equation 2.29 reduces to Equation 2.30:

$$\frac{P_A}{l} = \frac{D_{D,A} \cdot k_{D,A}}{l} \cdot \left(1 + \frac{F_A \cdot K_A}{1 + b_A \cdot f_{A,up} + b_B \cdot f_{B,up}} \right) \tag{2.30}$$

2.3.2 Frame of reference/Bulk flow model

In section 2.2.2, Fick's first law of diffusion was used to derive the expression for permeability. This is valid when the diffusional flux is the only contributor to the overall flux through the membrane. However, for mixed gas permeation, the flux of each component can be significantly affected by the flows of other components [28]. Sometimes, the bulk (convective) flux term has to be taken into consideration. For a binary system of components A and B, a complete expression of penetrant flux in polymer p is shown in Equations 2.31-2.34.

$$n_A = n_{A,diffusive} + n_{A,bulk} \tag{2.31}$$

$$n_A = -\rho \cdot D_{A,m} \cdot \frac{d\omega_A}{dx} + (n_A + n_B + n_p) \cdot \omega_A \tag{2.32}$$

$$n_B = -\rho \cdot D_{B,m} \cdot \frac{d\omega_B}{dx} + (n_A + n_B + n_p) \cdot \omega_B \tag{2.33}$$

$$n_p = -\rho \cdot D_{p,m} \cdot \frac{d\omega_p}{dx} + (n_A + n_B + n_p) \cdot \omega_p \tag{2.34}$$

where, $D_{i,m}$ (i = A, B and p) is the effective binary diffusion coefficient for component i in the polymer, ρ is the density of the polymer membrane, and ω_i is the mass fraction of component i in the polymer. Since the membrane is stationary, the flux term for the polymer (n_p) is zero.

Equations 2.32-2.33 show that a component with very high flux may effectively increase the flux of other components through the bulk flow term. Highly sorbing penetrant CO_2 is very likely to have measurable bulk flux contributions during mixed gas permeation, especially at low temperatures when the level of CO_2 sorption is high.

From Equations 2.32 and 2.33, the mutually dependent flux of penetrant A and B can be derived as:

$$n_A = \frac{-\rho \cdot D_{A,m} \cdot \frac{d\omega_A}{dx}}{\left[1-\left(1+\frac{1}{r}\right)\cdot \omega_A\right]} \tag{2.35}$$

$$n_B = \frac{-\rho \cdot D_{B,m} \cdot \frac{d\omega_B}{dx}}{\left[1-(1+r)\cdot \omega_B\right]} \tag{2.36}$$

$$r = {n_A}/{n_B} \tag{2.37}$$

where, ω_A and ω_B are the mobile concentration of penetrants A and B, as is defined by Equations 2.38 and 2.39 [28].

$$\omega_A = \frac{k_{D,A} \cdot f_A \cdot M_A}{22400 \cdot \rho} \cdot \left(1 + \frac{F_A \cdot K_A}{1 + b_A \cdot f_A + b_B \cdot f_B} \right) \tag{2.38}$$

$$\omega_B = \frac{k_{D,B} \cdot f_B \cdot M_B}{22400 \cdot \rho} \cdot \left(1 + \frac{F_B \cdot K_B}{1 + b_A \cdot f_A + b_B \cdot f_B} \right) \tag{2.39}$$

In Equations 2.38 and 2.39, M_A and M_B are the molecular weights of penetrants A and B. Applying the following boundary conditions to Equations 2.35 and 2.36, the flux of A and B can be obtained (Equations 2.40 and 2.42). Note that, when the downstream pressure of the membrane approaches zero, $\omega_{A,dowm}$ and $\omega_{B,dowm} \approx 0$.

Boundary conditions:

$x = 0; \omega_A = \omega_{A,up}; \omega_B = \omega_{B,up}$

$x = l; \omega_A = \omega_{A,dowm}; \omega_B = \omega_{B,down}$

$$n_A \cdot l = \frac{\rho \cdot D_{A,m} \cdot \ln \left[\frac{1 - \left(1 + 1/r \right) \cdot \omega_{A,down}}{1 - \left(1 + 1/r \right) \cdot \omega_{A,up}} \right]}{\left(1 + 1/r \right)} \tag{2.40}$$

$$n_B \cdot l = \frac{\rho \cdot D_{B,m} \cdot \ln\left[\frac{1-(1+r)\cdot \omega_{B,down}}{1-(1+r)\cdot \omega_{B,up}}\right]}{(1+r)} \tag{2.41}$$

The flux of components A (n_A) and B (n_B) can be determined by iterating Equations 2.40 and 2.41 with an initial guess of r value. A good initial value for r is the ratio of n_A and n_B in Equations 2.40 and 2.41 with the r term neglected. Solving for n_A and n_B, a new r value is obtained. Repeating this process until r converges upon the value given by Equation 2.37 allows taking the bulk flow effects into consideration, and the permeability of component A can be calculated by Equation 2.42.

$$P_A = \frac{22400 \cdot n_A \cdot l}{M_A \cdot \Delta f_A} \tag{2.42}$$

2.4 Temperature dependence of gas transport

The temperature dependence of the diffusion coefficient follows an Arrhenius relationship [13]:

$$D = D_0 \exp\left(\frac{-E_d}{RT}\right) \tag{2.43}$$

where D_0 is the pre-exponential factor; E_d is the activation energy for diffusion, which represents the energy required for a penetrant to jump between sorption sites within the

polymer matrix. For a given polymer, E_d is primarily dependent on penetrant size and shape. A larger penetrant size generally requires higher activation energy for diffusion [29].

The temperature dependence of sorption can be described by the van't Hoff equation:

$$S = S_0 \exp\left(\frac{-\Delta H_S}{RT}\right) \tag{2.44}$$

S_0 is the pre-exponential factor; ΔH_S is the heat of sorption, which is mainly governed by the condensability of the penetrant. The dissolution of a penetrant molecule into a polymer matrix can be described as a three-step thermodynamic process: (i) penetrant condensation, (ii) creation of a molecular scale gap of sufficient size to accommodate the penetrant, and (iii) mixing of the condensed penetrant with the polymer matrix [30, 31]. The heat of sorption can be expressed as:

$$\Delta H_s = \Delta H_{condensation} + \Delta H_{void\ \ formation} + \Delta H_{mixing} \tag{2.45}$$

where $\Delta H_{condensation}$ is the enthalpy of condensation of the penetrant, $\Delta H_{void\ \ formation}$ is the energy required to create a molecular gap, and ΔH_{mixing} is the partial molar enthalpy of mixing of the condensed penetrant within the polymer matrix. For highly condensable gases such as CO_2, ΔH_s is usually negative due to the large contribution of the

$\Delta H_{condensation}$ tem. As a result, the solubility increases with decreasing temperature. Since the energy associated with the condensation step is the dominant factor, gas solubility often scales with gas condensabilities. The more condensable the gas, the more negative heat of sorption it has [29].

Permeability is defined in Equation 2.8 as the product of a diffusion coefficient and a sorption coefficient; thus it is also affected by temperature. The temperature dependence of permeability follows an Arrhenius relationship:

$$P = P_0 \exp\left(\frac{-E_p}{RT}\right) \tag{2.46}$$

where P_0 is the pre-exponential factor, and E_p is the activation energy for permeation. E_p equals the sum of the activation energy for diffusion and the heat of sorption:

$$E_p = E_d + \Delta H_S \tag{2.47}$$

Typically, the activation energy for diffusion is larger in absolute magnitude than the heat of sorption, so permeability decreases and selectivity increases with decreasing temperature [29]. However, for the polyimide membranes identified in this work, it appears that the interaction between the polymer and CO_2 creates relatively high heats of sorption, making the activation energy for diffusion and heats of sorption similar in magnitude. In such a case with significantly lower permeation activation energy for CO_2,

a decrease in operating temperature reduces CO_2 permeance less than that for N_2, thus increasing the CO_2 selectivity with respect to N_2.

2.5 Temperature dependence of the upper bound

The two key characteristics of gas separation membranes are the permeability and selectivity. It was recognized that these are trade-off parameters as the selectivity generally decreases with increasing permeability of the more permeable gas component, and vice versa [32-35]. Robeson [32, 33] analyzed a large pool of literature data and empirically deduced the concept of an upper bound for a variety of gas pairs. Figure 2.6 shows the upper bound for the CO_2/N_2 penetrant pair. The upper bound represents the most favorable combinations of permeability and selectivity of soluble polymeric membranes, that can be formed into asymmetric structures, reported in literature, and the relationship is described by Equation 2.48.

$$\alpha_{A/B} = \frac{\beta_{A/B}}{P_A^{\lambda_{A/B}}} \tag{2.48}$$

where $\alpha_{A/B}$ is the selectivity, P_A is the permeability of the more permeable gas, $\lambda_{A/B}$ and $\beta_{A/B}$ are empirically determined parameters which depend on the gas pair of interest [36]. A theoretical model describing the upper bound behavior of polymeric membranes based on fundamental considerations was developed by Freeman [34].

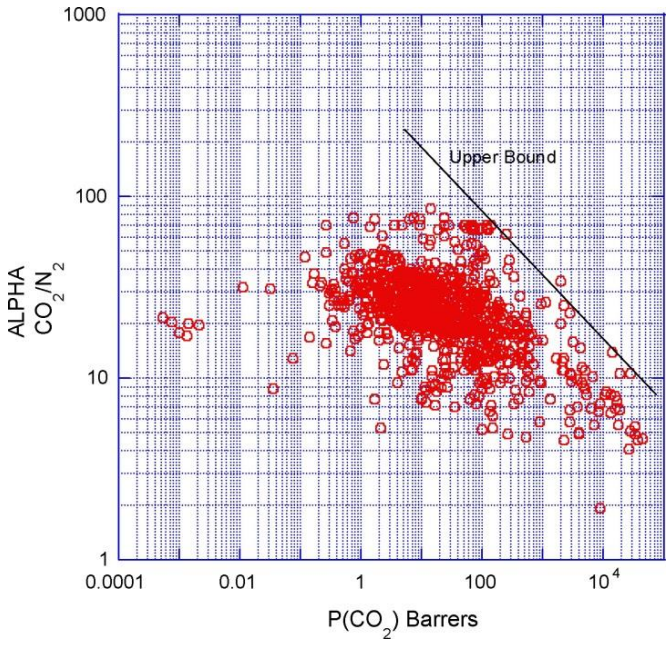

Figure 2.6: Upper bound correlation for CO_2/N_2 separation [33].

The tradeoff relationships described by Robeson and Freeman were developed based on membrane performance at 25-35 °C, primarily because most permeability data reported in literature were obtained from measurements carried out within this temperature range [32]. However, Rowe [36] pointed out that the temperature-dependent performance does not simply follow the upper bound behavior described by Robeson. Rather, as temperature decreases, the separation performance improves in the absence of plasticization. The upper bounds at sub-ambient temperatures are higher than at room temperature. Since the movement of penetrant molecules in polymeric membranes is dependent on thermally activated chain motion, and solubility is correlated to polymer-penetrant interactions and penetrant condensability, the influence of temperature on polymer properties such as chain stiffness, free volume, and polymer-penetrant interactions will have a strong impact on the membrane separation performance.

A model describing the influence of temperature on the permeability/selectivity tradeoff relationship of polymeric membranes was developed by Rowe from theoretical considerations [36]. This model was used to predict the influence of temperature on the upper bound behavior for several gas pairs. The predicted upper bound shifts vertically with temperature, and the direction and magnitude of the shift depend on the sizes and condensabilities of the gases considered. Figure 2.7 shows the influence of temperature on the predicted upper bound behavior for the CO_2/N_2 penetrant pair.

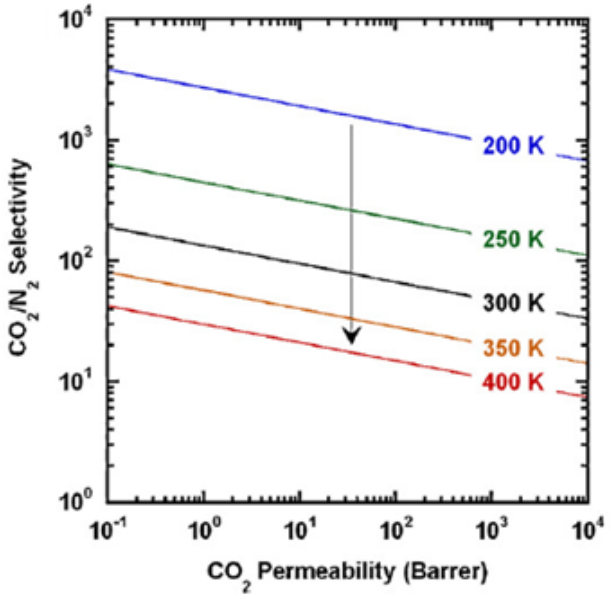

Figure 2.7 Influence of temperature on the predicted upper bound behavior for CO_2/N_2 separation [36].

2.6 Penetrant-polymer interactions

2.6.1 Conditioning

Conditioning is defined to be the hysteretic change in physical properties of glassy polymers following exposure to penetrants with high activities [37-41]. When the concentration of a highly sorbing penetrant in the polymer reaches the point of physical swelling, subtle packing disruptions occur in the non-equilibrium polymer matrix. These disruptions introduce additional excess free volume and enable energetically easier movement of penetrant molecules. After removal of the penetrant, the glassy polymer chain segments can't immediately resume their original configuration and the polymer is left in a slightly swollen state. A membrane in such a state is considered to be "conditioned". Conditioning results in an increase in the permeability of penetrants and causes hysteresis in sorption and permeation [37, 38, 40]

Significant and long-lived permeability increases have been produced for glassy polymers through high pressure CO_2 conditioning [42, 43]. The permeability enhancement is believed to be a result of increased solubility and diffusivity [37]. Swelling of the polymer by penetrants dissolved in the well packed region leads to a decrease in the inter-segmental steric resistance and a corresponding increase in penetrant diffusivity [44]. Previous studies show that asymmetric hollow fiber membranes are easier to be conditioned than dense films, and the reason was attributed to alterations in the super-molecular morphology of the fibers [42]. In this work, the highly condensable CO_2 will permeate through glassy polyimides hollow fiber membranes at sub-ambient temperatures, where the activity of CO_2 is much higher than at room temperature. The

increased CO_2 activity at such cold conditions will render the glassy membranes more prone to be conditioned.

2.6.2 Plasticization

Plasticization is said to occur when the presence of a highly sorbing penetrant causes an increase in a glassy polymer's segmental mobility, thereby increasing the diffusivity of all penetrants through the membrane [45-47]. Highly condensable penetrants, such as $CO_{2,}$ can cause plasticization. This phenomenon usually occurs when the partial pressure of the condensable penetrant is high or at low temperatures when the saturation vapor pressure of the penetrant is low. The increased molecular motions reduce the polymer's size discriminating capability. Thus, the permeation of the slower component is increased more than that for the faster component. On the permeation isotherm, an upswing in the penetrants permeability and a corresponding loss of selectivity is normally observed for a glassy membrane that has experienced plasticization. Macroscopically, plasticization has been evidenced by a decrease in the glass transition temperature and softening of the polymer materials [1, 47]. Figure 2.8 depicts the effects of plasticization on membrane permeation behaviors.

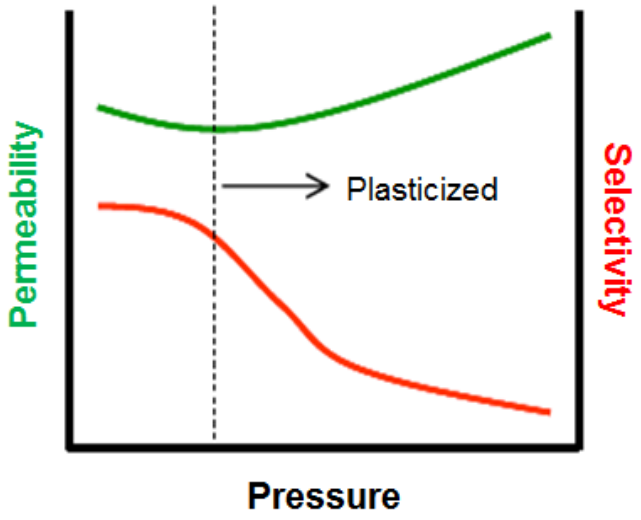

Figure 2.8: Effects of plasticization on membrane permeation behaviors.

The pressure at which the permeability starts to increase with increasing penetrant partial pressure is called the plasticization pressure [46]. This is usually defined on the basis of a zero downstream pressure. If the downstream pressure is not zero, the observed plasticization pressure is smaller. Before plasticization occurs, membrane permeability decreases slightly with the increase of penetrant partial pressure. This is due to the sorption of penetrants in the Langmuir environment when the Langmuir sites are becoming saturated. As penetrant partial pressure is increased to a certain point, the Henry's mode sorption begins to play a dominant role, and further increase in penetrant concentration causes swelling of the densely packed regions. When the level of swelling is high enough to initiate large scale segmental motions, plasticization occurs.

2.7 Effect of polymer chain orientation on gas transport properties

Drawing or stretching of an amorphous polymer is known to lead to reorientation of the polymer chain segments [48]. During the orientation process, the polymer chains become aligned in the direction of the applied stress, as is shown in Figure 2.9. Anisotropy is introduced in the polymer after orientation, and the change in the spatial distribution of the polymer chains will affect gas sorption and diffusion through the membrane. Due to better chain packing, the reduction in free volume leads to decreased solubility of the gases [49], and a decrease in gas diffusivity is caused by reduced polymer chain mobility. The drawing of a polymer increases its effective chain rigidity [50-52], and the path length for diffusion increases due to an increase in the tortuosity [53]. Moreover, the better chain packing coupled with reduced chain mobility leads to the redistribution of transient gap size in the polymer matrix, often improving the membrane's size discriminating capability.

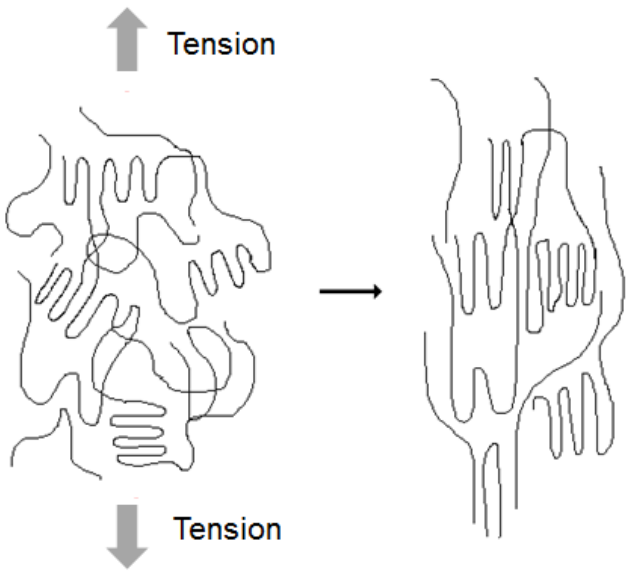

Figure 2.9: The orientation of polymer chains in the direction of applied stress.

2.8 Formation of asymmetric hollow fiber membranes

The hollow fiber configuration is currently the most desirable membrane geometry in terms of packing efficiency. Figure 2.10 shows a schematic of an asymmetric hollow fiber membrane. The asymmetric structure is composed of a thin skin layer and a porous substrate. The skin layer is the selective part of the hollow fiber membrane, with a thickness of ~ 0.1 micron, while the porous substrate provides structural integrity. Ideally, the substrate should not add significant mass transfer resistances to gas transport.

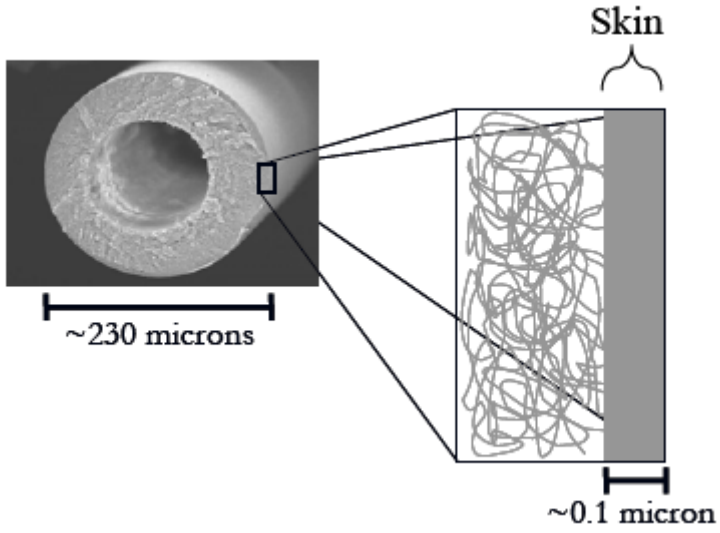

Figure 2.10: The macroscopic structure of an asymmetric hollow fiber membrane.

During the formation of asymmetric hollow fiber membranes, polymer molecules organize themselves into intrinsic morphologies that must selectively pass gas molecules and withstand high pressures (100-1000 psi). Since the size difference between gas molecules is on the order of Angstrom, 10 or 100 Å defects in the skin layer may result in

unselective membranes. In practice, the spinning of asymmetric hollow fiber membranes is an art.

2.8.1 Dope development criteria

The formation of asymmetric hollow fiber membranes begins with the development of a polymer solution. The polymer solution is usually referred as "dope", which contains polymer, solvents and non-solvents (including additives). Solvents and non-solvents are generally miscible with water and have varying degrees of volatility. The commonly used solvents are 1-methyl-2-pyrrolidinone (NMP), dimethylacetamide (DMAC) and tetrahydrofuran (THF) [54]. Compared to solvents, non-solvents have significantly lower polymer solubility, like water, alcohols and acetone.

A dope's spinnability and its capability to form desirable membranes largely depend on its rheological properties. Commonly used dopes are highly viscous and display zero shear viscosities in the range of 10^4 cP [55]. A good extensional viscosity allows it to tolerate the rigorous extensional stresses during fiber spinning. The rheological properties of the dope can be tuned by adjusting the polymer concentration and the polymer molecular weight, or by adding additives.

A dope's ability to phase separate and its phase separation rate are also critical parameters for the formation of desirable membranes. Instant phase separation is generally preferred because it allows the formation of circular fibers and is more likely to result in open pores in the substructure [56]. The dope's initial composition should be chosen as close to the binodal line as possible to ensure almost instant phase separation.

2.8.2 Phase separation mechanisms

Asymmetric hollow fiber membranes are typically formed via a "liquid-liquid" phase separation process. During fiber spinning, the dope is quenched in a non-solvent bath. Due to the rapid loss of solvent and influx of non-solvent in the quench bath, the nascent membrane phase separates into two phases, a polymer-rich phase and a polymer-lean phase. The polymer-rich phase forms the membrane structure while the polymer-lean phase contributes to the formation of pores in the membrane.

Although the formation process is controlled by a combination of thermodynamics and phase separation kinetics, the isothermal ternary phase diagram can provide qualitative understanding of the phase separation process (Figure 2.11) [57, 58]. The vertices of the equilateral triangle represent the polymer, solvent and non-solvent, respectively. The interior points represent ternary compositions. The ternary phase diagrams can be divided into three thermodynamic regions: (i) a stable single-phase region, (ii) two metastable two-phase regions, and (iii) an unstable two-phase region. The boundary between single-phase region and two-phase regions is referred to as the binodal line, and the boundary between metastable two-phase region and unstable two-phase region is referred to as the spinodal line. The intersection between these two lines is the critical point. The shadowed region is called the "vitrified" region, where the polymer chain mobility is considered sufficiently low that it may prevent macromolecular rearrangements on experimental time scales.

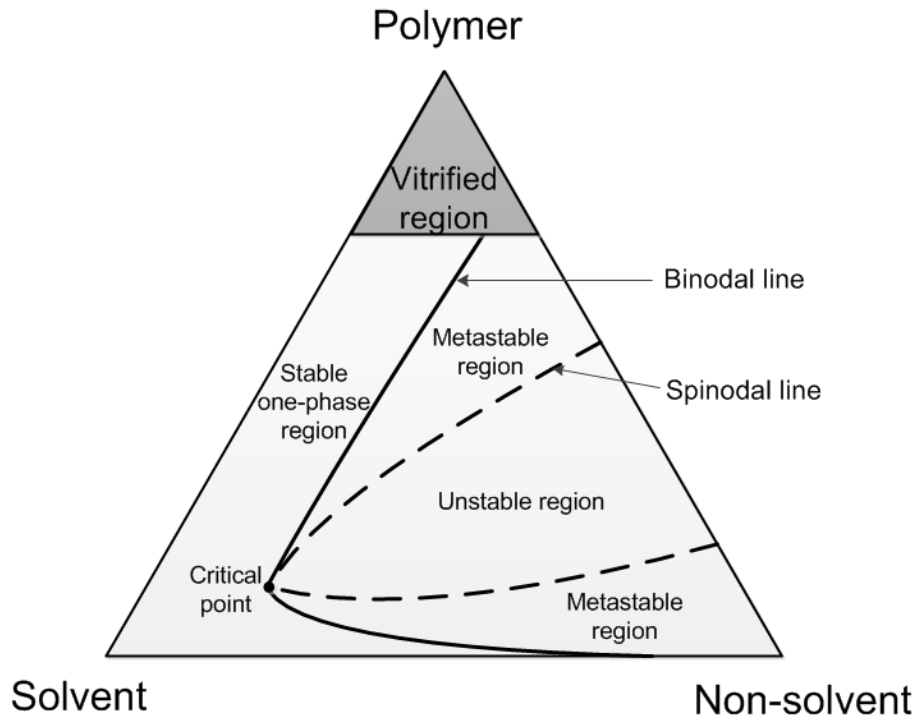

Figure 2.11: Ternary phase diagram for dope compositions: a general schematic showing the stable, metastable, unstable and vitrified regions.

During phase separation, the counter diffusion of solvent and non-solvent will change the dope composition from one-phase region to a two-phase region. In the two phase region, the polymer solution will be thermodynamically driven to phase separate into polymer-rich and polymer-lean phases in order to minimize the Gibbs free energy of mixing, ΔG_M . The Flory-Huggins theory [59] can be used to describe ΔG_M at constant temperature and pressure for a ternary system (Equation 2.49).

$$\frac{\Delta G_M}{RT} = n_1 \ln \phi_1 + n_2 \ln \phi_2 + n_3 \ln \phi_3 + \chi_{12} n_1 \phi_2 + \chi_{13} n_1 \phi_3 + \chi_{23} n_2 \phi_3 \quad (2.49)$$

The subscripts represent: (1) non-solvent, (2) solvent and (3) polymer. n_i are the moles, ϕ_i are the volume fractions and χ_{ij} are the binary interaction parameters.

Nucleation and growth

When the dope composition reaches the two-phase metastable regions, phase separation may follow the nucleation and growth mechanism. In the metastable regions, there is a thermodynamic barrier for the nucleation of a new phase. Nuclei that are smaller than a critical size are metastable and tends to re-dissolve into the homogeneous phase; while nuclei that are larger than the critical size can overcome the energy barrier and keeps growing. This phase separation mechanism is called nucleation and growth.

The equilibrium compositions of the polymer-rich and polymer-lean phases lie at the intersections of the binodal line and the tie lines on a ternary phase diagram (Figure 2.12). The location of the binodal line can be experimentally determined via the cloud point technique [60, 61], while the location of the tie lines can be determined using the Flory-Huggins theory. At equilibrium, the chemical potentials of each species in the polymer-rich and polymer-lean phases are equal, i.e.

$$\Delta\mu_i^A = \Delta\mu_i^B \tag{2.50}$$

The superscripts A and B represent the polymer-rich and polymer-lean phases, respectively. And $\Delta\mu_i$ is the difference between the chemical potential of component i in solution and in the pure state. The chemical potential is defined as:

$$\frac{\Delta\mu_i}{RT} = \frac{\partial}{\partial n_i}\left(\frac{\Delta G_M}{RT}\right)_{p,T,n_j} \tag{2.51}$$

Combining Equations 2.49-2.51, and under the material balance constraints, $\sum\phi_{i,A} = \sum\phi_{i,B} = 1$, the individual tie lines can be determined. Detailed analysis can be found in Yilmaz's paper [57].

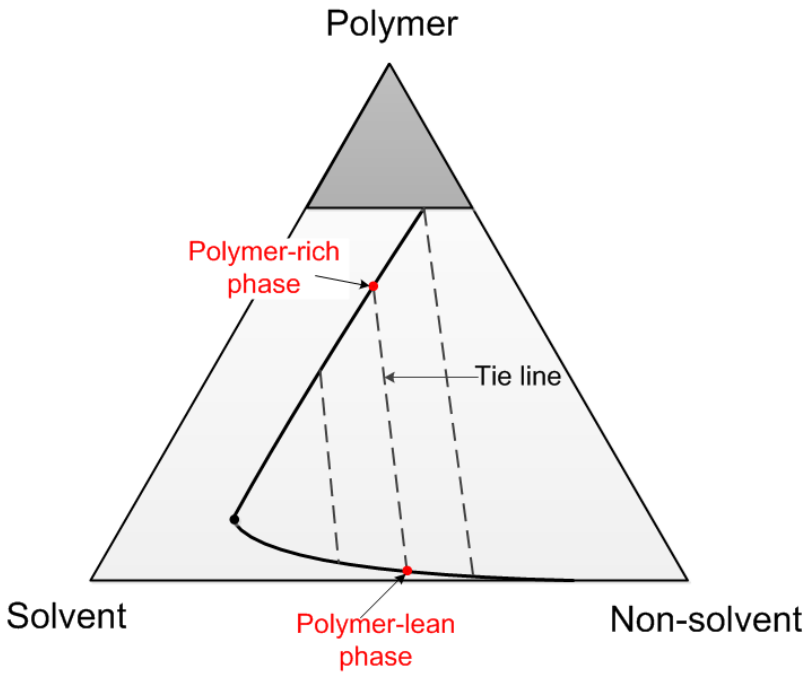

Figure 2.12: The determination of polymer-rich and polymer-lean phases on a ternary phase diagram.

Spinodal decomposition

Spinodal decomposition refers to a condition where there is no need for a nucleus to exist for phase separation to occur. Different from the nucleation and growth mechanism, the polymer-rich and polymer-lean phases are not at equilibrium at the start of spinodal decomposition. They instead, diffuse to equilibrium compositions during the course of the phase separation process.

The boundary of the unstable region (the spinodal line) is difficult to be determined experimentally. Under a large number of assumptions, the Flory-Huggins theory can be used to mathematically define the spinodal line at constant temperature, pressure and constant binary interaction parameters (Equation 2.52) [57, 58].

$$\left[\frac{1}{\phi_1}+\frac{\nu_1}{\nu_2\phi_2}-2\chi_{12}\right]\left[\frac{1}{\phi_1}+\frac{\nu_1}{\nu_3\phi_3}-2\chi_{13}\right]-\left[\frac{1}{\phi_1}+\frac{\nu_1}{\nu_2}\chi_{23}-\chi_{12}-\chi_{13}\right]^2=0 \quad (2.52)$$

where, ν_i is the molar volumes of species i. Spinodal decomposition usually promotes the formation of an "open-cell" substructure that is advantageous for gas separation.

2.8.3 Spinning of asymmetric hollow fiber membranes

The dry-jet/wet-quench spinning process (Figure 2.13) is used in this work to form asymmetric hollow fiber membranes. This process involves the simultaneous co-extrusion of the dope and bore fluid. The bore fluid is a neutral mixture of solvent and non-solvent which prevents the nascent fiber from collapsing during formation. The

composition of the bore fluid is selected so that it doesn't significantly phase separate or dissolve the nascent fiber. The dope is extruded through an annular orifice in the spinneret while the bore fluid is extruded in the center of the annulus. Spinneret design is critical since the dope and bore fluid must seamlessly join into the small annular configuration at high pressures. Once extruded, the nascent fiber is drawn to a gaseous region, known as the air gap, between the spinneret and the quench bath. In the air gap, solvent and/or non-solvent evaporation occurs at the outermost portion of the fiber and a nascent ultra-thin integral selective skin layer forms. The nascent fiber then enters a non-solvent quench bath (typically water) where phase separation occurs and a solid fiber is formed. The solid fiber is collected by a take-up drum at rates between 10-50 m/min. Figure 2.14 shows the trajectories of the dope compositions in the skin layer and the substrate during spinning. Ideally, the formation of the skin layer should follow the pathway AB until the vitrified region is reached; however, in this work, a different skin formation pathway has to be pursued, which will be discussed later. The porous substrate is formed in the water quench bath, where non-solvent water diffuses into the fiber and brings the composition of the support layer to the two-phase region (pathway AC).

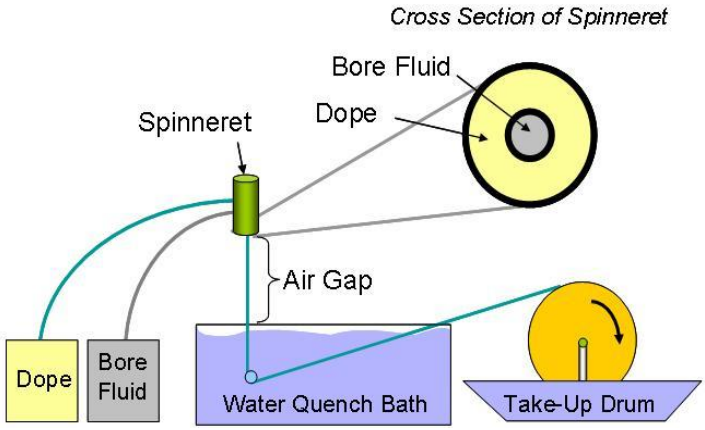

Figure 2.13: A simple schematic of dry-jet/wet-quench spinning process.

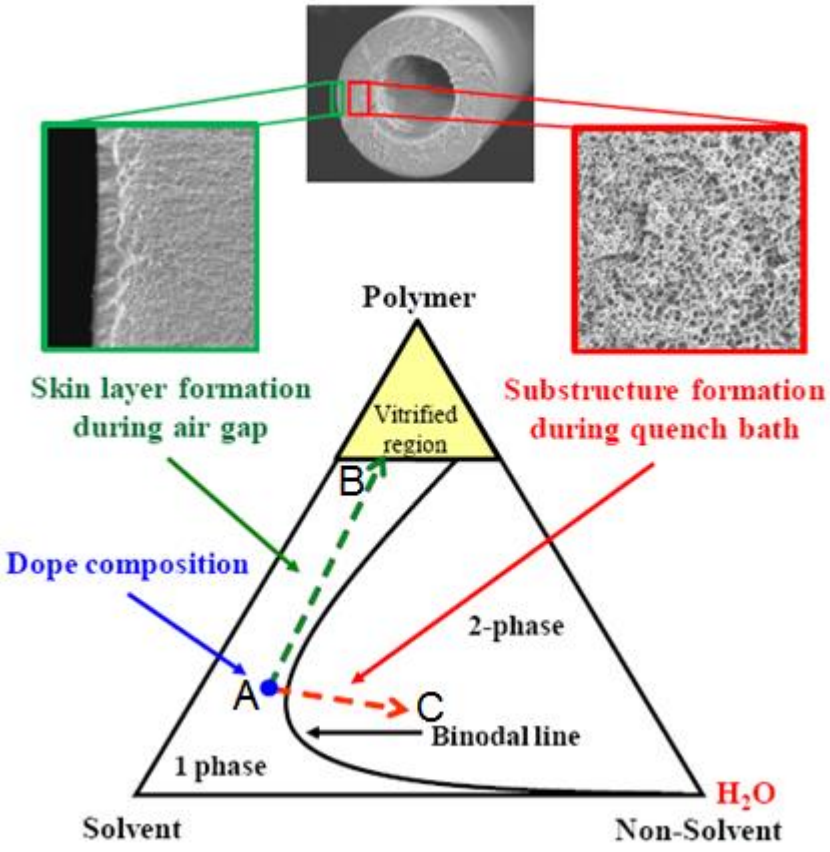

Figure 2.14: Hypothetical trajectories for dope composition in the skin layer and substrate during the formation of asymmetric hollow fiber membranes [62].

2.8.4 Dehydration

When freshly spun fibers are removed from the water bath, it is important to perform what is known as a “solvent exchange” procedure before drying. This is because the capillary forces generated during the drying of water-wet membranes can cause significant changes to the porous substructure. The substructure may collapse and cause significant decrease in membrane permeability [63, 64]. The purpose of solvent exchange is to replace water with volatile fluids of lower surface tension before drying. This process involves contacting the membrane with a water soluble alcohol and replacing the alcohol with a volatile organic compound of lower surface tension [54]. Once water is replaced by these lower surface tension fluids, the membrane can be dried at ambient or elevated temperatures with minimal morphological collapse.

2.8.5 Post-treatment

Most commercial hollow fiber membranes have very thin, yet defective, selective skin layers. After drying, the defects in the skin layer must be plugged by a “caulking" step, which is typically referred to as post-treatment process. Various post-treatment techniques can be found in the literature [65, 66], the purpose of which is to plug defects and force penetrants to permeate through the skin layer of the asymmetric membrane instead of the defects. The caulking material should be highly permeable to penetrants in order to minimize additional transport resistance, and at the same time, be able to effectively eliminate free flows through defects in the skin. A good caulking material can generate membrane selectivity close to the intrinsic values of the polymer while maintaining high gas flux.

2.9 References

[1] R. E. Kesting and A. Fritzsche, Polymeric gas separation membranes: Wiley New York, 1993.

[2] M. Rungta, Ph.D. thesis, Carbon molecular sieve dense film membranes for ethylene/ethane separations, Georgia Institute of Technology, 2012.

[3] Y. Tsujita, H. Hachisuka, T. Imai, A. Takizawa, and T. Kinoshita, Solubility and permeability of quenched poly (2, 6-dimethyl phenyleneoxide) with various microvoids, Journal of membrane science, vol. 60, pp. 103-111, 1991.

[4] H. Hachisuka, H. Takizawa, Y. Tsujita, A. Takizawa, and T. Kinoshita, Gas transport properties in polycarbonate films with various unrelaxed volumes, Polymer, vol. 32, pp. 2382-2386, 1991.

[5] H. Hachisuka, Y. Tsujita, A. Takizawa, and T. Kinoshita, Gas transport properties of annealed polyimide films, Journal of Polymer Science Part B: Polymer Physics, vol. 29, pp. 11-16, 1991.

[6] M. Mulder, Basic principles of membrane technology, 2nd edition: Kluwer Academic Pub, 1996.

[7] E. L. Cussler, Diffusion: mass transfer in fluid systems: Cambridge university press, 2009.

[8] W. Koros, Membranes-Learning a lesson from nature, Chemical engineering progress, vol. 91, pp. 68-81, 1995.

[9] M. Knudsen, The law of the molecular flow and viscosity of gases moving through tubes, Ann. Phys, vol. 28, pp. 75-130, 1909.

[10] R. N. Maddox and A. Hines, Mass transfer fundamentals and applications, Editorial Prentice-Hall, 1985.

[11] D. A. Reed and G. Ehrlich, Surface diffusion, atomic jump rates and thermodynamics, Surface Science, vol. 102, pp. 588-609, 1981.

[12] K. M. Steel, Ph.D. thesis, Carbon membranes for challenging gas separations, The University of Texas at Austin, 2000.

[13] W. J. Koros and G. K. Fleming, Membrane-based gas separation, Journal of Membrane Science, vol. 83, pp. 1-80, Aug 1993.

[14] J. G. Wijmans and R. W. Baker, The solution-diffusion model - A review, Journal of Membrane Science, vol. 107, pp. 1-21, Nov 1995.

[15] R. M. Barrer, J. A. Barrie, and J. Slater, Sorption and diffusion in ethyl cellulose. 3. Comparison between ethyl cellulose and rubber, Journal of Polymer Science, vol. 27, pp. 177-197, 1958.

[16] W. J. Koros, A. H. Chan, and D. R. Paul, Sorption and transport of various gases in polycarbonate, Journal of Membrane Science, vol. 2, pp. 165-190, 1977.

[17] W. J. Koros, Simplified analysis of gas polymer selective solubility behavior, Journal of Polymer Science Part B-Polymer Physics, vol. 23, pp. 1611-1628, 1985.

[18] H. Suda and K. Haraya, Gas permeation through micropores of carbon molecular sieve membranes derived from Kapton polyimide, The Journal of Physical Chemistry B, vol. 101, pp. 3988-3994, 1997.

[19] W. J. Koros, Barrier polymers and structures vol. 423: Amer Chemical Society, 1990.

[20] G. S. Park and J. Crank, Diffusion in polymers, 1968.

[21] J. S. Lee, Ph.D. thesis, Fundamentals of transport in advanced barrier materials based on engineered antiplasticization, Georgia Institute of Technology, 2011.

[22] D. R. Paul, Gas sorption and transport in glassy-polymers, Berichte Der Bunsen-Gesellschaft-Physical Chemistry Chemical Physics, vol. 83, pp. 294-302, 1979.

[23] W. Koros and D. Paul, CO_2 sorption in poly (ethylene terephthalate) above and below the glass transition, Journal of Polymer Science: Polymer Physics Edition, vol. 16, pp. 1947-1963, 1978.

[24] I. C. Omole, Ph.D. thesis, Crosslinked polyimide hollow fiber membranes for aggressive natural gas feed streams, Georgia Institute of Technology, 2008.

[25] W. Koros, R. Chern, V. Stannett, and H. Hopfenberg, A model for permeation of mixed gases and vapors in glassy polymers, Journal of polymer Science: polymer physics edition, vol. 19, pp. 1513-1530, 1981.

[26] W. Koros, Model for sorption of mixed gases in glassy polymers, Journal of Polymer Science: Polymer Physics Edition, vol. 18, pp. 981-992, 1980.

[27] W. Koros, D. Paul, and A. Rocha, Carbon dioxide sorption and transport in polycarbonate, Journal of Polymer Science: Polymer Physics Edition, vol. 14, pp. 687-702, 1976.

[28] H. Denny Kamaruddin and W. J. Koros, Some observations about the application of Fick's first law for membrane separation of multicomponent mixtures, Journal of membrane science, vol. 135, pp. 147-159, 1997.

[29] L. M. Costello and W. J. Koros, Temperature-dependence of gas sorption and transport-properties in polymers-measurement and applications, Industrial & Engineering Chemistry Research, vol. 31, pp. 2708-2714, Dec 1992.

[30] K. Ghosal and B. D. Freeman, Gas separation using polymer membranes: An overview, Polymers for advanced technologies, vol. 5, pp. 673-697, 1994.

[31] Y. Yampolskii, I. Pinnau, and B. D. Freeman, Materials science of membranes for gas and vapor separation: Wiley Online Library, 2006.

[32] L. M. Robeson, Correlation of separation factor versus permeability for polymeric membranes, Journal of Membrane Science, vol. 62, pp. 165-185, Oct 1991.

[33] L. M. Robeson, The upper bound revisited, Journal of Membrane Science, vol. 320, pp. 390-400, Jul 2008.

[34] B. D. Freeman, Basis of permeability/selectivity tradeoff relations in polymeric gas separation membranes, Macromolecules, vol. 32, pp. 375-380, 1999.

[35] S. Matteucci, Y. Yampolskii, B. D. Freeman, and I. Pinnau, Transport of gases and vapors in glassy and rubbery polymers, Materials science of membranes for gas and vapor separation, pp. 1-47, 2006.

[36] B. W. Rowe, L. M. Robeson, B. D. Freeman, and D. R. Paul, Influence of temperature on the upper bound: Theoretical considerations and comparison with experimental results, Journal of Membrane Science, vol. 360, pp. 58-69, Sep 2010.

[37] M. R. Coleman and W. J. Koros, Conditioning of fluorine containing polyimides .1. Effect of exposure to high pressure carbon dioxide on permeability, Macromolecules, vol. 30, pp. 6899-6905, Nov 1997.

[38] G. K. Fleming and W. J. Koros, Carbon-dioxide conditioning effects on sorption and volume dilation behavior for bisphenol-A-polycarbonate, Macromolecules, vol. 23, pp. 1353-1360, Mar 1990.

[39] N. R. Horn and D. R. Paul, Carbon dioxide plasticization and conditioning effects in thick vs. thin glassy polymer films, Polymer, vol. 52, pp. 1619-1627, Mar 2011.

[40] S. M. Jordan, W. J. Koros, and G. K. Fleming, The effects of CO_2 exposure on pure and mixed gas permeation behavior - Comparison of glassy polycarbonate and silicon-rubber, Journal of Membrane Science, vol. 30, pp. 191-212, Feb 1987.

[41] A. M. Kratochvil and W. J. Koros, Effects of supercritical CO_2 conditioning on cross-linked polyimide membranes, Macromolecules, vol. 43, pp. 4679-4687, May 2010.

[42] S. M. Jordan, M. A. Henson, and W. J. Koros, The effects of carbon-dioxide conditioning on the permeation behavior of hollow fiber asymmetric membranes, Journal of Membrane Science, vol. 54, pp. 103-118, Nov 1990.

[43] S. M. Jordan, W. J. Koros, and J. K. Beasley, Characterization of CO_2-induced conditioning of polycarbonate films using penetrants with different solubilities, Journal of Membrane Science, vol. 43, pp. 103-120, Apr 1989.

[44] E. Sanders, Penetrant-induced plasticization and gas permeation in glassy polymers, Journal of Membrane Science, vol. 37, pp. 63-80, 1988.

[45] J. D. Wind, S. M. Sirard, D. R. Paul, P. F. Green, K. P. Johnston, and W. J. Koros, Carbon dioxide-induced plasticization of polyimide membranes: pseudo-equilibrium relationships of diffusion, sorption, and swelling, Macromolecules, vol. 36, pp. 6433-6441, 2003.

[46] A. Bos, I. G. M. Punt, M. Wessling, and H. Strathmann, CO_2-induced plasticization phenomena in glassy polymers, Journal of Membrane Science, vol. 155, pp. 67-78, Mar 1999.

[47] A. F. Ismail and W. Lorna, Penetrant-induced plasticization phenomenon in glassy polymers for gas separation membrane, Separation and Purification Technology, vol. 27, pp. 173-194, Jun 2002.

[48] E. A. McGonigle, J. Liggat, R. Pethrick, S. Jenkins, J. Daly, and D. Hayward, Permeability of N_2, Ar, He, O_2, and CO_2 through as-extruded amorphous and biaxially oriented polyester films: Dependence on chain mobility, Journal of Polymer Science Part B: Polymer Physics, vol. 42, pp. 2916-2929, 2004.

[49] J. Foot and I. Ward, The cold drawing of amorphous polyethylene terephthalate, Journal of Materials Science, vol. 10, pp. 955-960, 1975.

[50] R. M. Gohil, Morphology-permeability relationships in biaxially oriented Pet films: A relationship between oxygen permeability and PROF, Journal of applied polymer science, vol. 48, pp. 1649-1664, 1993.

[51] D. Bower, D. Jarvis, E. Lewis, and I. Ward, Molecular orientation in biaxially oriented sheets of poly (ethylene terephthalate) II. Correlation of orientation

averages with measured mechanical compliances, Journal of Polymer Science Part B: Polymer Physics, vol. 24, pp. 1481-1492, 1986.

[52] T. Kotani, J. Sweeney, and I. Ward, The measurement of transverse mechanical properties of polymer fibres, Journal of materials science, vol. 29, pp. 5551-5558, 1994.

[53] J. Slee, G. Orchard, D. Bower, and I. Ward, The transport of oxygen through oriented poly (ethylene terephthalate), Journal of Polymer Science Part B: Polymer Physics, vol. 27, pp. 71-83, 1989.

[54] D. T. Clausi, Ph.D. thesis, Formation and characterization of asymmetric polyimide hollow fiber membranes for gas separations, The University of Texas at Austin, 1998.

[55] S. Pesek and W. Koros, Aqueous quenched asymmetric polysulfone membranes prepared by dry/wet phase separation, Journal of Membrane Science, vol. 81, pp. 71-88, 1993.

[56] A. Reuvers and C. Smolders, Formation of membranes by means of immersion precipitation: Part II. the mechanism of formation of membranes prepared from the system cellulose acetate-acetone-water, Journal of membrane science, vol. 34, pp. 67-86, 1987.

[57] L. Yilmaz and A. McHugh, Analysis of nonsolvent–solvent–polymer phase diagrams and their relevance to membrane formation modeling, Journal of applied polymer science, vol. 31, pp. 997-1018, 1986.

[58] F. W. Altena and C. Smolders, Calculation of liquid-liquid phase separation in a ternary system of a polymer in a mixture of a solvent and a nonsolvent, Macromolecules, vol. 15, pp. 1491-1497, 1982.

[59] P. J. Flory, Principles of polymer chemistry: Cornell University Press, 1953.

[60] M. R. Kosuri and W. J. Koros, Defect-free asymmetric hollow fiber membranes from Torlon®, a polyamide–imide polymer, for high-pressure CO_2 separations, Journal of Membrane Science, vol. 320, pp. 65-72, 2008.

[61] D. W. Wallace, C. Staudt-Bickel, and W. J. Koros, Efficient development of effective hollow fiber membranes for gas separations from novel polymers, Journal of Membrane Science, vol. 278, pp. 92-104, 2006.

[62] B. E. Kraftschik, Ph.D. thesis, Advanced crosslinkable polyimide membranes for aggressive sour gas separations, Georgia Institute of Technology, 2013.

[63] W. Macdonald and C.-y. Pan, Method for drying water-wet membranes, ed: US Patent 3,842,515, 1974.

[64] P. Manos, Solvent exchange drying of membranes for gas separation, ed: Google Patents, 1978.

[65] O. M. Ekiner, R. A. Hayes, and P. Manos, Reactive post treatment for gas separation membranes, ed: Google Patents, 1992.

[66] J. M. Henis and M. K. Tripodi, Multicomponent membranes for gas separations, ed: Google Patents, 1980.

CHAPTER 3

MATERIALS AND EXPERIMENTAL PROCEDURES

This chapter describes the materials and experimental procedures used in this work. Section 3.1 includes the polymers and gases used. Section 3.2 presents the asymmetric hollow fiber membrane fabrication procedures and post-treatment methods. Section 3.3 introduces the various membrane characterization techniques.

3.1 Materials

3.1.1 Polymers

High molecular weight aromatic polyimides were first synthesized in 1955 by two-stage polycondensation of pyromellitic dianhydride with diamines [1]. Since then, researchers' interest in this class of polymer has been growing steadily. Polyimides have been shown to be the preferred class of polymer materials for gas separation membranes due to their excellent thermal and chemical properties as well as their superior separation efficiency compared to most other polymers [2]. In this work, two polyimides were used: Matrimid® 5218 and 6FDA/BPDA-DAM (1:1). Matrimid® 5218 is a commercially available polyimide purchased from Huntsman International LLC in the form of a yellow powder. 6FDA:BPDA-DAM (1:1) was custom synthesized by Akron Polymer Systems following standard procedures [3]. The structures of the repeating unit of these two polyimides are shown in Figure 3.1.

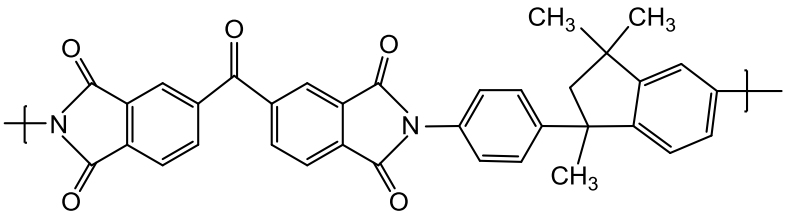

(a) Matrimid® 5218 (BTDA-DAPI)

BTDA: 3, 3', 4, 4'-benzophenone tetracarboxylic dianhydride
DAPI: 5(6)-amino-1-(4'-aminophenyl)-1,3,3-trimethylindane

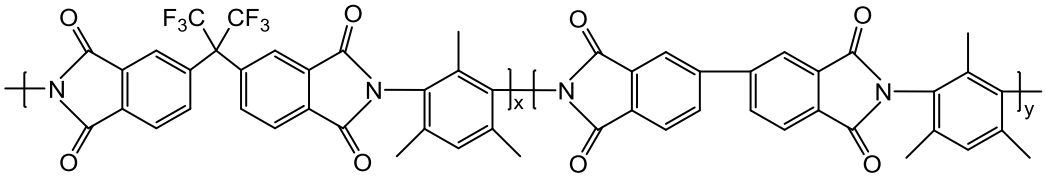

(b) 6FDA/BPDA-DAM (1:1)

6FDA: 5,5′-[2,2,2-trifluoro-1-(trifluoromethyl)ethylidene]bis-1,3-isobenzofurandione
BPDA: 3,3′,4,4′-biphenyl tetracarboxylic dianhydride
DAM: 2,4,6-trimethyl-1,3-phenylene diamine
The ratio of X to Y is 1:1

Figure 3.1: Structures of the repeating unit of polymers used in this work.

6FDA/BPDA-DAM (1:1) was synthesized via two-step polycondensation reactions [3]. The first step produces a high molecular weight polyamic acid via the reaction of stoichiometric amounts of the dianhydride (6FDA) and 3,3′,4,4′-biphenyl tetracarboxylic dianhydride (BPDA) in 1-methyl-2-pyrrolidinone (NMP) at low temperature (~ 5 °C). The second step is an imidization reaction which involves dehydration to close the imide ring. The synthesis scheme of 6FDA/BPDA-DAM is shown in Figure 3.2.

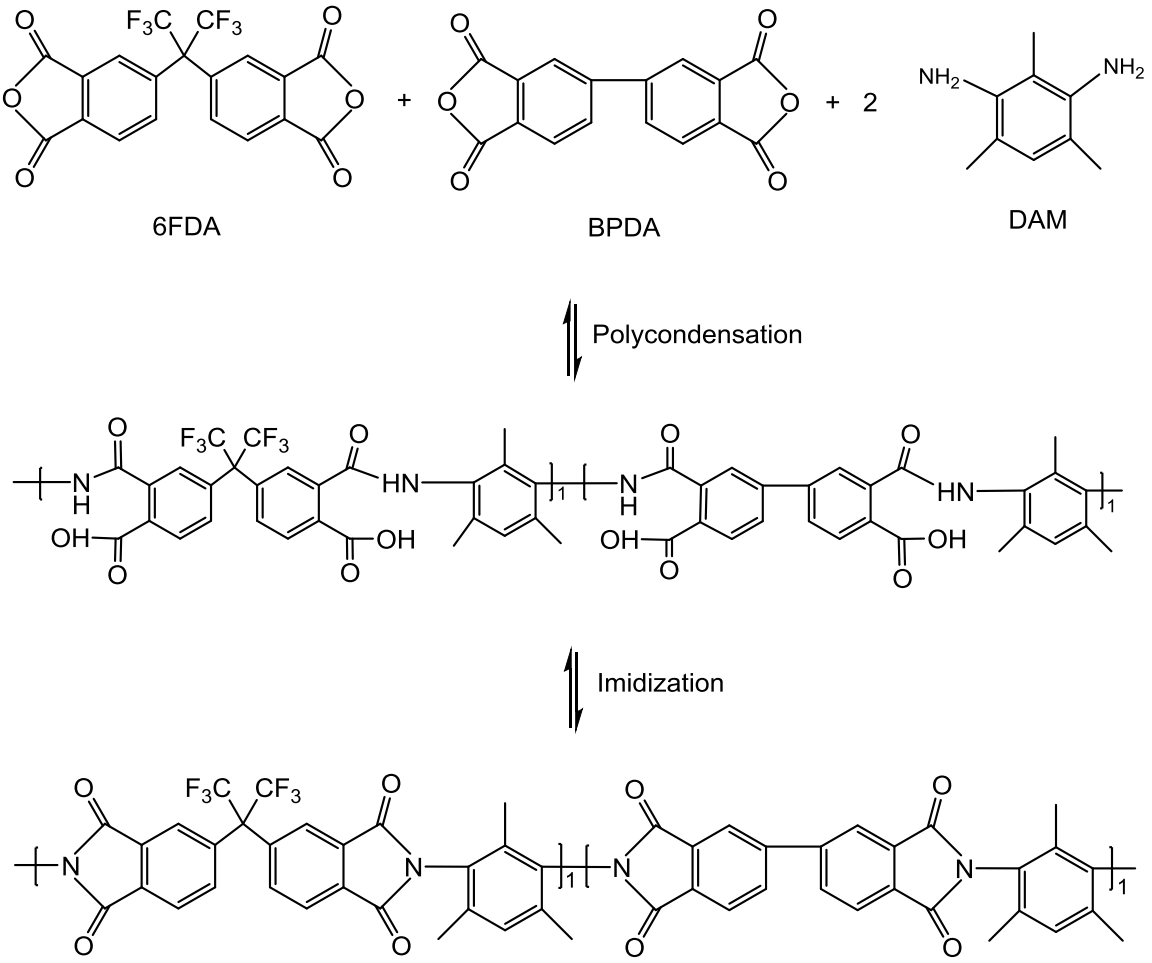

Figure 3.2: Synthesis scheme for 6FDA/BPDA-DAM (1:1) polyimide [3].

3.1.2 Gases

A binary mixture containing 20 mol% CO_2 and 80 mol% N_2 (Nexair) was the main gas used to evaluate the CO_2/N_2 separation properties of the hollow fiber membranes formed in this work.

O_2 (UHP Grade, Airgas), N_2 (UHP Grade, Airgas) and CO_2 (Research Grade, Airgas) were used for pure gas permeation measurements to characterize the defectiveness of the hollow fiber membrane's selective skin layer.

Other gases used to characterize the membranes include: SF_6 (CP Grade Airgas), CH_4 (Research Grade, Airgas), C_2H_4 (CP Grade, Airgas), C_2H_6 (CP Grade, Airgas), 20 mol% C_2H_4/80 mol% CH_4 (Nexair) and 50 mol% CO_2/50 mol% C_2H_6 (Nexair).

3.2 Formation of asymmetric hollow fiber membranes

3.2.1 Dope formulation

As is mentioned in Chapter 2, the dope for spinning is typically a mixture of the polymer, solvents and non-solvents. In this work, N-Methyl-2-pyrrolidone (NMP) was chosen as the non-volatile solvent due to its strong interaction with the polymer, miscibility with water, and it is relatively benign nature from a health standpoint [4]. Tetrahydrofuran (THF) was chosen as the volatile solvent due to its low boiling point and miscibility with water. Both ethanol (EtOH) and water were selected as the non-solvent. Compared to water's strong non-solvent power, the non-solvent property of EtOH is relatively weak which allows a big window to tune the dope formulation. Lithium nitrate ($LiNO_3$) was added as an additive in dopes containing 6FDA-based polymers to assist phase separation and build up viscosity [5].

To determine the composition of a specific dope, the "cloud point technique" was used [6, 7]. This technique allowed for the determination of a rough binodal line (the boundary between the one-phase and two-phase regions). At a fixed polymer

concentration, a series of dope samples with increasing non-solvent contents (and accordingly decreasing solvent contents) were made. After the dopes were well mixed, those with a composition that sit in the one-phase region were transparent, whereas those with a composition sitting in the two-phase region appeared cloudy. The dope composition on the phase boundary was the "cloud point". Same methods were repeated at a few different polymer concentrations, and all the cloud points were connected to form a rough binodal line. The initial dope composition was selected so that it was in the one-phase region but was close to the binodal line.

After the dope composition was fixed, the dopes were prepared with the following procedures. The polymers were dried under vacuum at 100 °C for at least 12 hours to remove moisture. When $LiNO_3$ was contained in the dope, it was also dried at 100 °C under vacuum for more than 12 hours because it absorbed moisture significantly. The anhydrous solvents and non-solvents (when water was used as the non-solvent, it didn't matter whether the solvents were anhydrous or not) were mixed in a 1 liter Qorpak glass jar according to the fixed concentrations. Then the polymer was added to the mixture. It was added last because this mixing sequence allowed for the polymer to dissolve faster. The jar was sealed with a Teflon® cap liner, and placed on a roller with a moderate speed (3 rpm). Due to the intrinsic viscosity of the dope, this simple low-shear mixing enables the homogenization of the mixture. It usually takes 2 weeks to 1 month for the dope to be well mixed, depending on the properties of the dopes. Sometimes, heat was applied to assist mixing. Once all the gas bubbles were eliminated and the dope was homogeneous to the naked eye, it was ready for spinning. Note that if the dope is too viscous to get rid of gas bubbles by rolling, it is helpful to let it sit still overnight.

3.2.2 Spinning of asymmetric hollow fiber membranes

The "dry-jet/wet-quench" spinning technique was used in this work to form asymmetric hollow fiber membranes. A picture of the spinning setup is shown in Figure 3.3. The well mixed dope was loaded into a 500-mL syringe pump (ISCO Inc., Lincoln, NE) and allowed to degas for 24 hours. Usually, heat was applied to facilitate the degas process. This step is important because the presence of gas bubbles in the dope can cause significant defects in the membrane and even spinning line breakage. The bore fluid was a mixture of NMP and water, and was loaded into a separate 100-mL syringe pump. The percentage of NMP in the bore fluid is between 80-95 %. The dope and bore fluid were co-extruded through a spinneret into the air gap ("dry-jet") and then into the aqueous quench bath ("wet-quench") where polymer solution solidified due to phase separation prior to being collected on a take-up drum. Temperatures of the dope-containing pump, dope line and spinneret were controlled via Benchtop Controllers (Omega Engineering Inc., Stamford, CT). Both dope and bore fluid were filtered in-line between the delivery pumps and the spinneret. Flow rates for the dope and bore fluid were controlled individually, with the bore fluid flow rate normally kept at 180 ml/hr and the dope flow rate at 60 ml/hr. The take-up drum is a 0.32 m diameter rotating polyethylene cylinder, the rotating speed of which is adjustable and can be used to control the draw ratio and fiber dimensions. To ensure complete phase separation and to facilitate the removal of solvent from newly spun fibers, the drum was partially submerged in a separate water bath at room temperature. Fibers were left on the rotating drum for ~15 minutes before being cut off. Table 3.1 lists the important spinning parameters than can be adjusted during the spinning of hollow fiber membranes. Once cut from the take-up drum, the

fibers were immersed in deionized (DI) water for at least 4 days with the water being changed daily. This promotes the removal of most of the solvent and non-solvent from the fibers. Right after the fibers were taken out of DI water, solvent exchange was carried out with sequential 1 hour baths of methanol and hexane, with the solvent being changed every 20 minutes. The fibers were then air-dried in a fume hood for 1 hour and dried under vacuum at appropriate temperatures (Matrimid® fibers were dried at 120 °C for 1 hour, and 6FDA-based fibers were dried at 75 °C for 3 hours).

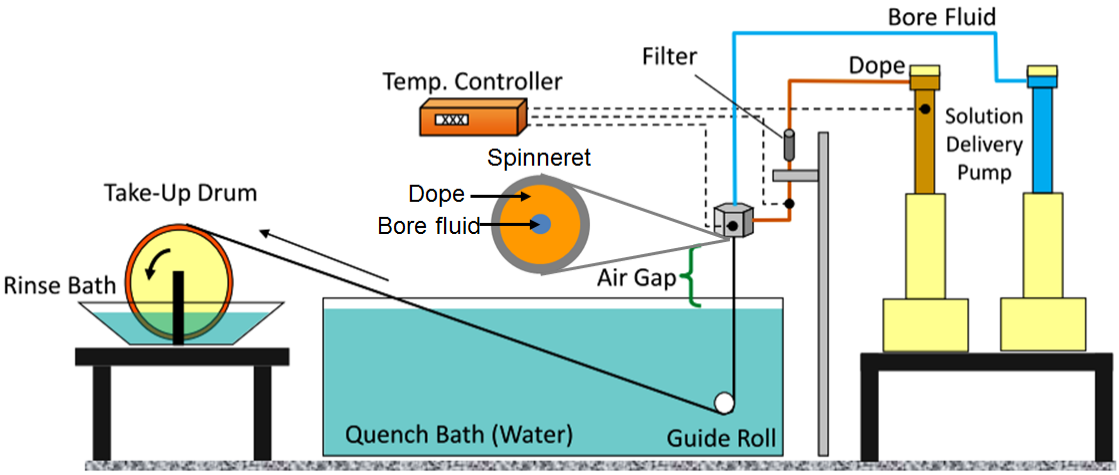

Figure 3.3: Dry-jet/wet-quench spinning setup.

Table 3.1: Some important parameters in the dry-jet/wet-quench spinning process

Dope Composition	Spinneret/Dope Temperature	Quench Bath Temperature
Bore Fluid Composition	Dope/Bore Fluid Flow Rates	Quench Bath Composition
Air Gap Height	Take-up Rate	Quench Bath Height

3.2.3 Hollow fiber module-making

Hollow fiber membranes were potted into laboratory-scale modules for permeation tests. A schematic of a typical hollow fiber module is shown in Figure 3.4. The detailed protocol for module making can be found in previous work [8, 9]. The epoxy should be selected based on performance requirements, such as operating temperature, cure time, thermal and chemical resistance, interaction with the membrane material, etc. In this work, epoxy DP100 (3M, St. Paul, MN) was chosen, which takes 5 minutes to cure and is effective within the temperature range of -54 to 163 °C. The number of fibers in each module was determined by the membrane transport properties as well as the gases being tested. When gas flux for single fiber was low, multiple fibers were potted into the module to build up flux for measurements. In this work, a typical module has an effective membrane length of 15-20 cm, and includes 10 Matrimid® fibers or 2 6FDA-based fibers.

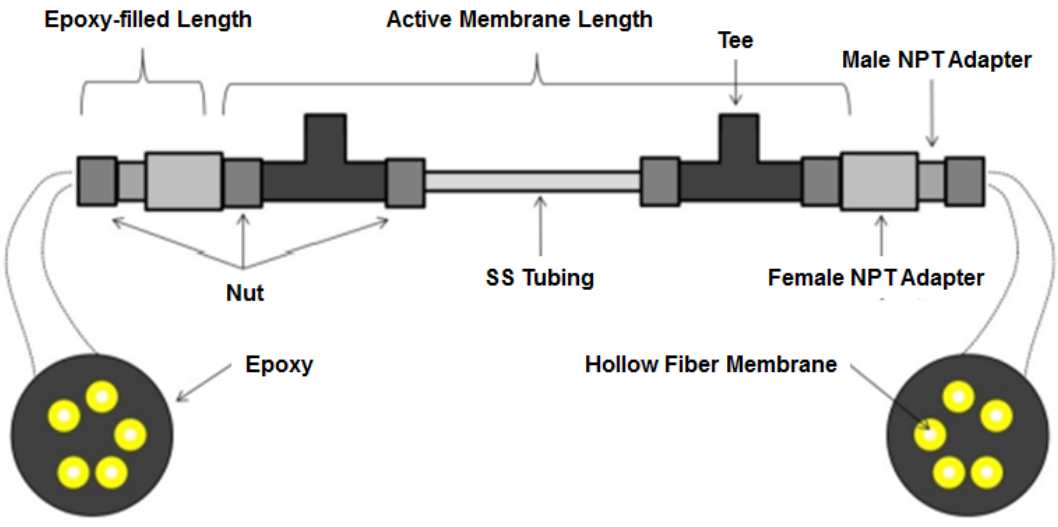

Figure 3.4: Schematic of laboratory-scale hollow fiber module.

3.3 Permeation characterization

3.3.1 Pure gas hollow fiber membrane permeation

3.3.1.1 Pure gas permeation system design

The pure gas permeation testing of hollow fiber membranes was carried out in a constant pressure system with a dead-end, counter-current flow configuration. Feed can be applied either on bore side or shell side of the membranes. In this work, the majority of the pure gas permeation test was conducted with bore side feed. Figure 3.5 depicts the permeation system setup. The entire feed stream permeates through the membrane and was collected on the shell side (the permeate side), where the flow-rates were measured using bubble flow-meters with appropriate range. This configuration allows for multiple fiber modules to be tested, with a common feed and under the same testing condition. This system was insulated and maintained at a constant temperature of 35 °C.

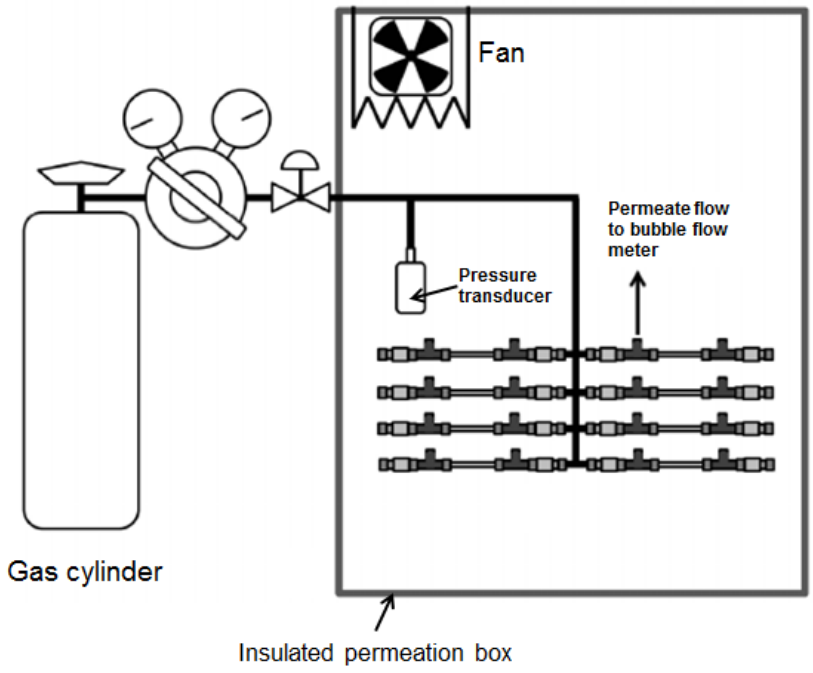

Figure 3.5: Constant pressure, pure gas permeation setup for hollow fiber membranes [10]. The modules are fed on the bore side.

3.3.1.2 Pure gas permeation testing

The pure gas permeation testing of hollow fiber membranes was performed according to the following procedures:

1) The modules were loaded into the pure gas permeation system with caps on the retentate side loosened to allow the bores of the fibers to be purged by the feed.
2) The feed gas was turned on to a pressure of 15-30 psig to purge the fibers for 1-2 minutes.
3) After purging, the caps on the retentate side were tightened (with the purge flow still active), so that a high pressure feed could be maintained within the modules.
4) The feed pressure was increased to the desired level and an initial 30 minutes time period was allowed for gas transport to reach steady state.
5) After the 30 minutes time period, the permeate flow rate of each individual module was measured by connecting the non-plugged port of the module (the outlet closest to the feed source, such that a counter-current flow configuration is established) to a bubble flowmeter with appropriate range. A stopwatch was used to measure the time required for a specific volume of gas to permeate through the fibers.
6) An additional 15 minutes was allowed and the permeate flow rate was measured again. When the flow rate difference between the first and second measurements was larger than 5 %, another 15 minute time period was waited. Subsequent measurements were repeated until steady state was reached (difference in flow rate is smaller than 5 %). Permeate flow rate of each module was then recorded.

7) Change the feed conditions and repeat steps 4-6. In this work, three pure gases were tested in the sequence of $N_2 \rightarrow O_2 \rightarrow CO_2$.

The pure gas permeance of an asymmetric hollow fiber membrane can be calculated using the following equation:

$$\left(\frac{P}{l}\right) = \frac{\left(\frac{\Delta V}{\Delta t}\right)_{STP}}{A \cdot \Delta f} \tag{3.1}$$

where, $\left(\frac{P}{l}\right)$ is the membrane permeance, $\left(\frac{\Delta V}{\Delta t}\right)_{STP}$ is the volumetric flow rate at standard temperature and pressure (273K, 1atm), A is the membrane area (sum of surface area of each individual fiber), and Δf is the transmembrane fugacity difference (If the feed gas is close to ideal state, fugacity difference can be replaced by pressure difference).

In Equation 3.1, permeance is in the unit of GPU, which is defined as:

$$1\ GPU = 1 \times 10^{-6} \frac{cm^3(STP)}{cm^2 \cdot s \cdot cmHg} \tag{3.2}$$

3.3.2 Mixed gas hollow fiber membrane permeation

3.3.2.1 Mixed gas permeation system design

The mixed gas permeation testing was also carried out in a constant pressure system, but was more complicated than pure gas testing. Constant flow over the upstream of the membrane had to be maintained, which generated a retentate stream (part of the feed stream that didn't permeate through the membrane). The use of a constant feed flow over the upstream surface of the membrane was necessary, which helped to prevent concentration polarization. Concentration polarization is a phenomenon that the concentration of the faster gas in the boundary layer is reduced, resulting in the change of the driving force for every component in the feed mixture [11]. The flow rate of the retentate stream could significantly affect the membrane performance. Mixed gas permeation test also involved the use of a gas chromatograph to analyze the composition of the permeate. In this work, the majority of mixed gas permeation testing was carried out at sub-ambient temperatures (-50 °C to 35 °C), therefore a special permeation box that could provide temperature within this range was required. The BTZ-475 benchtop temperature chamber (ESPEC North America, INC., Hudsonville, MI) was selected which could control temperature accurately within the range of -70 °C to 180 °C with ±0.5 °C fluctuation at control sensor after stabilization (Figure 3.6). Four mixed gas permeation testing lines were installed in this permeation box, with 2 modules sharing the same feed. A schematic of the mixed gas permeation setup is shown in Figure 3.7. To ensure the feed gas was cooled down before contacting the membrane, a long feed line was used to increase the cooling time. The permeate flow rate was measured by bubble flow meters with appropriate range and the permeate composition was analyzed by a gas

chromatograph (Bruker 430-GC, Agilent Technologies, CA). The retentate flow rate was controlled by needle valves and was measured by digital mass flowmeters (FMA Series, Omega Engineering, Inc.)

Figure 3.6: Cold membrane permeation box. Temperature range: -70°C to 180°C.

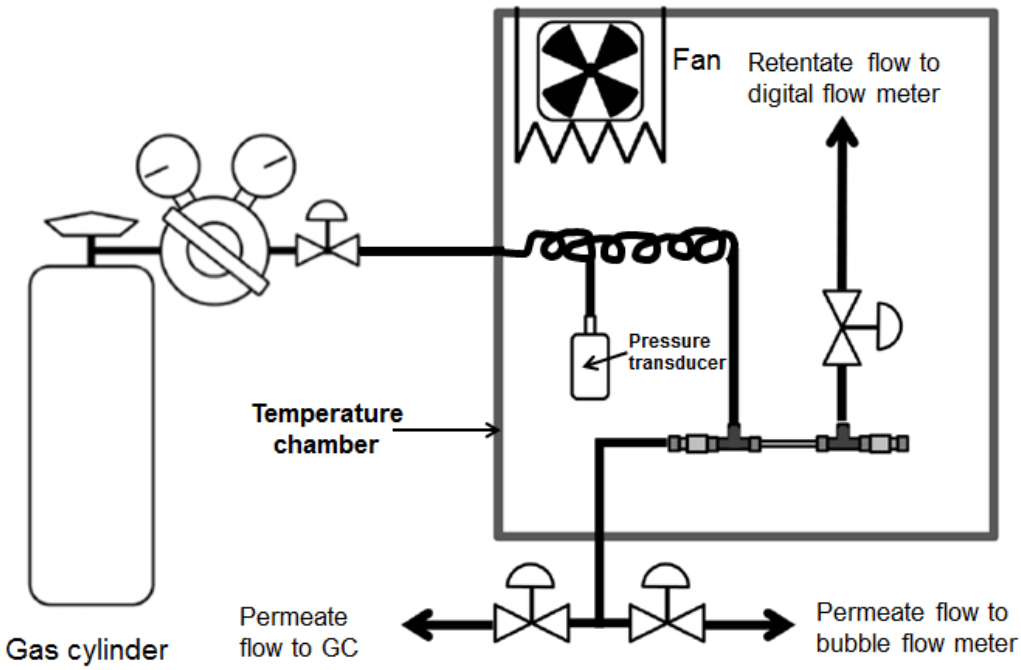

Figure 3.7: Constant pressure, mixed gas permeation setup for hollow fiber membranes. The module is fed on the shell side.

3.3.2.2 Mixed gas permeation testing

Mixed gas permeation tests are similar to pure gas permeation tests. The countercurrent flow configuration was used in this work, and feed was applied on either bore side or shell side of the fibers. To minimize concentration polarization and to maintain constant feed composition, the retentate flow rate was much greater than the permeate flow rate. The "stage cut" is a measure of the relative magnitude of permeate and retentate flow rates, which is defined as

$$Stage\ cut\ \% = \frac{Permeate\ \ flow\ rate}{Feed\ \ flow\ rate} \times 100\% \tag{3.3}$$

In this work, a stage cut of less than 1 % was maintained during mixed gas permeation tests. Steady state was confirmed by multiple measurements of permeation rates and analyses of permeate composition. The permeance of mixed gas can be calculated using Equation 3.4.

$$\left(\frac{P}{l}\right)_i = \frac{y_i \cdot \left(\frac{\Delta V}{\Delta t}\right)_{STP}}{A \cdot (\Phi_{i,up} \cdot x_i \cdot p_{up,total} - \Phi_{i,down} \cdot y_i \cdot p_{down,total})} \tag{3.4}$$

where, $\left(\frac{P}{l}\right)_i$ is the permeance of component i; x_i and y_i are the mole fractions of component i in the feed and permeate, respectively; $\left(\frac{\Delta V}{\Delta t}\right)_{STP}$ is the permeate volumetric flow rate at standard temperature and pressure (273K, 1atm); A is the membrane area (sum of surface area of each individual fiber); $\Phi_{i,up}$ and $\Phi_{i,down}$ are the fugacity coefficients of component i at the upstream and downstream of the membrane, respectively; $p_{up,total}$ and $p_{down,total}$ are the total pressures at the upstream and downstream of the membrane.

3.4 Sorption Characterization

3.4.1 Sorption system design

The pressure decay method was used in this work to determine the pure gas sorption of all polymers. The design considerations of a pressure-decay apparatus were originally described by Koros [12], and some modifications were made to construct the pressure-decay apparatus for cold condition sorption tests. The same BTZ-475 benchtop temperature chamber (ESPEC North America, INC., Hudsonville, MI) as used in the permeation system was selected to contain the pressure decay apparatus (2 apparatus in each temperature chamber). The apparatus was composed of two main compartments: the reservoir and the sample cell. The membranes were placed in the sample cell, and pressure transducers were used to keep track of the pressures in each compartment. All the valves installed in the temperature chamber were pneumatically-actuated, and were controlled by the National Instruments LabVIEW 8.6. A schematic and a real picture of the sorption system are shown in Figures 3.8 and 3.9, respectively.

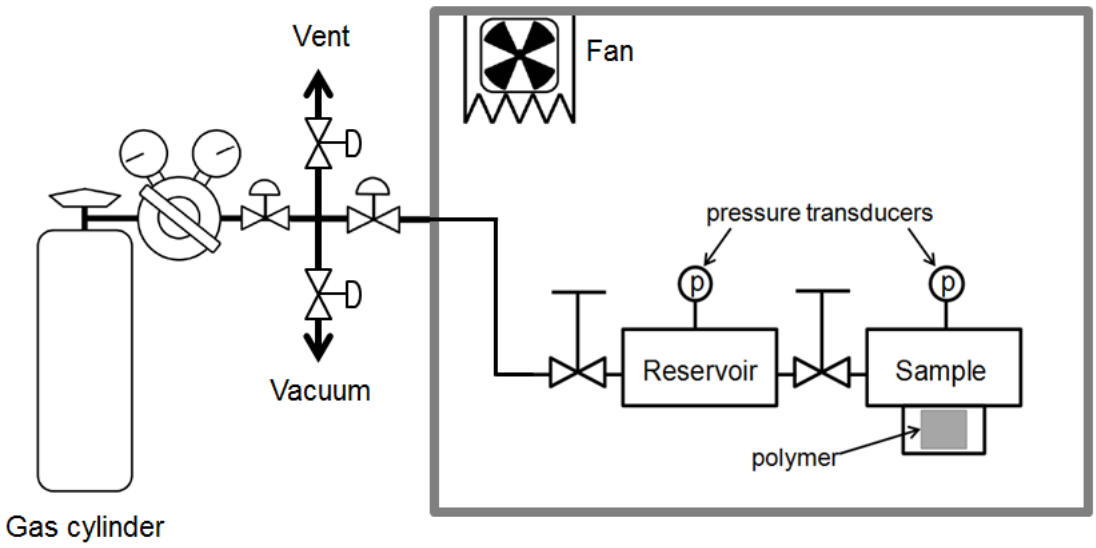

Figure 3.8: Schematic of pressure decay sorption system.

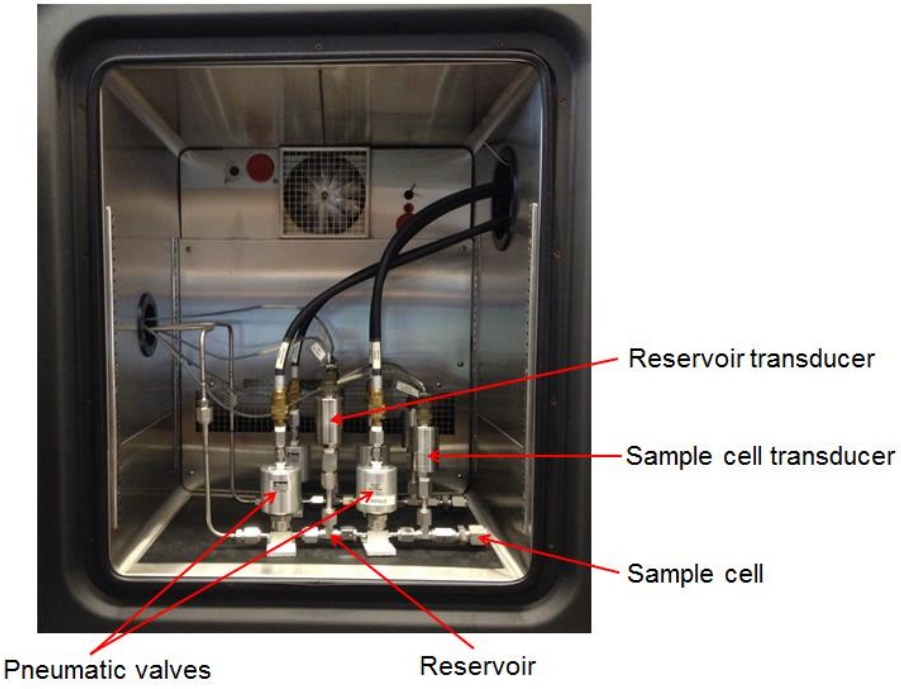

Figure 3.9: Real picture of the pressure decay sorption system used in this work.

3.4.2 Sorption testing

The pure gas sorption measurement using the pressure-decay method was carried out as follows:

1) The sample (hollow fiber membranes or polymer) was dried under vacuum at 100 °C overnight to remove moisture.
2) Loaded as much sample as possible into the sample cell and recorded the weight of the sample. The more sample was included in the cell, the more accurate the measurement was. Then the entire apparatus was put into the temperature chamber.
3) The temperature chamber was set at 50 °C and vacuum was applied on the reservoir and the sample cell for 24-48 hours.
4) The reservoir and the sample cell were closed and the chamber temperature was set at desired value.
5) When the temperature was stabilized, the reservoir and sample cell volumes were corrected by pressing the "Zero" button in the LabVIEW program.
6) Certain amount of pure gas of interest was introduced to the reservoir while the sample cell was kept closed.
7) The pressure versus time data recording was initiated. The LabVIEW® program was set to collect the pressure of reservoir and sample cell every 20 seconds. The valve connecting the reservoir and the sample cell was opened every 180 minutes automatically to allow gas flow between the reservoir and the sample cell. The valve open interval time was set at 2 seconds for all experiments throughout this

work. In the first few minutes after the gas entered the sample cell, the pressure in the sample cell "decayed" as some of the gas surrounding the sample was sorbed.

8) Once sorption reached equilibrium, data collection was manually stopped.

The equilibrium sorbed concentration of a pure gas was calculated through mole balance (Equation 3.5).

$$n_{sorbed} = (n_{R,i} - n_{R,f}) + (n_{C,i} - n_{C,f}) \tag{3.5}$$

where, $n_{R,i}$ and $n_{R,f}$ are the initial and final moles of gas in the reservoir, respectively. And $n_{C,i}$ and $n_{C,f}$ are the initial and final moles of gas in the sample cell, respectively.

Substitute the ideal gas law ($PV = nZRT$) in to Equation 3.5, the following expression can be derived:

$$n_{sorbed} = \frac{1}{RT} \times \left[V_R \left(\frac{P_{R,i}}{Z_{R,i}} - \frac{P_{R,f}}{Z_{R,f}} \right) + \left(V_C - V_P \right) \left(\frac{P_{C,i}}{Z_{C,i}} - \frac{P_{C,f}}{Z_{C,f}} \right) \right] \tag{3.6}$$

where, V_R, V_C and V_P are the volumes of the reservoir, sample cell and polymer sample, respectively. Table 3.2 lists the volumes of the reservoirs and sample cells of the four sub-ambient sorption systems used in this work. $P_{R,i}$ and $P_{R,f}$ are the initial and final pressures of the reservoir. $P_{C,i}$ and $P_{C,f}$ are the initial and final pressures of the sample

cell. $Z_{R,i}$ and $Z_{R,f}$ are the initial and final compressibility factors of the gas in the reservoir. $Z_{C,i}$ and $Z_{C,f}$ are the initial and final compressibility factors of the gas in the sample cell. The compressibility factors of different gases at different temperatures can be found in Appendix A. R is the universal gas constant which equals to 8.314 J/mol·K.

The sorbed gas concentration in the polymer can be determined using Equation 3.7.

$$C_{sorbed}\left[\frac{cm^3(STP)}{cm^3\,polymer}\right]=\frac{n_{sorbed}\left[mol\right]\times V_{STP}\left[\frac{cm^3}{mol}\right]}{V_P\left[cm^3\right]} \tag{3.7}$$

where, V_{STP} is the volume of 1 mol gas at standard temperature and pressure (273K, 1atm).

Table 3.2: Volumes of the reservoirs and sample cells of the sub-ambient pressure decay sorption systems used in the current work

Sorption system name	Reservoir volume (ml)	Sample cell volume (ml)
Seeglo	8.830	12.402
Ootah	8.935	12.567
Lindstrom	8.773	9.674
Wisting	8.811	9.202

3.5 Scanning Electron Microscopy (SEM)

The morphology and dimensions of the asymmetric hollow fiber membranes were examined by scanning electron microscopy (SEM). The high resolution SEMs (LEO 1530 and LEO 1550) were used for the majority of this work. The LEO 1530 and LEO 1550 SEM were equipped with a thermally assisted field emission gun, and an 8 kV operation voltage was selected. In the preparation of samples for SEM examination, dried fibers were soaked in hexane for ~ 1 minute and then quickly transferred into liquid N_2. The fibers were shear fractured in liquid nitrogen using tweezers and the morphology of the cross-section of the fibers was preserved. The fiber samples were then mounted vertically on sample mounts (Ted Pella, Inc.) using carbon tape. To get better images, the fibers' cross-sections that were of interest were usually placed a little higher than the edge of the mount. Samples were sputter coated with gold for 30 seconds prior to examination.

3.6 References

[1] H. Ohya, V. Kudryavsev, and S. I. Semenova, Polyimide membranes: applications, fabrications and properties: CRC Press, 1997.

[2] W. J. Koros and G. K. Fleming, Membrane-based gas separation, Journal of Membrane Science, vol. 83, pp. 1-80, Aug 1993.

[3] M. Kiyono, Ph.D. thesis, Carbon molecular sieve membranes for natural gas separations, Georgia Institute of Technology, 2010.

[4] D. T. Clausi, Ph.D. thesis, Formation and characterization of asymmetric polyimide hollow fiber membranes for gas separations, The University of Texas at Austin, 1998.

[5] L. Xu, Ph.D. thesis, Carbon molecular sieve hollow fiber membranes for olefin/paraffin separations, Georgia Institute of Technology, 2012.

[6] M. R. Kosuri and W. J. Koros, Defect-free asymmetric hollow fiber membranes from Torlon®, a polyamide–imide polymer, for high-pressure CO_2 separations, Journal of Membrane Science, vol. 320, pp. 65-72, 2008.

[7] D. W. Wallace, C. Staudt-Bickel, and W. J. Koros, Efficient development of effective hollow fiber membranes for gas separations from novel polymers, Journal of Membrane Science, vol. 278, pp. 92-104, 2006.

[8] S. Hussain, PhD. Thesis, Mixed matrix dual layer hollow fiber membranes for natural gas separation, Georgia Institute of Technology, 2006.

[9] D. Q. Vu, W. J. Koros, and S. J. Miller, High pressure CO_2/CH_4 separation using carbon molecular sieve hollow fiber membranes, Industrial & engineering chemistry research, vol. 41, pp. 367-380, 2002.

[10] B. E. Kraftschik, Ph.D. thesis, Advanced crosslinkable polyimide membranes for aggressive sour gas separations, Georgia Institute of Technology, 2013.

[11] I. C. Omole, Ph.D. thesis, Crosslinked polyimide hollow fiber membranes for aggressive natural gas feed streams, Georgia Institute of Technology, 2008.

[12] W. J. Koros and D. Paul, Design considerations for measurement of gas sorption in polymers by pressure decay, Journal of Polymer Science: Polymer Physics Edition, vol. 14, pp. 1903-1907, 1976.

CHAPTER 4

FORMATION OF COLD HIGH PERFORMANCE MATRIMID®

HOLLOW FIBER MEMBRANES

This chapter describes the different attempts to spin asymmetric Matrimid® hollow fiber membranes with good separation performance at cold conditions. An overview of Matrimid® 5218 is included in Section 4.1. Section 4.2 describes a post-treatment method that can effectively caulk pinhole defects in the selective layers of asymmetric membranes. Section 4.3 discusses the development of defect free asymmetric hollow fiber membranes and their cold performance. This type of membrane didn't show desirable separation performance at sub-ambient temperatures, and the reason was attributed to its homogeneous dense selective layer. A new type of hollow fiber membrane with "fused nodular" selective layer was developed and its formation protocols are included in Section 4.4. These "nodular fibers" showed even better performance than a known high performing cold membrane, and are used for subsequent studies in Chapter 5.

4.1 Overview of Matrimid® 5218

The first generation of membrane materials used in this work for cold conditions flue gas CO_2 capture is Matrimid® 5218, a commercially available polyimide. The structure of its repeating unit is shown in Chapter 3. Matrimid® 5218 is a thermally and chemically stable material, which is soluble in a variety of common solvents. It has

desirable selectivity and permeability for many gas pairs, including CO_2/N_2. Table 4.1 shows the pure gas transport properties of Matrimid® dense films.

Table 4.1: Pure gas transport properties of Matrimid® 5218 dense films at feed pressure < 100 psia and 35 °C [1]

Material	Permeability (Barrer)					Selectivity					
	O_2	CO_2	He	C_2H_4	C_3H_6	$\frac{O_2}{N_2}$	$\frac{CO_2}{N_2}$	$\frac{He}{N_2}$	$\frac{CO_2}{CH_4}$	$\frac{C_2H_4}{C_2H_6}$	$\frac{C_3H_6}{C_3H_8}$
Matrimid®	2.0	9.9	23	0.45	0.1	6.7	33	122	36	4.5	10

$$1\ Barrer = 1\times10^{-10}\ \frac{cm^3(STP)\cdot cm}{cm^2\cdot s\cdot cmHg}$$

4.2 PDMS post-treatment

Imperfections and defects in the selective layer of gas separation membranes arise in the membrane formation process and in subsequent membrane handling and module fabrication steps. The purpose of post-treatment was to seal defects and thus enhance membrane selectivity. Due to the addition of a second layer, increased gas transport resistance is expected [2]. A desirable "caulking" layer should be highly permeable to minimize its influence on the overall membrane permeability, while non-selective gas flow through the pinholes should be considerably reduced. The caulking layer is usually a pre-crosslinked polymer. In this work, the PDMS post-treatment was used to enhance the selectivity of defective hollow fiber membranes.

The PDMS post-treatment involves the use of a silicon elastomer kit (Sylgard® 184) to form a highly cross-linked polymer, polydimethylsiloxane (PDMS). Silicone elastomers are among the most versatile polymer materials due to their desirable properties, including good thermal and chemical stability, low electrical conductivity, biocompatibility, and good aging characteristics [3]. The Sylgard® 184 used in this work is a two-part, liquid silicone-based polymer manufactured by Dow Corning®, and its compositions are shown in Tables 4.2 and 4.3.

Table 4.2: Composition of Sylgard® 184 elastomer base [3]

CAS#	wt.%	Component
68083-19-2	>60.0	Dimethylsiloxane, dimethylvinyl-terminated 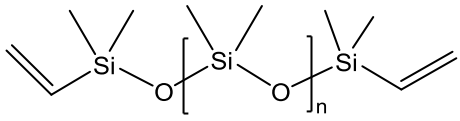
3555-47-3	1.0-5.0	Tetra(trimethylsiloxy)silane 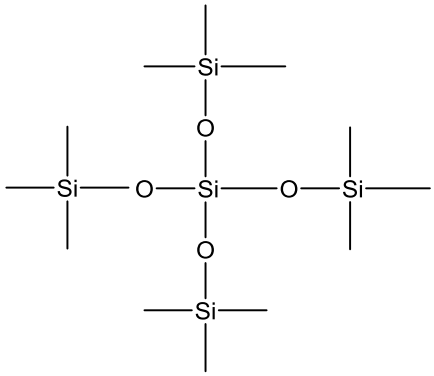 Branched volatile siloxane (VMS)
68988-89-6	30.0-60.0	Dimethylvinylated and trimehtylated silica 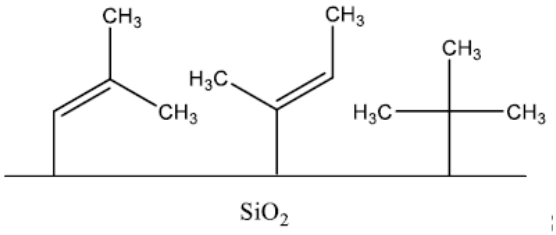 Surface modifier silica filler

Table 4.3: Composition of Sylgard® 184 curing agent [3]

CAS#	wt.%	Component
68037-59-2	40.0-70.0	Dimethyl, methylhydrogen siloxane 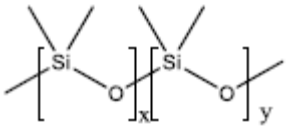
68083-19-2	15.0-40.0	Dimethylsiloxane, dimethylvinyl-terminated 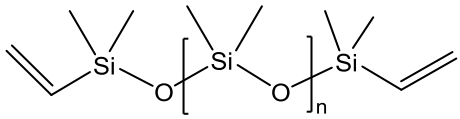
2554-06-5	1.0-5.0	Tetramethyl tetravinyl cyclotetrasiloxane 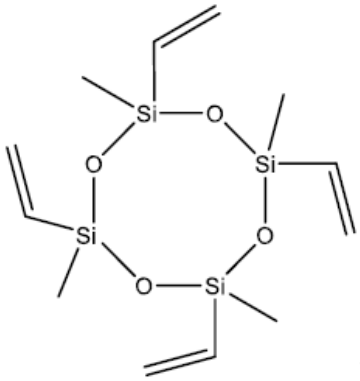 Network formation
68988-89-6	10.0-30.0	Dimethylvinylated and trimehtylated silica 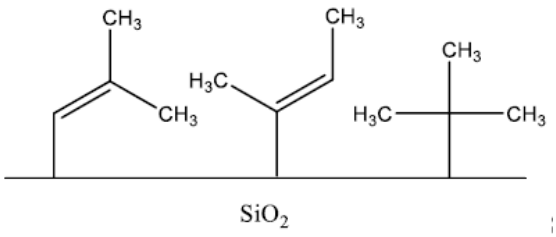 Surface modifier silica filler

Silicone elastomers are formed through the reaction of a base, dimethylvinyl-terminated dimethylsiloxane, with a crosslinking agent, such as tetra(trimethylsiloxy)silane, in the presence of a catalyst [3]. The crosslinking process is usually catalyzed using platinum species such as Karsted's catalyst or H_2PtCl_6 through a hydrosilylation mechanism (Figure 4.1). A more detailed illustration of the hydrosilylation mechanism can be found in Ortiz-Acosta's report [3].

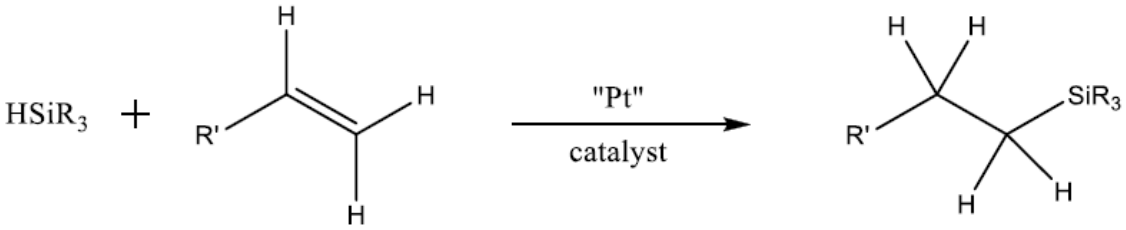

Figure 4.1: General hydrosilylation reaction mechanism [6].

In this work, a 2 wt% Sylgard® 184 was dissolved in heptane. The mixing ratio of the elastomer base and curing agent is 10:1 by weight. Note that, the base and the curing agent should be added to heptane separately to avoid pre-reaction. Usually, the base was mixed with heptane first, then the curing agent was added. To achieve a desirable molecular weight, the solution was heated at 100 °C in an oil bath for 4-6 hours with stirring until a slight increase in viscosity of the solution was observed. This increase in viscosity represented branching and incipient network formation of PDMS chains, which were more effective in caulking larger size defects in the membranes [4]. Fibers in a module were soaked (shell-side) in this mixture for 30 minutes, after which the solution

was drained. Then the module was dried in a fume hood for 24 hours at room temperature followed by curing at 78 °C for 2 hours under vacuum.

4.3 Formation of defect free Matrimid® hollow fiber membranes

The functional part that separates different penetrant molecules in an asymmetric hollow fiber membrane is the ultra-thin skin layer. To fabricate hollow fiber membranes with similar properties as Air Liquide membranes, our first attempt was to form fibers with integral defect free skin layers. The defect free skin layer is ideal for most applications, because it is able to differentiate gas molecules with sub-Angstrom size without the need of a post-treatment step. However, it is very challenging to be fabricated. Pores of ~ 5 Å wide in the skin layer exceeding area fractions of one in one million will render the entire membrane defective [5].

4.3.1 Membrane formation

The formation of defect free asymmetric hollow fiber membranes from Matrimid® was based on the previous work of Clausi [6]. After extensive optimization on a specific polymer solution, Clausi proposed an excellent dope formulation for the spinning of Matrimid® hollow fiber membranes, which was known to form defect-free integral skins under proper conditions. The resultant hollow fiber membranes displayed the same selectivity as Matrimid® dense film. There were four components in Clausi's dope: polymer (Matrimid®), less volatile solvent n-methyl-2-pyrrolidone (NMP), volatile solvent tetrahydrofuran (THF), and non-solvent ethanol (EtOH). The specific dope compositions are listed in Table 4.4. The 1-Methyl-2-pyrrolidinone (NMP) was used as

the less volatile solvent due to its strong interaction with the polymer, miscibility with water, and the fact that it is relatively benign from a health standpoint. The inclusion of volatile THF promoted ample evaporation in the air gap, which was conducive to the formation of defect-free dense skins [7, 8]. As for the volatile solvent, the selection was limited. A desirable volatile solvent should have sufficient volatility and good miscibility with water, but most solvents which interact strongly with water have relatively low volatilities [9]. Tetrahydrofuran (THF) was one of the only convenient solvents which were found to be both highly volatile and miscible with water. The selection of EtOH as the non-solvent additive allowed for flexibility in refining dope composition [10].

Table 4.4: Dope compositions for the formation of defect free Matrimid® hollow fiber membranes proposed by Clausi [6]

	Components	wt%
Polymer	Matrimid®	26.2
Solvent	NMP	53
	THF	5.9
Non-solvent	EtOH	14.9

The dope compositions and spinning conditions suggested by Clausi had been adopted in the Koros Research Group for many years, and were found to be quite desirable. However, before the start of the current project, the previous batch of Matrimid® was consumed, and a new batch of polymer was purchased from Huntsman International LLC. This new batch showed different molecular weight (Mw) and

polydispersity index (PDI) than the previous batch (Table 4.5), which required proper tuning and further optimization of dope compositions and spinning conditions based on Clausi's work.

Table 4.5: GPC results of the old and new batches of Matrimid® [1]. The old batch was used in Clausi's work, and the new batch was used in the current work

Batch	Mw (kDa)	PDI (Mw/Mn)
Old	63.6	3.79
New	72.5	4.12

In order to confirm the phase behavior of the new batch of Matrimid®, a previous group member Xu constructed a binodal line using a 90 wt%/10 wt% NMP/THF mixture as the solvent [1]. On the new phase diagram, the dope composition suggested by Clausi sat in the one-phase region and was close to the binodal line, indicating it was still suitable for spinning. However, following the same dope composition, the dope made from the new batch of Matrimid® was found to be more viscous than made from the previous batch (Figure 4.2), and the spinning conditions suggested by Clausi were not suitable to produce defect free hollow fiber membranes. Xu discovered that some of the resultant fibers showed oval shape, rather than the ideally round shape [1]. The reason was attributed to insufficient phase separation in the water quench bath. Due to the high viscosity of the new dope, the mass transfer rate of solvents and non-solvents in the

quench bath was reduced [11]. The slow phase separation resulted in nascent fibers with poor mechanical strength, whose overall shape collapsed when contacting the guiding roll in the quench bath.

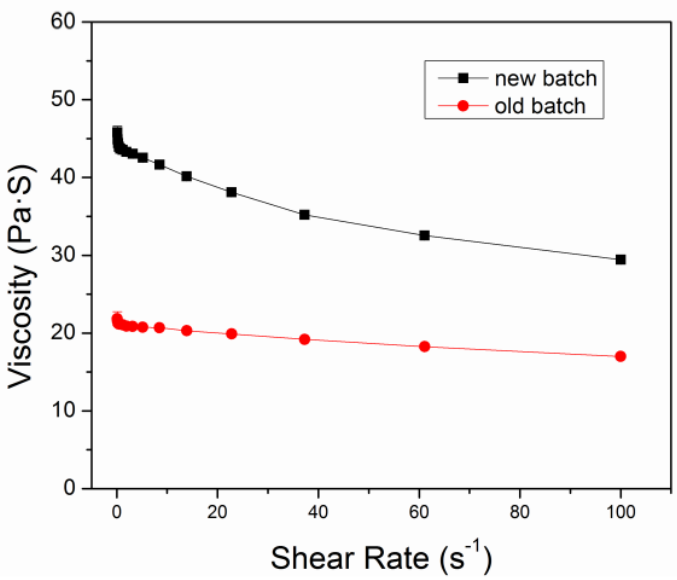

Figure 4.2 Viscosity of spinning dopes made from the old and new batches of Matrimid® [1]. Measurements were carried out at 50 °C.

Based on the foundation laid out by Clausi and the detective work done by Xu, the same dope composition as suggested by Clausi was used in the current work, but the spinning parameters were changed to promote phase separation and skin formation. Table 4.6 compares the spinning conditions in the current work and Clausi's work. The increased air gap and increased spinneret temperature promoted the evaporation of solvents and non-solvents in the dope, and thus facilitated the formation of skin layer. The elevated quench bath temperature allowed for faster phase separation and promoted fiber solidification prior to encountering the first fiber guide, thereby preventing fiber

deformation. Decreased take-up rate increased the residential time of spinning line in the air gap and the water quench bath, which was also beneficial to skin formation and phase separation. With the spinning conditions listed in Table 4.6, defect free Matrimid® hollow fiber membranes were successfully formed. The SEM images of the fiber's cross section and the selective skin layer are shown in Figure 4.3.

Table 4.6 Comparison of spinning parameters used in the current work and Clausi's work for the formation of defect-free Matrimid® hollow fiber membranes

Spinning parameter	Current work	Clausi's work
Dope flow rate	180 ml/h	180 ml/h
Bore flow rate	60 ml/h	60 ml/h
Bore fluid composition	95%/5% NMP/H_2O	96%/4% NMP/H_2O
Take-up rate	15 m/min	50 m/min
Quench temperature	45.7 °C	25 °C
Spinneret temperature	60 °C	50 °C
Air gap height	20 cm	2.5-18.5 cm

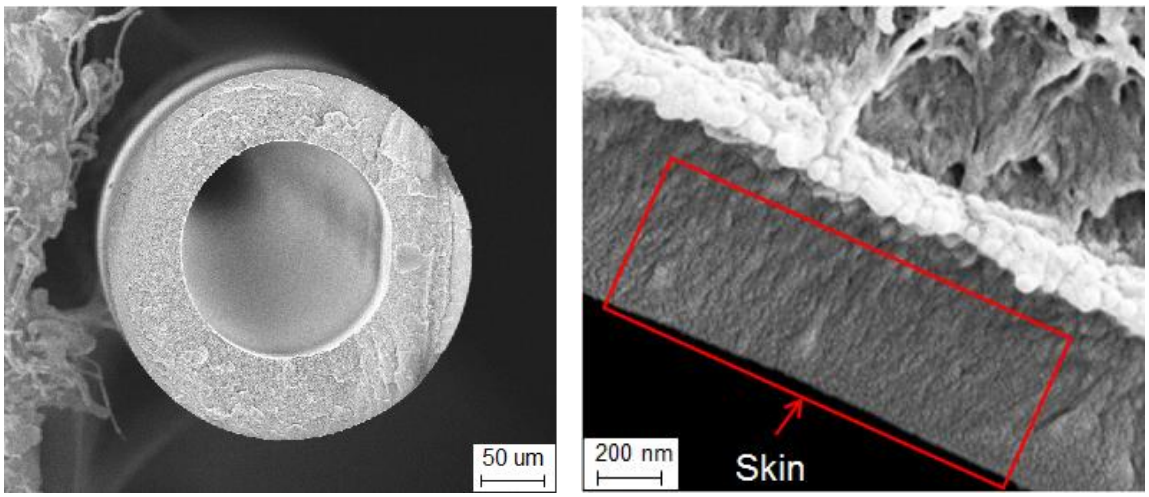

(a) (b)

Figure 4.3: SEM images of defect free Matrimid® hollow fiber membranes. (a) Overview of the cross-section, (b) selective skin layer.

4.3.2 Pure and mixed gas permeation tests

Skin integrity of the defect free Matrimid® hollow fiber membranes was confirmed by permeating pure O_2, N_2 and CO_2 at 35 °C. Feed pressure for O_2 and N_2 was 100 psig; and for CO_2, 50 psig. The O_2/N_2 selectivity of untreated fibers was 6.77 (Table 4.7). Such value was higher than the intrinsic selectivity of Matrimid® dense film at 35 °C, suggesting the fibers were defect free (The O_2/N_2 selectivity of Matrimid® dense film at 35 °C is 6.7 [4]). The O_2/N_2 penetrant pair is commonly used to verify a membrane's defect free properties, due to its low degree of interaction with polymer materials [1]. Generally speaking, a selective skin is conventionally considered to be defect free if its selectivity for a given gas pair is higher than 90 % of the polymer's intrinsic dense film value [5]. The PDMS post-treatment had negligible influence on the membrane's selectivity (Table 4.7), because there were no pinhole defects in the selective skin layers. However, additional transport resistance resulted in decreased membrane permeance. In

order to maintain a relatively higher permeance, PDMS post-treatment was not applied to defect free Matrimid® fibers for the rest of this work.

Table 4.7: Pure gas permeation results of defect free Matrimid® hollow fiber membranes at 35 °C. Feed pressure for O_2 and N_2 was 100 psig; for CO_2, 50 psig. The feed was introduced at the bore side

	$\frac{P_{O_2}}{l}$ (GPU)	$\frac{P_{N_2}}{l}$ (GPU)	$\frac{P_{CO_2}}{l}$ (GPU)	α_{O_2/N_2}	α_{CO_2/N_2}
No PDMS	6.1 ± 0.5	0.9 ± 0.1	28.5 ± 2.4	6.77 ± 0.08	31.7 ± 0.2
With PDMS	5.6 ± 0.4	0.8 ± 0.1	25.9 ± 3	6.85 ± 0.12	32.0 ± 1.8

The defect free Matrimid® hollow fiber membranes without PDMS post-treatment was tested with a mixture of 20 mol% CO_2/80 mol% N_2. Feed was introduced at the bore side of the fibers at 100 psig. The permeation results are shown in Figure 4.4. The selectivity increased with the decrease of temperature. According to the Arrhenius relationship and the definition of selectivity, the CO_2/N_2 selectivity can be expressed as:

$$\alpha_{CO_2/N_2} = \frac{P_{0,CO_2}}{P_{0,N_2}} \cdot \exp\left(\frac{E_{p,N_2} - E_{p,CO_2}}{RT}\right) \tag{4.1}$$

In Equation 4.1, the term $\frac{P_{0,CO_2}}{P_{0,N_2}}$ is a pre-exponential factor, which is considered to be constant over the temperature range of the experiment. The temperature dependence of CO_2/N_2 selectivity was thus largely determined by the difference in permeation activation energy ($E_{p,N_2} - E_{p,CO_2}$).

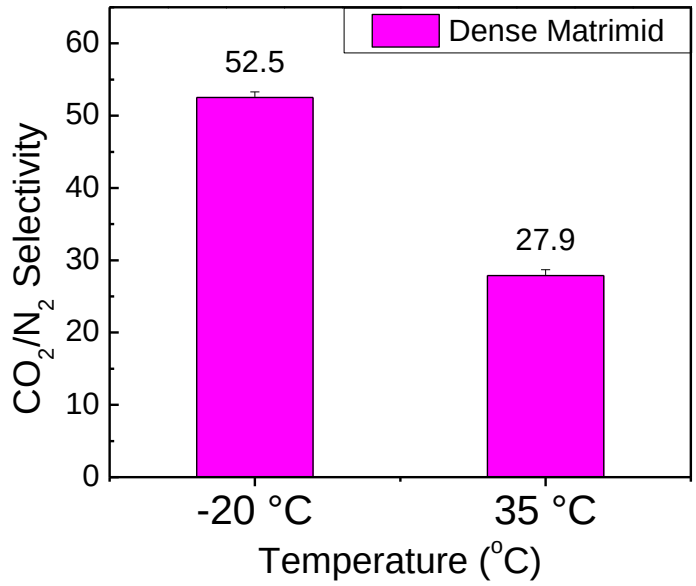

(a)

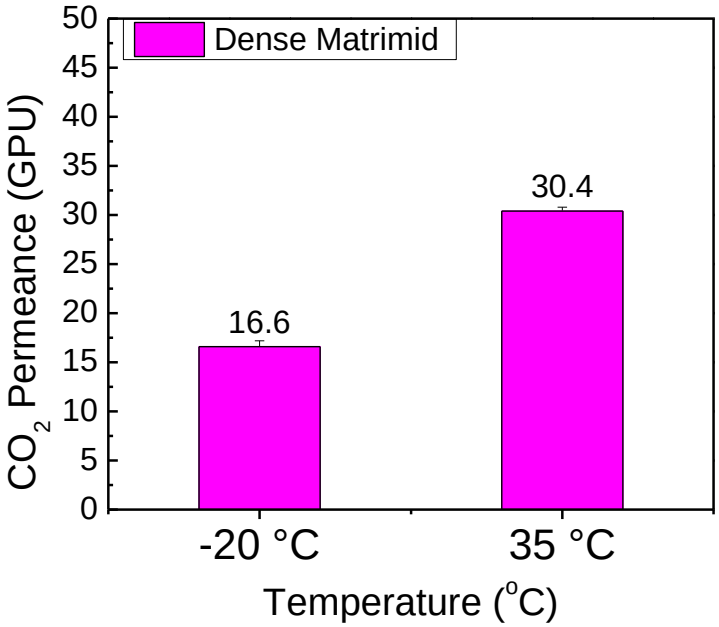

(b)

Figure 4.4: Separation performance of defect free Matrimid® hollow fiber membranes spun in the current work. The feed was a mixture of 20 mol% CO_2/80 mol% N_2, and was introduced at the bore side at 100 psig.

The natural logarithm of permeance for defect free Matrimid® hollow fiber membranes was plotted against the reciprocal of temperature (Figure 4.5), and the slopes of the linear fitting curves were used to calculate the permeation activation energy for CO_2 and N_2. The permeation activation energy for N_2 and CO_2 is listed in Table 4.8. The permeation activation energy for N_2 is larger than for CO_2, so the selectivity increased with the decrease of temperature. However, the permeance of the membrane was too low. A desirable permeance of CO_2 at -20 ºC is over 100 GPU. The permeance of the defect free Matrimid® was far below this value.

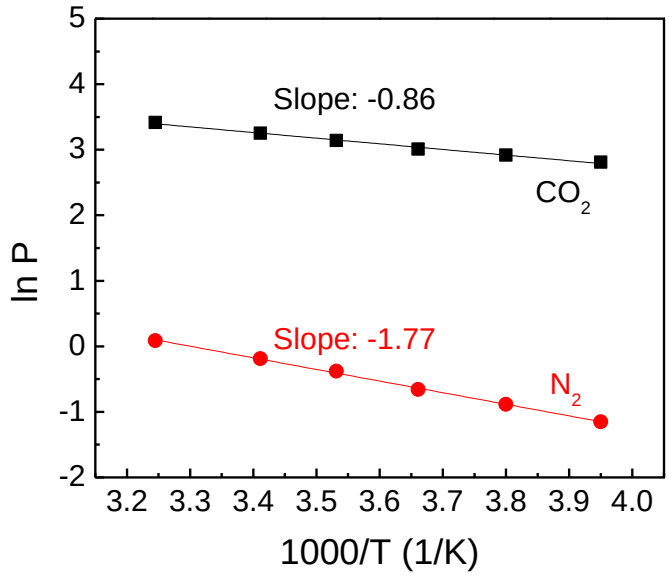

Figure 4.5: Temperature dependence of permeance for defect free Matrimid® hollow fiber membranes spun in the current work. Permeation measurements were performed with 20 mol% CO_2/80 mol% N_2.

Table 4.8: Permeation activation energy for CO_2 and N_2 in defect free Matrimid® hollow fiber membranes spun in the current work

	Defect free Matrimid®
E_{p,CO_2}	7.2 ± 0.3 kJ/mol
E_{p,N_2}	14.7 ± 0.2 kJ/mol
$E_{p,N_2} - E_{p,CO_2}$	7.5 ± 0.4 kJ/mol

4.4 Formation of "nodular" Matrimid® hollow fiber membranes

4.4.1 Motivating hypothesis

As is discussed above, the defect free hollow fiber membranes showed much lower permeance than the desired value. Theoretically, the permeance can be increased by reducing the thickness of the selective skin layer; however, in practice, it is very challenging to form a very thin skin layer that is defect free. On the other hand, the difference in the permeation activation energy between N_2 and CO_2 is believed to be related to the microscopic structure of the skin layer. To form a membrane with high cold performance, a motivating hypothesis was proposed. Our motivating hypothesis was: asymmetric hollow fiber membranes with "fused-nodular" structure in the skin layer might show a combination of high permeance and high selectivity at cold conditions. Figure 4.6 shows a hypothetical morphology of the "fused nodular" selective layer. Compared to the homogeneous dense skin possessed by defect free hollow fiber membranes, the nodular skin is hypothesized to be comprised of several layers of so-called "nodules". Although the nodules are depicted as being spherical, they actually

have no well-defined shape and are thought to be interconnected by polymers chains, which are referred to as “tie-chains”.

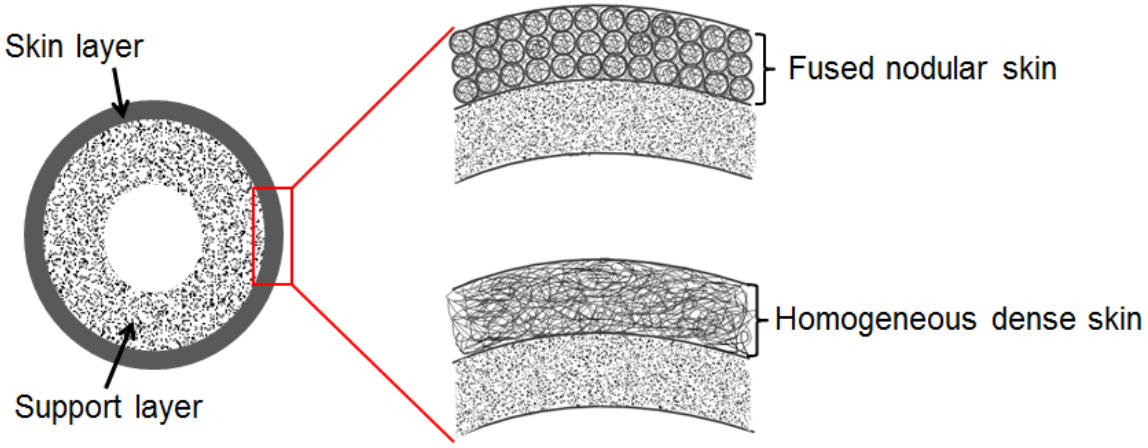

Figure 4.6: Hypothetical morphologies of “fused nodular” and “homogeneous dense” selective skin layers.

The idea of a nodular structure in the membrane’s effective separation layer appeared in the earlier works of several researchers. Jordan [12] used this model to explain the larger permeance enhancement of CO_2 in hollow fiber membranes than in dense films. She believed the sorption of CO_2 molecules in or near the nodules might affect the connections between that nodule and those adjacent to it. The tie chains between the nodules might either elongate or disengage, depending on the stability of the chains and the degree of swelling caused by the CO_2 molecules. As long as the tie chains were not disengaged, adjacent nodules were “fused” together, and viscous flow through the volume between nodules was not generally possible. Kesting [13] observed the physical morphologies of the nodules and proposed a four tier structure theory

(macromolecules, nodules, nodular aggregates, and super-nodular aggregates) for phase inversion membranes. Dong [14] linked the nodular structure to the membrane microscopic CO_2 sorption and believed the formation of nodules was caused by nucleation and growth mechanism during phase separation.

We speculated that hollow fiber membranes with nodular selective skin layers might possess similar properties as Air Liquide membranes after proper caulking. Specifically, the highly sorbing penetrant, CO_2, should be able to dilate the inter-nodular interfaces and introduce packing disruptions. Those packing disruptions might serve as sources of local volume to accommodate sorbed penetrant molecules, similar to the function of a sorption site. Compared to the dissolved mode, the packing disruptions would reduce the need to dilate the matrix by the full amount. Energetic considerations would favor reutilization of such locally available volume rather than requiring the molecule to overcome the full cohesive energy resistance of the matrix by opening totally new gaps of the required volume for dissolution. Since CO_2 is more condensable than N_2, especially at cold conditions, most of the packing disruptions would be utilized by CO_2 molecules, increasing its selectivity with respect to N_2.

4.4.2 Theoretical considerations of nodular skin formation

The formation of the skin layer in an asymmetric hollow fiber membrane results from a higher local polymer concentration in the outermost region of a nascent fiber. In the dry-jet/wet-quench spinning process, the asymmetric distribution of polymer concentration is believed to be caused by solvent and/or non-solvent evaporation in the air gap [9, 15]. The evaporation of solvent and/or non-solvent increases the polymer

concentration of the nascent skin layer to the point where it surpasses a certain vitrification boundary that phase separation in this layer is kinetically hindered in the quench bath [16, 17]. The increased polymer concentration has the potential to stabilize the dense skin morphology during phase separation of the substrate. However, the mechanism for the formation of a nodular skin is different, which requires the nascent skin layer to phase separate in the quench bath.

Three types of membrane morphology can be resulted from phase separation [18, 19]. When the nascent membrane composition falls in in region (I) in Figure 4.7, a local concentrated polymer solution is produced, nucleating and growing as the dispersed phase of the developing membrane (Figure 4.8). This situation forms a latexlike suspension of polymer spheroids. Upon further coalescence, the spherical structures will tend to meld, leaving interstitital pores between the basically spherical structures. On the contrary, in region (II), the polymer rich phase is the continuous phase, and dispersed spheroids of nearly polymer-free fluid are nucleated. In this case, a foam structure whose walls are composed of the solidified dispersed polymer phase results. In region (III), phase separation follows the spinodal decomposition mechanism, and excellent uniformity, highly open-cell foam support structures can be formed.

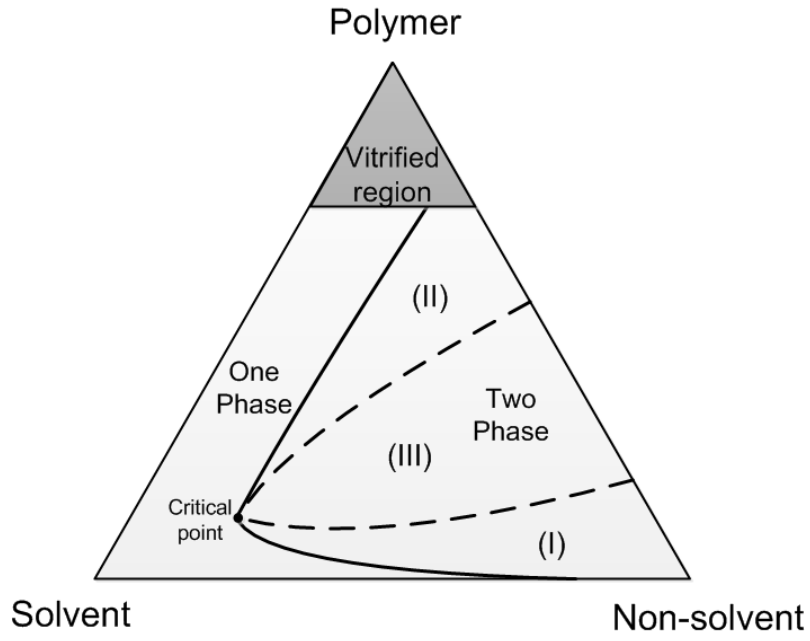

Figure 4.7: Ternary phase diagram showing different two-phase regimes where different phase separation mechanisms occur. Regimes (I) and (II) are nucleation & growth; regime (III) is spinodal decomposition.

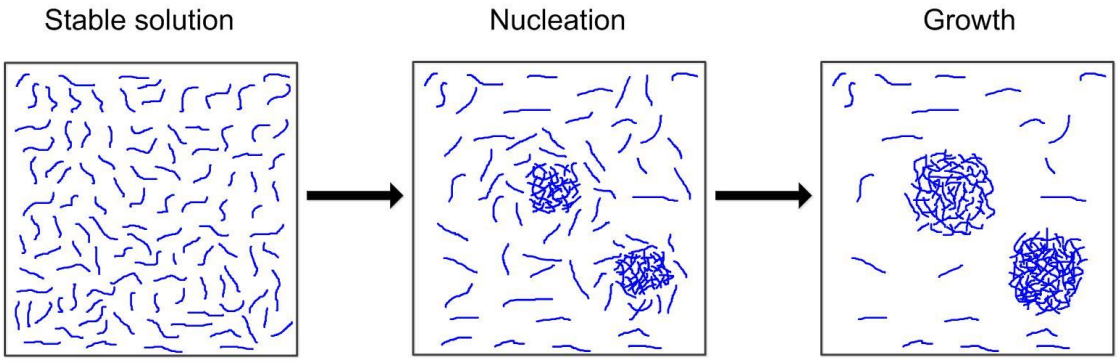

Figure 4.8: Evolution of idealized membrane structures: nucleation & growth of a polymer-rich phase [19].

In this work, the morphology formed via nucleation & growth mechanism is the preferred skin morphology. To create such structure, the evaporation of solvent and/or non-solvent in the air gap should be reduced to allow the skin layer to phase separate in the quench bath. Figure 4.9 shows the different pathways for the formation of dense and nodular skins on a ternary phase diagram. The qualitative pathway AA' leads to the formation of homogeneous dense skins, whereas pathway AB' shows the route to form nodular skins. Sections 4.4.3 to 4.4.5 in this chapter discuss the spinning attempts to fabricate Matrimid® hollow fiber membranes with nodular skins that can achieve a combination of high selectivity and high permeance at cold conditions.

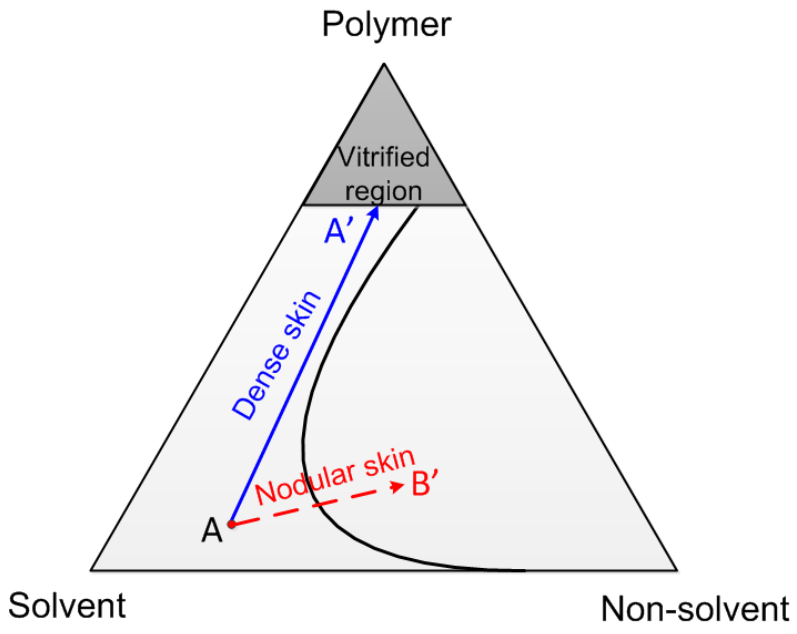

Figure 4.9: Ternary phase diagram showing qualitative pathways for the formation of dense and nodular skins.

4.4.3 First attempt to form nodular Matrimid® hollow fiber membranes

As is discussed above, the difference between the formation of nodular and dense hollow fiber membranes lies in the skin formation process. The dope composition and spinning conditions for the formation of dense Matrimid® fibers had been proved to be successful; and they were a good starting point for tuning to fabricate nodular fibers. The same batch of Matrimid® was used; however, the dope composition and spinning parameters were changed to reduce the evaporation of solvents and non-solvents in the air gap, allowing phase separation to occur in the selective skin layer.

In the first attempt, the non-solvent Ethanol (EtOH) was replaced with less volatile H_2O. The non-solvent additive plays an important role in determining membrane structure and gas separation properties. Carruthers [15] investigated the influence of several non-solvents on the formation of Matrimid® hollow fiber membranes: Ethanol (EtOH), Methanol (MeOH), acetone and water. The strong non-solvent property of water promoted phase separation, and fibers with compacted nodular skins were formed with the water containing dope. Therefore, in my first spinning attempt, the same dope composition as Carruthers' water containing dope was used, as is listed in Table 4.9. The spinning parameters are listed in Table 4.10, and the SEM images of the resultant fiber's cross-section and skin layer are shown in Figure 4.10. The membranes showed minimal asymmetry, with the skin layer barely seen (Figure 4.10b), indicating the membranes are very likely to be defective. Finger-like pores exist in the fiber wall (Figure 4.10a), which might be caused by fast precipitation of nascent fibers in the quench bath [20].

Table 4.9: Dope composition for the formation of nodular Matrimid® hollow fiber membranes (1st attempt)

	Components	wt%
Polymer	Matrimid®	26
Solvent	NMP	65
	THF	6
Non-solvent	H_2O	3

Table 4.10: Spinning parameters for the formation of nodular Matrimid® hollow fiber membranes (1st attempt)

Spinning parameters	1st attempt
Dope flow rate	180 ml/h
Bore flow rate	60 ml/h
Bore fluid composition	85%/15% NMP/H_2O
Take-up rate	15 m/min
Quench temperature	45.9 °C
Spinneret temperature	50 °C
Air gap height	10 cm
Room temperature	24.5 °C
Relative humidity	34 %

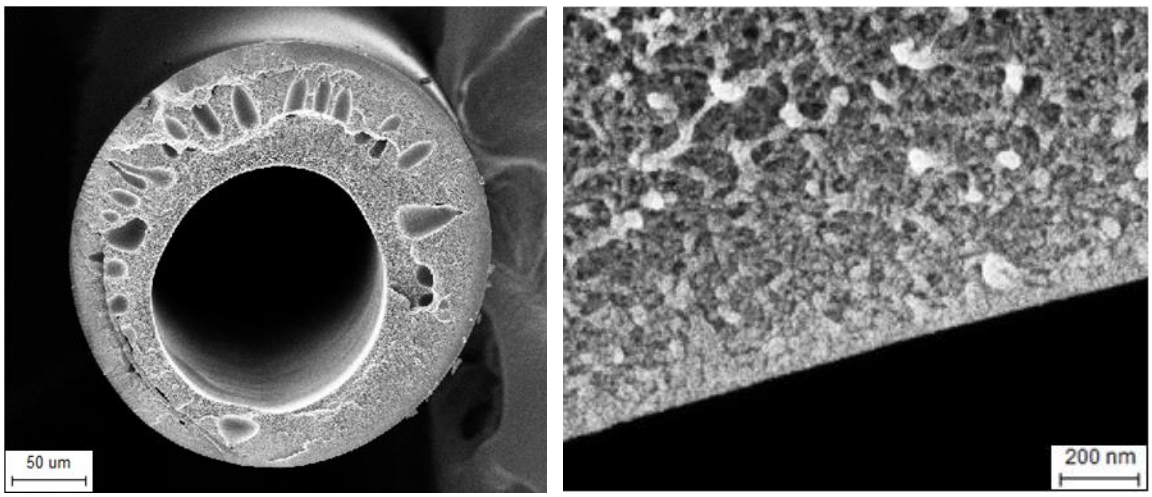

(a) (b)

Figure 4.10: SEM images of nodular Matrimid® hollow fiber membranes formed in the 1st spinning attempt. (a) Overview of the cross-section, (b) barely seen selective skin layer.

Pure gas permeation measurements confirmed that fibers formed from the water containing dope were highly defective, as was indicated by the high flux and low selectivity shown in Table 4.11 (The O_2/N_2 and CO_2/N_2 selectivity for dense Matrimid® film at 35 °C is 6.7 and 36, respectively [4]). Even PDMS caulking was not able to seal the defects. The selectivity was still far below the polymer's intrinsic dense film value.

Table 4.11: Pure gas permeation results of nodular Matrimid® hollow fiber membranes formed in the 1st spinning attempt at 35 °C. Feed pressure for O_2 and N_2 was 100 psig; for CO_2, 50 psig. The feed was introduced at the bore side

	$\frac{P_{O_2}}{l}$ (GPU)	$\frac{P_{N_2}}{l}$ (GPU)	$\frac{P_{CO_2}}{l}$ (GPU)	α_{O_2/N_2}	α_{CO_2/N_2}
No PDMS	979 ± 25	1046 ± 12	867 ± 20	0.94 ± 0.02	0.83 ± 0.01
With PDMS	110 ± 5	47.6 ± 3.5	302 ± 12.5	2.31 ± 0.1	6.34 ± 0.2

For such defective membranes, cold operating conditions didn't lead to enhanced selectivity. A mixture of 20 mol% CO_2/80 mol% N_2 was permeated through the PDMS post-treated fibers at -20 °C. The CO_2/N_2 selectivity was similar to the value at 35 °C, and was significantly lower than the desired selectivity (Figure 4.11). The desired selectivity at -20 °C is over 60. The defectiveness of the membrane was attributed to the strong non-solvent property of water, which made the dope very sensitive to phase separation. Even improper handling might cause significant defects in the membranes.

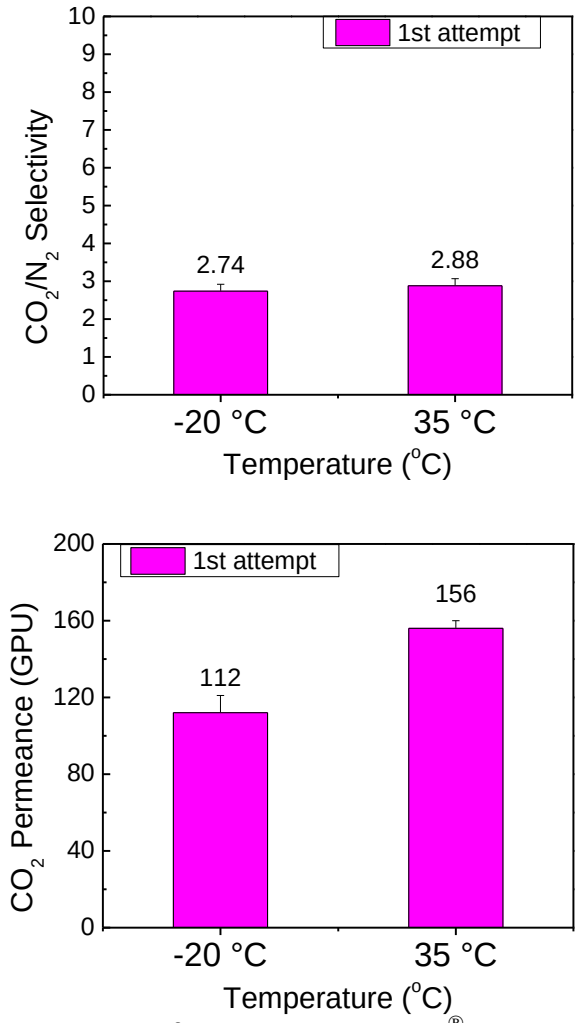

Figure 4.11: Permeation results for nodular Matrimid® hollow fiber membranes spun in the 1st attempt. Both membranes were post-treated with PDMS. The feed was a mixture of 20 mol% CO_2/80 mol% N_2, and was introduced at the bore side at 100 psig.

4.4.4 Second attempt to form nodular Matrimid® hollow fiber membranes

In the second spinning attempt, the strong non-solvent water was replaced by Ethanol, a weak non-solvent. Ethanol is a good candidate because it not only has good miscibility with the coagulant (water), but also possesses weak solvent property. In order to reduce solvent and/or non-solvent evaporation in the air gap, the volatile solvent THF was removed from the dope. Dope composition was tuned, based on the formation of defect free membranes (Table 4.12).

Table 4.12: Comparison of dope compositions for the formation of nodular (2nd attempt) and dense Matrimid® hollow fiber membranes

	Defect free fiber	wt%	Nodular fiber (2nd attempt)	wt%
Polymer	Matrimid®	26.2	Matrimid®	26.2
Solvent	NMP	53	NMP	58.9
	THF	5.9	-	-
Non-solvent	EtOH	14.9	EtOH	14.9

The spinning parameters were also changed to reduce evaporation in the air gap (Table 4.13): (i) the take up rate was increased from 15 m/min to 30 m/min, (ii) the spinneret temperature was reduced from 60 °C to 50 °C, and (iii) the air gap height was reduced from 20 cm to 10 cm. Increasing take up rate and shortening air gap reduced the residence time of nascent fiber in the air gap, thus allowed for less time for dope components to evaporate. Reducing the spinneret temperature reduced the driving force for evaporation.

Table 4.13: Comparison of spinning parameters for the formation of nodular (2^{nd} attempt) and dense Matrimid® hollow fiber membranes

Spinning parameter	Defect free fiber	Nodular fiber (2^{nd} attempt)
Dope flow rate	180 ml/h	180 ml/h
Bore flow rate	60 ml/h	60 ml/h
Bore fluid composition	95%/5% NMP/H_2O	95%/5% NMP/H_2O
Take-up rate	15 m/min	30 m/min
Quench temperature	45.7 °C	44.2 °C
Spinneret temperature	60 °C	50 °C
Air gap height	20 cm	10 cm
Room temperature	25	26 °C
Relative humidity	50 %	53 %

The SEM image in Figure 4.12a shows that the fibers spun in the second attempt were more circular and concentric than those spun in the first attempt, and most of the finger-like pores were eliminated. Moreover, a desirable nodular selective skin layer was formed (Figure 4.12b). Pure gas permeation characterization was carried on the bare fibers using O_2, N_2, and CO_2 at 35 °C in a constant pressure permeation system. The untreated membranes were found to be defective, with O_2/N_2 selectivity being 2.08 and CO_2/N_2 selectivity being 8.07 (The O_2/N_2 and CO_2/N_2 selectivity of dense Matrimid® film is 6.7 and 36 at 35 °C, respectively). However, after PDMS post-treatment, the selectivity was greatly enhanced (Table 4.14). And PDMS post-treatment didn't change the morphology of the selective skin layer, as can be seen in Figure 4.12c.

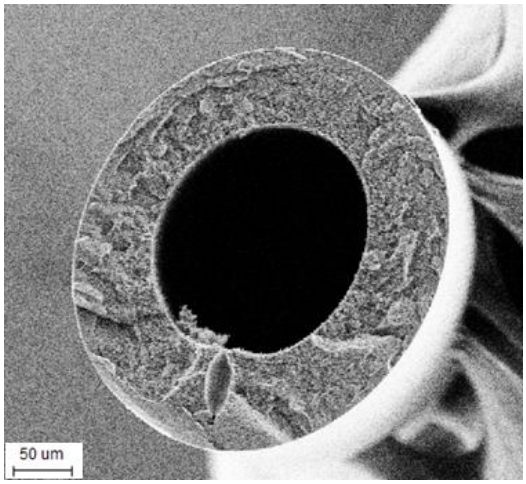

(a)

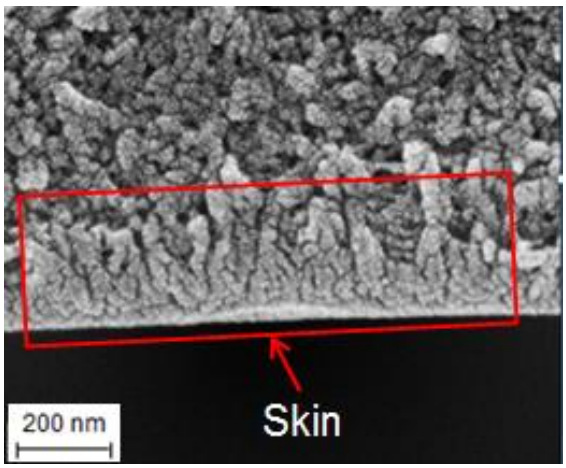

(b) untreated

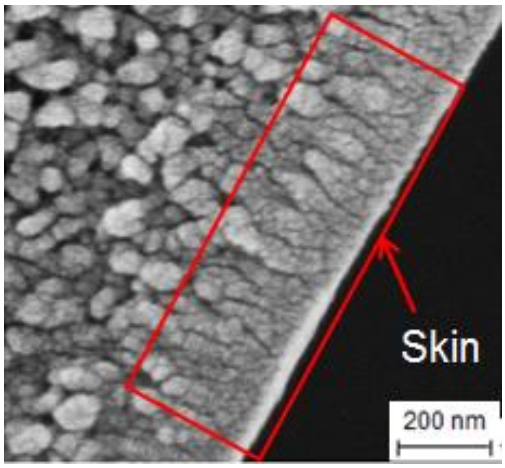

(c) post-treated with PDMS

Figure 4.12: SEM images of nodular Matrimid® hollow fiber membranes formed in the 2nd spinning attempt. (a) Overview of the cross-section, (b) selective skin layer without PDMS post-treatment, (c) selective skin layer after PDMS post-treatment.

Table 4.14: Pure gas permeation results of nodular Matrimid® hollow fiber membranes formed in the 2nd spinning attempt at 35 °C. Feed pressure for O_2 and N_2 was 100 psig; for CO_2, 50 psig. Feed was introduced at the bore side

	$\frac{P_{O_2}}{l}$ (GPU)	$\frac{P_{N_2}}{l}$ (GPU)	$\frac{P_{CO_2}}{l}$ (GPU)	α_{O_2/N_2}	α_{CO_2/N_2}
No PDMS	47.1 ± 0.5	22.6 ± 0.3	187 ± 6	2.08 ± 0.07	8.27 ± 0.15
With PDMS	23.2 ± 0.7	3.95 ± 0.13	118 ± 5	5.87 ± 0.14	29.9 ± 0.5

The 20 mol% CO_2/80 mol% N_2 mixed gas permeation results are shown in Figure 4.13. The selectivity increased with the decrease of temperature. At -20 °C, the selectivity was around 90, which was much higher than the desired value (over 60). Although the permeance at -20 °C was a little lower than the desired value (over 100 GPU), it was much higher than the defect free Matrimid®. The natural logarithm of the permeance of CO_2 and N_2 for PDMS post-treatment membranes spun in the second attempt were plotted against the reciprocal of temperature (Figure 4.14), and the calculated permeation activation energy is listed in Table 4.15. The nodular fibers spun in the second attempt showed much larger N_2 and CO_2 permeation activation energy difference ($E_{p,N_2} - E_{p,CO_2}$) than the defect free Matrimid®, indicating a faster increase in selectivity can be obtained from the nodular fibers.

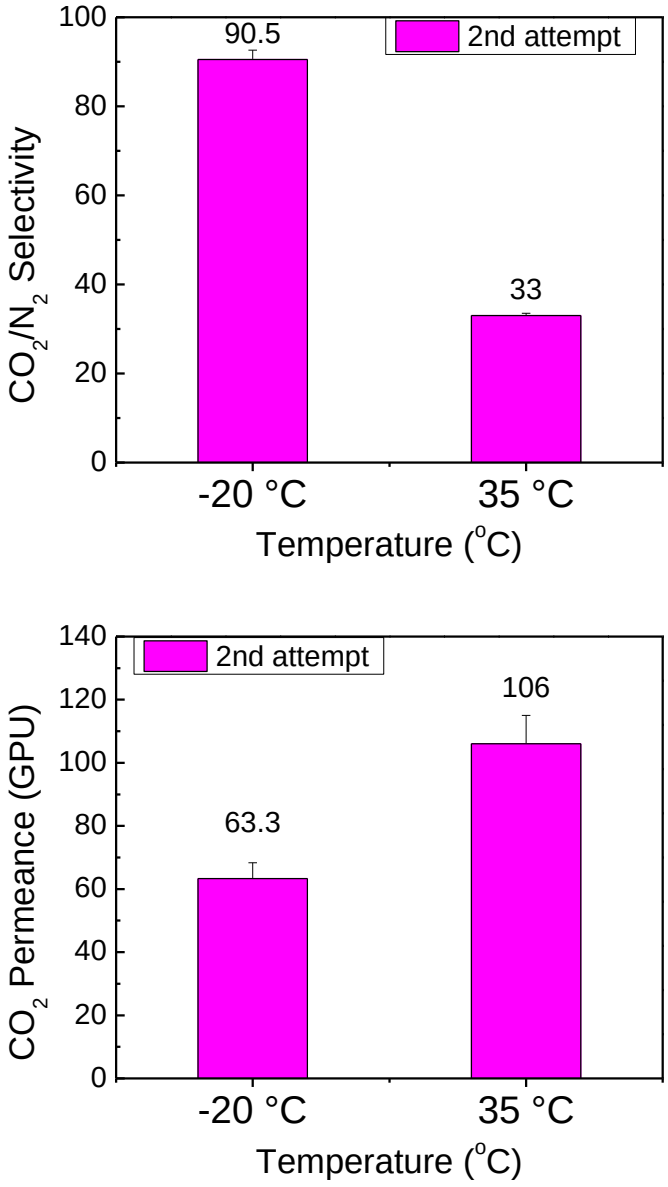

Figure 4.13: Permeation results for nodular Matrimid® hollow fiber membranes spun in the 2nd attempt. Both membranes were post-treated with PDMS. Feed was a mixture of 20 mol% CO_2/80 mol% N_2, and was introduced at the bore side at 100 psig.

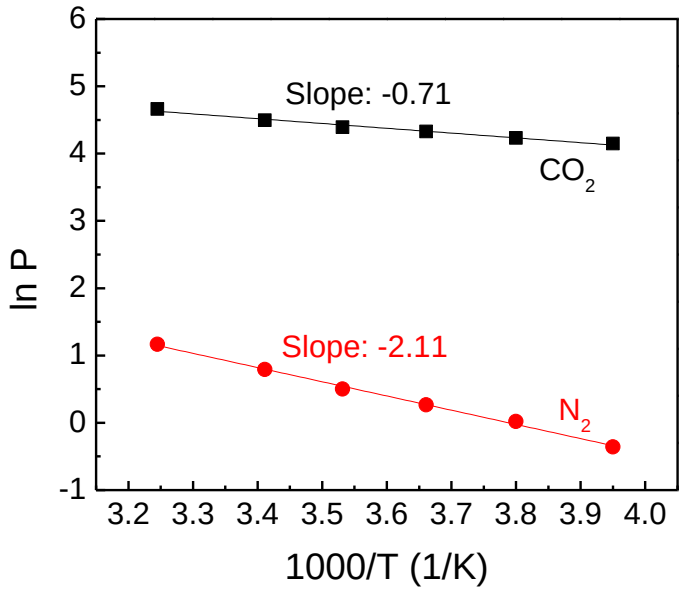

Figure 4.14: Temperature dependence of permeance for nodular Matrimid® hollow fiber membranes spun in the 2nd attempt. The fibers were post-treated with PDMS. Permeation measurements were performed with 20 mol% CO_2/80 mol% N_2.

Table 4.15: Permeation activation energy for CO_2 and N_2 in nodular Matrimid® hollow fiber membranes spun in the 2nd attempt and defect free Matrimid®

	Nodular fiber (2nd attempt)	Defect free Matrimid®
E_{p,CO_2}	5.9 ± 0.4 kJ/mol	7.2 ± 0.3 kJ/mol
E_{p,N_2}	17.5 ± 0.5 kJ/mol	14.7 ± 0.2 kJ/mol
$E_{p,N_2} - E_{p,CO_2}$	11.6 ± 0.6 kJ/mol	7.6 ± 0.4 kJ/mol

4.4.5 Third attempt to form nodular Matrimid® hollow fiber membranes

Although the nodular hollow fiber membranes formed in the second attempt showed good selectivity, the permeance of CO_2 was still not desirable. The objective of the third spinning was to increase membrane permeance. The dope composition and most spinning parameters remained the same as the second spin, except the air gap, which was reduced from 10 cm to 5 cm (Table 4.16).

Table 4.16: Comparison of spinning parameters in the 2nd and 3rd attempts for the formation of Matrimid® hollow fiber membranes

Spinning parameter	Nodular fiber (2nd attempt)	Nodular fiber (3rd attempt)
Dope flow rate	180 ml/h	180 ml/h
Bore flow rate	60 ml/h	60 ml/h
Bore fluid composition	95%/5% NMP/H_2O	95%/5% NMP/H_2O
Take-up rate	30 m/min	30 m/min
Quench temperature	44.2 °C	46.7 °C
Spinneret temperature	50 °C	50 °C
Air gap height	10 cm	5 cm
Room temperature	26 °C	25 °C
Relative humidity	53%	49%

The resultant membranes showed different skin morphologies from those spun in the second attempt (Figure 4.15). A possible reason was attributed to the changed air gap. Carruthers [15] pointed out three possible compositional paths for the skin layer in the air gap: (i) Solvent loss due to the evaporation of volatile solvent; (ii) Non-solvent loss due

to the evaporation of volatile non-solvent; and (iii) Non-solvent gain due to the infusion of non-solvent (moisture) from the surrounding environment. In the current work, the small vapor pressure of NMP (0.0004 bar at 20 °C) would likely cause the air gap to be relatively saturated with it, making it hard to evaporate. Therefore, the loss of NMP in the air gap should be minimal. However, the non-solvent EtOH has appreciable volatility (0.0595 bar at 20 °C), and the high spinneret temperature (50 °C) promotes its evaporation in the air gap, driving the dope composition in the skin layer of nascent fiber away from the point of phase separation. On the contrary, the infusion of non-solvent moisture due to environment humidity brings the dope composition close to phase separation. These two compositional paths can be visualized from the ternary phase diagram in Figure 4.16. The change of air gap would affect the evaporation of solvent and non-solvent as well as the infusion of moisture, resulting in different skin morphology.

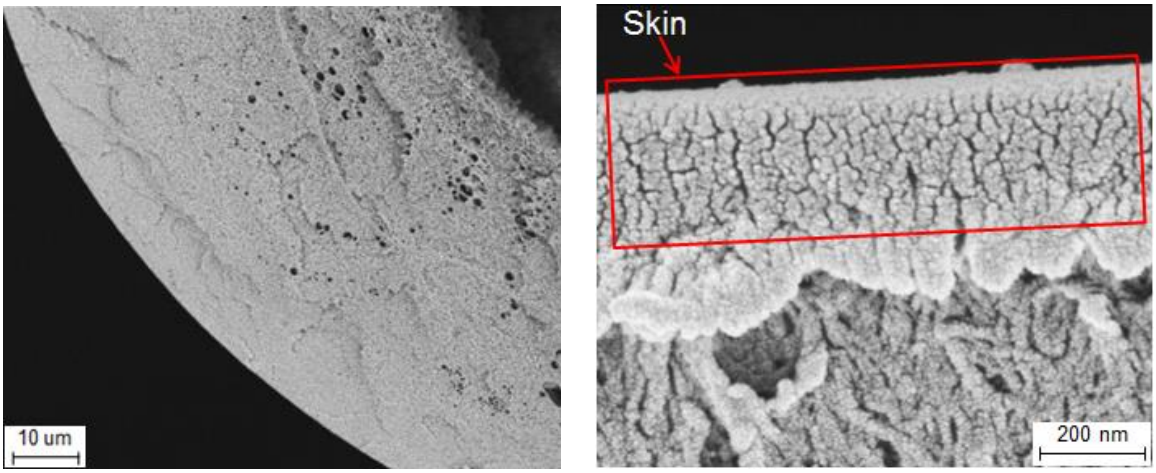

(a) (b)

Figure 4.15: SEM images of nodular Matrimid® hollow fiber membranes formed in the 3rd spinning attempt. (a) Fiber wall, (b) selective skin layer.

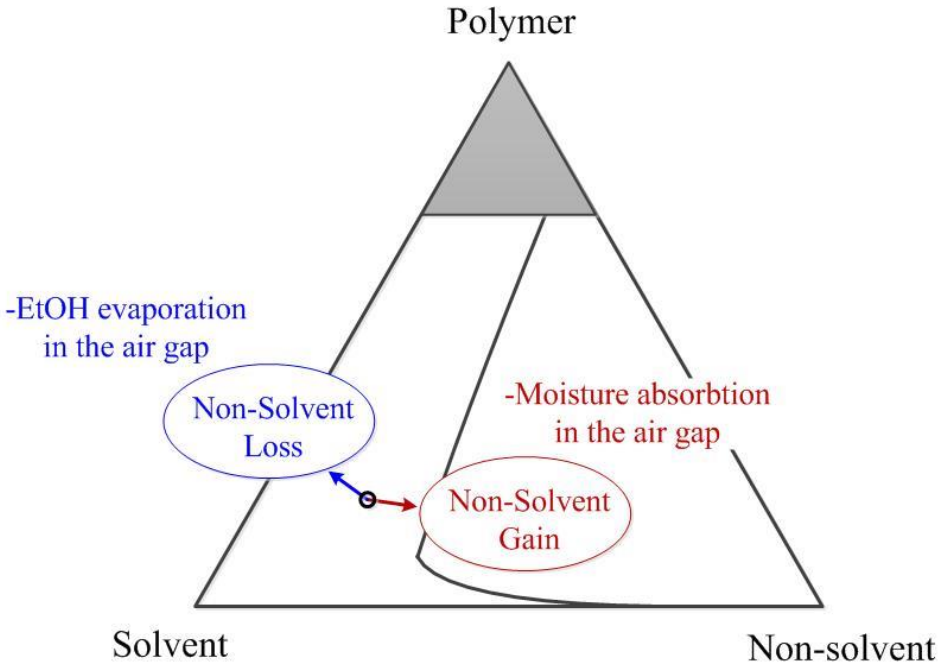

Figure 4.16: Ternary phase diagram illustrating potential skin layer dope composition change in the air gap.

Pure gas permeation tests of untreated fibers at 35 °C showed lower selectivity, but much higher permeance (Figure 4.17) than the untreated fibers spun in the second spin, suggesting membranes spun with a smaller air gap were more defective. However, unlike the fibers formed with the water containing dope, membranes formed in the third spin could be effectively caulked by PDMS. After PDMS post-treatment, fibers formed in the third spin displayed similar selectivity as those formed in the second spin, and the permeance was much higher (Figure 4.18).

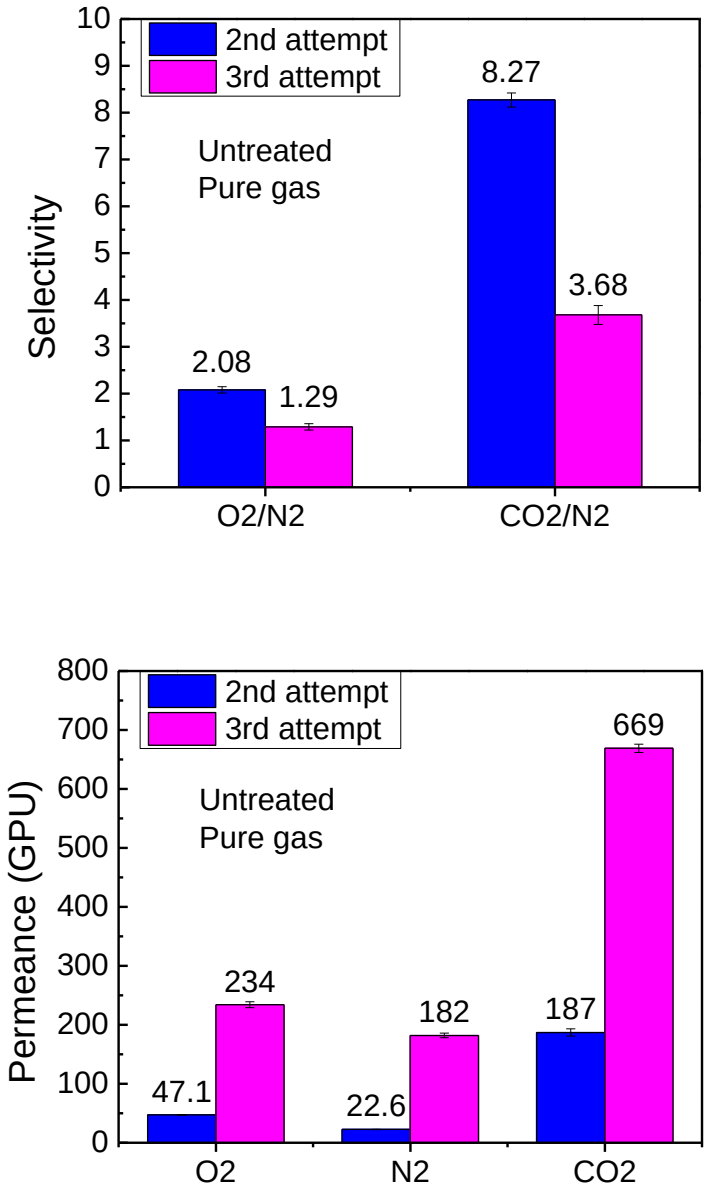

Figure 4.17: Comparison of pure gas permeation results of untreated nodular Matrimid® hollow fiber membranes spun in the 2nd and 3rd attempt at 35 °C. Feed pressure for O_2 and N_2 was 100 psig; for CO_2, 50 psig. The feed was introduced at the bore side.

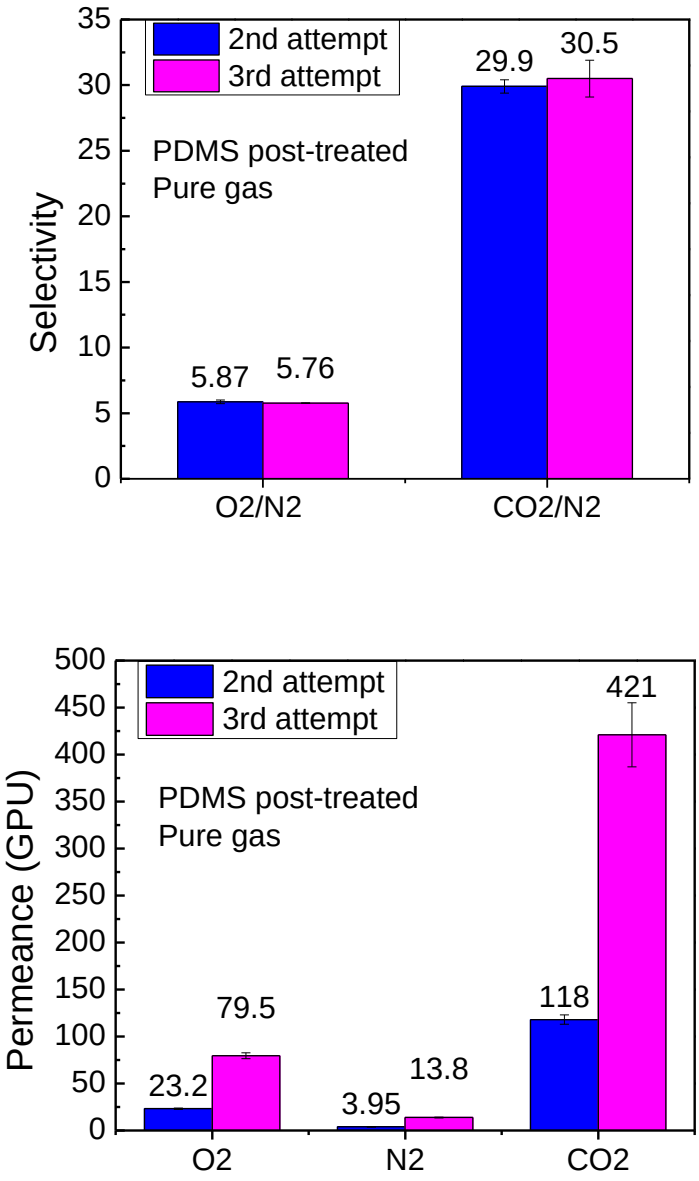

Figure 4.18: Pure gas permeation results of PDMS post-treated nodular Matrimid® hollow fiber membranes spun in the 2nd and 3rd attempt at 35 °C. Feed pressure for O_2 and N_2 was 100 psig; for CO_2, 50 psig. Feed was introduced at the bore side.

The membrane's performance at cold conditions was even more exciting. The 20 mol% CO_2/80 mol% N_2 gas mixture was fed to the bore side of the fibers in a constant pressure permeation system. The membranes showed both higher selectivity and higher permeance than the desired values (Figure 4.19). Figure 4.20 shows the plot of the natural logarithm of permeance versus the reciprocal of temperature, and the permeation activation energy is listed in Table 4.17. Membranes spun in the third attempt showed even higher N_2 and CO_2 permeation activation energy difference ($E_{p,N_2} - E_{p,CO_2}$) than those spun in the second attempt, enabling more pronounced increment in selectivity with the decrease of temperature. Therefore, the speculation that some Matrimid® hollow fiber membranes can achieve both high permeance and high selectivity at cold conditions was verified.

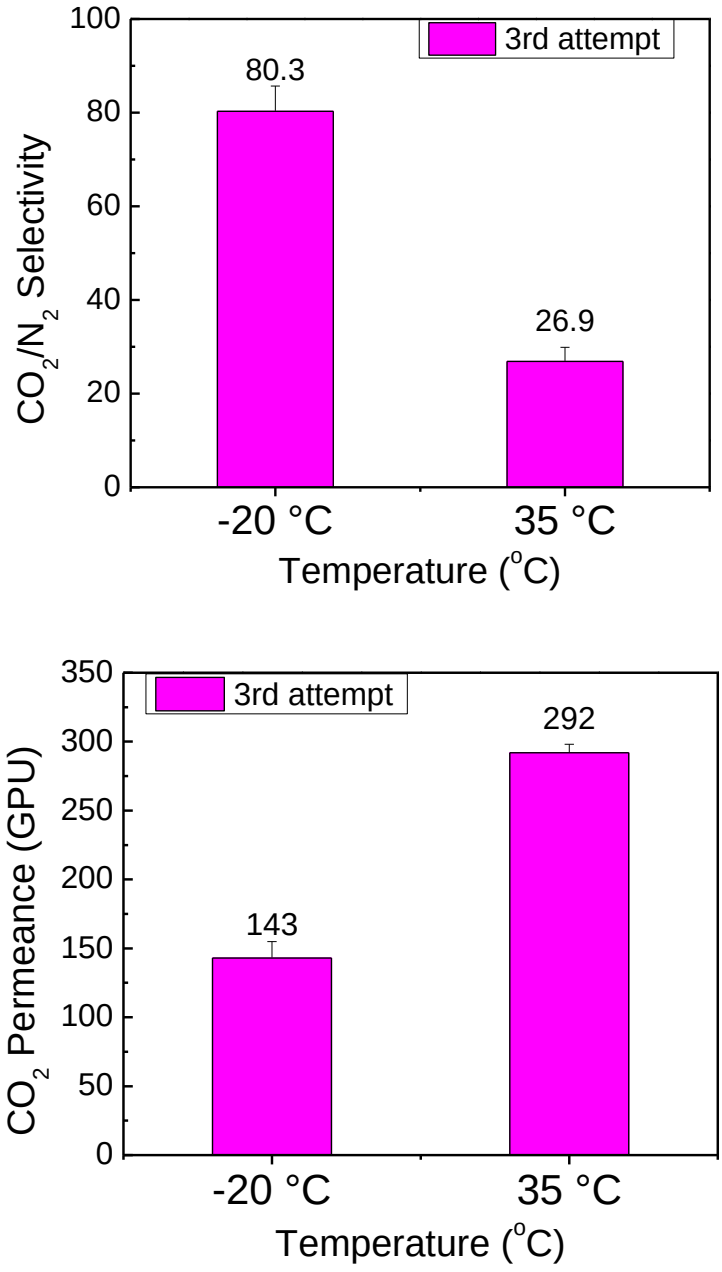

Figure 4.19: Permeation results of nodular Matrimid® hollow fiber membranes spun in the 3rd attempt. Both membranes were post-treated with PDMS. Feed was a mixture of 20 mol% CO_2/80 mol% N_2, and was introduced at the bore side at 100 psig.

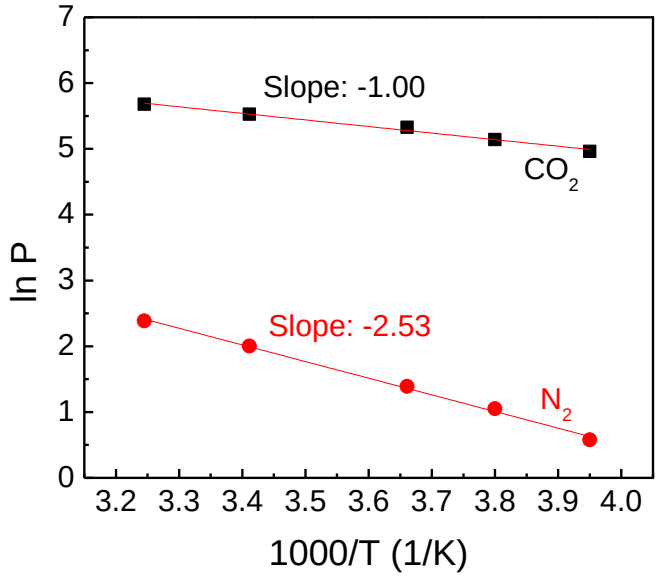

Figure 4.20: Temperature dependence of permeance for nodular Matrimid® hollow fiber membranes spun in the 3rd attempt. The fibers were post-treated with PDMS. Permeation measurements were performed with 20 mol% CO_2/80 mol% N_2.

Table 4.17: Permeation activation energy for CO_2 and N_2 in nodular Matrimid® hollow fiber membranes spun in the 2nd and 3rd attempt

	Nodular fiber (3rd attempt)	Nodular fiber (2nd attempt)
E_{p,CO_2}	8.3 ± 0.5 kJ/mol	5.9 ± 0.4 kJ/mol
E_{p,N_2}	21.0 ± 0.6 kJ/mol	17.5 ± 0.5 kJ/mol
$E_{p,N_2} - E_{p,CO_2}$	12.7 ± 0.8 kJ/mol	11.6 ± 0.6 kJ/mol

4.5 Summary

Defect free asymmetric Matrimid® hollow fiber membranes were successfully formed, but they failed to show a desirable separation performance at cold conditions. A motivating hypothesis suggesting membranes with nodular selective layers might display high cold performance was proposed and verified. Several spinning attempts were carried out to fabricate hollow fiber membranes with nodular skins. Dope compositions and spinning conditions were optimized step by step. Permeation activation energy for CO_2 and N_2 for the fibers spun in each attempt was analyzed. The nodular fibers showed a combination of high permeance and high selectivity at cold conditions.

4.6 References

[1] L. Xu, Ph.D. thesis, Carbon molecular sieve hollow fiber membranes for olefin/paraffin separations, Georgia Institute of Technology, 2012.

[2] J. Henis and M. K. Tripodi, Composite hollow fiber membranes for gas separation: the resistance model approach, Journal of Membrane Science, vol. 8, pp. 233-246, 1981.

[3] D. Ortiz-Acosta and C. Densmore, Sylgard® Cure Inhibition Characterization, Los Alamos National Laboratory, Report ID: LA-UR-12-25325.

[4] S. Hussain, PhD. Thesis, Mixed matrix dual layer hollow fiber membranes for natural gas separation, Georgia Institute of Technology, 2006.

[5] S. B. Carruthers, G. L. Ramos, and W. J. Koros, Morphology of integral skin layers in hollow fiber gas separation membranes, Journal of applied polymer science, vol. 90, pp. 399-411, 2003.

[6] D. T. Clausi and W. J. Koros, Formation of defect-free polyimide hollow fiber membranes for gas separations, Journal of Membrane Science, vol. 167, pp. 79-89, 2000.

[7] S. Pesek and W. Koros, Aqueous quenched asymmetric polysulfone membranes prepared by dry/wet phase separation, Journal of Membrane Science, vol. 81, pp. 71-88, 1993.

[8] S. C. Pesek, PhD. Thesis, Aqueous quenched asymmetric polysulfone flat sheet and hollow fiber membranes prepared by dry/wet phase separation, University of Texas at Austin, 1993.

[9] D. T. Clausi, Ph.D. thesis, Formation and characterization of asymmetric polyimide hollow fiber membranes for gas separations, The University of Texas at Austin, 1998.

[10] D. W. Wallace, C. Staudt-Bickel, and W. J. Koros, Efficient development of effective hollow fiber membranes for gas separations from novel polymers, Journal of Membrane Science, vol. 278, pp. 92-104, 2006.

[11] R. N. Maddox and A. Hines, Mass transfer fundamentals and applications, Editorial Prentice-Hall, 1985.

[12] S. Jordan, M. Henson, and W. Koros, The effects of carbon dioxide conditioning on the permeation behavior of hollow fiber asymmetric membranes, Journal of membrane science, vol. 54, pp. 103-118, 1990.

[13] R. Kesting, The four tiers of structure in integrally skinned phase inversion membranes and their relevance to the various separation regimes, Journal of applied polymer science, vol. 41, pp. 2739-2752, 1990.

[14] G. Dong, H. Li, and V. Chen, Plasticization mechanisms and effects of thermal annealing of Matrimid hollow fiber membranes for CO_2 removal, Journal of Membrane Science, vol. 369, pp. 206-220, 2011.

[15] S. B. Carruthers, Ph.D. thesis, Integral-skin formation in hollow fiber membranes for gas separations, The University of Texas at Austin, 2001.

[16] L. Broens, F. Altena, C. Smolders, and D. Koenhen, Asymmetric membrane structures as a result of phase separation phenomena, Desalination, vol. 32, pp. 33-45, 1980.

[17] D. Koenhen, M. Mulder, and C. Smolders, Phase separation phenomena during the formation of asymmetric membranes, Journal of Applied Polymer Science, vol. 21, pp. 199-215, 1977.

[18] E. R. W. Rousseau, Handbook of separation process technology: John Wiley & Sons, 2009.

[19] D. R. Paul and Y. P. Yampol'skii, Polymeric gas separation membranes: CRC Press, 1993.

[20] H. Strathmann, K. Kock, P. Amar, and R. Baker, The formation mechanism of asymmetric membranes, Desalination, vol. 16, pp. 179-203, 1975.

CHAPTER 5

SUB-AMBIENT TEMPERATURE GAS TRANSPORT IN NODULAR MATRIMID® HOLLOW FIBER MEMBRANES

In Chapter 4, high performance Matrimid® hollow fiber membranes with fused nodular selective layers were successfully formed. This chapter presents gas transport properties in the nodular membranes at sub-ambient temperatures. The permeation and sorption of CO_2 and N_2 are included in Section 5.1. Section 5.2 discusses performance difference between membranes with nodular and dense selective layers. A hypothetical explanation with regards to the better performance of the nodular fibers is proposed and described in Section 5.3. The introduction of additional sorption sites and a local orientation of polymer chain segments are suggested to be the likely reasons for the superior separation properties of the nodular fibers. Section 5.4 provides supporting evidences for the hypothesis.

5.1 Gas transport in nodular Matrimid® hollow fiber membranes

5.1.1 Mixed gas permeation at sub-ambient temperatures

In glassy polymers, even in the absence of plasticization, mixed gas transport behaviors are usually different from pure gases due to the competition of different penetrant molecules for the fixed number of Laugmuir sorption sites [1] as well as the competition for diffusion pathways through the polymer matrix [2]. Mixed gas permeation is a better representation of practical membrane performance, because it takes

into account the competition effects. In this chapter, mixed gases were used for all permeation measurements.

5.1.1.1 Temperature influence on permeation

The temperature influence on the separation of CO_2/N_2 with PDMS post-treated nodular Matrimid® hollow fiber membranes was evaluated within the range of -50 °C to 35°C. A mixture of 20 mol% CO_2/80 mol% N_2 was introduced at the bore side of the fibers at 100 psig. Temperature was reduced step by step from 35 °C to -50 °C, with the feed continuously purging through the module. Selectivity increased with the decrease of temperature (Figure 5.1a). At -50 °C, the CO_2/N_2 selectivity was 157 ± 1.3, about 5.8 times higher than at 35 °C. This result is exciting, because so far, few materials showed CO_2/N_2 selectivity close to 100, and often the high selectivity corresponded to a low permeability [3]. Note that, at sub-ambient temperatures, the non-idealities of the gases should be taken into account. The effect of non-ideal behavior on permeation calculations is especially pronounced for systems containing somewhat condensable components, like CO_2. The true driving force for gas penetrants to permeate through the membrane is the chemical potential gradient, which is more accurately represented by the transmembrane fugacity difference. Therefore, fugacity was used instead of partial pressure in the permeation calculation. Detailed discussion can be found in Appendix A. Moreover, due to the high flow rate of the retentate stream for bore-feed mixed gas permeation tests, and due to the small diameters of the hollow fiber membranes used in the current work, pressure drop along the fibers were also considered. More details can be found in Appendix B.

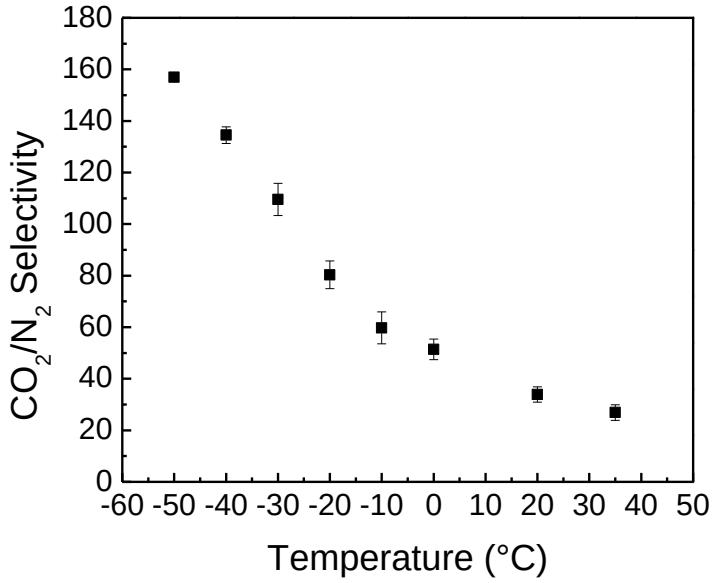

(a)

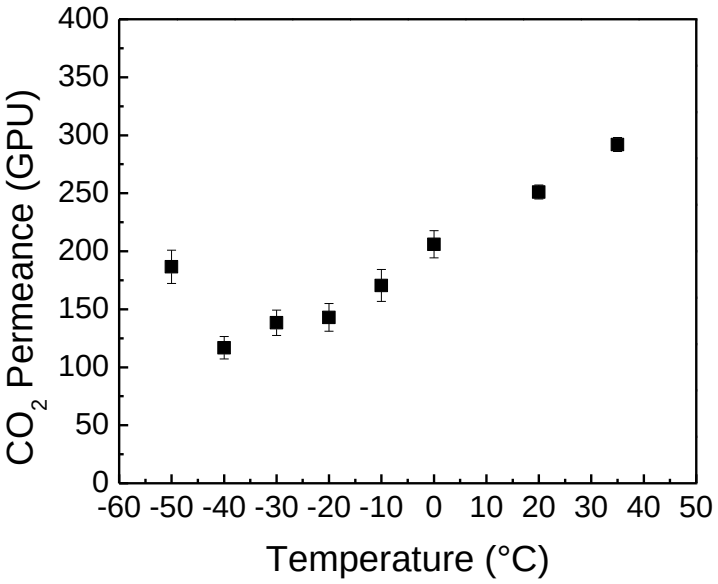

(b)

Figure 5.1: Mixed gas permeation results of PDMS post-treated nodular Matrimid® hollow fiber membranes at different temperatures. The feed was a mixture of 20 mol% CO_2/80 mol% N_2, and was introduced at the bore side at 100 psig. (a) CO_2/N_2 selectivity, (b) CO_2 permeance.

From 35 °C to -40 °C, the permeance of CO_2 decreased with the decrease of temperature, which was expected; however, as temperature decreased further, the permeance *increased* (Figure 5.1b). This seemed like an experimental anomaly, but it was verified for more than three times, and similar trend was also shown by Hasse [4]. The reason for the exceptionally high CO_2 permeance at -50 °C was attributed to conditioning of the polymer matrix by highly sorbing CO_2. The high activity of CO_2 at -50 °C is discussed in Section 5.3 in terms of a hypothesis in which the swelling of the polymer matrix makes it energetically easier for penetrant molecules to be absorbed and to diffuse. Here, activity is defined as the ratio of gas partial pressure to its pure gas vapor pressure [5, 6]. For non-ideal gases, pressure is replaced by fugacity. The vapor pressures of CO_2 and the corresponding fugacities at different temperatures are listed in Table 5.1. The lower the temperature, the lower the CO_2 vapor pressure, and thus the higher its activity for a fixed partial pressure. As is shown later, activity alone is insufficient to explain the observed phenomenon, since when the shell side is at the same feed activity, the same result is not observed as for bore-side feed. The combination of elevated CO_2 activity and bore-side feed is, therefore, necessary to cause the desirable phenomenon.

Table 5.1: The vapor pressures of CO_2 and the corresponding fugacities at different temperatures [7, 8]

T (°C)	CO_2 vapor pressure (psia)	Corresponding fugacity (psia)
31.1	1072	708
20.56	837.5	588
10.56	658.9	485
0.56	511.3	394
-10	384.8	308
-20	289.0	238
-30	207.1	178
-40	145.8	129
-50	99.09	90.2

5.1.1.2 Pressure influence on permeation

The performance of PDMS post-treated nodular Matrimid® hollow fiber membranes with different feed pressures was investigated at -20 °C, -30 °C, -40 °C and -50 °C. The feed was a mixture of 20 mol% CO_2/80 mol% N_2, and was introduced at bore side of the hollow fiber module. At each temperature, feed pressure was increased from 50 psig to 350 psig, with stepped increments of 50 psia. Merkel [9] pointed out that flue gas CO_2 capture is pressure-ratio-limited, and in most practical separation applications, since the pressure ratio (feed pressure to permeate pressure) is usually between 5 and 15. This range is limited by the capital and energy costs of generating the required pressure difference across the membrane. The cold membrane process developed at Air Liquide is highly energy integrated [4]; thus potentially economically allowing the use of relatively

high feed pressures (150-220 psig), thereby removing the pressure ratio problem. In this laboratory study, feed pressure was varied from 50 psig to 350 psig, giving rise to a maximum pressure ratio of 24. Increased selectivity is of clear benefit under high pressure ratio operating conditions.

To ensure gas transport reached steady state, 12 hrs of runtime was allowed before permeation results were recorded at each pressure. Note that high sorption of CO_2 can cause the membrane to swell, changing membrane properties, especially at low temperatures and high partial pressures when CO_2 interaction with the polymer matrix is strong. To eliminate such complications, a new module was used after each set of experiment (feed pressure being increased from 50 psig to 350 psig). At each temperature, two samples were run. All the fibers tested were from the same spinning state, so module to module difference should be minimal. From Figure 5.2 we can see that, the highest CO_2/N_2 selectivity and highest CO_2 permeance were achieved at -50 °C. With a feed pressure of 150 psig, the CO_2/N_2 selectivity was 209 ± 13 and CO_2 permeance was 227 ± 9 GPU, a combination of high selectivity and high permeance. Moreover, as feed pressure increased, the permeance of CO_2 increased with slight change in CO_2/N_2 selectivity. Similar selectivity and permeance trend for water permeation and salt rejection was observed in polyamide desalination membranes [10] , but the formation mechanism and the structure of the selective layer *are different from the membranes formed in this work*. The phenomenon of increased productivity with minimal change in selectivity is unusual and exciting. A gas separation membrane's selectivity and productivity are typically trade-off parameters, and under normal conditions, the selectivity generally decreases with increasing permeance of the more permeable gas

component [11, 12]. The reason for the unusual behavior of membranes produced in this work is attributed to the special morphology of the fiber's selective skin layer, which will be discussed in detail in Section 5.3.

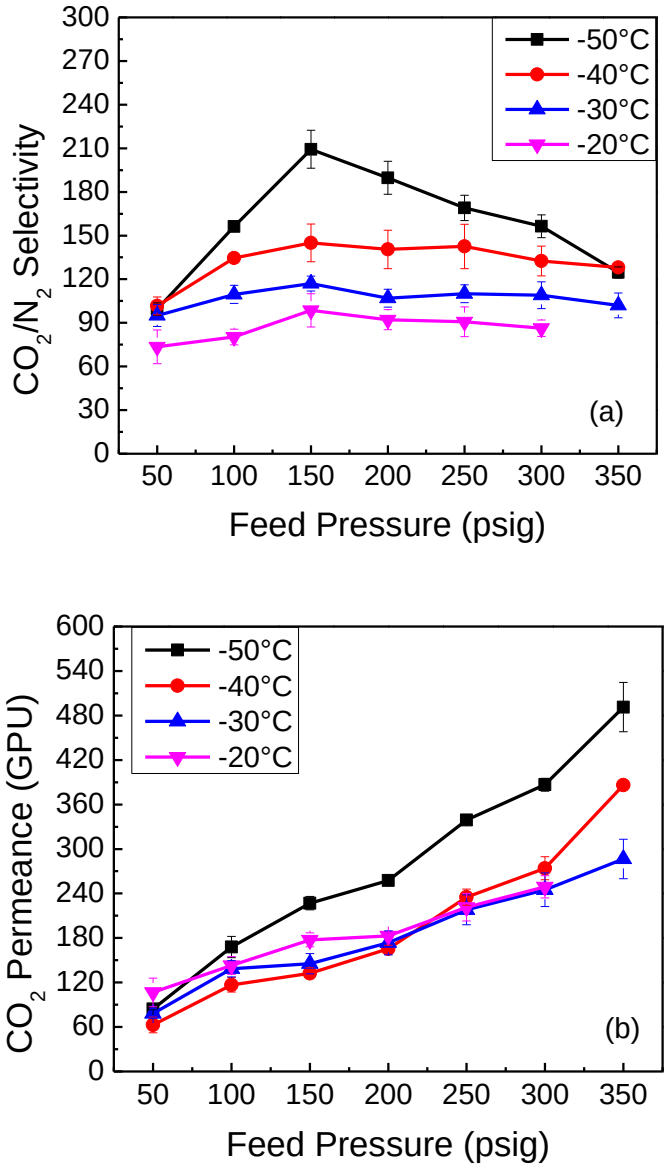

Figure 5.2: PDMS post-treated nodular Matrimid® hollow fiber membrane performances at different pressures. The feed was a mixture of 20 mol% CO_2/80 mol% N_2, and was introduced at the bore side. At each pressure, a 12 hour equilibration period was allowed before permeation results were recorded.

5.1.2 Sorption at sub-ambient temperatures

Sorption of CO_2 and N_2 in polyimides at sub-ambient temperatures is rarely reported in the literature. To better analyze the transport behaviors of CO_2 and N_2 in nodular Matrimid® hollow fiber membranes, pure CO_2 and N_2 sorption measurements were carried out within the temperature range of -50 °C to 35 °C. The examination of the sorption behavior can provide information on the interaction of penetrant molecules with the polymer matrix, which is helpful for understanding their permeation through the membranes.

The "pressure decay method" was used in this work [13], and gas uptake was calculated by a mole balance, as is described in Chapter 3. Similar to permeation calculation, the non-idealities of gases at sub-ambient temperatures were taken into account. Different compressibility factors were used for different operating temperatures, and fugacity was used instead of partial pressure. The pressure dependent compressibility factor and fugacity coefficient equations of pure CO_2 and N_2 are listed in Appendixes C and D.

The sorption of CO_2 at high pressures may cause the swelling of the polymer matrix, resulting in higher gas uptake for subsequent measurements. Such effect would be more pronounced at low temperatures when the vapor pressures of CO_2 are low. Figure 5.3 shows the sorption isotherms of pure CO_2 at -40 °C in a pressurization and depressurization cycle. In the depressurization cycle, the uptake of CO_2 was higher than in the pressurization cycle, suggesting the polymer matrix was swelled by the sorption of CO_2 at high pressures. To avoid such swelling effect, a new sample was used after each CO_2 sorption measurement. Figure 5.4 shows the sorption isotherms of CO_2 and N_2 at

different temperatures. For each set of data, two measurements were made, which showed similar results (error: ±1 CC_{STP}/CC). The data shown in Figure 5.4 is the average of the two measurements. The points are experimental data, and the solid lines are fit of concentration versus pressure data to the dual-mode model. The good fit of the experimental data to the model is at least consistent with the presence of a dual sorption environment in the nodular fibers. Specifically, some of the gas molecules maybe sorbed in microvoids in the polymer matrix corresponding to the unrelaxed free volume, while some maybe sorbed to the more densely packed region via an ordinary dissolution process. The uptake of CO_2 and N_2 at 35 °C was similar to the values reported for neat Matrimid® polymer in the literature [14]. The increase in the uptake of CO_2 and N_2 with the decrease of temperature was a result of an increase in the unrelaxed volume per unit volume of the polymeric membrane as well as an increase of gas solubility in the Henry's law environment.

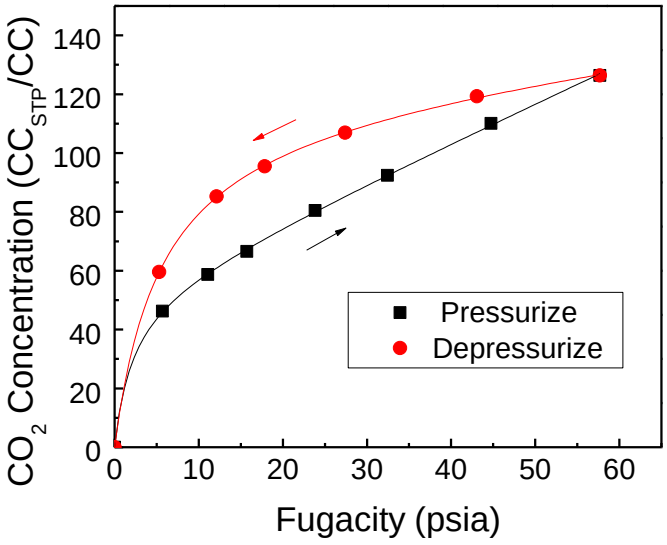

Figure 5.3: Sorption isotherms of CO_2 in nodular Matrimid® hollow fiber membranes at -40 °C in a pressurization and depressurization cycle. At each pressure, 1 to 2 days were waited before the pressure was changed to the next.

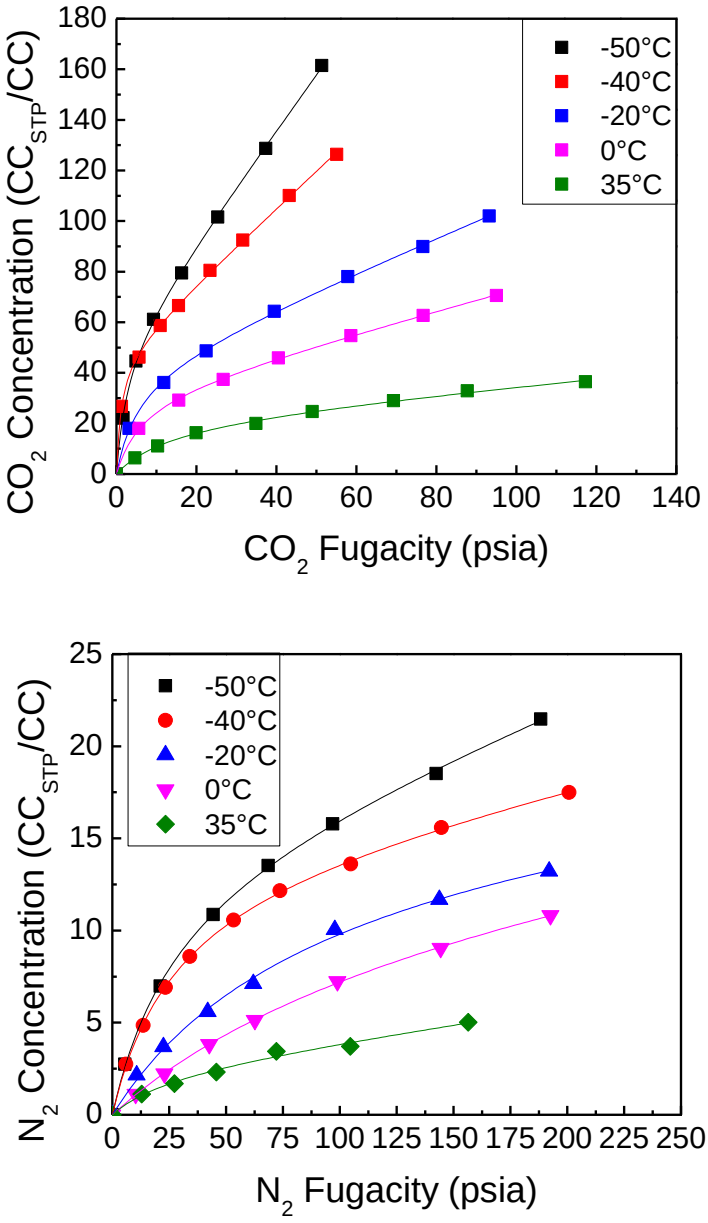

Figure 5.4: Sorption isotherms of Matrimid® hollow fiber membranes at different temperatures. The points are experimental data and the solid lines are fit of concentration versus pressure data to the dual-mode model. At -20 °C, -40 °C and -50 °C, 1 to 2 days were waited at each pressure before it was increased to the next.

The dual mode parameters derived from the sorption isotherms are listed in Tables 5.2 and 5.3. The higher condensability of CO_2 and its stronger interaction with the polymer matrix with respect to N_2 are suggested by its larger hole filling capacity (C_H'), hole affinity constant (b) and Henry's law constant (k_D). The hole filling capacity (C_H') correlates with the relative condensability of the gas as measured by its critical temperature (T_c) [15], and is a reflection of the amount of unrelaxed free volume in the samples being tested. The hole affinity constant (b) and the Henry's law constant (k_D) are equilibrium constants, which reflect the interaction of penetrant molecules with the polymer matrix.

Table 5.2: Dual-mode parameters for the sorption of CO_2 in nodular Matrimid® hollow fiber membranes

T (°C)	$C_H'\left(\frac{cm^3[STP]}{cm^3 poly}\right)$	$b\left(\frac{1}{psia}\right)$	$k_D\left(\frac{cm^3[STP]}{cm^3 poly \cdot psia}\right)$
35	22.5 ± 2.5	0.07 ± 0.01	0.14 ± 0.02
0	32.8 ± 1.2	0.16 ± 0.02	0.42 ± 0.01
-20	43.1 ± 1.7	0.17 ± 0.02	0.66 ± 0.02
-40	47.4 ± 1.0	0.82 ± 0.08	1.47 ± 0.03
-50	52.6 ± 2.0	0.35 ± 0.04	2.16 ± 0.04

Table 5.3: Dual-mode parameters for the sorption of N_2 in nodular Matrimid® hollow fiber membranes

T (°C)	$C_H'(\frac{cm^3[STP]}{cm^3 poly})$	$b\left(\frac{1}{psia}\right)$	$k_D(\frac{cm^3[STP]}{cm^3 poly \cdot psia})$
35	2.6 ± 1.3	0.035 ± 0.028	0.018 ± 0.006
0	14.1 ± 2.8	0.007 ± 0.001	0.014 ± 0.005
-20	17.0 ± 6.1	0.011 ± 0.004	0.009 ± 0.015
-40	14.0 ± 0.5	0.036 ± 0.002	0.026 ± 0.002
-50	14.5 ± 0.8	0.035 ± 0.003	0.047 ± 0.003

The sorption coefficients of CO_2 and N_2 were obtained by dividing the gas uptake with the corresponding fugacity:

$$S = \frac{C}{f} \tag{5.1}$$

where, S is the sorption coefficient; C is the penetrant concentration in the sample, and f is the fugacity. Higher sorption coefficients were obtained for CO_2 and N_2 at lower temperatures (Table 5.4), with CO_2 displaying larger values than N_2. The sorption

selectivity ($\frac{S_{CO_2}}{S_{N_2}}$) was also increased with the decrease of temperature, suggesting stronger competitive power of CO_2 molecules for the sorption sites at lower temperatures.

Table 5.4: Sorption coefficients and sorption selectivity ($\frac{S_{CO_2}}{S_{N_2}}$) for CO_2 and N_2 in nodular Matrimid® hollow fiber membranes

T (°C)	$S_{CO_2}(\frac{cm^3[STP]}{cm^3 poly \cdot psia})$	$S_{N_2}(\frac{cm^3[STP]}{cm^3 poly \cdot psia})$	$\frac{S_{CO_2}}{S_{N_2}}$
35	0.75 ± 0.02	0.04 ± 0.002	18.8 ± 1.2
0	1.51 ± 0.03	0.08 ± 0.006	20.1 ± 1.5
-20	2.13 ± 0.04	0.10 ± 0.005	21.3 ± 1.2
-40	3.43 ± 0.02	0.14 ± 0.005	24.5 ± 1.0
-50	4.18 ± 0.02	0.16 ± 0.005	26.1 ± 0.9

The diffusion coefficient was calculated by factoring out the sorption coefficient from permeability. For hollow fiber membranes, the actual skin thickness is not easily known, and permeance is commonly used to represent a normalized permeability. Factoring out the sorption coefficient from permeance gives a skin thickness normalized diffusivity:

$$\frac{D}{l} = \frac{P/l}{S} \tag{5.2}$$

where, l is the thickness of hollow fiber membrane's selective skin layer.

The diffusivity of CO_2 and N_2 decreased as temperature dropped from 35 °C to -40 °C; however, the trend was reversed from -40 °C to -50 °C (Table 5.5), which might be the cause of the trend shown in Figure 5.1. Normally, the diffusivity of gases should decrease with the decrease of temperature, due to lower frequency of diffusive jumps within the membrane. The unexpected high diffusivity at -50 °C might be caused by the swelling of the polymer matrix due to the sorption of highly active CO_2, thereby promoting the movement of polymer chain segments.

Table 5.5: Skin thickness normalized diffusion coefficients and diffusion selectivity ($\frac{D_{CO_2}}{D_{N_2}}$) for CO_2 and N_2 in nodular Matrimid® hollow fiber membranes

T (°C)	$\left(\frac{D}{l}\right)_{CO_2} \times 10^{-6}(cm/s)$	$\left(\frac{D}{l}\right)_{N_2} \times 10^{-6}(cm/s)$	$\frac{D_{CO_2}}{D_{N_2}}$
35	2013 ± 72	1438 ± 177	1.4 ± 0.2
0	705 ± 42	271 ± 34	2.6 ± 0.4
-20	347 ± 30	91.3 ± 11	3.8 ± 0.6
-40	176 ± 15	32 ± 4	5.5 ± 0.8
-50	231 ± 18	38.5 ± 3	6.0 ± 0.7

5.2 Comparison of nodular and dense Matrimid® hollow fiber membranes

5.2.1 Mixed gas permeation

It was identified in Chapter 4 that defect free Matrimid® hollow fiber membranes with homogeneous dense selective layers showed undesirable separation performance under cold conditions, whereas the PDMS post-treated nodular fibers displayed a combination of high selectivity and high permeance. A comparison of the permeation results between the nodular and dense hollow fiber membranes is shown in Figure 5.5. The same feed (100 psig, 20 mol% CO_2/80 mol% N_2 mixture) was applied to the bore side of the fibers, and the downstream was maintained at atmospheric pressure. An increase in selectivity and decrease in permeance was observed for both membranes; however, the PDMS post-treated nodular fibers showed higher selectivity and higher permeance than the untreated dense fibers. At lower temperatures, the selectivity difference was more pronounced, which was a result of the nodular membranes' larger difference in N_2 and CO_2 permeation activation energy ($E_{p,N_2} - E_{p,CO_2}$) (Figure 5.6 and Table 5.6). As was discussed in Chapter 4, a larger difference in permeation activation energy would lead to greater increment in selectivity with decreasing temperature. As for the permeance, although PDMS caulking added additional transport resistance to the nodular fibers, the permeance was still much higher than the untreated defect free fibers.

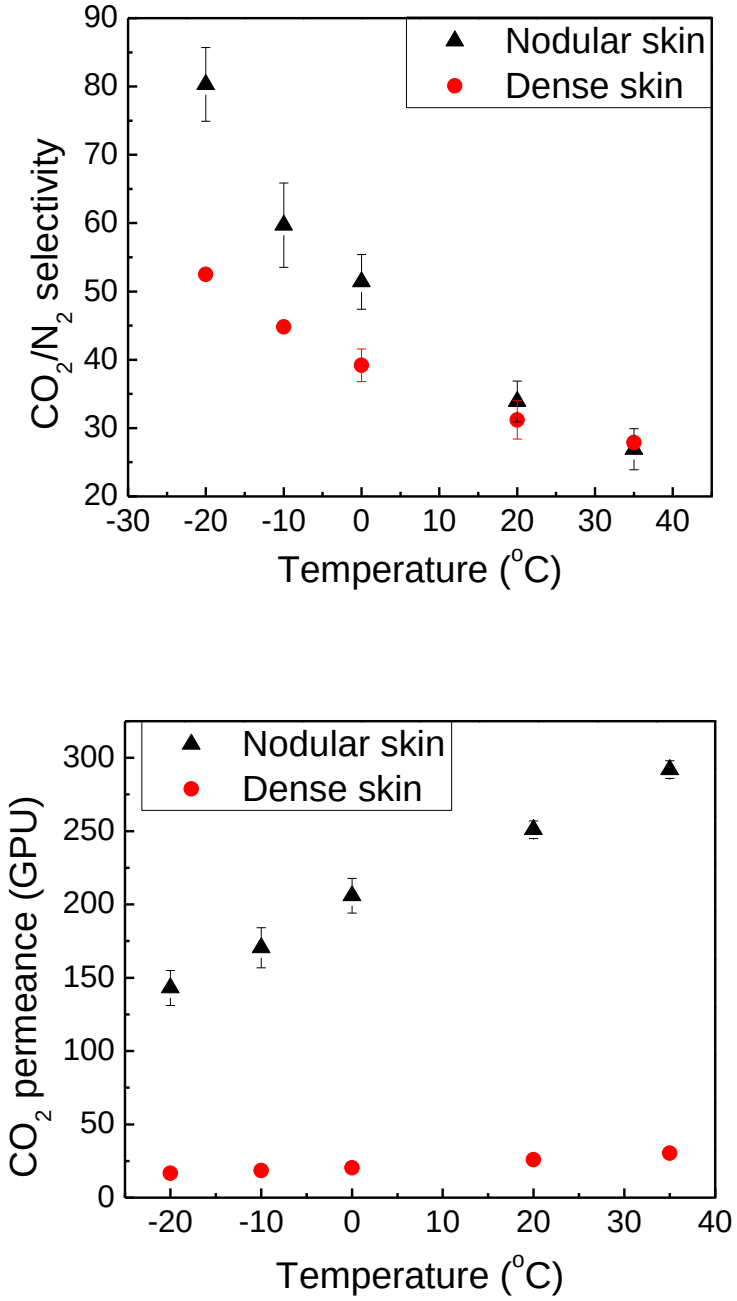

Figure 5.5: Comparison of permeation results of nodular and dense Matrimid® hollow fiber membranes. The nodular fibers were post-treated with PDMS, and the dense fibers were not post-treated. The feed was a mixture of 20 mol% CO_2/80 mol% N_2, and was introduced at the bore side at 100 psig.

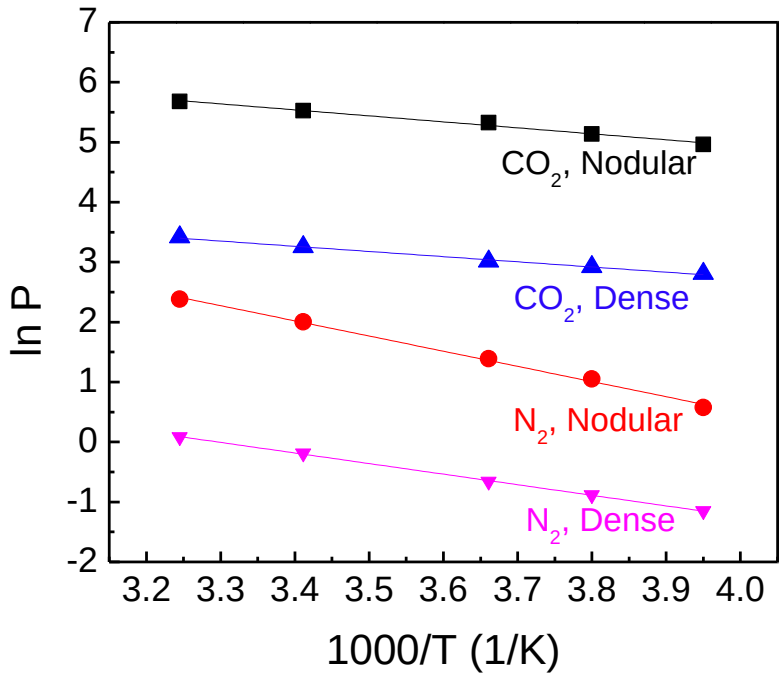

Figure 5.6: Temperature dependence of permeance for nodular and dense Matrimid® hollow fiber membranes. The nodular fibers were post-treated with PDMS, and the dense fibers were not post-treated. Permeation measurements were performed with 20 mol% CO_2/80 mol% N_2.

Table 5.6: Permeation activation energy for CO_2 and N_2 in nodular and dense Matrimid® hollow fiber membranes

	Nodular fiber	Dense fiber
E_{p,CO_2}	8.3 ± 0.5 kJ/mol	7.2 ± 0.3 kJ/mol
E_{p,N_2}	21.0 ± 0.6 kJ/mol	14.7 ± 0.2 kJ/mol
$E_{p,N_2} - E_{p,CO_2}$	12.7 ± 0.8 kJ/mol	7.7 ± 0.4 kJ/mol

5.2.2 Influence of PDMS post-treatment

Two possible reasons were envisioned as being possible causes for the higher selectivity of the nodular membranes: (i) PDMS post-treatment and (ii) the special structure of the nodular skin. In order to see whether PDMS post-treatment was the reason, the same post-treatment procedure was performed on the defect free Matrimid® hollow fiber membranes. It was believed that if the selectivity of the defect free membranes could be raised to a point comparable the selectivity of nodular fibers, then PDMS, per se, would be the dominant reason for the high selectivity at cold conditions. However, it turned out that minimal improvement in the selectivity of defect free fibers was achieved, and the selectivity was still far below the value of the nodular fibers (Figure 5.7). Meanwhile, a decrease in permeance resulted, due to the additional transport resistance. Therefore, it was concluded that the special structure of the nodular skin was more likely to be the reason for the performance difference.

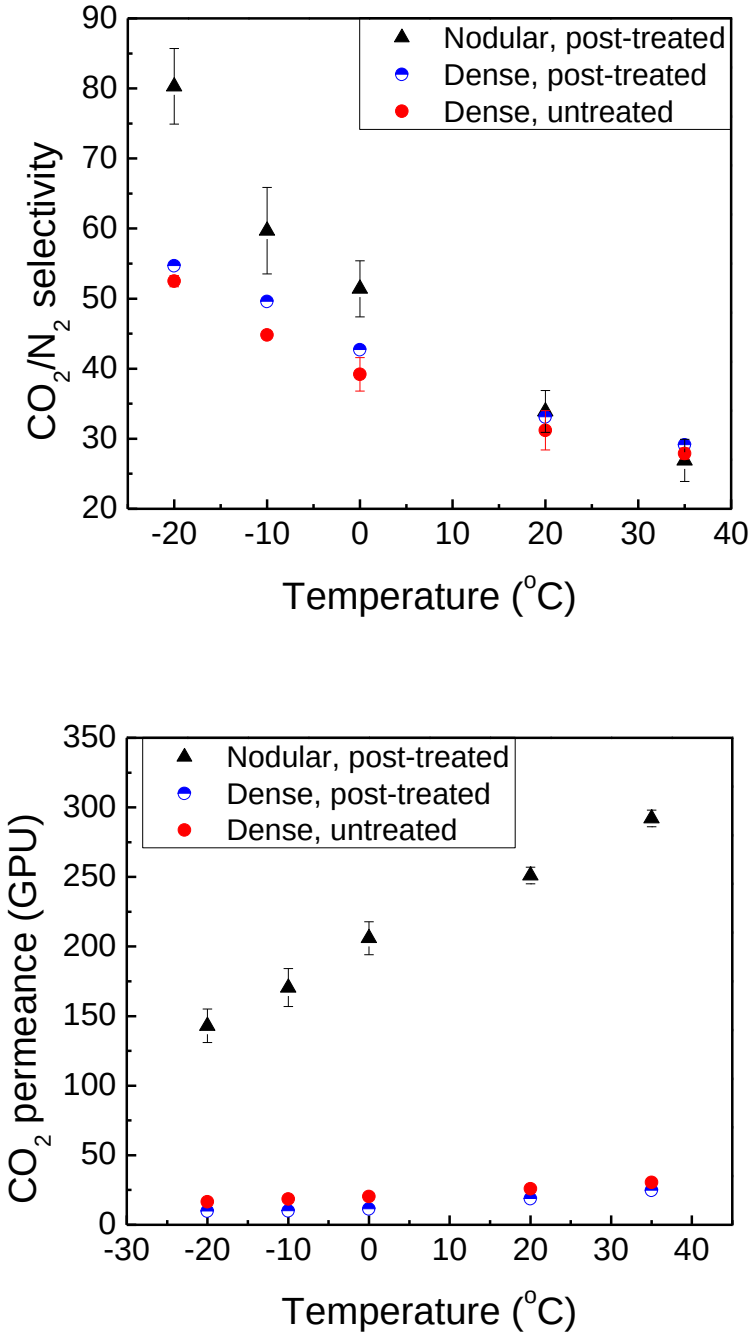

Figure 5.7: Permeation results of dense Matrimid® hollow fiber membranes before and after PDMS post-treatment. The performance is compared with the PDMS post-treated nodular Matrimid® fibers. The feed was a mixture of 20 mol% CO_2/80 mol% N_2, and was introduced at the bore side at 100 psig.

5.2.3 SEM images of selective skin layers

The SEM images of the selective skin layers for nodular and dense Matrimid® hollow fiber membranes are compared in Figure 5.8. It is clearly seen that the heterogeneous structure of the nodular skin is quite different from the homogeneous morphology of the dense skin. The interstices in the nodular skin are believed to be domains of low polymer density, which greatly affect membrane separation properties. Detailed discussion can be found in Section 5.3.

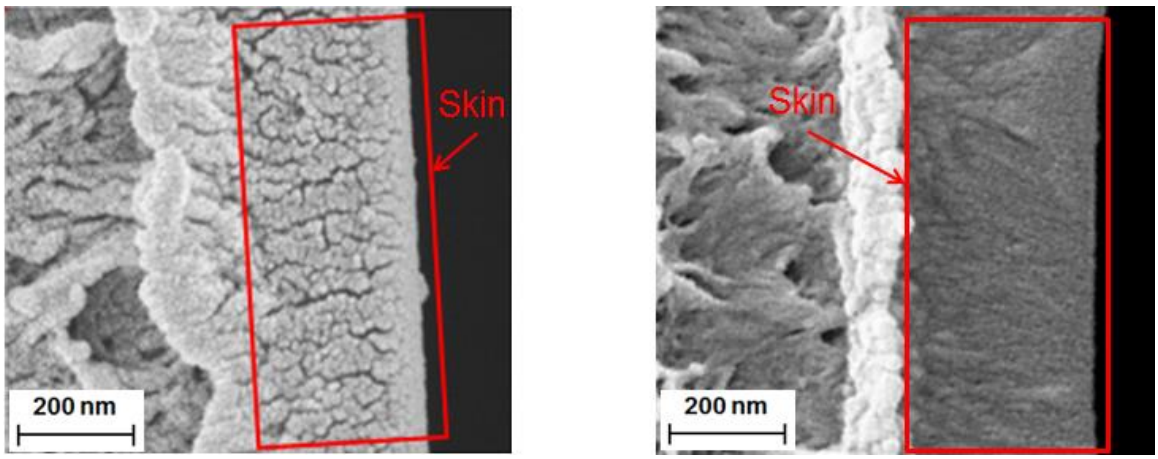

(a) Nodular skin (b) Dense skin

Figure 5.8: SEM images of the nodular and dense selective skin layers.

5.2.4 Sorption comparison

The more porous structure of the nodular selective layer was believed to contribute to higher sorption of penetrant molecules. Pure CO_2 and N_2 sorption measurements were performed on nodular and dense Matrimid® hollow fiber membranes.

It was considered that the nodular fibers might show higher uptake of both gases. The sorption measurements were carried out at 35 °C, -20 °C and -40 °C, and the isotherms are shown in Figure 5.9. In fact, the sorption isotherms were very similar, except for slight difference in the sorption of CO_2 at -40 °C under high CO_2 fugacities. The similar sorption isotherms show that it is very challenging to prove any difference between nodular and dense selective layers by sorption characterization. The skin layer accounts for only about 1 % of total fiber wall, and any difference in gas uptake within this layer would be compromised by the bulk support layer.

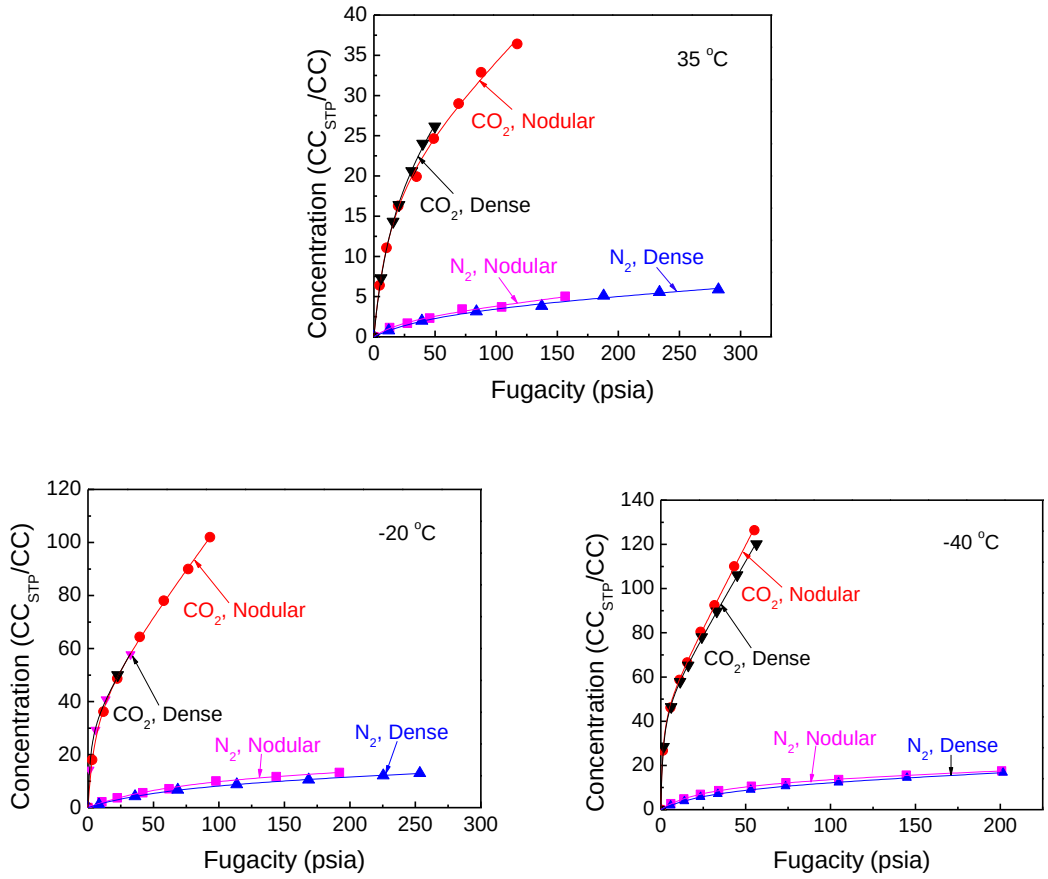

Figure 5.9: Sorption isotherms for CO_2 and N_2 in nodular and dense Matrimid® hollow fiber membranes at different temperatures.

5.3 Hypothesis regarding the great performance of nodular hollow fiber membranes

Although the nodular morphology was believed to be the reason for the better membrane performance at cold conditions, the underlying reason was still not well understood. A somewhat speculative hypothesis with regards to the addition of sorption sites and a local orientation of polymer chain segments was thus proposed.

5.3.1 Hypothetical skin layer morphologies

To explain the observations, a speculation regarding the morphology of the nodular selective layer was considered. As was described in Chapter 4, the nodular skin is envisioned to be comprised of several layers of so-called "nodules". The nodules are depicted as being spherical and are interconnected by "tie-chains". Since the tie-chains keep adjacent nodules "fused" together, viscous flow through the volume between the nodules is not generally possible. Figure 5.10 shows a schematic of the hypothetical nodular skin. The nodules are assumed to have high polymer density, typical of normal dense polymer matrix, while the interstitial domains between nodules are envisioned as having lower polymer density, but not defects. Similar structure was also suggested in the previous work of Kesting [16] and Dong [17]. These authors suggested that sorption within the nodules might correspond to Henry's sorption sites, whereas sorption in the interstitial domains may constitute Langmuir sorption sites. However, typical of any dense glassy matrix, we believe that *both* Langmuir and Henry's sorption sites exist within the nodules *and* the interstitial domains, but to different degrees. Since the interstitial domain has higher fractional free volume (FFV), more gas molecules are sorbed to this region than to the surrounding nodules.

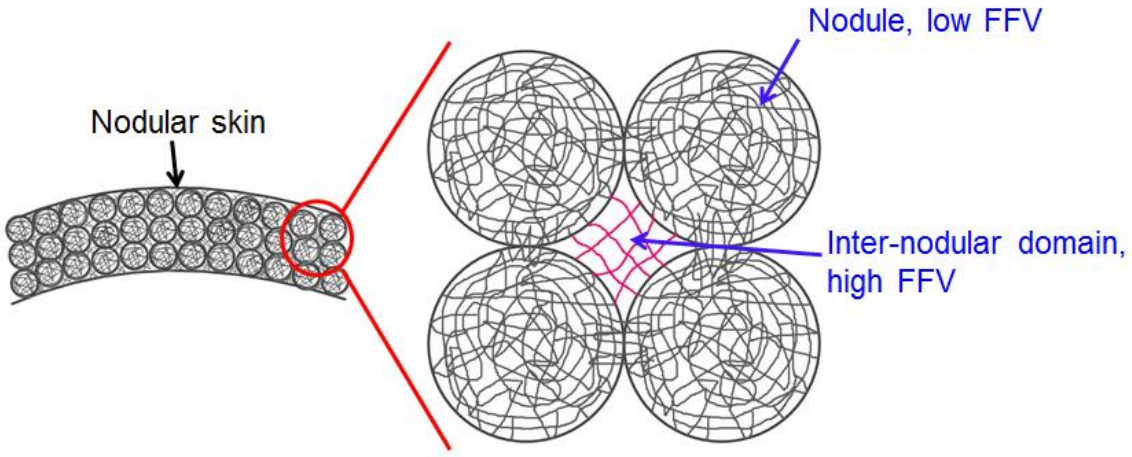

Figure 5.10: Hypothetical structure of the nodular skin.

5.3.2 Hypothesis regarding the introduction of sorption sites

It was shown in Section 5.1.1.2 that the permeance of CO_2 for nodular Matrimid® hollow fiber membranes increased with the increase of feed pressure. This behavior doesn't follow the dual mode transport model, which predicts the permeance of penetrant molecules to decrease with increasing pressure until the Langmuir sorption sites are saturated, and then level off (in the absence of plasticization). Plasticization can cause an upswing in the plot of permeance versus pressure, however, a corresponding loss of selectivity is normally observed. Since the selectivity for the nodular membranes didn't drop with the increase of permeance, the possibility of plasticization was ruled out. In fact, the abnormal behavior was believed to be correlated with the nodular structure of the selective layer. The presence of inter-nodular tie-chains would allow the nodules to be

separated to a certain point without losing the membrane's separation capability. The morphology of the nodular skin with pressure on the bore side is shown in Figure 5.11.

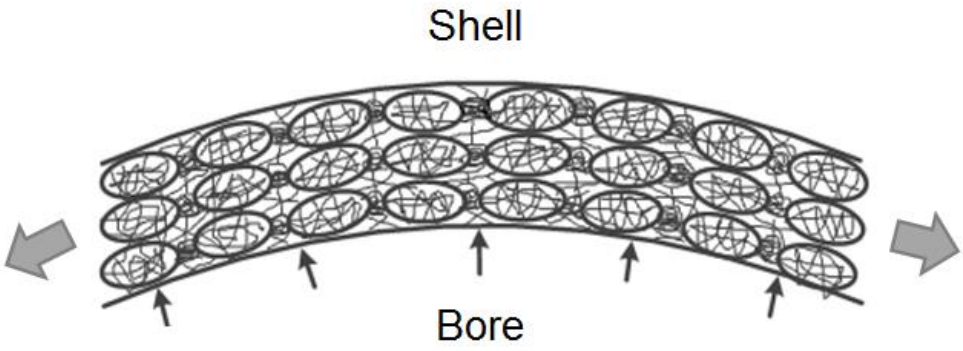

Figure 5.11: Hypothetical morphology of the nodular skin when the bore side of the hollow fiber membrane is pressurized.

Two possible factors might lead to the increase in permeance with increasing bore feed pressure for the nodular hollow fiber membranes: (i) reduction of effective separation layer thickness. The higher the feed pressure, the thinner the effective separation layer is. Since membrane permeance is skin thickness normalized flux, thinner effective separation layer gives rise to higher permeance. (ii) Increase in sorption capacity. Bore side feed causes the interstitial sites between nodules to be enlarged (Figure 5.12), thereby introducing more excess free volume. The excess free volume in glassy polymers is distributed as molecular- and submolecular-scale microvoids [18]. For the microvoids that are large enough to accommodate penetrant molecules, they serve as Langmuir sorption sites. As for the smaller ones that can't completely accommodate a

penetrant molecule, they have the potential to be dilated by highly condensable penetrants, like CO_2, to become Langmuir sorption sites. Such local volume reduces the need to dilate the polymer matrix by the full amount needed to accommodate a given "dissolved" penetrant [19]. Energetic considerations would favor the reutilization of such locally available volume rather than requiring the molecule to overcome the full cohesive energy resistance of the matrix by opening totally new gaps of the required volume for dissolution. Therefore, the enlarged interstitial sites due to bore side feed would introduce more Langmuir sorption sites, increasing sorption capacity.

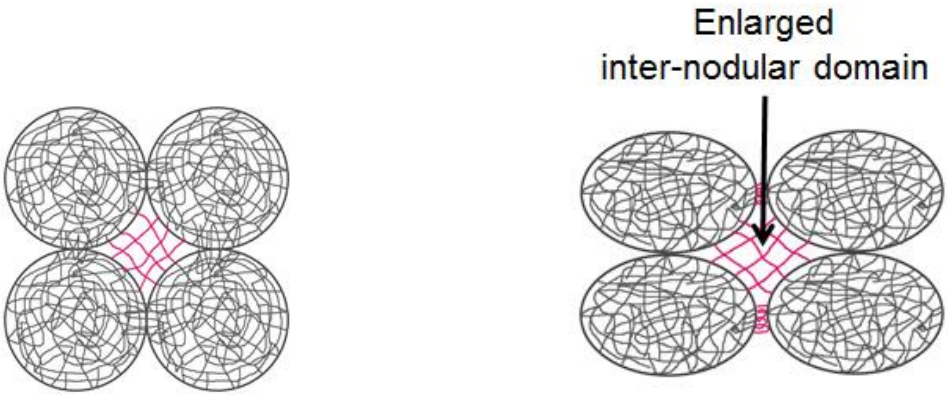

No feed Bore feed

Figure 5.12: Schematic showing the enlargement of the inter-nodular site when feed is applied to the bore side of the hollow fiber membrane.

5.3.3 Hypothesis regarding the orientation of polymer chains

The CO_2/N_2 diffusion selectivity calculated by factoring out the sorption selectivity from permselectivity in Section 5.1.2 showed an increasing trend with the decrease of temperature. Although the sorption selectivity was calculated under the assumption that gas solubility in the selective skin layer was equal to the solubility in the entire hollow fiber membrane (it was impossible to separate the ultra-thin selective skin layer from the support layer), and the increased sorption selectivity with bore feed was not taken into account, it was still wondered whether the gas diffusion behavior was affected by the nodular morphology as well. A local orientation of polymer chain segments was hypothesized to possibly contribute to an increase in diffusion selectivity. Specifically, when feed was applied to the bore side of the nodular hollow fiber membranes, the polymer chains connecting adjacent nodules might be stretched uniaxially and become aligned in the direction of the applied stress (Figure 5.13). We expected that the orientation and conformational change of the tie-chains will affect the diffusion of penetrant molecules.

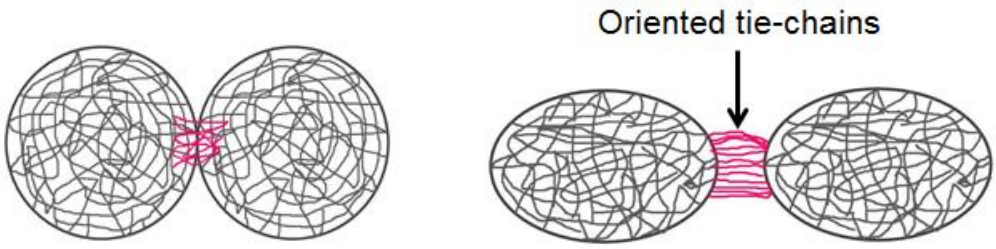

No feed Bore feed

Figure 5.13: Schematic showing the orientation of tie-chains when feed is applied to the bore side of the hollow fiber membrane. The picture is exaggerated from reality for illustration purpose.

The influence of polymer chain alignment on gas transport properties has been reported in the literature. El-Hibri and Paul investigated the effect of uniaxial orientation of poly(vinyl chloride) (PVC), a glassy and primarily amorphous material, on the permeation of He, Ar and N_2 [20]. The permeability of all gases was found to decrease with orientation. The decrease in the permeability of Ar and N_2 was more pronounced than He, due to the relatively larger sizes of Ar and N_2 (Table 5.7). The solubility coefficients for all gases decreased up to a certain birefringence value and remained constant afterwards, whereas the decrease in the diffusion coefficients was accelerated after that particular value. The birefringence is a physically meaningful correlating parameter representing a quantitative measure of the actual extent of chain alignment in the polymer [20]. The effects of uniaxial drawing and processing temperature of poly(viny1idene fluoride) (PVF) on the gas sorption and transport properties were also reported [21]. Sorption, diffusion, and permeability coefficients were measured for He, H_2, Ar, O_2, N_2, CH_4 and CO_2. The permeability and diffusion coefficient were found to decline significantly with uniaxial drawing, the magnitude of which was dependent on both the drawing temperature and the molecular size of the penetrant being considered. Increasing molecular diameter and decreasing drawing temperature resulted in more pronounced reduction in permeability and diffusion coefficients. However, the solubility was not sensitive to drawing and thermal treatments, which was in agreement with the relatively small changes in the free volume observed [21]. In the current case, however, it is not possible measure local birefringe changes in the inter-nodular zones.

Wang and Porter [22] investigated the permeation of CO_2 in uniaxially hot-drawn atactic polystyrene (PS) films. The permeability and the diffusion coefficient were found

to decrease with drawing, which was attributed to the restriction in diffusion caused by orientation; whereas the sorption coefficient remained constant, in agreement with the unaffected glass transition temperature and sample density.

Barker et al. studied the influence of mechanical strain on the permeation of polar and nonpolar gases through noncrystalline acrylic polymers. The polymer films were stretched to the maximum obtainable elongations. The diffusion coefficients of O_2 and CO were found to decrease with increasing orientation [23].

E.-A. McGonigle et al. [24] reported gas transport properties of Ar, CO_2 and N_2 in biaxially orientated polyester films: poly(ethylene terephthalate) [PET] and poly(ethylene naphthalate) [PEN]. A clear reduction in the diffusion coefficient for all gases was observed, and the reason was mainly attributed to a decrease in segmental mobility of the polymer chains that were oriented. Meanwhile, an increase in the diffusion selectivity for CO_2/N_2, CO_2/Ar and Ar/N_2 was identified.

Table 5.7: Size (kinetic diameter) of different gas molecules [25]

Gas	He	H_2	CO_2	O_2	Ar	N_2	CH_4
Size **(Å)**	2.6	2.89	3.3	3.46	3.5	3.64	3.8

In this work, it was hypothesized that the oriented polymer chains in the inter-nodular region would result in higher CO_2/N_2 diffusion selectivity. As was introduced in Chapter 2, the diffusion of gas molecules in polymeric membranes is an activated

process, in which diffusive jumps of gases within the polymer matrix occur when thermally activated motions of chain segments generate transient gaps that are larger than the size of the diffusing penetrant (Figure 5.14). In the case of bore side feed, the inter-nodular tie-chains are under tension; a reduction in the chain segmental motion should be expected. The restricted movement of chain segments would change the distribution of the transient gaps by reducing the frequency of the chain openings that are large enough for penetrant molecules to jump through (Figure 5.15). Due to the larger size of N_2 molecules, the reduction in the diffusion of N_2 is more severe than CO_2, thus increasing CO_2/N_2 diffusion selectivity.

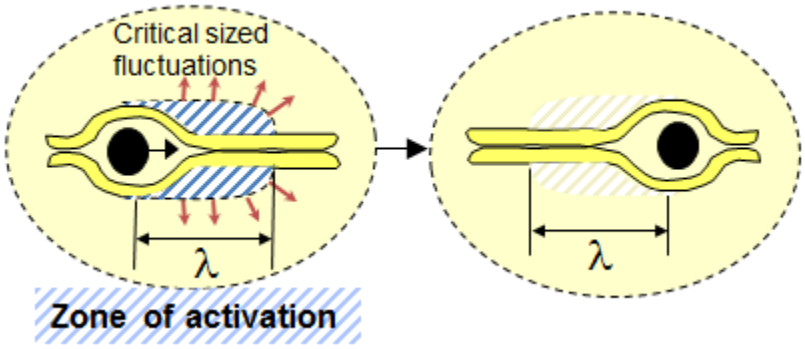

Figure 5.14: Conceptual depiction of a penetrant molecule jump through the polymer matrix.

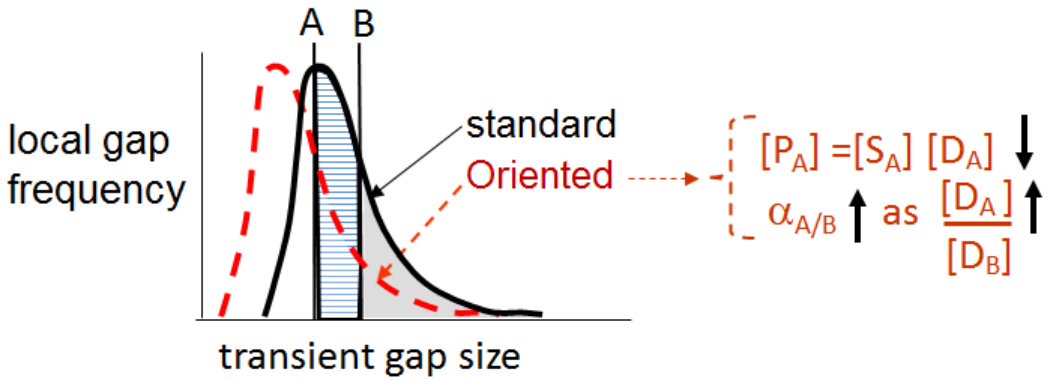

Figure 5.15: Schematic plot showing the change of the distribution of transient gaps due to the orientation of polymer chains. "A" represents CO_2, and "B" represents N_2.

5.4 Hypothesis validation

5.4.1 Considerations of direct characterization of the nodular skin

There are three challenges that make the direct characterization of the nodular selective skin layer very difficult:

Challenge 1: The thickness of the skin layer is around 0.1 um, accounting for only ~ 1 % of the total thickness of the fiber wall. It is very challenging to exclude the influence of the bulk support layer by probing only 0.1 um deep down from the surface.

Challenge 2: The characterization has to be carried out at cold conditions: -50 °C ~ -20 °C.

Challenge 3: According to the hypothesis, gas transport in the nodular selective layers is not only morphology dependent, but also "directional". The uniaxial draw of the nodular skin layer due to bore feed resulting in oriented tie-chains has to be taken into account.

In the beginning, a pulsed field gradient (PFG) NMR technique was considered, which could be carried out at -50 °C to -20 °C. The PFG-NMR technique can detect self-diffusion coefficient of a penetrant in a porous material by applying a stimulated spin echo sequence [26]. It can measure self-diffusivities for different mean square displacement (MSD) values over a macroscopic length scale. Although it can't select the location of the displacements relative to the membrane surface, measurements for a broad range of MSD values would allow the obtaining of diffusivities for different depth from the membrane surface by data analysis. To perform the measurement, a stack of more than 100 vertically oriented hollow fiber membranes would be required to form a cylindrical sample, which would be placed in a NMR resonator. It was believed that the diffusivities inside the nodular selective layer would be essentially the same along the direction of the membrane length and along the radial direction. The molecules diffusing inside the separation and support layers during the diffusion time used in the measurement would have different effective diffusivities, and the smallest value would correspond to the diffusivity in the nodular separation layer. Measurements of the time dependencies of the effective diffusivity and population fraction of the CO_2 molecules corresponding to the smallest diffusivity was expected to provide some information about the thickness of the layer where this diffusion occurred.

Although the pulsed field gradient (PFG) NMR was able to meet Challenges 1 and 2, it failed to meet Challenge 3, because the measurement could only be performed under conditions of sorption equilibrium with a fixed pressure of CO_2 in the gas phase. In that case, there would be no pressure difference between the bore and shell side of the membrane, and thus, the effect of oriented tie-chains due to uniaxial draw of the nodular

skin layer would be eliminated. However, the orientation effect was believed to be a very important factor affecting CO_2 diffusivity in the nodular selective layer. With no pressure difference across the membrane, the nodules in the selective layer would be closed together, as is shown in Figure 5.16. Since the experiment doesn't fit into our picture, we didn't pursue this measurement. Instead, we used indirect evidence to support our hypothesis.

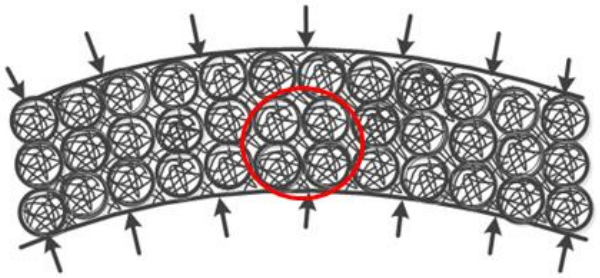

Figure 5.16: Schematic showing the hypothesized morphology of the nodular skin layer when the membrane is under sorption equilibrium in an NMR resonator.

5.4.2 Indirect evidence I: bore feed versus shell feed

To verify the hypothesis regarding the skin layer's fused-nodular morphology, feed was introduced at both bore and shell side of the hollow fiber membranes. In contrast to the inflating effect of bore feed, shell feed would compress the fibers, forcing nodules to stay together, as is shown in Figure 5.17. With shell side feed, the effects of dilated inter-nodular domains and oriented tie-chains would be minimized, and the membrane performance was expected to drop.

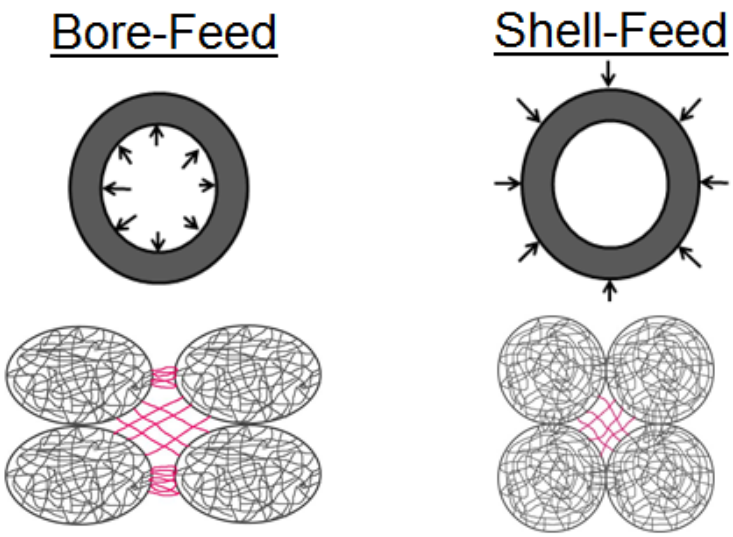

Figure 5.17: Hypothetical morphologies of the nodules in the fiber's selective skin layer during bore and shell feed.

5.4.2.1 Temperature influence

A gas mixture of 20 mol% CO_2/80 mol% N_2 was introduced to the bore and shell side of the nodular Matimid® hollow fiber membranes at different temperatures between -50 °C and 35 °C. The upstream pressure was 100 psig, and the downstream was at atmospheric pressure for both cases. The selectivity for bore and shell feed was similar at 35 °C; however, significant difference arose as temperature decreased, with the bore feed displaying higher selectivity (Figure 5.18). The membrane permeance for bore feed was also higher than for shell feed over the temperature range of the experiment, and slight increase of permeance from -40 °C to -50 °C was also observed for shell feed, but to a much less extent than bore feed.

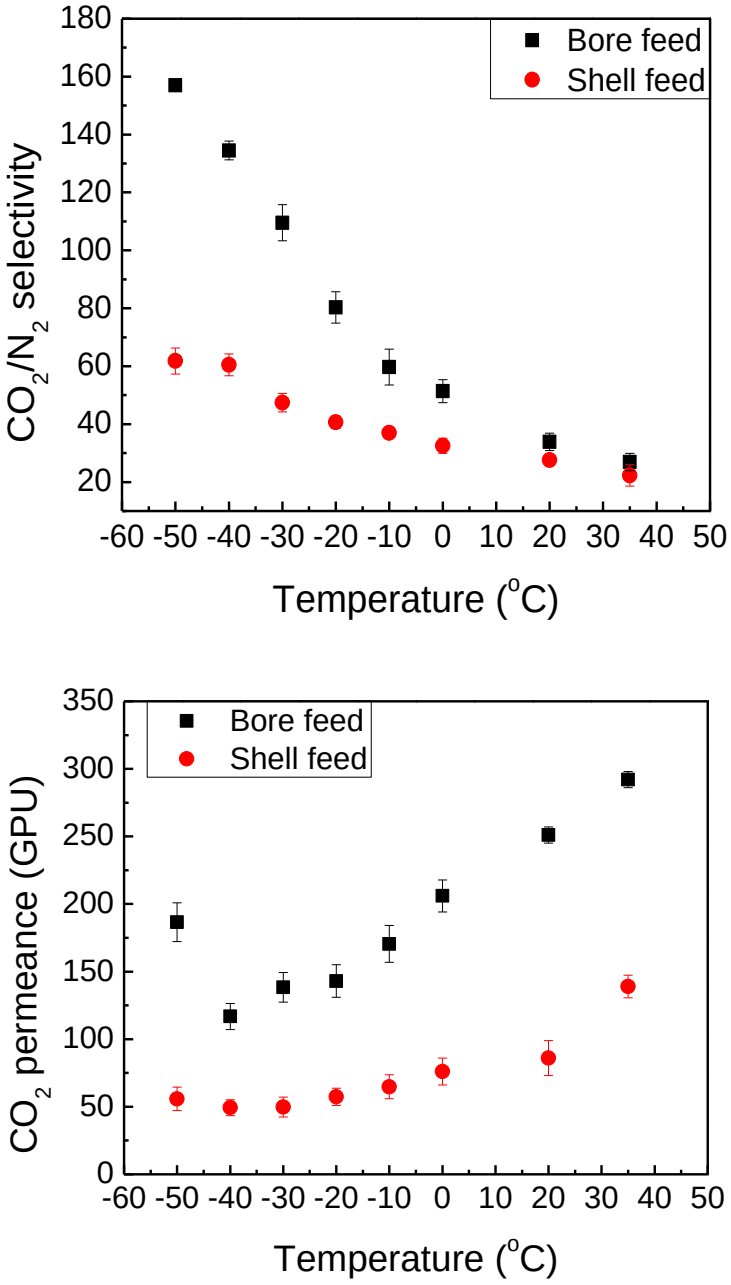

Figure 5.18: Bore versus shell feed permeation results for PDMS post-treated nodular Matrimid® hollow fiber membranes at different temperatures. The feed was a mixture of 20 mol% CO_2/80 mol% N_2 at 100 psig. The downstream was at atmospheric pressure.

The diffusion activation energy for CO_2 and N_2 was calculated under the approximation that gas solubility in the selective skin layer was equal to the solubility in the entire hollow fiber membrane, and solubility for bore feed was similar to that for shell feed. The temperature dependence of skin thickness normalized diffusion coefficient is given by:

$$\frac{D}{l} = \frac{D_0}{l} \exp\left(\frac{-E_d}{RT}\right) \tag{5.3}$$

where the skin thickness normalized diffusion coefficient was obtained by factoring out the sorption coefficient from permeance. Equation 5.3 can be written as:

$$\ln\left(\frac{D}{l}\right) = -\frac{E_d}{RT} + \ln\left(\frac{D_0}{l}\right) \tag{5.4}$$

The natural logarithm of the skin thickness normalized diffusion coefficient was plotted against the reciprocal of temperature (Figure 5.19), and the activation energy for diffusion was obtained from the slope of the linear fitting curve. It is shown in Table 5.8 that bore feed required higher diffusion activation energy for both CO_2 and N_2 than shell feed. The difference in the diffusion activation energy ($E_{d,N_2} - E_{d,CO_2}$) for bore feed was larger than for shell feed, suggesting more pronounced increase in diffusion selectivity for bore feed with the decrease of temperature.

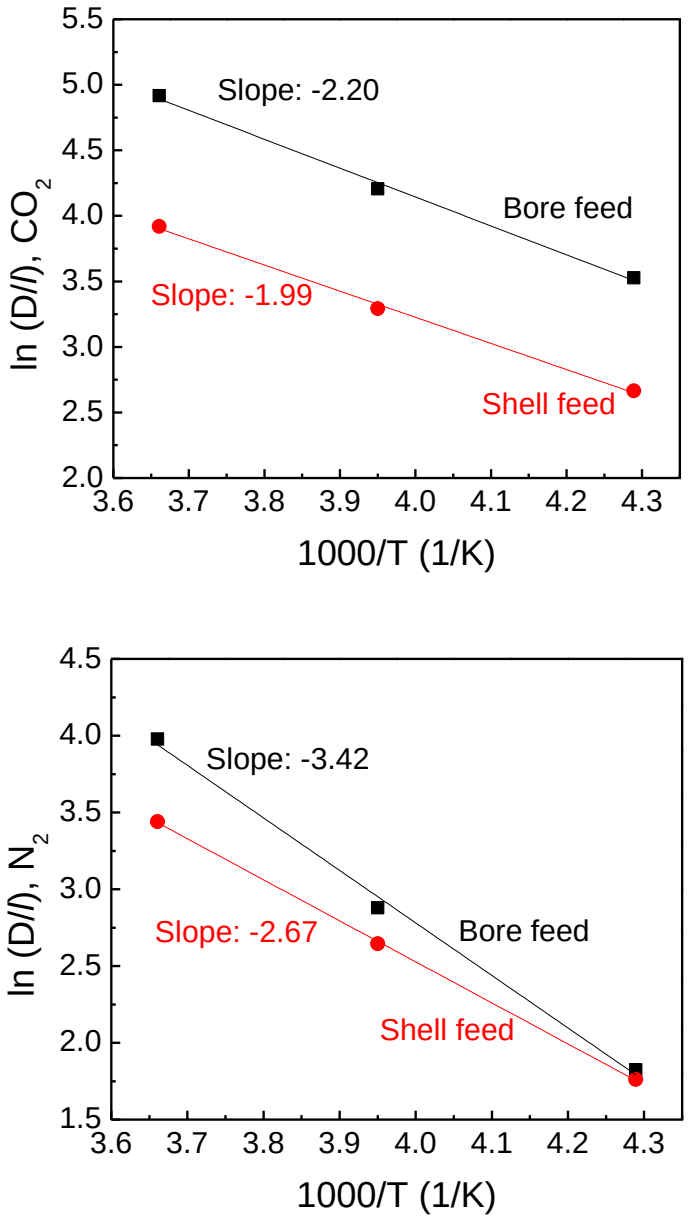

Figure 5.19: Temperature dependence of skin thickness normalized diffusion coefficient for PDMS post-treated nodular Matrimid® hollow fiber membranes. Permeation measurements were performed with 20 mol% CO_2/80 mol% N_2.

Table 5.8: Diffusion activation energy for CO_2 and N_2 in nodular Matrimid® hollow fiber membranes with bore and shell feed. Temperature range: -40 °C to 0 °C

	Bore feed	Shell feed
E_{d,CO_2}	18.3 ± 1.1 kJ/mol	16.5 ± 0.8 kJ/mol
E_{d,N_2}	28.4 ± 1.6 kJ/mol	22.2 ± 0.3 kJ/mol
$E_{d,N_2} - E_{d,CO_2}$	10.1 ± 1.9 kJ/mol	5.7 ± 0.9 kJ/mol

5.4.2.2 Pressure influence

The bore versus shell feed effects were also compared under different upstream pressures. Figure 5.20 shows the permeation results at -40 °C with a feed of 20 mol% CO_2/80 mol% N_2. The upstream pressure was increased from 50 psig to 350 psig, with a stepped increment of 50 psig. One day was allowed at each pressure before it was increased to the next. The selectivity difference between bore and shell feed didn't change too much with pressure, with bore feed displaying higher selectivity; however, significant difference in CO_2 permeance was observed. The higher the upstream pressure, the more pronounced the difference is. Unlike the increasing permeance for bore feed, slight change in the permeance for shell feed was observed. The reason was attributed to minimized dilation of the inter-nodular domains, which is consistent with our expectations, based on our hypothesis.

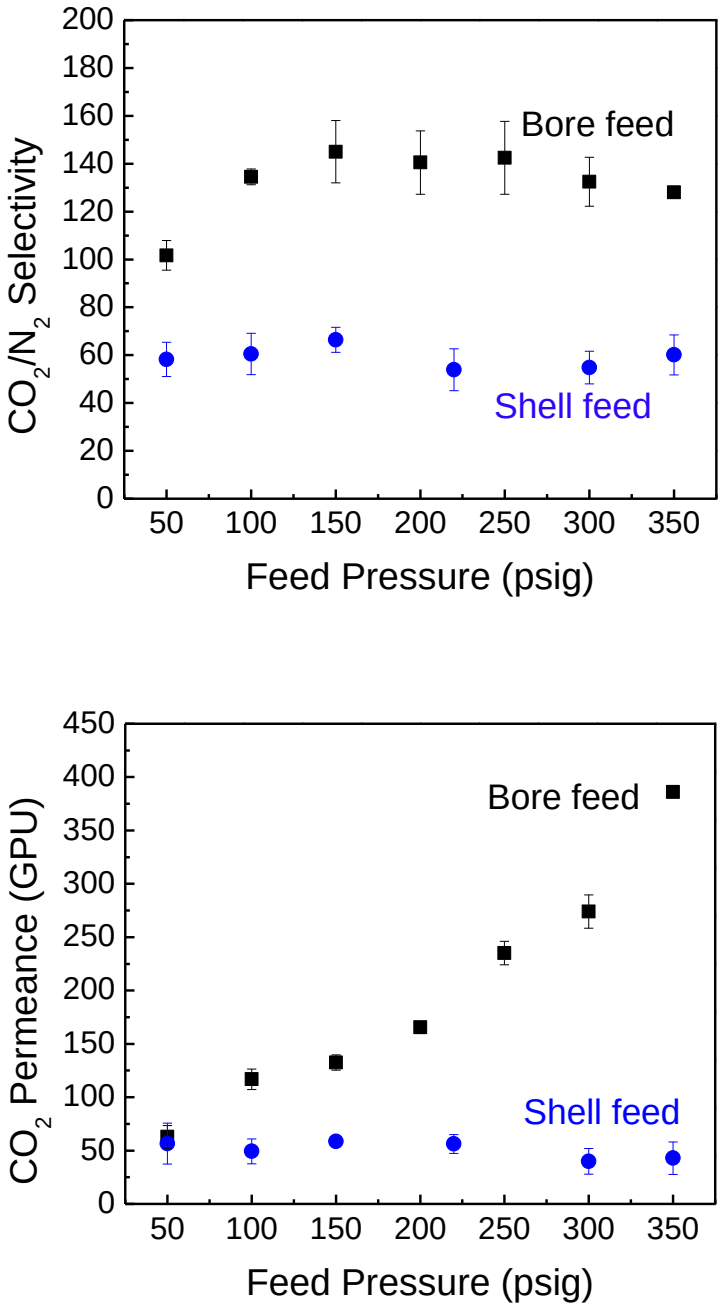

Figure 5.20: Bore versus shell feed permeation results for PDMS post-treated nodular Matrimid® hollow fiber membranes at different pressures. The operating temperature was -40 °C. The feed was a mixture of 20 mol% CO_2/80 mol% N_2. The downstream was at atmospheric pressure.

5.4.2.3 Bore versus shell feed for dense skin hollow fiber membranes

The bore versus shell feed experiment was also carried out on dense skin Matrimid® hollow fiber membranes, in order to compare with the performance of nodular fibers. The same gas mixture (20 mol% CO_2/80 mol% N_2) was introduced at the bore and shell side of the fibers at different temperatures, and the same upstream and downstream pressures were used (The upstream pressure was 100 psig, and the downstream was at atmospheric pressure). Small difference in selectivity and permeance was observed between bore and shell feed (Figure 5.21), suggesting the homogeneous structure of the dense selective layer experienced similar change when the fibers were inflated and pressurized. This evidence indirectly supported the hypothesis that a different morphology of the nodular skin was resulted when the fibers were inflated or pressurized.

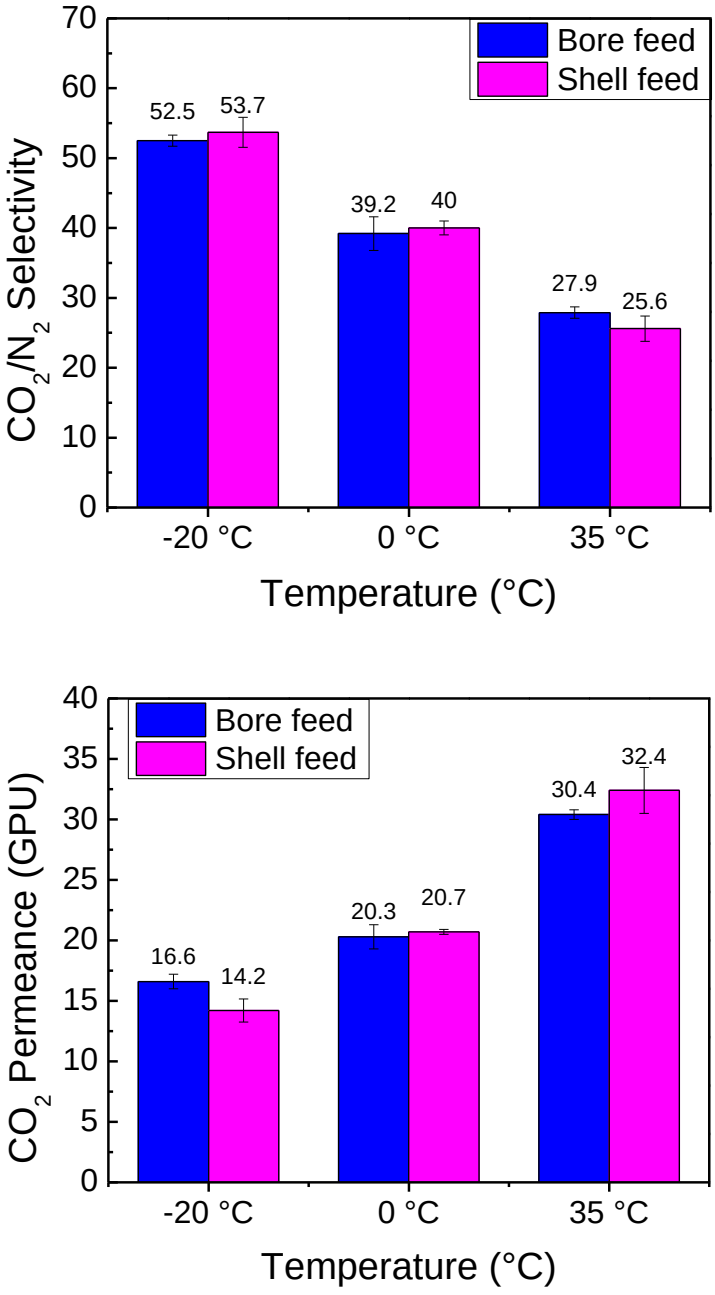

Figure 5.21: Bore versus shell feed permeation results for dense skin Matrimid® hollow fiber membranes at different temperatures. The feed was a mixture of 20 mol% CO_2/80 mol% N_2 at 100 psig. The downstream was at atmospheric pressure.

5.4.3 Indirect evidence II: influence of back pressure

Another piece of evidence to support the hypothesis with regards to the selective layer's nodular morphology of the high performing Matrimid® hollow fiber membranes was obtained by adding back pressure to the shell side of the fibers while exposing the bore side to the CO_2/N_2 binary feed, as is shown in Figure 5.22. The additional back pressure would reduce the enlargement of the inter-nodular domains and alleviate the tension exerted on the inter-nodular tie-chains, as compared to the case without back pressure. The "tightened" inter-nodular domains were expected to reduce membrane separation performance.

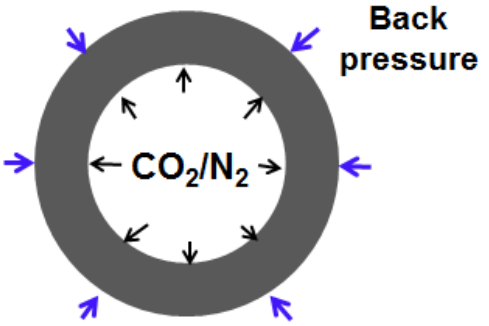

(a)

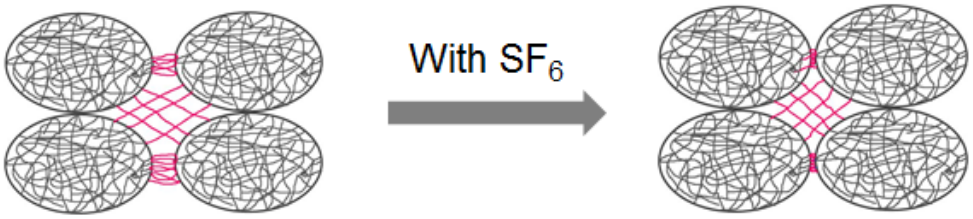

(b)

Figure 5.22: Schematic showing (a) the addition of back pressure on the shell side of the nodular fibers and (b) the resultant morphology of tightened inter-nodular domain.

The back pressure was created by introducing a pure gas to the shell side of the hollow fiber membranes. At first, the non-condensable gases Ar and He was considered due to their low solubility in the membranes, as suggested by their low critical temperatures (Table 5.9). The low uptake of the gases would minimize their influence on the sorption of CO_2 and N_2, and the counter diffusion effects due to the transport of Ar or He from the shell side of the fibers to the bore side could be factored out by the frame of reference analysis. The frame of reference analysis would take into account the influence of bulk (convective) flow on gas permeation, the detailed explanation of which can be found in Chapter 2. However, the already calibrated Gas Chromatography (GC) was using helium as the carrier gas, which made Ar and He undesirable candidates to be introduced to the shell side of the fibers. This was because, in order to calculate the permeance of CO_2 and N_2, the composition of the permeate stream (included CO_2, N_2 and the gas introduced to the shell side) had to be determined; however, the GC was not able to distinguish Ar or He from the carrier gas. Therefore, another candidate, SF_6, was chosen. The permeation of SF_6 through the nodular Matrimid® hollow fiber membranes under the experimental conditions (-40 °C) was not measureable, so the counter diffusion effect was fortunately negligible. Moreover, although the critical temperature of SF_6 was high (318.7 °C, as compared to 304.2 °C for CO_2), its sorption in the membrane was low. Figures 5.23 and 5.24 show the sorption isotherms of SF_6 in nodular Matrimid® hollow fiber membranes at -20 °C and -40 °C as compared to CO_2 and N_2, and the dual-mode parameters are shown in Tables 5.10 and 5.11. The uptake of SF_6 was slightly higher than N_2, but much lower than CO_2. This was attributed to the large size and bulky shape of SF_6 (Table 5.9), possibly making it excluded from most of the Langmuir sorption sites (It

would take extremely high energy to create a sorption site), as suggested by its low Langmuir sorption capacity ($C_H^{'}$). Therefore, SF_6 was an ideal candidate to compress the fibers from the shell side.

Table 5.9: Size and critical temperature (T_c) of different gases [25]

	Size ($\dot{A}$)	Tc (°C)
He	2.6	5.3
CO_2	3.3	304.2
Ar	3.5	151.0
N_2	3.64	126.2
C_2H_4	3.75	282.4
CH_4	3.8	190.7
C_2H_6	3.9	305.4
SF_6	5.5	318.7

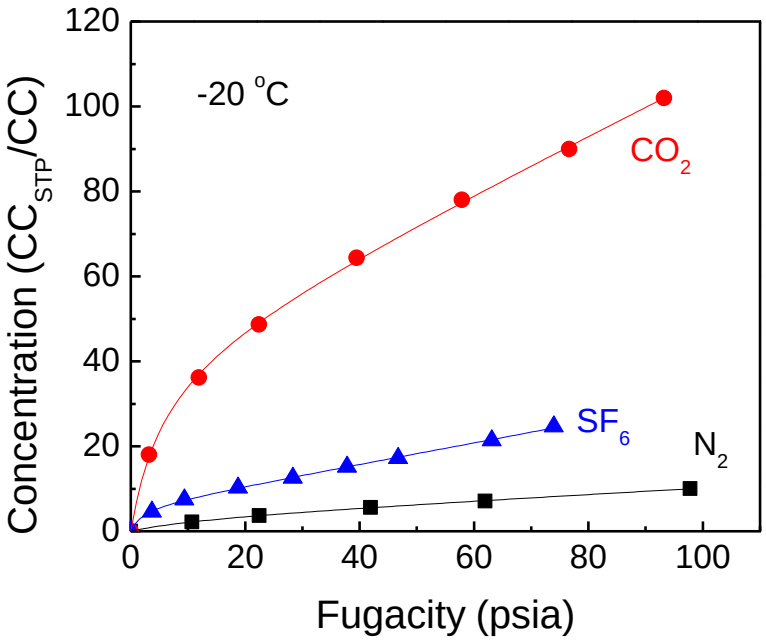

Figure 5.23: Sorption isotherm for SF_6 in nodular Matrimid® hollow fiber membranes at -20 °C as compared to CO_2 and N_2.

Table 5.10: Dual-mode parameters for SF_6 in nodular Matrimid® hollow fiber membranes at -20 °C as compared to CO_2 and N_2

Gas	$C_H'\left(\frac{cm^3[STP]}{cm^3 poly}\right)$	$b\left(\frac{1}{psia}\right)$	$k_D\left(\frac{cm^3[STP]}{cm^3 poly \cdot psia}\right)$
SF_6	6.03 ± 0.4	0.46 ± 0.122	0.25 ± 0.006
CO_2	43.1 ± 1.7	0.17 ± 0.019	0.66 ± 0.019
N_2	17.0 ± 6.1	0.01 ± 0.004	0.01 ± 0.015

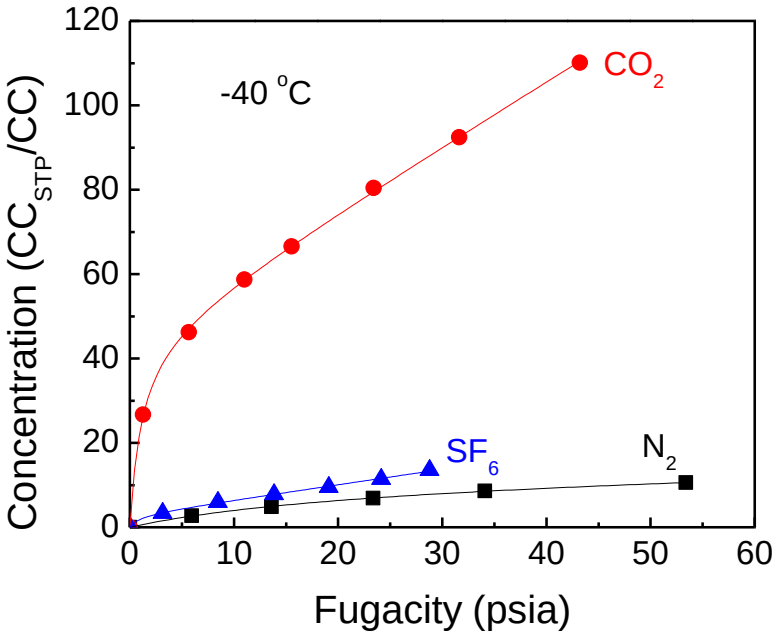

Figure 5.24: Sorption isotherm for SF_6 in nodular Matrimid® hollow fiber membranes at -40 °C as compared to CO_2 and N_2.

Table 5.11: Dual-mode parameters for SF_6 in nodular Matrimid® hollow fiber membranes at -40 °C as compared to CO_2 and N_2

Gas	$C_H'\left(\frac{cm^3[STP]}{cm^3 poly}\right)$	$b\left(\frac{1}{psia}\right)$	$k_D\left(\frac{cm^3[STP]}{cm^3 poly \cdot psia}\right)$
SF_6	2.98 ± 0.6	1.04 ± 0.992	0.36 ± 0.020
CO_2	47.4 ± 1.0	0.82 ± 0.077	1.47 ± 0.025
N_2	14.0 ± 0.5	0.04 ± 0.002	0.03 ± 0.002

The experiment was carried out at -20 °C. The 20 mol% CO_2/80 mol% N_2 mixture was introduced to the bore side of the nodular Matrimid® hollow fiber membranes at 100 psig, and at the same time, pure SF_6 with certain pressure was introduced at the shell side. To maintain SF_6 in the gas phase, its pressure should be lower than its vapor pressure (The vapor pressure of SF_6 at -20 °C is 100.64 psia, Table 5.12 [27]). In this work, SF_6 with a pressure of 50 psia was applied to the shell side of the hollow fiber membranes. The permeance of CO_2 and N_2 through the membrane was obtained by measuring the flow rate of the CO_2, N_2 and SF_6 ternary mixture and by analyzing the ternary composition with GC (Figure 5.25). Note that, the flow rate of the ternary mixture was controlled manually, the value of which would significantly affect the measured permeance of CO_2 and N_2. If the flow rate were too low, the CO_2 and N_2 on the permeate side would accumulate, resulting in lower driving force for permeation; on the contrary, if the flow rate were too high, the composition of CO_2 and N_2 in the ternary stream would be uncertain. Figure 5.26 shows the measured CO_2/N_2 selectivity and CO_2 permeance at different flow rates of the ternary mixture. The results were considered to be reasonable with the permeate flow rate between 3.7 to 6.3 ml/min, as indicated in the shadowed region in the figures. Therefore, the flow rate of the permeate stream was controlled within this range during the experiment.

Table 5.12: Vapor pressures of SF_6 at different temperatures [27]

T (°C)	SF_6 vapor pressure (psi)
35	431.24
20	304.55
0	182.08
-10	136.91
-20	100.64
-30	72.055
-40	50.058

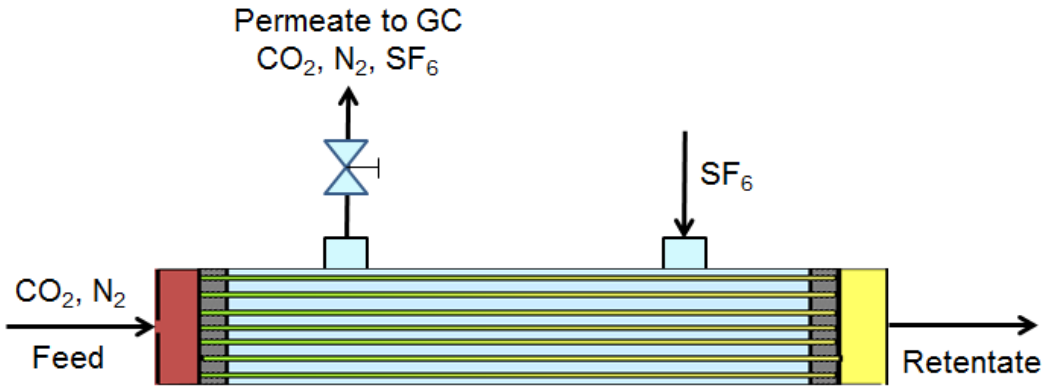

Figure 5.25: Schematic showing the experimental setup for permeation measurement with SF_6 introduced at the shell side.

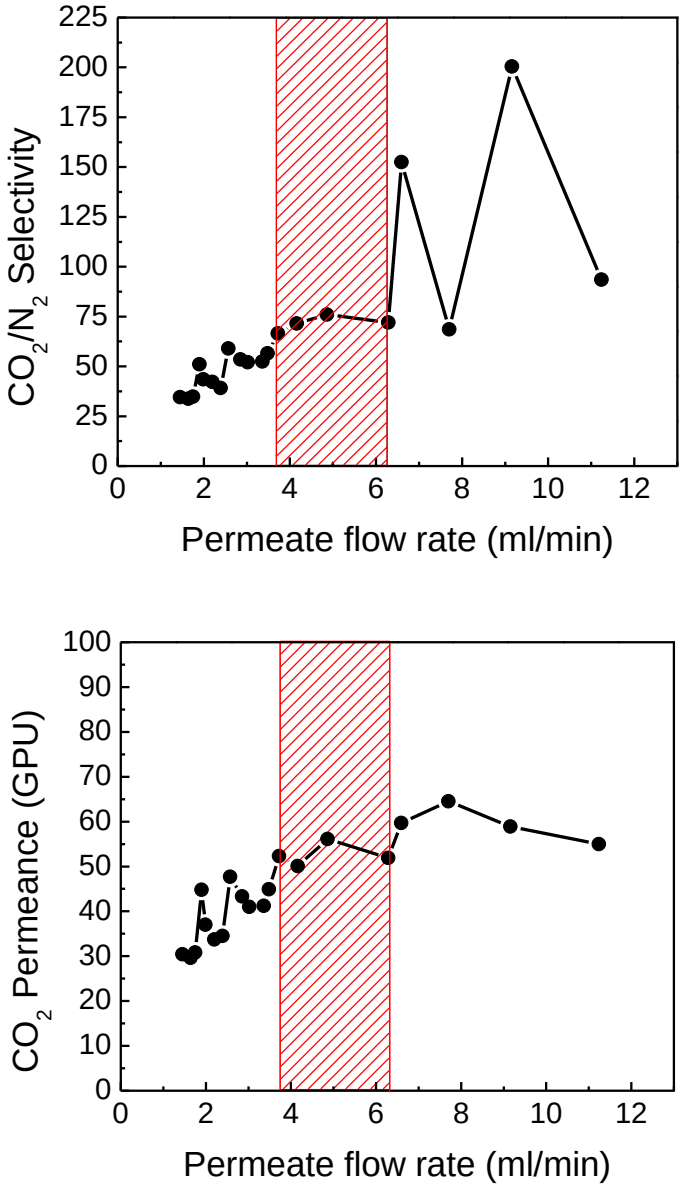

Figure 5.26: Influence of controlled permeate flow rate on the measured CO_2/N_2 selectivity and CO_2 permeance at -20 °C. The feed was a mixture of 20 mol% CO_2/80 mol% N_2 introduced at the bore side. Pure SF_6 was introduced at the shell side with a pressure of 50 psia.

The same experiment was carried out on dense skin Matrimid® hollow fiber membranes as a control group. Experimental results showed that the application of SF_6 on the shell side reduced the selectivity and permeance for both nodular and dense Matrimid® hollow fiber membranes (Table 5.13), but the reduction for the nodular fibers was more pronounced than for the dense fibers. The performance drop for the dense hollow fiber membranes was believed to be caused *only* by the competitive sorption of SF_6. Although the uptake of SF_6 was not high, it still competed with CO_2 and N_2 for the sorption sites. However, the more severe performance drop observed for the nodular fibers was attributed to not only competitive sorption, but also the effect of tightened inter-nodular domains.

Table 5.13: Performance drop of nodular and dense Matrimid® hollow fiber membranes with 50 psia SF_6 on the shell side at -20 °C. The feed was a mixture of 20 mol% CO_2/80 mol% N_2 introduced at the bore side at 100 psig.

	Nodular Fiber	Dense Fiber
CO_2/N_2 Selectivity Drop	24 ± 3 %	15 ± 3 %
CO_2 Permeance Drop	58 ± 4 %	35 ± 2 %

5.4.4 Indirect evidence III: the separate study of sorption and diffusion

The hypothesis proposed in Section 5.3 suggested that the enlarged inter-nodular region for bore feed would result in both increased sorption selectivity and diffusion selectivity, as compared to shell feed. The increased sorption selectivity would arise from increased sorption capacity of the inter-nodular region and the strong competitive power of CO_2 for the additional sorption sites. The increased diffusion selectivity would arise from a local orientation of tie-chains, resulting in better size discrimination capability. In order to separately investigate the influence of the nodular structure on gas sorption and diffusion, special gas pairs were chosen to deconvolute the effects of penetrant condensability (related to sorption) from penetrant size (related to diffusion). The gas pair C_2H_4/CH_4 was chosen to study the effect of the dilation and compression of the nodular skin on membrane sorption selectivity. The C_2H_4 and CH_4 are similar in size, but different in critical temperature (Table 5.9); so the difference in diffusion would be minimized and *the sorption selectivity would be the main contributing factor to the permselectivity*. On the contrary, the gas pair CO_2/C_2H_6 was chosen to study the effect of the dilation and compression of the nodular skin on membrane diffusion selectivity. The CO_2 and C_2H_6 have similar critical temperatures, but different sizes (Table 5.9); so the difference in sorption would be minimized and *the diffusion selectivity would be the main contributing factor to the permselectivity*.

5.4.4.1 C_2H_4/CH_4

To verify that C_2H_4 and CH_4 have different solubility in the nodular Matrimid® hollow fiber membranes, pure C_2H_4 and CH_4 sorption measurements were carried out.

The sorption isotherms at -20 °C and -40 °C are shown in Figure 5.27. The uptake of C_2H_4 was much higher than CH_4, which was consistent with its higher critical temperature.

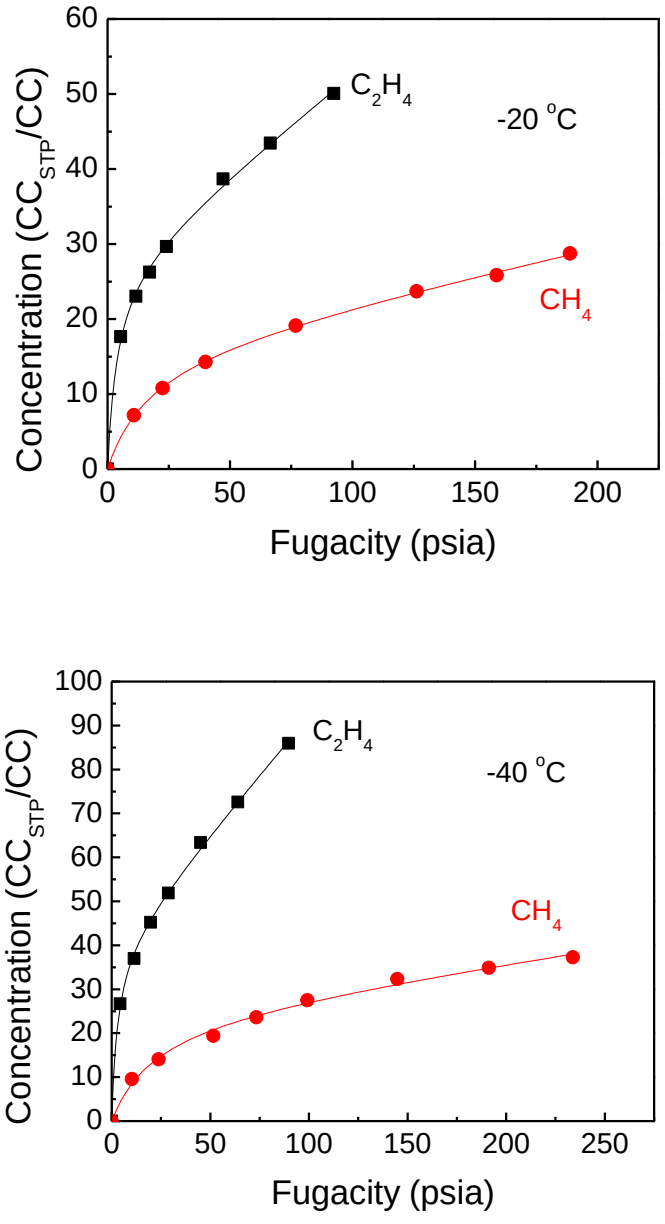

Figure 5.27: Sorption isotherms for C_2H_4 and CH_4 in nodular Matrimid® hollow fiber membranes at -20 °C and -40 °C.

A mixture of 20 mol% C_2H_4/80 mol% CH_4 was introduced at the bore and shell side of the nodular Matrimid® hollow fiber membranes at -40 °C. The upstream pressure was increased from 50 psig to 350 psig, with stepped increments of 50 psig. At each pressure, one day was allowed before the pressure was increased to the next. The downstream was at atmospheric pressure. A higher C_2H_4/CH_4 selectivity was obtained with bore feed (Figure 5.28), which was 1.2-1.6 times of the selectivity for shell feed at the same upstream pressure (Table 5.14). The selectivity difference between bore and shell feed was more pronounced at higher upstream pressures. As discussed above, the permselectivity of C_2H_4/CH_4 was mainly contributed by the sorption selectivity. The higher selectivity for bore feed suggested the dilated inter-nodular region gave rise to higher sorption selectivity. The permeance of C_2H_4 for bore feed was also higher, which was 1.3-8.6 times of shell feed.

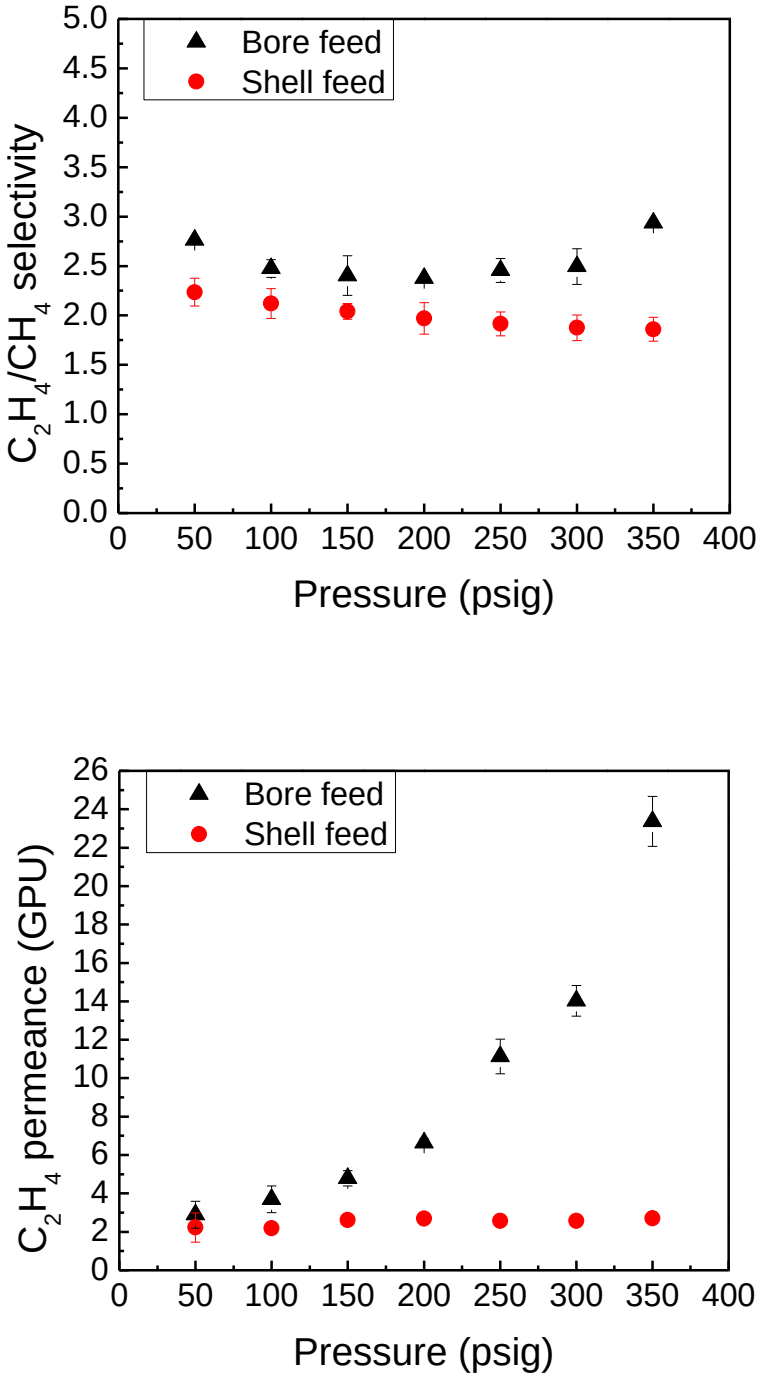

Figure 5.28: Permeation results for 20 mol% C_2H_4/80 mol% CH_4 in PDMS post-treated nodular Matrimid® hollow fiber membranes at -40 °C. The downstream was at atmospheric pressure.

Table 5.14: Selectivity and permeance difference between bore and shell feed for 20 mol% C_2H_4/80 mol% CH_4 in nodular Matrimid® hollow fiber membranes at -40 °C

Feed pressure (psig)	50	100	150	200	250	300	350
$\frac{\alpha(bore)}{\alpha(shell)}$	1.2x	1.2x	1.2x	1.2x	1.3x	1.3x	1.6x
$\frac{Perm(bore)}{Perm(shell)}$	1.3x	1.7x	1.8x	2.5x	4.3x	5.5x	8.6x

5.4.4.2 CO_2/C_2H_6

Although CO_2 and C_2H_6 have similar critical temperatures, it was still important to verify their solubility in the membranes. The CO_2 and C_2H_6 pure gas sorption measurements were carried out on nodular Matrimid® hollow fiber membranes, and the sorption isotherms at -20 °C and -40 °C are shown in Figure 5.29. It was interesting to note that the sorption isotherms for CO_2 and C_2H_6 were not exactly the same, with the uptake of CO_2 higher than C_2H_6. This was probably due to the larger size of C_2H_6, which required higher energy to create a sorption site. However, it will be shown later that the diffusion selectivity for CO_2/C_2H_6 was much higher than the sorption selectivity, indicating the CO_2/C_2H_6 transport in the nodular Matrimid® hollow fiber membranes was diffusion dominant.

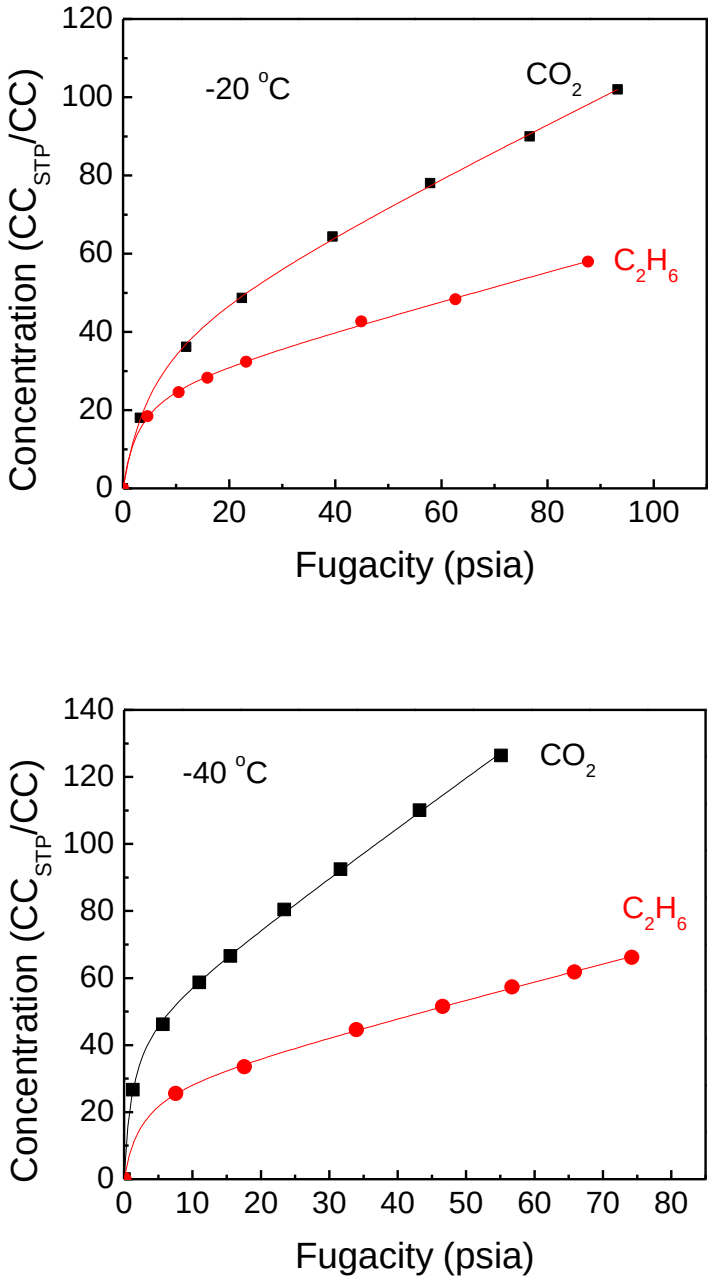

Figure 5.29: Sorption isotherms for CO_2 and C_2H_6 in nodular Matrimid® hollow fiber membranes at -20 °C and -40 °C.

A mixture of 50 mol% CO_2/50 mol% C_2H_6 was introduced at the bore and shell side of the nodular Matrimid® hollow fiber membranes at -40 °C. The upstream pressure was increased from 40 psig to 70 psig, with stepped increments of 10 psig. Such low pressure range was selected in order to avoid plasticization, due to the high sorption of CO_2 and C_2H_6. At each pressure, one day was allowed before the pressure was increased to the next. The permeation results for bore and shell feed are shown in Figure 5.30. The bore feed displayed higher selectivity and higher permeance than shell feed. By factoring out the sorption selectivity from the permselectivity, the diffusion selectivity was obtained, as is shown in Table 5.13. The CO_2/C_2H_6 diffusion selectivity was much higher than the sorption selectivity (The CO_2/C_2H_6 sorption selectivity at -40C was 2.2, obtained from the sorption isotherm), suggesting the separation of CO_2/C_2H_6 was diffusion dominant. The higher diffusion selectivity for bore feed indicates better size discrimination capability (Table 5.15). Although the dilation of the inter-nodular region was compromised due to the low upstream pressure, as compared to the C_2H_4/CH_4 case, the CO_2/C_2H_6 diffusion selectivity for bore feed was still 1.3-1.9 times of shell feed, and the permeance was 1.7-4.2 times higher (Table 5.16).

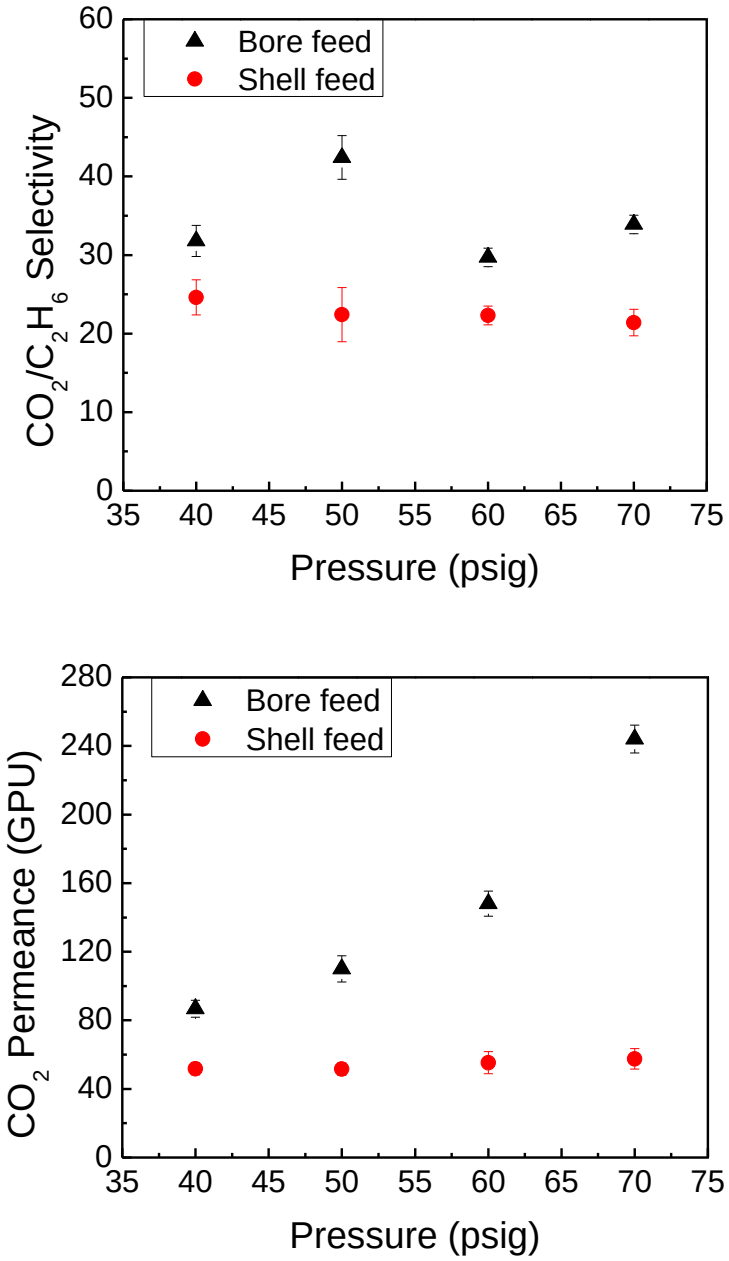

Figure 5.30: Permeation results for 50 mol% CO_2/50 mol% C_2H_6 in PDMS post-treated nodular Matrimid® hollow fiber membranes at -40 °C. The downstream was at atmospheric pressure.

Table 5.15: Diffusion selectivity for CO_2/C_2H_4 in PDMS post-treated nodular Matrimid® hollow fiber membranes at -40 °C. The feed was 50 mol% CO_2/50 mol% C_2H_4

Feed pressure (psig)	40	50	60	70
Bore feed	14.5	19.3	13.5	15.4
Shell feed	11.2	10.2	10.1	9.7

Table 5.16: Selectivity and permeance difference between bore and shell feed for 50 mol% CO_2/50 mol% C_2H_6 in nodular Matrimid® hollow fiber membranes at -40 °C

Feed pressure (psig)	40	50	60	70
$\frac{\alpha(bore)}{\alpha(shell)}$	1.3x	1.9x	1.3x	1.6x
$\frac{Perm(bore)}{Perm(shell)}$	1.7x	2.1x	2.7x	4.2x

5.4.4.3 *C_2H_4/CH_4 and CO_2/C_2H_6 for dense hollow fiber membranes*

The same C_2H_4/CH_4 and CO_2/C_2H_6 gas mixtures were used to test the performance of dense Matrimid® hollow fiber membranes. Mixtures of 20 mol% C_2H_4/80 mol% CH_4 and 50 mol% CO_2/50 mol% C_2H_6 were applied to the bore and shell side of the fibers. The upstream pressure for C_2H_4/CH_4 was 100 psig, and for CO_2/C_2H_6, was 50 psig. Small difference in selectivity and permeance was observed between bore and shell

feed (Figure 5.31 and Table 5.17), suggesting the homogeneous dense selective layer displayed similar gas sorption and diffusion properties whether it was dilated or compressed.

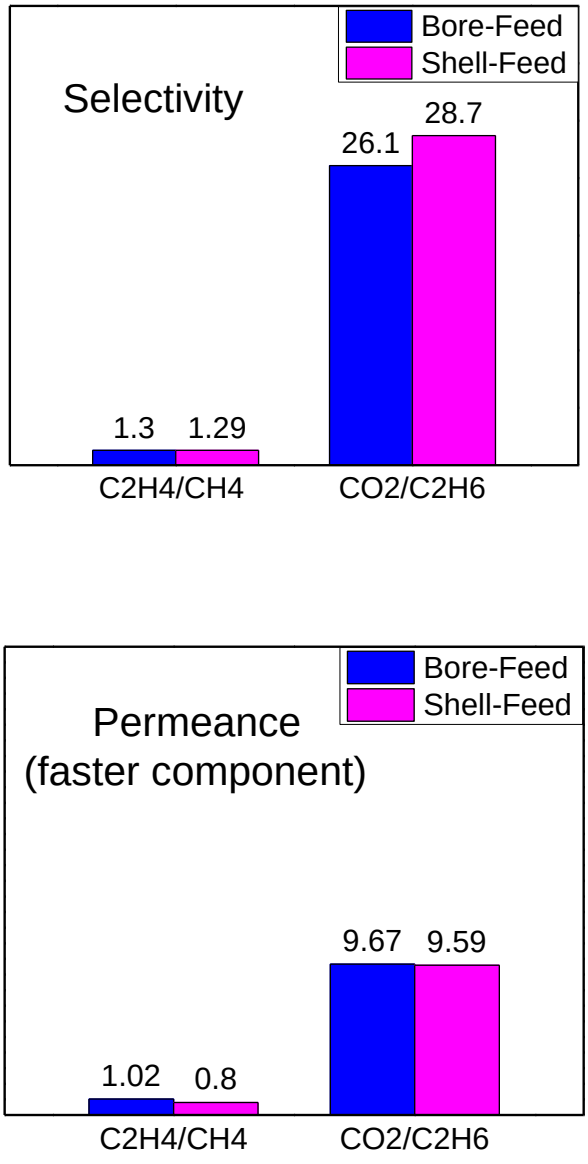

Figure 5.31: Permeation results for C_2H_4/CH_4 and CO_2/C_2H_6 in dense Matrimid® hollow fiber membranes at -20 °C. The feeds were 20 mol% C_2H_4/80 mol% CH_4 (100 psig) and 50 mol% CO_2/50 mol% C_2H_6 (40 psig). The downstream was at atmospheric pressure.

Table 5.17: Selectivity and permeance difference between bore and shell feed for C_2H_4/CH_4 and CO_2/C_2H_6 in dense Matrimid® hollow fiber membranes at -20 °C

	C_2H_4/CH_4	CO_2/C_2H_6
$\frac{\alpha(bore)}{\alpha(shell)}$	1.0x	0.9x
$\frac{Perm(bore)}{Perm(shell)}$	1.3x	1.0x

5.5 Summary

The PDMS post-treated nodular Matrimid® hollow fiber membranes showed a combination of high selectivity and high permeance for the penetrant pair CO_2/N_2 at cold conditions. Under constant feed pressure, the selectivity increased with a decrease of temperature; and the permeance dropped at first, but the trend was reversed at lower temperatures when the activity of CO_2 was high. At constant temperature, the membrane permeance increased with the increase of feed pressure, while minimal change in selectivity was observed. A higher sorption of both CO_2 and N_2 was obtained at lower temperatures. The PDMS post-treated nodular Matrimid® fibers displayed higher selectivity and higher permeance than the dense skin fibers, especially at cold conditions. The reason was attributed to the different morphologies of the membrane selective skin layers. The nodular selective layer was hypothesized to be heterogeneous, with the inter-nodular domains easy to be dilated; whereas the dense selective layers were assumed to be isotropic, and pressurization from the bore and from the shell side of the fibers would not cause much difference. The higher selectivity for the bore-fed nodular fibers was hypothesized result from enhanced sorption selectivity as well as enhanced diffusion

selectivity due to the dilation and orientation of the inter-nodular domains. Enhanced sorption selectivity was believed to arise from increased sorption capacity due to the introduction of more Langmuir sites coupled with the stronger competitive power of CO_2 molecules for the additional sorption sites. Enhanced diffusion selectivity was believed to arise from a local orientation of polymer chain segments due to the uniaxial draw of the selective layer, resulting in increased size discrimination capability.

To support the proposed hypothesis, direct characterization was found to be very challenging due to the difficulties in tailoring the ultra-thin selective skin layer from the bulk support layer and the creation of the realistic stressed conditions. Three indirect experiments were carried out instead. By dilating or compressing the nodular selective layer, the sorption capacity of the inter-nodular domains and the orientation of the polymer chain segments were assumed to be changed accordingly; and the subsequent gas separation properties of the membrane were found to be consistent with the hypothesis. Moreover, the same experiments were carried out on dense Matrimid® hollow fiber membranes. Similar results were obtained whether the homogeneous skin layer was dilated or compressed.

5.6 References

[1] P. Raymond, W. Koros, and D. Paul, Comparison of mixed and pure gas permeation characteristics for CO_2 and CH_4 in copolymers and blends containing methyl methacrylate units, Journal of membrane science, vol. 77, pp. 49-57, 1993.

[2] B. J. Story and W. Koros, Comparison of three models for permeation of CO_2/CH_4 mixtures in poly(phenylene oxide), Journal of Polymer Science Part B: Polymer Physics, vol. 27, pp. 1927-1948, 1989.

[3] C. E. Powell and G. G. Qiao, Polymeric CO_2/N_2 gas separation membranes for the capture of carbon dioxide from power plant flue gases, Journal of Membrane Science, vol. 279, pp. 1-49, 2006.

[4] D. Hasse, S. Kulkarni, E. Sanders, E. Corson, and J.-P. Tranier, CO_2 capture by sub-ambient membrane operation, Energy Procedia, vol. 37, pp. 993-1003, 2013.

[5] M. Mulder, Basic principles of membrane technology, 2nd ed. Dordrecht: Kluwer Academic Publishers, 1996.

[6] O. A. Hougen, K. M. Watson, and R. A. Ragatz, Chemical process principles - Part II : thermodynamics, 2nd ed. New York: John Wiley & Sons, Inc., 1964.

[7] C. D. Hodgman, CRC Handbook of chemistry and physics, 44th ed. UK: CRC Press, Inc., 1963.

[8] N. A. Lange and J. A. Dean, Lange's handbook of chemistry, 10th ed. New York: McGraw-Hill Inc., 1969.

[9] T. C. Merkel, H. Lin, X. Wei, and R. Baker, Power plant post-combustion carbon dioxide capture: An opportunity for membranes, Journal of Membrane Science, vol. 359, pp. 126-139, 2010.

[10] A. K. Ghosh, B.-H. Jeong, X. Huang, and E. Hoek, Impacts of reaction and curing conditions on polyamide composite reverse osmosis membrane properties, Journal of Membrane Science, vol. 311, pp. 34-45, 2008.

[11] L. M. Robeson, The upper bound revisited, Journal of Membrane Science, vol. 320, pp. 390-400, Jul 2008.

[12] L. M. Robeson, Correlation of separation factor versus permeability for polymeric membranes, Journal of Membrane Science, vol. 62, pp. 165-185, Oct 1991.

[13] W. J. Koros and D. Paul, Design considerations for measurement of gas sorption in polymers by pressure decay, Journal of Polymer Science: Polymer Physics Edition, vol. 14, pp. 1903-1907, 1976.

[14] T. T. Moore and W. J. Koros, Gas sorption in polymers, molecular sieves, and mixed matrix membranes, Journal of applied polymer science, vol. 104, pp. 4053-4059, 2007.

[15] W. Koros, A. Chan, and D. Paul, Sorption and transport of various gases in polycarbonate, Journal of Membrane Science, vol. 2, pp. 165-190, 1977.

[16] R. Kesting, The four tiers of structure in integrally skinned phase inversion membranes and their relevance to the various separation regimes, Journal of applied polymer science, vol. 41, pp. 2739-2752, 1990.

[17] G. Dong, H. Li, and V. Chen, Plasticization mechanisms and effects of thermal annealing of Matrimid hollow fiber membranes for CO_2 removal, Journal of Membrane Science, vol. 369, pp. 206-220, 2011.

[18] G. K. Fleming and W. J. Koros, Dilation of polymers by sorption of carbon-dioxide at elevated pressures. 1. Silicon-rubber and unconditioned polycarbonate, Macromolecules, vol. 19, pp. 2285-2291, Aug 1986.

[19] G. K. Fleming and W. J. Koros, Carbon-dioxide conditioning effects on sorption and volume dilation behavior for bisphenol-A-polycarbonate, Macromolecules, vol. 23, pp. 1353-1360, Mar 1990.

[20] M. El-Hibri and D. Paul, Effects of uniaxial drawing and heat-treatment on gas sorption and transport in PVC, Journal of applied polymer science, vol. 30, pp. 3649-3678, 1985.

[21] M. El-Hibri and D. Paul, Gas transport in poly (vinylidene fluoride): effects of uniaxial drawing and processing temperature, Journal of applied polymer science, vol. 31, pp. 2533-2560, 1986.

[22] L. Wang and R. S. Proter, On the CO_2 permeation of uniaxially drawn polymers, Journal of Polymer Science: Polymer Physics Edition, vol. 22, pp. 1645-1653, 1984.

[23] R. Barker, R. Tsai, and R. Willency, Entropy correlation theory and diffusion measurements for oriented polymers, in Journal of Polymer Science: Polymer Symposia, 1978, pp. 109-129.

[24] E. A. McGonigle, J. Liggat, R. Pethrick, S. Jenkins, J. Daly, and D. Hayward, Permeability of N_2, Ar, He, O_2, and CO_2 through as-extruded amorphous and

biaxially oriented polyester films: Dependence on chain mobility, Journal of Polymer Science Part B: Polymer Physics, vol. 42, pp. 2916-2929, 2004.

[25] M. Rungta, Ph.D. thesis, Carbon molecular sieve dense film membranes for ethylene/ethane separations, Georgia Institute of Technology, 2012.

[26] h. F. Stallmach, Fundamentals of pulsed field gradient nuclear magnetic resonance, Fakultat fur Physik und Geowissenschaften, 2004.

[27] NIST Chemistry Webbook, Standard Reference Database Number 69.

CHAPTER 6

SUB-AMBIENT TEMPERATURE GAS TRANSPORT IN 6FDA/BPDA-DAM HOLLOW FIBER MEMBRANES

This chapter discusses the possible identification of a second generation, improved membrane material for sub-ambient temperature flue gas CO_2 capture. The high free volume, rigid 6FDA/BPDA-DAM was chosen as a potential candidate. Section 6.1 includes the properties of 6FDA/BPDA-DAM (1:1). Section 6.2 presents the preliminary investigation of defect free 6FDA/BPDA-DAM hollow fiber membrane and its viability for being operated at cold conditions. The 6FDA/BPDA-DAM (1:1) hollow fiber membranes for the preliminary study showed better CO_2/N_2 separation properties than Matrimid® at -20 °C. The formation protocols of defect free 6FDA/BPDA-DAM and the resultant membrane separation properties are discussed in Section 6.3. Section 6.4 presents the formation protocols of nodular 6FDA/BPDA-DAM hollow fiber membranes. The membrane performance at cold conditions was compared with dense 6FDA/BPDA-DAM and nodular Matrimid® hollow fiber membranes.

6.1 Overview of 6FDA/BPDA-DAM

The interest in 6FDA-based polyimides as membrane materials has been growing in recent years, due to the high rigidity and versatility of monomer choices of such materials. Moreover, the presence of bulky $-CF_3$ groups in the rigid polymer backbone hinders the packing of the polymer chains, leading to a higher fractional free volume

(FFV) compared to Matrimid®. The higher fraction free volume contributes to higher membrane permeability [1, 2]. In this work, 6FDA/BPDA-DAM (1:1) was chosen as a potential candidate for the second generation of membrane material for cold conditions CO_2/N_2 separation. This material has been well studied in the literature as well as in the Koros Research Group in terms of its physical and gas separation properties [3-7], and it has been successfully made into asymmetric hollow fiber configuration with attractive selectivity and permeance. The structure of its repeating unit is shown in Figure 6.1, and its physical and gas transport properties are listed in Tables 6.1 and 6.2.

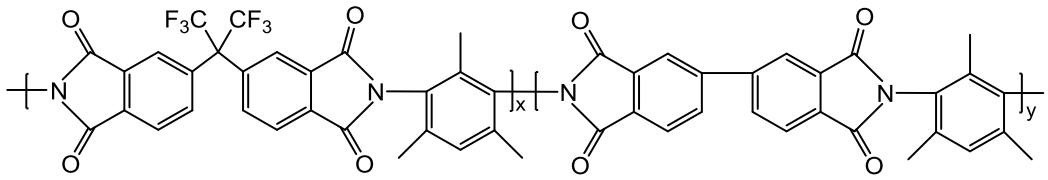

Figure 6.1: The repeating unit of 6FDA/BPDA-DAM. The ratio of X to Y is 1:1.

Table 6.1: Physical properties of 6FDA/BPDA-DAM and Matrimid® [7]

Polymer	Density (g/cm^3)	FFV	Tg (°C)
Matrimid®	1.25	0.110	305
6FDA/BPDA-DAM (1:1)	1.32	0.145	424

Table 6.2: Pure gas transport properties of 6FDA/BPDA-DAM (1:1) dense films at feed pressures < 100 psia and 35 °C [6]

Material	Permeability (Barrer)				Selectivity				
	O_2	CO_2	C_2H_4	C_3H_6	$\frac{O_2}{N_2}$	$\frac{CO_2}{N_2}$	$\frac{CO_2}{CH_4}$	$\frac{C_2H_4}{C_2H_6}$	$\frac{C_3H_6}{C_3H_8}$
6FDA/BPDA-DAM	64	309	46	11.8	4.1	19.8	22	3.3	13

$$1\ Barrer = 1\times10^{-10}\ \frac{cm^3(STP)\cdot cm}{cm^2\cdot s\cdot cmHg}$$

6.2 Preliminary results

In the preliminary study, the cold performance of 6FDA/BPDA-DAM hollow fiber membranes was evaluated at -20 °C. The membranes for the preliminary study were offered by a previous group member Xu [6]. The molecular weight and the polydispersity index of the membrane material are listed in Table 6.3, and the pure gas permeation results at 35 °C are shown in Table 6.4. The pure gas O_2/N_2 selectivity was 4.3 ± 0.1, which was higher than the value of 6FDA/BPDA-DAM dense film (The O_2/N_2 selectivity for 6FDA/BPDA-DAM dense film at 35 °C is 4.1). The higher selectivity for 6FDA/BPDA-DAM hollow fiber membranes than the dense film value is presumably due to the molecular orientation in the skin layer induced by shear stress during spinning [8-11]. It was mentioned in Chapter 4 that, the O_2/N_2 penetrant pair is commonly used to verify a membrane's defect free properties, due to its low degree of interaction with polymer materials. The high O_2/N_2 selectivity for the 6FDA/BPDA-DAM hollow fiber membranes relative to dense films used in the preliminary study suggested the selective layer of the membranes was defect free.

Table 6.3: Molecular weight and polydispersity index of the 6FDA/BPDA-DAM (1:1) for the preliminary study

Polymer	M_w (kDa)	PDI (M_w/M_n)
6FDA/BPDA-DAM (1:1)	160	1.85

Table 6.4: Pure gas permeation results of 6FDA/BPDA-DAM hollow fiber membranes for the preliminary study. The membranes were offered by previous group member Xu [6]. Pure gas permeation tests were carried out at 35 °C

Polymer	$\frac{P_{O_2}}{l}$ (GPU)	$\frac{P_{N_2}}{l}$ (GPU)	α_{O_2/N_2}
6FDA/BPDA-DAM (1:1)	52.6 ± 2.9	12.2 ± 0.7	4.3 ± 0.1

In the preliminary study, the CO_2/N_2 mixed gas permeation measurement of defect free 6FDA/BPDA-DAM hollow fiber membranes were carried out at 35 °C and -20 °C. The feed was 20 mol% CO_2/80 mol% N_2, and was introduced at the bore side at 100 psig. Figure 6.2 shows the membrane selectivity at room and sub-ambient temperatures, as compared to the defect free Matrimid® hollow fiber membranes spun in the current work. A significant increase in the selectivity of 6FDA-DAM/DABA was observed as temperature was decreased from 35 °C to -20 °C, which was more pronounced than for Matrimid® (Figure 6.2a). The different extent of selectivity increment with the decrease of temperature was attributed to the different values of

permeation activation energy for CO_2 and N_2. The larger the difference between E_{p,N_2} and E_{p,CO_2}, the larger the increase in selectivity with the decrease of temperature. As is shown in Table 6.5, the permeation activation energy for CO_2 (E_{p,CO_2}) in 6FDA/BPDA-DAM was very small (1.1 ± 0.2 kJ/mol), due to the similar magnitude of its diffusion activation energy and heats of sorption in the 6FDA/BPDA-DAM material. The smaller value of E_{p,CO_2} contributed to larger difference between the permeation activation energy for N_2 and CO_2, leading to a much higher selectivity increment than Matrimid® with similar drop in temperature. The higher permeance of CO_2 in 6FDA/BPDA-DAM hollow fiber membranes was attributed to the material's higher fractional free volume (Table 6.1), which allowed higher sorption uptake of CO_2 (Figure 6.2b).

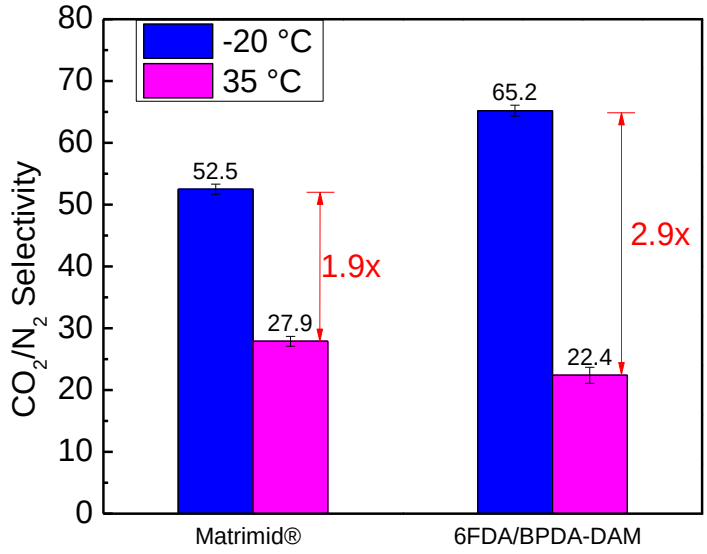

(a)

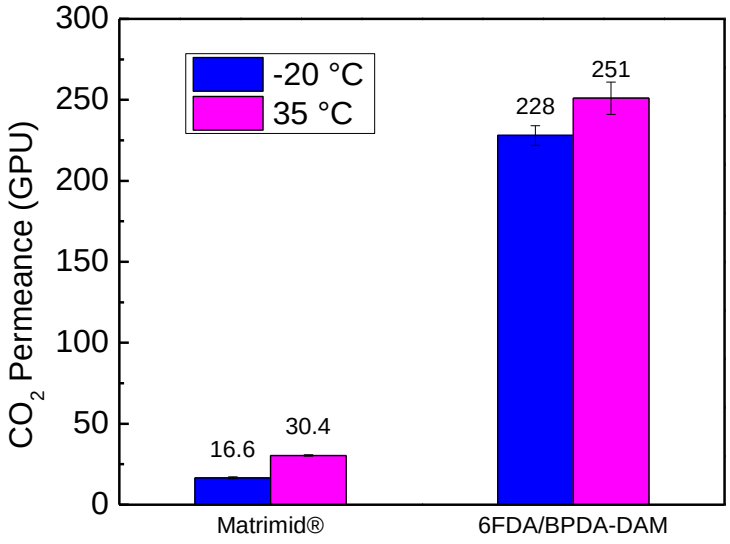

(b)

Figure 6.2: Mixed gas permeation results for defect free Matrimid® and preliminary defect free 6FDA/BPDA-DAM hollow fiber membranes at 35 °C and -20 °C. The 6FDA/BPDA-DAM fibers were obtained from previous group member Xu [6]. The feed was a mixture of 20 mol% CO_2/80 mol% N_2, and was introduced at the bore side at 100 psig.

Table 6.5: Permeation activation energy for defect free Matrimid® and 6FDA/BPDA-DAM hollow fiber membranes. The values were obtained from the 20 mol% CO_2/80 mol% N_2 mixed gas permeation measurement between 35 °C and -20 °C

	Matrimid®	6FDA/BPDA-DAM
E_{p,CO_2}	7.2 ± 0.3 kJ/mol	1.1 ± 0.2 kJ/mol
E_{p,N_2}	14.7 ± 0.2 kJ/mol	13.7 ± 0.2 kJ/mol
$E_{p,N_2} - E_{p,CO_2}$	7.8 ± 0.4 kJ/mol	12.6 ± 0.3 kJ/mol

The sorption isotherms for CO_2 and N_2 in 6FDA/BPDA-DAM at different temperatures are shown in Figure 6.3, which are compared with the sorption isotherms in Matrimid®. At each temperature, a new sample was used to avoid the influence of polymer matrix swelling and conditioning due to the high sorption of CO_2 at high partial pressures on measured gas uptake. The sorption of N_2 was measured first, followed by the sorption measurement of CO_2. The gas uptake in 6FDA/BPDA-DAM was higher than in Matrimid®, indicating higher CO_2 and N_2 solubility in 6FDA/BPDA-DAM. The Langmuir capacity for CO_2 in 6FDA/BPDA-DAM and Matrimid® are compared in Table 6.6. The higher Langmuir saturation capacity for 6FDA/BPDA-DAM is consistent with its higher fractional free volume.

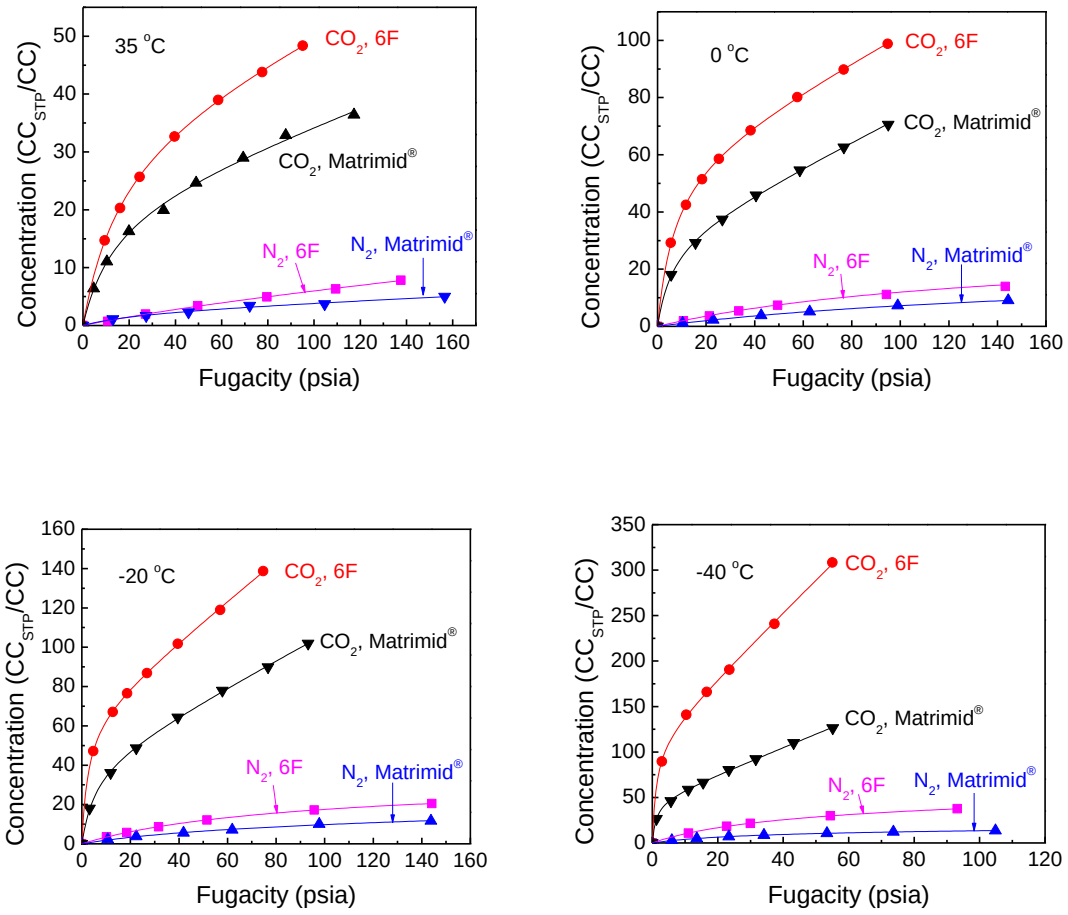

Figure 6.3: The sorption isotherms for CO_2 and N_2 in 6FDA/BPDA-DAM (1:1) at different temperatures as compared to Matrimid®. The points are experimental data and the solid lines are fit of concentration versus pressure data to the dual-mode model. Samples for the sorption measurement were 6FDA/BPDA-DAM (Mw = 123 kDa, PDI = 2.0) polymer. At each temperature, a new sample was used, and the sorption of N_2 was measured first, followed by the sorption measurement of CO_2.

Table 6.6: Langmuir capacity ($C_H^{'}$) for CO_2 in 6FDA/BPDA-DAM (1:1) and Matrimid® at different temperatures

T (°C)	$C_H^{'}(\frac{cm^3[STP]}{cm^3 poly})$	
	6FDA/BPDA-DAM	Matrimid®
35	35.9 ± 1.2	22.5 ± 2.5
0	60.5 ± 1.0	32.8 ± 1.2
-20	65.9 ± 1.0	43.1 ± 1.7
-40	112 ± 3.1	47.4 ± 1.0

6.3 Defect free 6FDA/BPDA-DAM hollow fiber membranes

6.3.1 Spinning of defect free 6FDA/BPDA-DAM hollow fiber membranes

As was shown in Section 6.2, defect free 6FDA/BPDA-DAM (1:1) hollow fiber membranes offered by previous group membrane Xu displayed higher selectivity and higher permeance than defect free Matrimid® hollow fiber membranes at -20 °C, so the 6FDA/BPDA-DAM (1:1) material was considered as a promising candidate for the second generation of membrane materials which could achieve a combination of high permance and high selectivity for the penetrant pair CO_2/N_2 at cold conditions. Unlike the Matrimid® 5218 used in the previous chapters, 6FDA/BPDA-DAM has not been commercially available yet. The 6FDA/BPDA-DAM used in our lab is custom synthesized by the Akron Polymer Systems. Obtaining similar polymer molecular weight and molecular weight distribution from different synthesis batches remain issues for

consistent lab-scale hollow fiber spinning. The different batches of 6FDA/BPDA-DAM polymers possess somewhat different properties, which could affect the resultant hollow fiber membranes performance. To avoid the influence of different material properties on final membrane behaviors, the same batch of 6FDA/BPDA-DAM (1:1) was used in the current work for the formation of defect free and nodular hollow fiber membranes. The molecular weight and polydispersity index of the polymer used in the current work are shown in Table 6.7.

Table 6.7: Molecular weight and polydispersity index of 6FDA/BPDA-DAM (1:1) used in the current work

Polymer	Mw (kDa)	PDI (M_w/M_n)
6FDA/BPDA-DAM (1:1)	123	2.0

6.3.1.1 First attempt to form defect free 6FDA/BPDA-DAM hollow fiber membranes

The 6FDA/BPDA-DAM is more "hydrophilic" than Matrimid®, which requires more non-solvents for phase separation on the same level of polymer concentration. On the ternary phase diagram, the binodal line for 6FDA/BPDA-DAM is somewhat closer to the non-solvent vertex. Due to the need of more non-solvents to phase separate, slower phase separation than Matrimid® should be expected. Therefore, the determination of the initial dope composition is critical for the formation of desirable hollow fiber membranes, and the spinning conditions are secondary factors to consider.

The dope composition and spinning conditions used by Xu for the successful formation of defect free 6FDA/BPDA-DAM hollow fiber membranes from a different batch of polymer (Mw = 160 kDa, PDI = 1.85) were referred to as a guide in the current work [6]. The binodal line for the polymer used in the current work was determined via the "cloud point" technique, detailed description of which can be found in Chapter 2. Specifically, three polymer concentrations were chosen: 18 wt.%, 20 wt.% and 22 wt.%. The NMP and THF were selected as the solvents, with the concentration of THF fixed at 10 wt.%; and ethanol was selected as the non-solvent. At each polymer concentration, a series of dope samples with increasing ethanol contents (and accordingly decreasing NMP contents) were made. The dope samples were then placed on a roller for more than one week until they are well mixed. The dope samples with a composition sitting in the one-phase region were transparent, whereas those with a composition sitting in the two-phase region appeared cloudy. The composition on the phase boundary was the "cloud point", and all the cloud points were connected to form an approximate binodal line. Figure 6.4 shows the binodal lines for the 6FDA/BPDA-DAM (1:1) used in Xu's work and in the current work. The binodal line for the polymer used in the current work was slightly closer to the non-solvent vertex. However, the difference between the two binodal lines was not significant, so the same dope composition as Xu's dope was used in my first spinning attempt (Table 6.8).

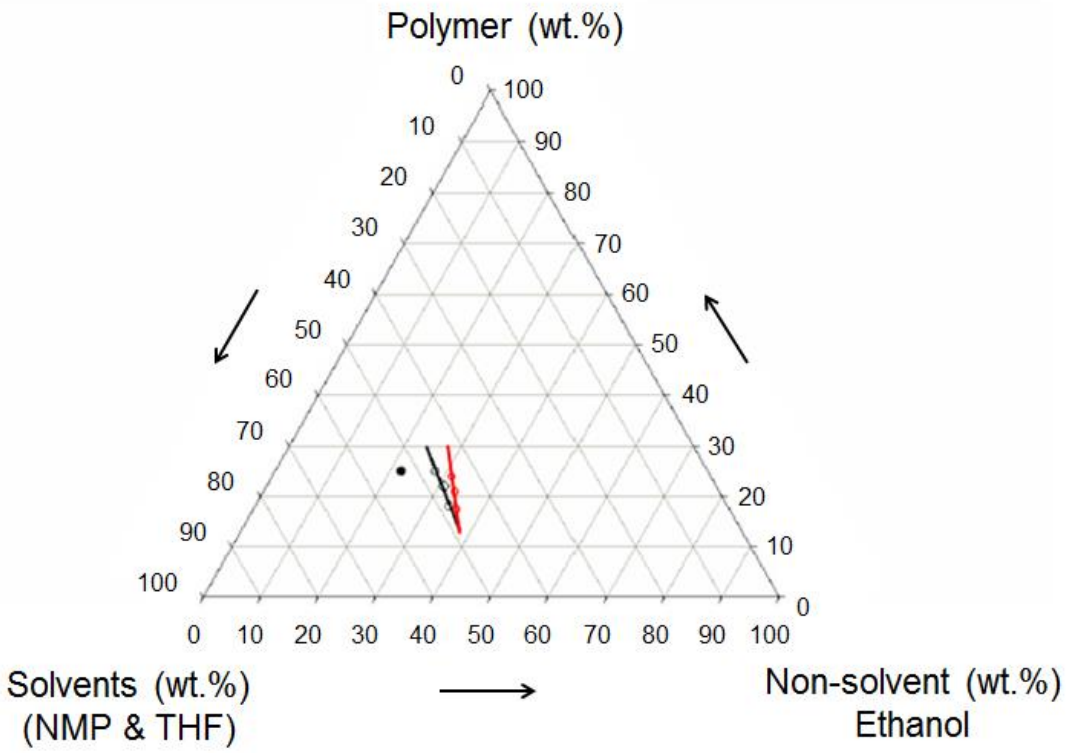

Figure 6.4: Comparison of the binodal lines for the 6FDA/BPDA-DAM(1:1) used in Xu's work and in the current work. The black line is the binodal line for Xu's work, and the red line is the binodal line for the current work. Open circles represent cloud points, and the solid circle represents the initial dope composition.

Table 6.8: Dope composition for the 1st spinning of defect free 6FDA/BPDA-DAM hollow fiber membranes

Component	wt.%
6FDA/BPDA-DAM	25
NMP	43
THF	10
Ethanol	22

The first spinning attempt was not successful. A hollow fiber shape of membrane could not be produced no matter how the spinning conditions were changed. The resultant "fibers" had alternating large and small segments. The reason was attributed to low dope viscosity and slow phase separation in the water quench bath.

6.3.1.2 Second attempt to spin defect free 6FDA/BPDA-DAM hollow fiber membranes

In the 2nd attempt to spin defect free 6FDA/BPDA-DAM hollow fiber membranes, the aim was to increase the dope viscosity and the phase separation rate. Lithium nitrate ($LiNO_3$) was introduced to the dope as an additive to assist phase separation. Lithium nitrate is generally considered a non-solvent, which can complex with the solvent NMP molecules in the dope [6]. In the water quench bath, the complex dissociates and accelerates phase separation. A 6.5 wt.% lithium nitrate level had been used successfully by several researchers in the past [6, 12, 13], so the same concentration was chosen for the current work. Since lithium nitrate can significantly increase the dope viscosity, a lower polymer concentration (20 wt.%, as compared to 25 wt.%) was selected. The 20 wt.% polymer concentration was used by Xu in his successful spinning of defect free 6FDA/BPDA-DAM with $LiNO_3$ contained in the dope [6]. The determination of the polymer concentration was based on visual observation of the dope viscosity to create a dope with the viscosity of honey ($\mu \sim 10^4 cP$).Table 6.9 lists the dope composition for the 2nd spinning of defect free 6FDA/BPDA-DAM hollow fiber membranes. In the 2nd spinning attempt, defect free membranes were successfully formed, and the spinning conditions are listed in Table 6.10. A high spinneret temperature (70 °C) was used to accelerate the evaporation of volatile dope components,

and a high water quench temperature (50 °C) was used to accelerate phase separation. The SEM images of the resultant fiber's cross section and the selective skin layer are shown in Figure 6.5.

Table 6.9: Dope composition for the 2nd spinning of defect free 6FDA/BPDA-DAM hollow fiber membranes

Component	wt.%
6FDA/BPDA-DAM	20
NMP	47.5
THF	10
Ethanol	16
$LiNO_3$	6.5

Table 6.10: Spinning conditions for the 2nd attempt to form defect free 6FDA/BPDA-DAM hollow fiber membranes

Spinning parameter	Value
Dope flow rate	180 ml/h
Bore flow rate	60 ml/h
Bore fluid composition	85%/15% NMP/H_2O
Take-up rate	30 m/min
Quench temperature	49 °C
Spinneret temperature	70 °C
Air gap height	10, 15, 20 cm
Room temperature	25 °C
Relative humidity	33-36 %

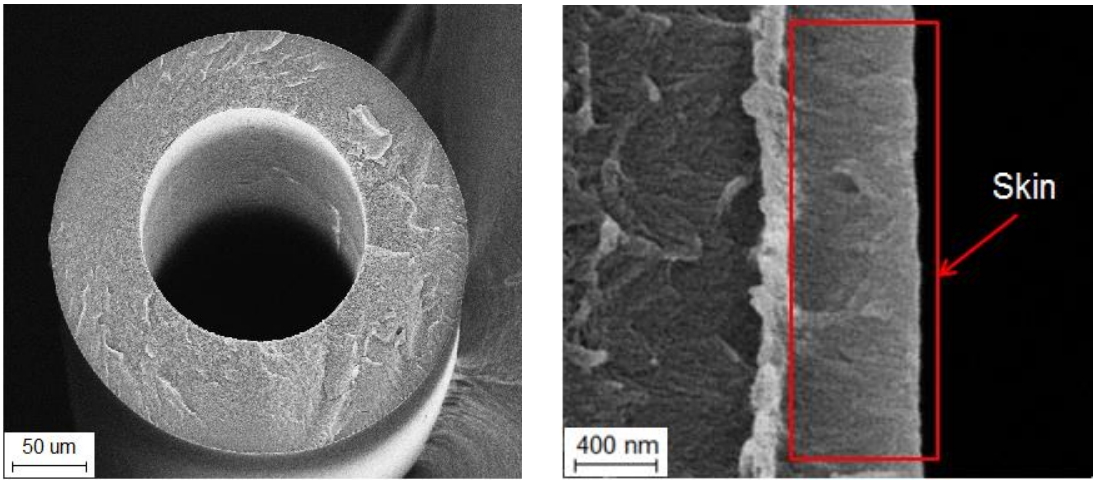

(a) (b)

Figure 6.5: SEM images of defect free 6FDA/BPDA-DAM hollow fiber membranes formed in the 2nd spinning attempt. (a) Overview of the cross-section, (b) selective skin layer.

6.3.2 Permeation in defect free 6FDA/BPDA-DAM hollow fiber membranes

6.3.2.1 Pure gas permeation

Skin integrity of the defect free 6FDA/BPDA-DAM hollow fiber membranes spun in the current work was confirmed by permeating pure O_2, N_2 and CO_2 at 35 °C. Feed pressure for O_2 and N_2 was 100 psig; and for CO_2, 50 psig. The O_2/N_2 selectivity was 3.93 ± 0.11 (Table 6.11), which was higher than 90 % of the 6FDA/BPDA-DAM dense film value, suggesting the hollow fiber membranes were defect free. (The O_2/N_2 selectivity of 6FDA/BPDA-DAM dense film at 35 °C is 4.1 [2]). The pure gas permeation results were also compared with Matrimid® hollow fiber membranes, as is shown in Figure 6.6. The selectivity of defect free 6FDA/BPDA-DAM hollow fiber membranes was lower than Matrimid® hollow fiber membranes (Figure 6.6a), but the

permeance was much higher (Figure 6.6b). This was consistent with the dense film results.

Table 6.11: Pure gas permeation results for defect free 6FDA/BPDA-DAM hollow fiber membranes at 35 °C. Feed pressure for O_2 and N_2 was 100 psig; for CO_2, 50 psig. The feed was introduced at the bore side

$\frac{P_{O_2}}{l}$ (GPU)	$\frac{P_{N_2}}{l}$ (GPU)	$\frac{P_{CO_2}}{l}$ (GPU)	α_{O_2/N_2}	α_{CO_2/N_2}
82.8 ± 4	21.1 ± 0.5	498 ± 8	3.93 ± 0.11	23.7 ± 0.1

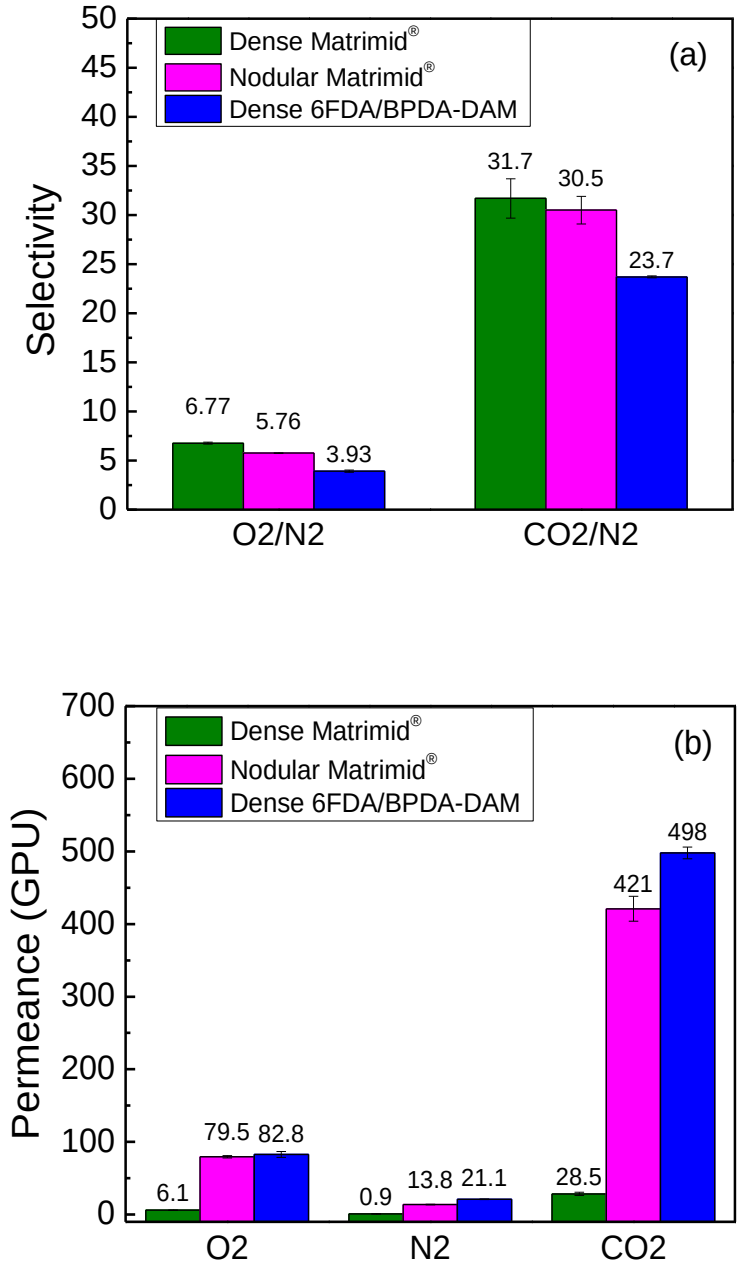

Figure 6.6: Comparison of pure gas permeation results for defect free 6FDA/BPDA-DAM and Matrimid® hollow fiber membranes at 35 °C.

6.3.2.2 Mixed gas permeation

The mixed gas permeation measurement was carried out on the defect free 6FDA/BPDA-DAM hollow fiber membranes. A mixture of 20 mol% CO_2/80 mol% N_2 was introduced at the bore side of the fibers at 100 psig. Temperature was reduced step by step from 35 °C to -50 °C, with the feed continuously purging the module. As temperature was decreased from 35 °C to 0 °C, an increase in selectivity and decrease in permeance was observed, which was expected; however, as temperature was decreased further, a slight increase in selectivity followed by a sharp drop at temperatures below -10 °C was recorded (Figure 6.7a). Meanwhile, the drop in selectivity was accompanied by an increase in permeance (Figure 6.7b). This unusual trend suggested the membranes might either be plasticized due to the high sorption of CO_2 at low temperatures or developed some defects at cold conditions.

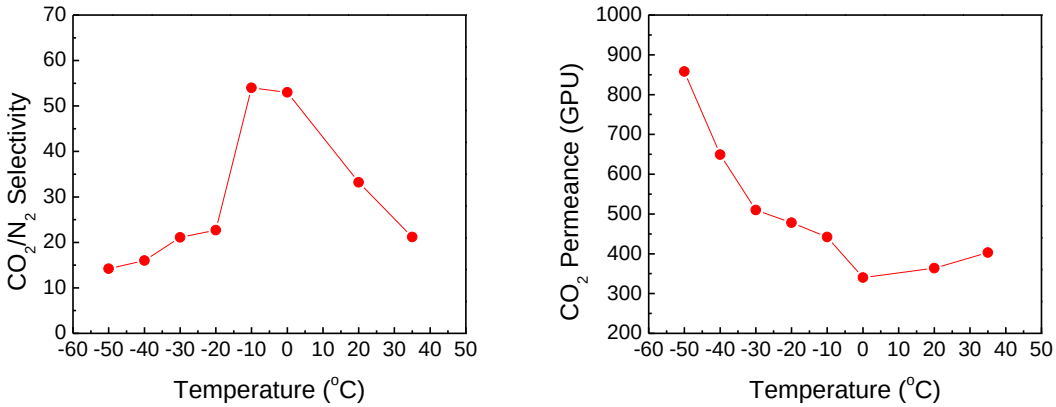

Figure 6.7: Mixed gas permeation results of defect free 6FDA/BPDA-DAM hollow fiber membranes at different temperatures. The feed was a mixture of 20 mol% CO_2/80 mol% N_2, and was introduced at the bore side at 100 psig.

6.3.2.3 Influence of PDMS post-treatment

It was interesting to discover that the PDMS post-treatment could prevent the defect free 6FDA/BPDA-DAM hollow fiber membranes from losing selectivity at low temperatures. Figure 6.8 shows the mixed gas permeation results of the defect free 6FDA/BPDA-DAM hollow fiber membranes at sub-ambient temperatures after PDMS post-treatment. The feed was a mixture of 20 mol% CO_2/80 mol% N_2, and was introduced at the bore side of the fibers at 100 psig. The membrane selectivity kept increasing with the decrease of temperature, suggesting PDMS post-treatment was able to prevent the membranes from being plasticized (Figure 6.8a). Meanwhile, the membrane permeance was decreased at first, and then the trend was reversed at temperatures below 0 °C (Figure 6.8b). The increase in membrane permeance was believed to be an outcome of increased CO_2 solubility at lower temperatures, which became the dominant factor in affecting membrane permeance with respect to the decrease in diffusivity. Due to the additional transport resistance brought about by the PDMS caulking layer, the membrane permeance was slightly lower than the un-treated 6FDA/BPDA-DAM hollow fiber membranes.

It was highly surprising that PDMS post-treatment could prevent the defect free 6FDA/BPDA-DAM hollow fiber membranes from losing selectivity at low temperatures, and the underlying reason is still not clear. However, this result is highly reproducible, which has been replicated for at least three times. It is assured that the untreated defect free 6FDA/BPDA-DAM hollow fiber membranes do lose selectivity at cold conditions, and this problem is corrected by PDMS post-treatment. This phenomenon was identified at the very end of this work, and there was insufficient time to perform further

investigations. It is suggested to do permeation measurement on untreated and PDMS post-treated 6FDA/BPDA-DAM dense films at cold conditions to see whether similar phenomenon can be observed.

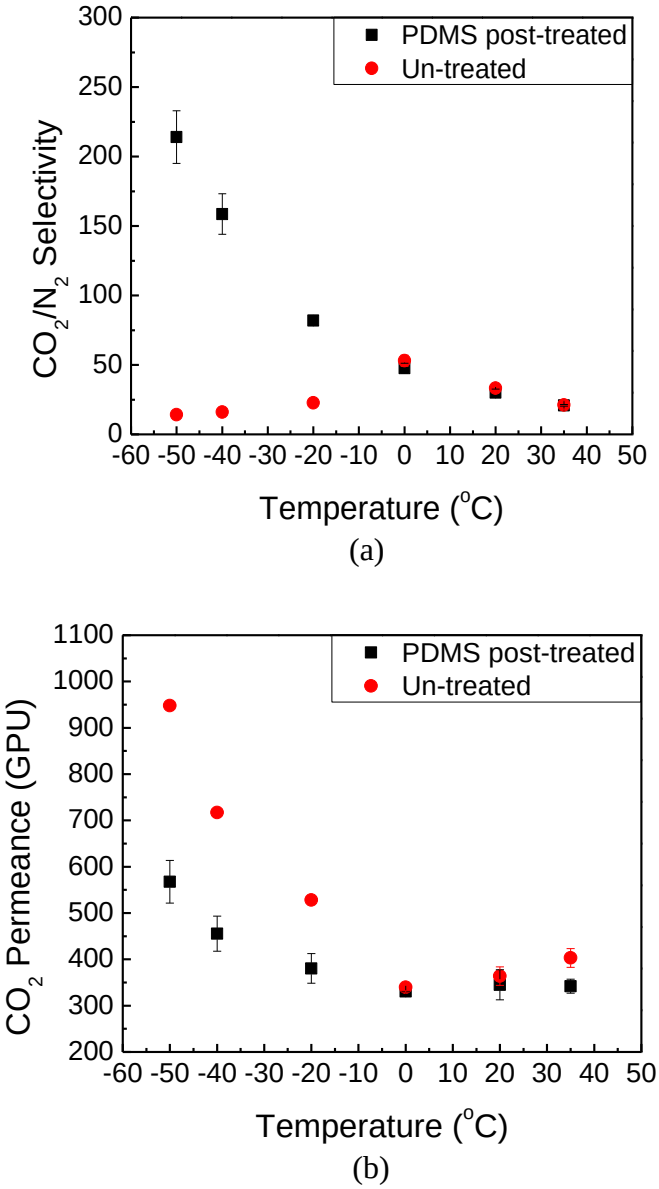

Figure 6.8: Comparison of the performance of PDMS post-treated and un-treated defect free 6FDA/BPDA-DAM hollow fiber membranes at different temperatures. The feed was a mixture of 20 mol% CO_2/80 mol% N_2, and was introduced at the bore side at 100 psig.

The performance of the PDMS post-treated defect free 6FDA/BPDA-DAM hollow fiber membranes were also compared with nodular Matrimid® hollow fiber membranes. As was shown in Chapter 5, the PDMS post-treated nodular Matrimid® hollow fiber membranes displayed a combination of high selectivity and high permeance at cold conditions. It was exciting to discover that the PDMS post-treated defect free 6FDA/BPDA-DAM hollow fiber membranes showed even better performance (Figure 6.9). The selectivity (Figure 6.9a) was similar to the nodular Matrimid® within the temperature range of 35 °C to -20 °C; however, higher selectivity was observed from 6FDA/BPDA-DAM at temperatures lower than -40 °C. Moreover, the permeance (Figure 6.9b) of defect free 6FDA/BPDA-DAM was much higher than nodular Matrimid®.

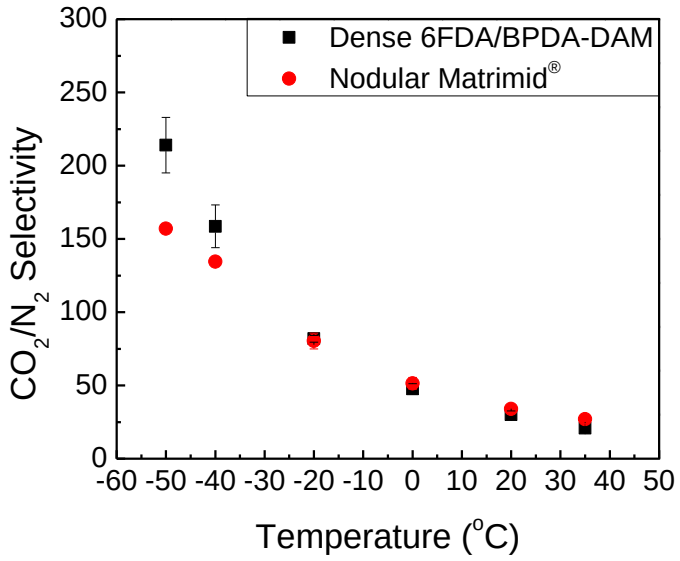

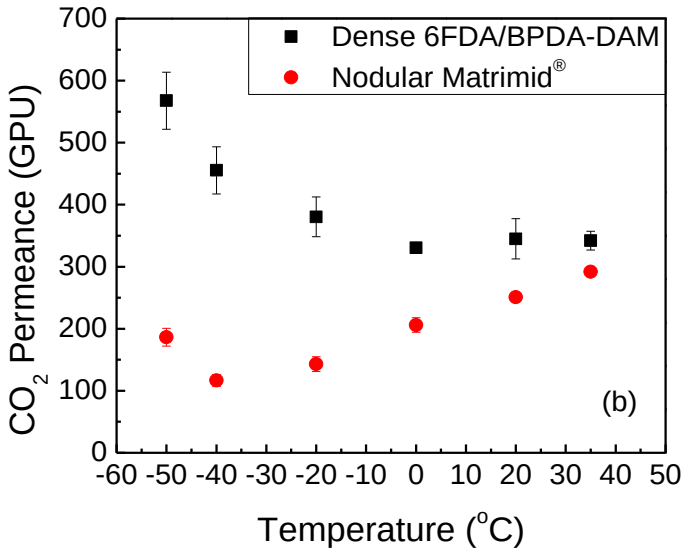

Figure 6.9: Comparison of the performance of PDMS post-treated defect free 6FDA/BPDA-DAM and nodular Matrimid® hollow fiber membranes at different temperatures. The feed was a mixture of 20 mol% CO_2/80 mol% N_2, and was introduced at the bore side at 100 psig.

6.4 Nodular 6FDA/BPDA-DAM hollow fiber membranes

It was shown in Chapter 5 that Matrimid® hollow fiber membranes with nodular selective layers displayed higher selectivity and higher permeance than those with homogeneous dense selective layers at cold conditions. Thus, it was anticipated that similar improvements would be seen for 6FDA/BPDA-DAM hollow fiber membranes. Specifically, we expected that the selectivity for a nodular layer formed from the high free volume, rigid 6FDA/BPDA-DAM material would be still higher than that found for the dense layer in Figure 6.9a at cold conditions, so the nodular 6FDA/BPDA-DAM hollow fiber membranes were expected to outperform the defect free hollow fiber membranes as was found for the Matrimid® case. To investigate these expectations, the spinning of nodular 6FDA/BPDA-DAM hollow fiber membranes was studied first.

6.4.1 Spinning of nodular 6FDA/BPDA-DAM hollow fiber membranes

It was shown in Chapter 4 that Matrimid® hollow fiber membranes with nodular selective layers could be formed by reducing the evaporation of solvent and/or non-solvent in the air gap, allowing the skin layer to go through phase separation in the quench bath. The same guide was employed in the spinning of nodular 6FDA/BPDA-DAM hollow fiber membranes. Based on the successful formation of defect free 6FDA/BPDA-DAM hollow fiber membranes, the dope composition and spinning conditions were changed to promote phase separation of the selective skin layer during spinning.

The same batch of 6FDA/BPDA-DAM (Mw = 123 kDa, PDI = 2.0) was used, and the volatile solvent THF was removed from the dope. Table 6.12 shows the dope

composition for the spinning of nodular 6FDA/BPDA-DAM hollow fiber membranes, and the spinning conditions are listed in Table 6.13. The spinneret temperature was reduced from 70 °C to 60 °C compared to defect free 6FDA/BPDA-DAM spinning, which helped to reduce solvent and non-solvent evaporation in the air gap. And a shorter air gap was selected. The SEM images of the resultant fibers' cross section and selective layer are shown in Figure 6.10. Nodules are clearly seen in the selective skin layer, suggesting nodular 6FDA/BPDA-DAM hollow fiber membranes were successfully formed.

Table 6.12: Dope composition for the spinning of nodular 6FDA/BPDA-DAM hollow fiber membranes

Component	wt.%
6FDA/BPDA-DAM	18
NMP	59.5
Ethanol	16
$LiNO_3$	6.5

Table 6.13: Spinning conditions for the formation of nodular 6FDA/BPDA-DAM hollow fiber membranes

Spinning parameter	Value
Dope flow rate	180 ml/h
Bore flow rate	60 ml/h
Bore fluid composition	85%/15% NMP/H_2O
Take-up rate	30 m/min
Quench temperature	49 °C
Spinneret temperature	60 °C
Air gap height	5, 10 cm
Room temperature	25 °C
Relative humidity	43 %

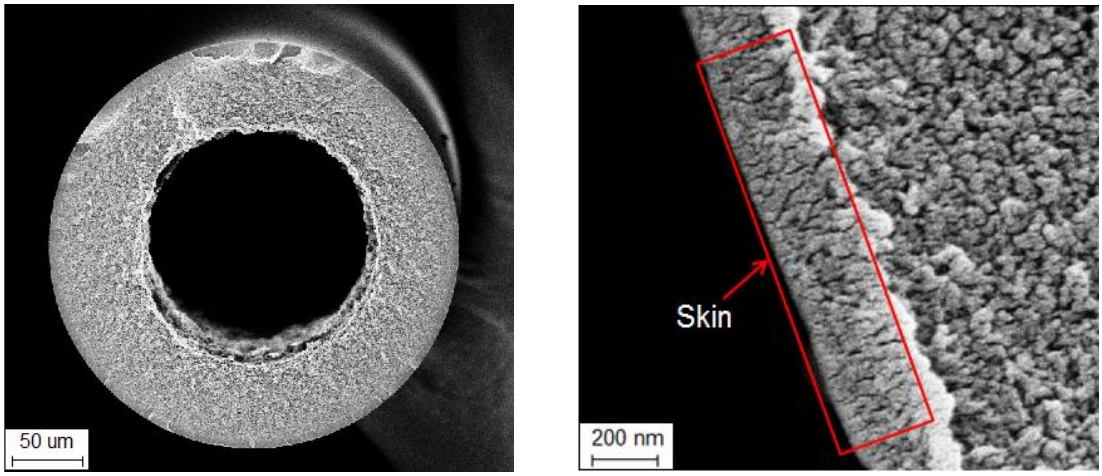

(a) (b)

Figure 6.10: SEM images of nodular 6FDA/BPDA-DAM hollow fiber membranes. (a) Overview of the cross-section, (b) selective skin layer.

6.4.2 Permeation in nodular 6FDA/BPDA-DAM hollow fiber membranes

6.4.2.1 Pure gas permeation

The pure gas permeation results of un-treated and PDMS post-treated nodular 6FDA/BPDA-DAM hollow fiber membranes at 35 °C are shown in Figure 6.11. The feed pressure for O_2 and N_2 was 100 psig; and for CO_2, 50 psig. The PDMS post-treatment helped to enhance membrane selectivity. For the un-treated nodular 6FDA/BPDA-DAM hollow fiber membranes, the O_2/N_2 selectivity was 2.67 ± 0.02, and the CO_2/N_2 selectivity was 14.6 ± 0.4 (Figure 6.11a). And after PDMS post-treatment, the O_2/N_2 selectivity was increased to 3.15 ± 0.02, and the CO_2/N_2 selectivity was increased to 19.8 ± 0.5.

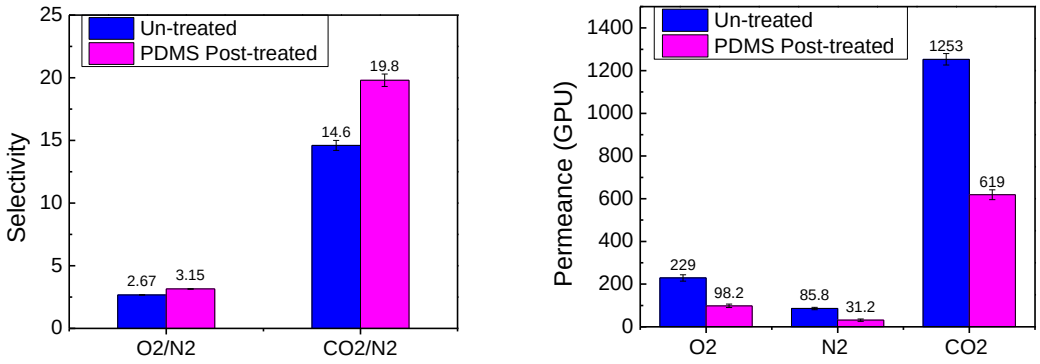

(a) (b)

Figure 6.11: Pure gas permeation results of PDMS post-treated and un-treated nodular 6FDA/BPDA-DAM hollow fiber membranes at 35 °C. Feed pressure for O_2 and N_2 was 100 psig; for CO_2, 50 psig. The feed was introduced at the bore side.

6.4.2.2 Mixed gas permeation

The separation performance of PDMS post-treated nodular 6FDA/BPDA-DAM hollow fiber membranes at sub-ambient temperatures were evaluated by permeating a mixture of 20 mol% CO_2/80 mol% N_2. The mixture was continuously fed to the bore side of the fibers at 100 psig, with the temperature reduced step by step from 35 °C to -50 °C. The permeation results were compared with PDMS post-treated defect free 6FDA/BPDA-DAM and nodular Matrimid® hollow fiber membranes (Figure 6.12). The selectivity of nodular 6FDA/BPDA-DAM was a little lower than defect free 6FDA/BPDA-DAM (Figure 6.12a), but the permeance was much higher (Figure 6.12b). This contradicts the phenomena observed from Matrimid® hollow fiber membranes that the nodular selective layer should show higher CO_2/N_2 selectivity than the dense selective layer at cold conditions. The lower selectivity of the nodular 6FDA/BPDA-DAM was presumably due to the defectiveness of the membranes, which compromised the selectivity advantage of the nodular structure. Due to the constraint of time, further optimization of the spinning conditions were not able to be carried out. However, the nodular 6FDA/BPDA-DAM hollow fiber membranes developed so far was still very selective, with the CO_2/N_2 selectivity above 100 at temperatures below -40 °C.

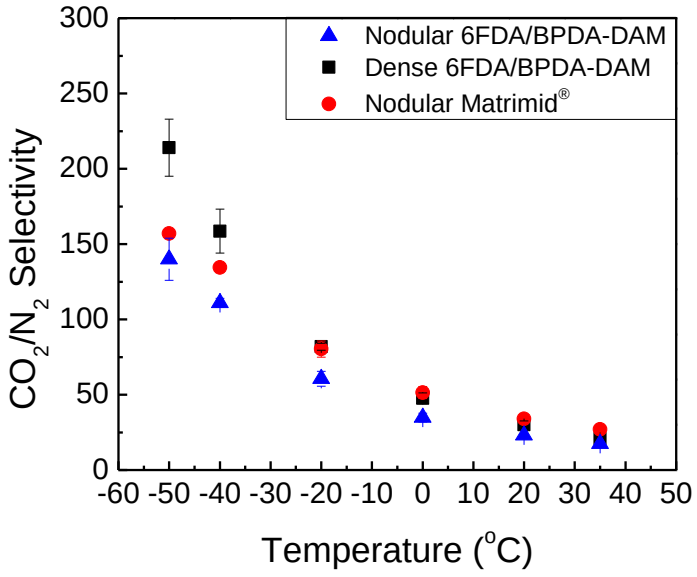

(a)

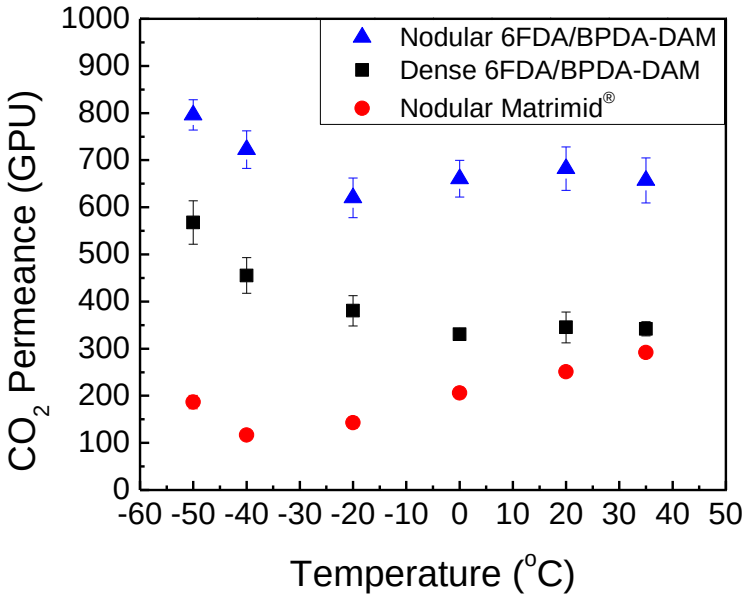

(b)

Figure 6.12: Comparison of permeation results of nodular 6FDA/BPDA-DAM, dense 6FDA/BPDA-DAM and nodular Matrimid® at sub-ambient temperatures. All membranes were post-treated with PDMS. The feed was a mixture of 20 mol% CO_2/80 mol% N_2, and was introduced at the bore side at 100 psig.

6.5 Summary

Preliminary study identified the high free volume, rigid 6FDA/BPDA-DAM (1:1) as a promising membrane material for cold conditions CO_2/N_2 separation. This material was successfully made into the hollow fiber configuration with both homogeneous dense and fused nodular selective layers, and the PDMS post-treatment was found to be desirable for both types of membranes. The dense 6FDA/BPDA-DAM membranes lost selectivity at temperatures below 0 °C, but this problem was fixed by PDMS post-treatment. Hollow fiber membranes made from 6FDA/BPDA-DAM showed similar selectivity but much higher permeance than the nodular Matrimid® at sub-ambient temperatures, suggesting a second generation of membranes for cold conditions flue gas CO_2 capture has been successfully developed.

6.6 References

[1] M. Kiyono, Ph.D. thesis, Carbon molecular sieve membranes for natural gas separations, Georgia Institute of Technology, 2010.

[2] K. M. Steel, Ph.D. thesis, Carbon membranes for challenging gas separations, The University of Texas at Austin, 2000.

[3] K. M. Steel and W. J. Koros, An investigation of the effects of pyrolysis parameters on gas separation properties of carbon materials, Carbon, vol. 43, pp. 1843-1856, 2005.

[4] D. Q. Vu, W. J. Koros, and S. J. Miller, High pressure CO_2/CH_4 separation using carbon molecular sieve hollow fiber membranes, Industrial & engineering chemistry research, vol. 41, pp. 367-380, 2002.

[5] M. Kiyono, P. J. Williams, and W. J. Koros, Effect of pyrolysis atmosphere on separation performance of carbon molecular sieve membranes, Journal of Membrane Science, vol. 359, pp. 2-10, 2010.

[6] L. Xu, Ph.D. thesis, Carbon molecular sieve hollow fiber membranes for olefin/paraffin separations, Georgia Institute of Technology, 2012.

[7] M. Rungta, Ph.D. thesis, Carbon molecular sieve dense film membranes for ethylene/ethane separations, Georgia Institute of Technology, 2012.

[8] M. Niwa, H. Kawakami, T. Kanamori, T. Shinbo, A. Kaito, and S. Nagaoka, Surface orientation effect of asymmetric polyimide hollow fibers on their gas transport properties, Journal of membrane science, vol. 230, pp. 141-148, 2004.

[9] A. Ismail, S. Shilton, I. Dunkin, and S. Gallivan, Direct measurement of rheologically induced molecular orientation in gas separation hollow fibre membranes and effects on selectivity, Journal of membrane science, vol. 126, pp. 133-137, 1997.

[10] A. Ismail, I. Dunkin, S. Gallivan, and S. Shilton, Production of super selective polysulfone hollow fiber membranes for gas separation, Polymer, vol. 40, pp. 6499-6506, 1999.

[11] S. Gordeyev and S. Shilton, Forced convection spinning of gas separation hollow fibre membranes: some underlying factors, mechanisms and effects, Journal of membrane science, vol. 229, pp. 225-233, 2004.

[12] C.-C. Chen, W. Qiu, S. J. Miller, and W. J. Koros, Plasticization-resistant hollow fiber membranes for CO2/CH_4 separation based on a thermally crosslinkable polyimide, Journal of Membrane Science, vol. 382, pp. 212-221, 2011.

[13] I. C. Omole, Ph.D. thesis, Crosslinked polyimide hollow fiber membranes for aggressive natural gas feed streams, Georgia Institute of Technology, 2008.

CHAPTER 7

SUMMARY, CONCLUSIONS AND RECOMMENDATIONS

7.1 Summary

Increasing atmospheric CO_2 concentration has been suggested as a factor causing climate change. Flue gas emissions from coal-based power plants are a main source of CO_2 emissions. The U.S. Department of Energy (DOE) is actively pursuing the goal of achieving at least 90 % CO_2 removal from flue gas, with less than 35 % increase in the cost of delivered electricity. Three technological pathways can be pursued for flue gas CO_2 capture: pre-combustion, post-combustion and oxy-fuel combustion. Post-combustion has the greatest near-term potential because it can be retrofitted to existing state-of-the-art power plants with reasonable changes in the plants themselves. Membranes are attractive for this application; however, the low CO_2 concentration and the low feed pressure of flue gas lead to a high energy penalty due to low membrane driving force and large capture system requirements. To achieve cost effective CO_2 capture, a hybrid membrane and cryogenic distillation process was developed at American Air Liquide. This process integrates energy between a cold membrane system and a CO_2 cryo-phase separator, significantly reducing the overall energy penalty. The low cost commercially available membrane produced at Air Liquide showed an unprecedented combination of permeability and selectivity at cold conditions for the important CO_2/N_2 penetrant pair; however, the underlying reason for such great performance was not clear. The aim of this research was to clarify fundamentals of the

cold membrane CO_2/N_2 separation process, in order to engineer membrane performance and identify second generation improved membrane materials for this application. The primary target to address in this work is to understand the phenomena of cold temperature CO_2 and N_2 permeation in glassy polyimide membranes.

A sub-ambient lab was built with the help of JR Johnson and Oguz Karvan to create the cold conditions required by this project. The unprecedented performance of the Air Liquide membranes was successfully reproduced under our sub-ambient lab environment. A post-treatment step was found to be necessary for the Air Liquide membranes to display desirable selectivity. Two post-treatment methods were pursued in the current work: PDMS post-treatment and reactive post-treatment. The PDMS post-treatment was identified as a better option considering the influence of the post-treatment step on both membrane permeance and selectivity, and this method was used throughout the current work to caulk defective membranes.

7.2 Conclusions

7.2.1 Matrimid®

The high performance of the Air Liquide membranes at sub-ambient temperatures was related to the different interactions of the penetrant molecules with the membrane material. The permeation activation energy for CO_2 was smaller than for N_2, due to the stronger interaction of CO_2 molecules with the polymer matrix. A higher heat of sorption for CO_2 resulted, making the heats of sorption in similar magnitude as the activation energy for diffusion. The smaller permeation activation energy for CO_2 contributed to smaller decrease in permeance with the drop of temperature, leading to higher selectivity

with respect to N_2. Therefore, the selection of membrane material is critical for achieving high cold separation performance.

The use of Matrimid® 5218 as a starting material to investigate the influence of membrane selective layer structure on cold conditions CO_2/N_2 separation was logical, because it was the material that formed the effective separation layer of the high performing Air Liquide membranes. Asymmetric Matrimid® hollow fiber membranes with "homogeneous dense" and "fused nodular" selective layers were successfully formed. Different skin formation mechanisms were pursued. In the formation of the nodular selective layers, phase separation in the selective layer was induced, and the SEM images of resultant membranes confirmed the formation of nodules in the selective layer. The PDMS post-treatment was necessary for the nodular fibers to display desirable selectivity.

The PDMS post-treated Matrimid® nodular fibers showed better cold performance than the dense fibers under bore side feed. And PDMS, per se, was excluded to be the reason, because the dense fibers post-treated with PDMS showed minimal performance enhancement. A hypothesis with regards to the different morphologies of the selective layers was thus proposed. The nodular skin was hypothesized to be a heterogeneous layer, comprised of several layers of so-called nodules; the nodules were assumed to have higher polymer density than the interstitial domains. Whereas the dense skin was envisioned to be an isotropic layer, the density of which was similar to the density of the nodules in the nodular skin. The higher selectivity for the bore-fed nodular fibers was hypothesized to result from enhanced sorption selectivity as well as enhanced diffusion selectivity due to the dilation of the inter-nodular domains. Enhanced sorption selectivity

was believed to arise from increased sorption capacity due to the introduction of more Langmuir sites coupled with the stronger competitive power of CO_2 molecules for the additional sorption sites. Enhanced diffusion selectivity was believed to arise from a local orientation of polymer chain segments due to the uniaxial draw of the selective layer, resulting in increased size discrimination capability.

To support the proposed hypothesis, direct characterization was found to be very challenging due to the difficulties in tailoring the ultra-thin selective skin layer from the bulk support layer and the creation of the realistic stressed conditions. Three indirect experiments were carried out instead. By dilating or compressing the nodular selective layer, the sorption capacity of the inter-nodular domains and the orientation of the polymer chain segments were assumed to be changed accordingly; and the subsequent gas separation properties of the membrane were found to be consistent with the hypothesis. Moreover, the same experiments were carried out on dense Matrimid® hollow fiber membranes. Similar results were obtained whether the homogeneous skin layer was dilated or compressed.

The temperature and pressure influence on PDMS post-treated nodular Matrimid® hollow fiber membranes was also analyzed. This study was not only useful for predicting the membrane behavior from a practical stand point, but also contributes to the better understanding of sub-ambient temperature gas separation. The CO_2/N_2 selectivity was found to increase with the decrease of temperature; while the CO_2 permeance decreased at first, but the trend was reversed at lower temperatures when the activity of CO_2 was high. The study of pressure dependence of CO_2/N_2 separation at cold conditions revealed increased membrane permeance with pressure accompanied by minimal change in

selectivity. This phenomenon was unusual but exciting, which didn't follow the trade-off relationship between selectivity and permeability predicted for gas separation membranes.

7.2.2 6FDA/BPDA-DAM

The high free volume, rigid 6FDA/BPDA-DAM (1:1) was found to be a better membrane material than Matrimid® for cold conditions CO_2/N_2 separation. The asymmetric hollow fiber membranes made from 6FDA/BPDA-DAM showed similar selectivity but much higher permeance than the nodular Matrimid® hollow fiber membranes. In this work, 6FDA/BPDA-DAM hollow fiber membranes with both homogeneous dense and fused nodular selective layers were successfully formed, and PDMS post-treatment was found to be necessary for both types of membranes. It was interesting to note that the dense 6FDA/BPDA-DAM hollow fiber membranes lost selectivity at temperatures below 0 °C, but this problem was corrected by PDMS post-treatment. Although the underlying reason why PDMS post-treatment could prevent the membranes from losing selectivity at cold conditions, this phenomenon was highly reproducible. Further investigations into this topic are highly recommended.

7.3 Recommendations for future work

The research objectives proposed for the current project have been successfully achieved. A better understanding of the nature of CO_2 and N_2 transport in polyimide membranes at sub-ambient temperatures was obtained. This research was successful in developing attractive membranes for cold conditions CO_2/N_2 separation. However, there

remain many opportunities in this field for further study. The areas that need more investigation are briefly outlined in this section.

7.3.1 The study of PDMS influence on membrane separation layer

It was found in Chapter 7 that PDMS post-treatment could prevent the dense 6FDA/BPDA-DAM hollow fiber membranes from losing selectivity at low temperatures, and the underlying reason was not well understood. The coating of PDMS seemed to enhance the selective layer's "anti-plasticization" capability; however, the role that PDMS played in preventing the membranes from being plasticized is not clear. This phenomenon was identified at the very end of this work, so there was insufficient time to fully understand the reason. However, this result is highly reproducible, which has been replicated for at least three times. It is assured that the untreated defect free 6FDA/BPDA-DAM hollow fiber membranes do lose selectivity at cold conditions, and this problem is corrected by PDMS post-treatment. It is suggested to do permeation measurement on untreated and PDMS post-treated 6FDA/BPDA-DAM dense films at cold conditions to see whether similar phenomenon can be observed. Besides, it is also recommended that further exploration into the interaction of PDMS with the polyimide membrane material is performed, as it seems to represent a truly unique and important finding in the application of the polyimide membranes for cold conditions gas separation.

7.3.2 Material chemistry and membrane property relationship

In the current work, asymmetric hollow fiber membranes were derived from two polyimides: Matrimid® 5218 and 6FDA/BPDA-DAM (1:1). Both membranes showed

CO_2/N_2 selectivity advantage at low temperatures, and the reason was attributed to the different interactions of CO_2 and N_2 molecules with the polymer matrix. However, the correlation between the polymer chemistry and the resulting membrane cold performance is an area that is not well understood.

Correlating material chemistry to the membrane cold performance would shed light on the selection of appropriate polymers for sub-ambient temperature gas separation. So far, all the materials studied were polyimides. It would be interesting to explore the cold performance of other classes of polymers. Polysulfone, polyethersufone and tetrabrominated polycarbonate are good starting candidates, because they have been successfully made into hollow fiber configurations and shown desirable gas separation properties [1-7]. Figure 7.1 shows the repeating units of these three materials. The interaction of the sulfonyl and carbonyl groups with CO_2 at cold conditions would be an interesting topic to study.

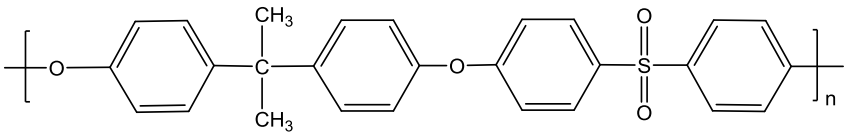

(a) Polysulfone

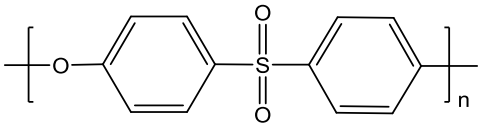

(b) Polyethersulfone

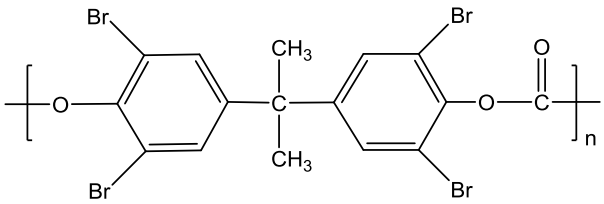

(c) Tetrabrominated Polycarbonate

Figure 7.1: The repeating unit of polysulfone, polyethersulfone and polycarbonate.

7.3.3 Polymer property versus nodular structure

It was shown in Chapter 7 that the 6FDA/BPDA-DAM hollow fiber membranes with homogeneous dense selective layers showed higher selectivity and higher permeance than nodular Matrimid® hollow fiber membranes at cold conditions. This discovery led us wonder which was the dominant factor in determining the membrane's cold separation performance, the polymer property or the nodular selective layer structure. If the polymer property is the dominant factor, it would make the development of further generations of membranes for cold conditions gas separation easier, because the right membrane material would allow a wide range of selective layer properties to achieve desirable cold separation performance. This would significantly reduce the difficulties in forming hollow fiber membranes with specialized selective layers. Good candidates for this study are materials that have the potential to achieve desirable CO_2/N_2 separation at cold conditions.

7.3.4 Nodular 6FDA/BPDA-DAM hollow fiber membranes spinning optimization

In Chapter 7, the 6FDA/BPDA-DAM hollow fiber membranes with nodular selective layers showed lower selectivity but higher permeance than those with homogeneous dense selectivity layers, which contradicts the hypothesis derived from Matrimid® hollow fiber membranes that, the nodular structure should outperform the dense structure at cold conditions. The lower selectivity of the nodular 6FDA/BPDA-DAM was attributed to the defectiveness of the membranes' selective layers. It was discovered in the study of Matrimid® hollow fiber membranes that, the defectiveness of the nodular selective layers would significantly affect the membrane separation

properties. Highly defective nodular Matrimid® hollow fiber membranes had been formed in this work, which showed lower selectivity than the dense Matrimid® hollow fiber membranes. Therefore, future effort may be made to optimize the membrane formation conditions to produce less defective nodular 6FDA/BPDA-DAM hollow fiber membranes. A successful spinning was expected to lead to higher selectivity than the dense 6FDA/BPDA-DAM membranes. To achieve that purpose, a higher polymer concentration or a higher air gap might be used.

7.3.5 Evaluating membrane performance under realistic conditions

The Matrimid® and 6FDA/BPDA-DAM hollow fiber membranes developed in the current work showed a combination of high permeance and high selectivity at cold conditions with a binary feed containing CO_2 and N_2; however, the lab-scale permeation tests were too idealized, which didn't take into account the influence of impurities on membrane performance. For practical applications, flue gas impurities, like SO_x, NO_x, H_2O and O_2 etc., may significantly affect the cold performance of the membranes. It would be wise to perform more systematic studies under realistic testing conditions.

The amount of water vapor that the membranes can withstand is an interesting topic that worth pursuit. Flue gas contains a significant amount of water, which may freeze into ice under the cold operating conditions. Although the cold membrane process developed at Air Liquide involves a drying step, it is very challenging to remove 100 % of the water. Therefore, it is important to know how much water the membranes can tolerate under the cold operating conditions.

Another issue that has to be considered for the realistic application of the membranes is pressure drop. It was discovered in the current work that, bore side feed gave rise to much higher permeance and higher selectivity than shell side feed. However, the pressure drop related to bore side feed cannot be neglected, especially during scaling up. The modules for practical applications are much longer than the lab-scale modules, and the pressure drop would be more pronounced. The determination of appropriate stage cut would be important to balance the CO_2 concentration in the feed and pressure drop along the fibers to achieve optimum driving force for separation.

7.4 References

[1] A. Ismail, I. Dunkin, S. Gallivan, and S. Shilton, Production of super selective polysulfone hollow fiber membranes for gas separation, Polymer, vol. 40, pp. 6499-6506, 1999.

[2] D. Wang, K. Li, and W. Teo, Polyethersulfone hollow fiber gas separation membranes prepared from NMP/alcohol solvent systems, Journal of membrane science, vol. 115, pp. 85-108, 1996.

[3] P. Machado, A. Habert, and C. Borges, Membrane formation mechanism based on precipitation kinetics and membrane morphology: flat and hollow fiber polysulfone membranes, Journal of membrane science, vol. 155, pp. 171-183, 1999.

[4] T. S. Chung, S. K. Teoh, and X. Hu, Formation of ultrathin high-performance polyethersulfone hollow-fiber membranes, Journal of membrane science, vol. 133, pp. 161-175, 1997.

[5] W. Ward III, W. Browall, and R. Salemme, Ultrathin silicone/polycarbonate membranes for gas separation processes, Journal of Membrane Science, vol. 1, pp. 99-108, 1976.

[6] T. Kim, W. Koros, G. Husk, and K. O'brien, Relationship between gas separation properties and chemical structure in a series of aromatic polyimides, Journal of Membrane Science, vol. 37, pp. 45-62, 1988.

[7] C. E. Powell and G. G. Qiao, Polymeric CO_2/N_2 gas separation membranes for the capture of carbon dioxide from power plant flue gases, Journal of Membrane Science, vol. 279, pp. 1-49, 2006.

APPENDIX A

FUGACITY REPLACING PARTIAL PRESSURE IN THE PERMEATION CALCULATION

When dealing with highly non-ideal gases, fugacity should be used instead of partial pressure in the permeation calculation in order to obtain more accurate results. The true driving force for gas penetrants to permeate through the membrane is the chemical potential gradient, which is more accurately represented by the transmembrane fugacity difference. The effect of non-ideal behavior on permeation calculations is especially pronounced for systems containing highly interacting components, like CO_2, at high pressures or low temperatures.

The fugacity coefficients for CO_2/N_2 mixture used in this work were calculated using a program developed by previous group member Kraftschik [1]. This program takes into account the interaction between various components within a gaseous mixture, thus allowing for calculation of the fugacity coefficient of component i in a multicomponent mixture. For the CO_2/N_2 binary system, the binary interaction parameters were obtained from the literature. In this program, the fugacity coefficient (Φ_i), a measure of the deviation of the chemical potential of a real gas from that of an ideal gas, was calculated based on the Peng-Robinson equation of state, and the fugacity was obtained via the following equation:

$$f_i = \Phi_i \cdot p_i \tag{A.1}$$

where, f_i is the fugacity of component i, and p_i is the partial pressure.

The permeation results calculated via fugacity difference and partial pressure difference are shown in Figures A.1 and A.2. The experimental data used in the calculation were obtained by permeating a gas mixture of 20 mol% CO_2/80 mol% N_2 at various temperatures and pressures. Higher selectivity and higher permance were obtained when fugacity was used in the calculation. At constant feed pressure (100 psig), the selectivity was 6-22 % higher, and the permeance was 6-24 % higher (Figure A.1). Larger deviation was observed at lower temperatures, when the non-ideal property of the mixture was more pronounced. Similarly, at constant temperature (-40 °C), the selectivity was 17-29 % higher, and the permeance was 19-30 % higher (Figure A.2), with larger deviation observed at higher pressures. In this work, fugacity difference was used in all permeation calculations.

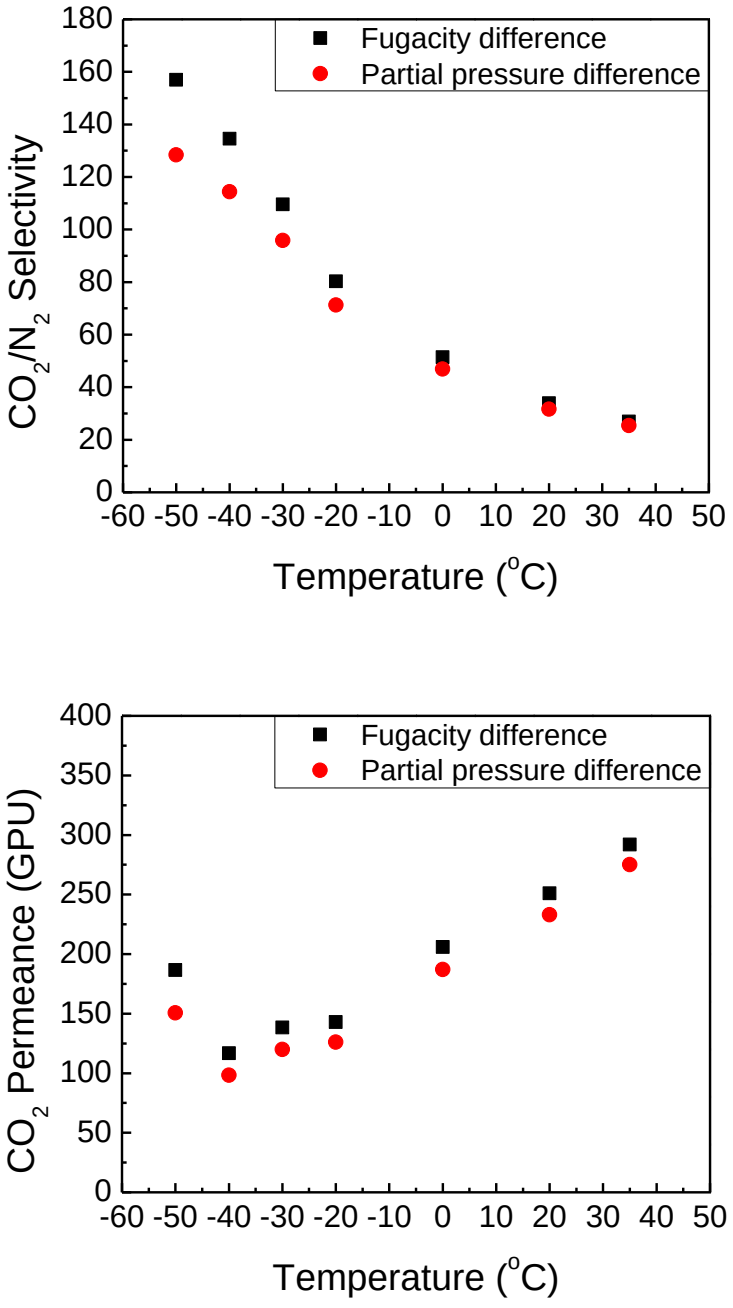

Figure A.1: Comparison of permeation calculations via fugacity difference versus partial pressure difference. Experimental data used in the calculation were obtained by permeating 100 psig, 20 mol% CO_2/80 mol% N_2 at different temperatures.

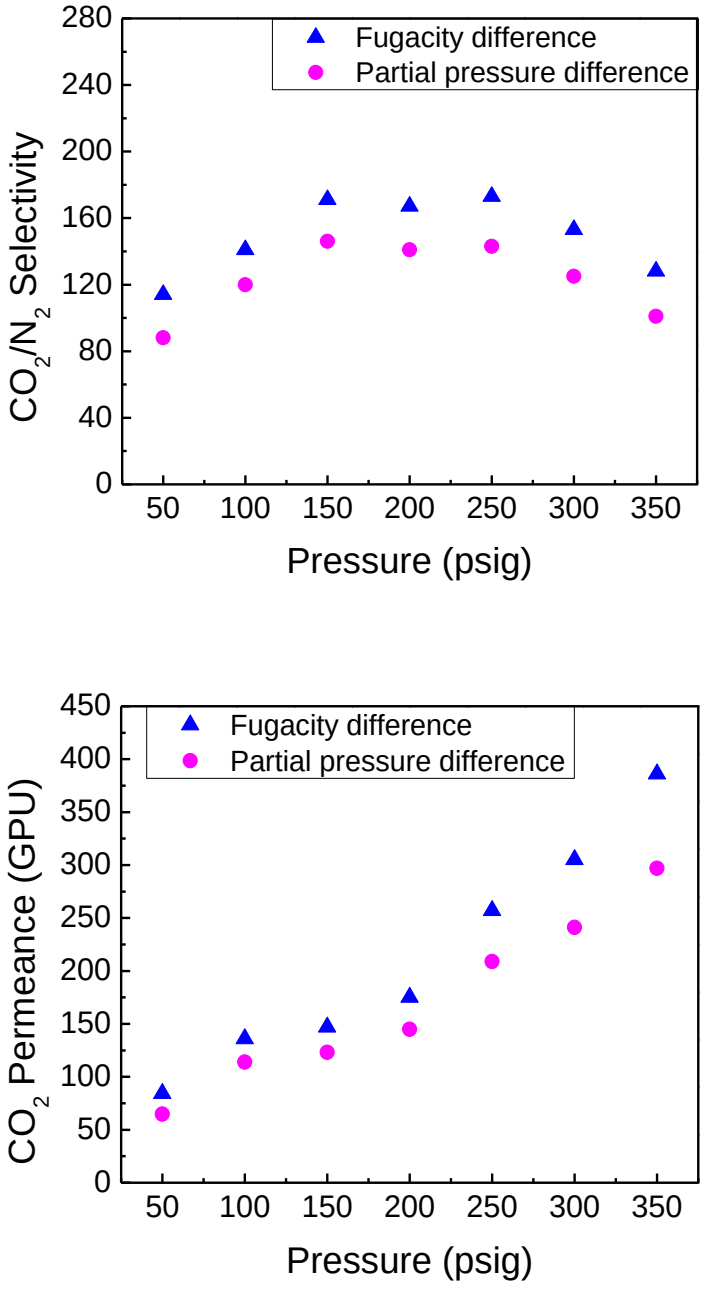

Figure A.2: Comparison of permeation calculations via fugacity difference versus partial pressure difference. Experimental data used in the calculation were obtained by permeating 20 mol% CO_2/80 mol% N_2 at different pressures at -40 °C.

Reference

[1] B. E. Kraftschik, Ph.D. thesis, Advanced crosslinkable polyimide membranes for aggressive sour gas separations, Georgia Institute of Technology, 2013.

APPENDIX B

PRESSURE DROP WITH BORE SIDE FEED

Gases flow in the bore of a hollow fiber membrane may cause significant pressure drop, especially when the flow rate is high. The pressure drop along the fiber can be calculated by the Hagen-Poiseuille equation:

$$\Delta P = \frac{128 \mu L Q}{\pi d^4} \tag{B.1}$$

where, ΔP is the pressure drop; L is the length of the fiber; μ is the dynamic viscosity of the feed gas; Q is the volumetric flow rate; and d is the inner diameter of the fiber.

In this work, bore side feed was used for most cases. Due to the high flux of nodular Matrimid® hollow fiber membranes, a large pressure drop in the feed was often resulted. For example, the length of a typical lab-scale module was 20 cm, the inner diameter of the nodular Matrimid® hollow fiber membrane was 188 um. To maintain a stage cut of less than 1 %, the gas flow rate through the bore of the fiber was around 350 ml/min (with a feed of 350 psig at -50 °C). According to the Hagen-Poiseuille equation, the pressure drop is around 75 psia. Such high pressure drop seriously affected the pressure ratio of the feed and the permeate streams, and had to be taken into account during the permeation calculation. In this work, a log mean average fugacity difference between the upstream and downstream of the membrane was used to represent the transmembrane fugacity difference (As discussed Appendix A, the true driving force is

more accurately represented by the fugacity difference when the gas is non-ideal), which is given by:

$$\Delta f = \frac{\Delta f_A - \Delta f_B}{\ln\left(\frac{\Delta f_A}{\Delta f_B}\right)} \tag{B.2}$$

$$\Delta f_A = f_1 - f_3 \tag{B.3}$$

$$\Delta f_b = f_2 - f_3 \tag{B.4}$$

where f_1, f_2 and f_3 are the fugacities at the feed, retentate and permeate sides of the hollow fiber membrane, respectively, as is shown in Figure B.1.

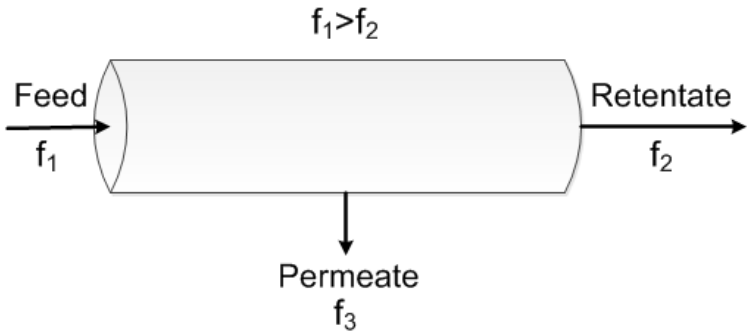

Figure B.1: Schematic showing fugacities at the feed, retentate and permeate sides of a hollow fiber membrane.

To confirm the reliability of the log mean average fugacity difference approximation, a gas membrane simulator developed by the UT Separations Research Program and the Koros' Research Group was used to simulate the performance of the nodular Matrimid® hollow fiber membranes. The simulator can model countercurrent, cocurrent and radial crossflow configurations in a gas membrane module, and is capable of simulating multicomponent gas separation. Feed compositions, process conditions and membrane properties were input into the program and the membrane simulator output separation performance (stream compositions, flow rates…) Theoretical considerations of this software can be found in Thundyil's work [1]. Note that, fugacity was input into the program instead of partial pressure due to the non-ideal effects at cold conditions. To calculate the permeance of CO_2 and N_2, trial and error was performed. An initial guess of the permeance of CO_2 and N_2 were input into the program, and the membrane simulator output the compositions and flow rates of the feed, permeate and retentate, which were compared with experimental values. This process was repeated until the experimental values were matched. Permeation results calculated using log mean average fugacity difference approximation matched the results given by the membrane simulator very well (Figure B.2), suggesting the log mean average pressure drop approximation was reasonable.

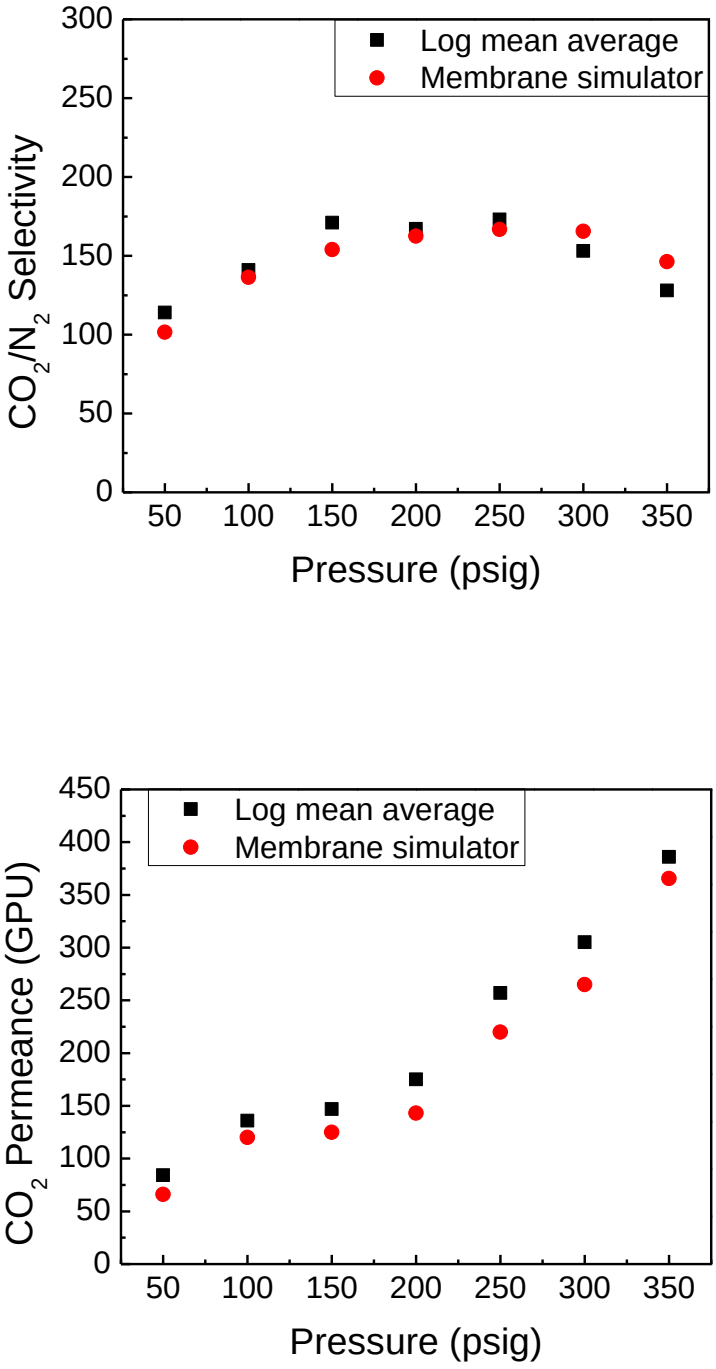

Figure B.2: Permeation calculation results from the log mean average fugacity difference method and membrane simulator. The eed was a mixture of 20 mol% CO_2/80 mol% N_2, and was introduced at the bore side at -40 °C.

Reference

[1] M. J. Thundyil, Ph.D. thesis, Characterization, analysis and modeling of non-ideal effects in polymeric membrane based natural gas processing, The University of Texas at Austin, 1998.

APPENDIX C

GAS COMPRESSIBILITY FACTORS

The compressibility factor (z) is a thermodynamic property used to account for the deviation of a real gas behavior from the ideal state, which is defined as

$$Z = \frac{pV_m}{RT} \tag{C.1}$$

where, V_m is the molar volume, p is the pressure, T is the temperature, and R is the gas constant. At constant temperature, the pressure dependent compressibility factor equation is given by

$$Z = 1 + (A)p + (B)P^2 + (C)P^3 + ... \tag{C.2}$$

where A, B and C are constants. The higher order terms in the equation are negligible and were ignored in the calculation of gas equilibrium uptake in this work. The pressure dependent compressibility factor equations of the gases used in the current work at different temperatures were obtained from the National Institute of Standards and Technology (NIST) Software Standard Reference Database 12, Version 5.0 and NIST Chemistry WebBook, Standard Reference Database Number 69. The compressibility factor equations for different gases are shown in Tables C.1-C.6.

Table C.1: Compressibility factor equations for CO_2 at different temperatures

T (°C)	Compressibility Equation	P range (psia)
35	$Z = 1-(3.607E-04)p+(4.904E-08)P^2-(1.452E-10)P^3+...$	0~1000
0	$Z = 1-(4.678E-04)p-(3.709E-08)P^2-(4.607E-10)P^3+...$	0~500
-10	$Z = 1-(5.252E-04)p-(8.377E-08)P^2-(6.478E-10)P^3+...$	0~380
-20	$Z = 1-(5.909E-04)p-(1.848E-07)P^2-(8.215E-10)P^3+...$	0~280
-30	$Z = 1-(6.721E-04)p-(2.982E-07)P^2-(1.138E-09)P^3+...$	0~200
-40	$Z = 1-(7.704E-04)p-(4.565E-07)P^2-(1.609E-09)P^3+...$	0~140
-50	$Z = 1-(8.909E-04)p-(6.716E-07)P^2-(2.373E-09)P^3+...$	0~90

Table C.2: Compressibility factor equations for N_2 at different temperatures

T (°C)	Compressibility Equation	P range (psia)
35	$Z = 1-(2.431E-05)p+(1.546E-08)P^2-(9.567E-13)P^3+...$	0~1000
0	$Z = 1-(3.128E-05)p+(1.277E-08)P^2+(1.147E-12)P^3+...$	0~1000
-10	$Z = 1-(4.034E-05)p+(1.352E-08)P^2+(1.635E-12)P^3+...$	0~1000
-20	$Z = 1-(5.088E-05)p+(1.416E-08)P^2+(2.304E-12)P^3+...$	0~1000
-30	$Z = 1-(6.320E-05)p+(1.461E-08)P^2+(3.218E-12)P^3+...$	0~1000
-40	$Z = 1-(7.766E-05)p+(1.469E-08)P^2+(4.487E-12)P^3+...$	0~1000
-50	$Z = 1-(9.469E-05)p+(1.407E-08)P^2+(6.306E-12)P^3+...$	0~1000

Table C.3: Compressibility factor equations for SF_6 at different temperatures

T (°C)	Compressibility Equation	P range (psia)
35	$Z = 1-(6.918E-04)p-(3.234E-07)P^2-(5.355E-10)P^3+...$	0~100
-20	$Z = 1-(1.289E-03)p-(1.130E-06)P^2-(1.034E-08)P^3+...$	0~100
-40	$Z = 1-(1.647E-03)p-(2.576E-06)P^2-(2.263E-08)P^3+...$	0~50

Table C.4: Compressibility factor equations for CH_4 at different temperatures

T (°C)	Compressibility Equation	P range (psia)
35	$Z = 1-(1.053E-04)p+(4.979E-09)P^2+(4.411E-12)P^3+...$	0~1000
0	$Z = 1-(1.617E-04)p-(4.815E-09)P^2+(8.625E-12)P^3+...$	0~1000
-20	$Z = 1-(2.075E-04)p-(1.958E-08)P^2+(1.200E-11)P^3+...$	0~1000
-40	$Z = 1-(2.684E-04)p-(4.804E-08)P^2+(1.081E-11)P^3+...$	0~1000

Table C.5: Compressibility factor equations for C_2H_4 at different temperatures

T (°C)	Compressibility Equation	P range (psia)
35	$Z = 1-(3.560E-04)p-(4.490E-08)P^2-(8.149E-11)P^3+...$	0~730
0	$Z = 1-(5.521E-04)p+(1.167E-07)P^2-(7.839E-10)P^3+...$	0~590
-20	$Z = 1-(6.788E-04)p+(6.411E-08)P^2-(1.576E-09)P^3+...$	0~360
-40	$Z = 1-(8.389E-04)p-(2.829E-07)P^2-(2.574E-09)P^3+...$	0~210

Table C.6: Compressibility factor equations for C_2H_6 at different temperatures

T (°C)	Compressibility Equation	P range (psia)
35	$Z = 1-(5.070E-04)p+(1.093E-07)P^2-(5.453E-10)P^3+...$	0~710
0	$Z = 1-(7.166E-04)p+(9.504E-08)P^2-(1.894E-09)P^3+...$	0~340
-20	$Z = 1-(8.717E-04)p-(2.424E-07)P^2-(3.152E-09)P^3+...$	0~200
-40	$Z = 1-(1.107E-03)p-(6.754E-07)P^2-(6.877E-09)P^3+...$	0~110

APPENDIX D

PURE GAS FUGACITY COEFFICIENT

The fugacity (f) of a real gas is an effective pressure which is equal to the pressure of an ideal gas that has the same chemical potential as the real gas. The fugacity coefficient (Φ) is a dimensionless factor, which relates the real gas fugacity to the ideal gas pressure:

$$\Phi = f / p \tag{D.1}$$

where, p is the ideal gas pressure. At constant temperature, the pressure dependent fugacity coefficient equation is given by

$$\Phi = 1 + (A')p + (B')P^2 + (C')P^3 + ... \tag{D.2}$$

where A', B' and C' are constants. The higher order terms in the equation are negligible. The pressure dependent fugacity of the different pure gases used in the current work at different temperatures was obtained from the National Institute of Standards and Technology (NIST) Software Standard Reference Database 12, Version 5.0 and NIST Chemistry WebBook, Standard Reference Database Number 69. The resultant fugacity coefficient equations are shown in Tables D.1-D.6.

Table D.1: Fugacity coefficient equations for CO_2 at different temperatures

T (°C)	Fugacity Coefficient Equation	P range (psia)
35	$\Phi = 1-(3.068E-04)p+(1.699E-08)P^2-(6.288E-12)P^3+...$	0~400
0	$\Phi = 1-(4.574E-04)p+(3.575E-08)P^2-(5.459E-11)P^3+...$	0~500
-10	$\Phi = 1-(5.166E-04)p+(3.936E-08)P^2-(8.092E-11)P^3+...$	0~380
-20	$\Phi = 1-(5.863E-04)p+(4.013E-08)P^2-(1.133E-10)P^3+...$	0~280
-30	$\Phi = 1-(6.693E-04)p+(4.145E-08)P^2-(1.684E-10)P^3+...$	0~200
-40	$\Phi = 1-(7.690E-04)p+(4.263E-08)P^2-(2.621E-10)P^3+...$	0~140
-50	$\Phi = 1-(8.899E-04)p+(4.038E-08)P^2-(4.164E-10)P^3+...$	0~90

Table D.2: Fugacity coefficient equations for N_2 at different temperatures

T (°C)	Fugacity Coefficient Equation	P range (psia)
35	$\Phi = 1-(8.189E-06)p+(5.037E-09)P^2+(6.695E-14)P^3+...$	0~400
0	$\Phi = 1-(3.126E-05)p+(6.822E-09)P^2+(2.247E-13)P^3+...$	0~1000
-10	$\Phi = 1-(4.031E-05)p+(7.512E-09)P^2+(3.081E-13)P^3+...$	0~1000
-20	$\Phi = 1-(5.085E-05)p+(8.312E-09)P^2+(4.249E-13)P^3+...$	0~1000
-30	$\Phi = 1-(6.318E-05)p+(9.265E-09)P^2+(5.706E-13)P^3+...$	0~1000
-40	$\Phi = 1-(7.767E-05)p+(1.041E-08)P^2+(7.551E-13)P^3+...$	0~1000
-50	$\Phi = 1-(9.478E-05)p+(1.175E-08)P^2+(1.021E-12)P^3+...$	0~1000

Table D.3: Fugacity coefficient equations for SF_6 at different temperatures

T (°C)	Fugacity Coefficient Equation	P range (psia)
35	$\Phi = 1-(7.193E-04)p+(1.715E-07)P^2-(2.466E-10)P^3+...$	0~100
-20	$\Phi = 1-(1.403E-03)p+(6.593E-07)P^2-(3.638E-09)P^3+...$	0~100
-40	$\Phi = 1-(1.800E-03)p+(1.162E-16)P^2-(1.735E-18)P^3+...$	0~50

Table D.4: Fugacity coefficient equations for CH_4 at different temperatures

T (°C)	Fugacity Coefficient Equation	P range (psia)
35	$\Phi = 1-(1.056E-04)p+(8.695E-09)P^2+(4.162E-13)P^3+...$	0~1000
0	$\Phi = 1-(1.623E-04)p+(1.226E-08)P^2+(1.108E-12)P^3+...$	0~1000
-20	$\Phi = 1-(2.090E-04)p+(1.524E-08)P^2+(1.472E-12)P^3+...$	0~1000
-40	$\Phi = 1-(2.714E-04)p+(1.908E-08)P^2+(1.196E-12)P^3+...$	0~1000

Table D.5: Fugacity coefficient equations for C_2H_4 at different temperatures

T (°C)	Fugacity Coefficient Equation	P range (psia)
35	$\Phi = 1-(3.518E-04)p+(2.766E-08)P^2-(8.989E-12)P^3+...$	0~730
0	$\Phi = 1-(5.131E-04)p+(6.173E-08)P^2-(7.948E-11)P^3+...$	0~590
-20	$\Phi = 1-(6.450E-04)p+(7.872E-08)P^2-(1.746E-10)P^3+...$	0~360
-40	$\Phi = 1-(8.236E-04)p+(7.683E-08)P^2-(3.270E-10)P^3+...$	0~210

Table D.6: Fugacity coefficient equations for C_2H_6 at different temperatures

T (°C)	Fugacity Coefficient Equation	P range (psia)
35	$\Phi = 1-(4.690E-04)p+(5.487E-08)P^2-(5.125E-11)P^3+...$	0~710
0	$\Phi = 1-(6.791E-04)p+(9.012E-08)P^2-(2.090E-10)P^3+...$	0~340
-20	$\Phi = 1-(8.540E-04)p+(9.607E-08)P^2-(4.144E-10)P^3+...$	0~200
-40	$\Phi = 1-(1.096E-03)p+(1.129E-07)P^2-(1.083E-09)P^3+...$	0~110